The University of Sheffield

Characterization of InGaN Thin Films and Nanowires by Analytical Transmission Electron Microscopy

by

Xiaoyi Wang

Abstract

$In_xGa_{1-x}N$ are attractive semiconductor systems due to their emission wavelengths covering the range from ultraviolet to infrared. This makes them desirable for next generation visible light communication. The understanding of the relationship between emission wavelength and $In_xGa_{1-x}N$ chemistry can benefit InGaN growth and device fabrication. Photoluminescence, electroluminescence and cathodoluminescence are often sufficient to demonstrate the emission wavelength from $In_xGa_{1-x}N$, therefore the relationship between In concentration and emission wavelength can be revealed if the In content in the sample is well understood.

This research is started from the chemical analysis of $In_xGa_{1-x}N$ ($In_xGa_{1-x}N$/GaN) thin film heterostructures, which were grown on sapphire substrates. The nominal concentration is not always very reliable and therefore needs to be measured by analytical transmission electron microscopy. Electron energy loss spectroscopy (EELS) and energy-dispersive X-ray spectroscopy (EDXS) in a JEOL JEM 2010 F field emission gun TEM have been combined in the first part of this thesis, to evaluate the local indium concentration in those $In_xGa_{1-x}N$ thin films. The quantification of In concentration from EDXS is based on our X-ray absorption correction method, which provided a consistent In content, quantified from Ga K and Ga L X-ray lines. The results can serve as a calibration point for evaluating the bulk plasmon energy in low- loss EELS, as a function of In concentration.

An important aspect for growing high indium concentration InGaN heterostructure is phase separation. Phase separation means Ga-rich and In-rich regions form, rather than in growth where a perfect InGaN alloy is produced under the high temperatures of metal organic chemical vapour phase deposition (MOCVD). In the second part of this thesis, the EDXS absorption correction method is applied to analyse the In distribution from element maps, collected from a scanning transmission electron microscopy (STEM) mode, where the In-rich region (x>0.8) underneath the big island in $In_{0.68}Ga_{0.32}N$ can be directly observed. To further analyse the

components which form the In-rich area, and quantify the degree of phase separation, experimental low loss EELS spectrum were fitted with GaN, InN and InGaN reference spectra. The components in the In-rich area can be targeted by using reference spectra in the fitting routine, and their corresponding weights can represent the degree of phase separation. In this study, we have used the NION Ultra-STEM 100 TEM equipped with a monochromator, operating at 60kV to enhance the spectrum energy resolution and minimize electron beam induced damage. The result indicates the In-rich area is mainly formed of InN, rather than high In content InGaN ternary alloy. The averaged In concentration maps, which were calculated from EELS, correlated well with the EDXS mapping.

Finally, the EDXS absorption correction method is applied to quantify the In and Al concentration in $Al_yIn_xGa_{1-x-y}N$ nanowires. The analysis is mainly focused on the reliable quantification of In and Al content from low X-ray counts and noisy element maps. The result indicates a proper background subtraction for Ga L, Al K and Ga K, and geometry simulations for nanowires are necessary to obtain a consistent result with PL measurements. This approach will certainly benefit the beam sensitive material, and nanoparticle chemical analysis.

Acknowledgement

This thesis work was performed at the electrical and electronics engineering department at University of Sheffield, Sheffield, United Kingdom. During my last 3 years academic career, many people are providing their help and advices, the list is too long to name them all in this thesis. However, there are some people must be presented.

I would like to express my sincere gratitude to my PhD supervisor, Dr Thomas Walther for providing me a chance to work with the electron microscope group in EEE department. His intelligence and wealth of knowledge have guided me throughout my PhD research. Under his supervision, I have learned how to critically thinking and objectively analyse my result, also

how to create mathematically model to solve the physical problem. I really appreciate his tolerance of my working spirit during my tough time and also my English grammar issues. Special thanks also to Dr Ian Mark Ross, whose un-reserved TEM training makes me a qualified PhD student and qualified TEM user. I also appreciate the ion milling knowledges he provided in my first year PhD.

I would like to give my special thanks all members of Nanostructured Materials Microscopy group in Aristotle University of Thessaloniki, where I started to prepare my first TEM sample. A sincere gratitude is also going to my second supervisor, Prof Tao Wang for providing me the opportunity to be an experienced teaching assistant.

To my group members, Veerendra C Angadi and Guo Ran, thanks for their fruitful discussions, I really appreciate the quarrel with Mr Veerendra C Angadi about how to effectively model EELS spectrum with matlab coding.

And the last but not the least, I would like to thank my parents and my precious wife for their tolerance of my periodic short temper and frequently bank corruption. It is impossible to get my PhD without their endless love and financial support.

List of publications

1. X Wang, M P Chauvat, P Ruternana and T Walther (2015) Combination of electron energy-loss spectroscopy and energy-dispersive X-ray spectroscopy to determine indium concentration in InGaN thin film structures. *Semicond. Sci.Technol*. **30**(11), 114011.

2. T Walther and X Wang (2015), Self-consistent absorption correction for quantitative energy-dispersive X-ray spectroscopy of InGaN layers in analytical transmission electron microscopy. *Journal of Physics: Conference series* **644** (1).

3. T Walther and X Wang (2016) Self-consistent method for quantifying indium content from X-ray spectra of thick compound semiconductor specimens in a transmission electron microscope. *J. Microsc.* **262**(2),151-156.

4. X Wang, M-P Chauvat, P Ruterana and T Walther (2016), Investigation of phase separation in InGaN alloys by plasmon loss spectroscopy in a TEM. *MRS Advances* (2016) **1**:40, pp 2749-2756

5. X Wang and T Walther (2016), Joint plasmon and core-loss fitting for electron energy loss spectroscopy of InGaN. *European Microscopy Congress: proceeding*.

6. T Walther, X Wang, V C Angadi, P Ruterana, P Longo and T Aoki (2017) Study of phase separation in an InGaN alloy by electron energy loss spectroscopy in an aberration corrected monochromated scanning transmission electron microscope. *J. Mater. Res*. **32**(5), 983-995.

7. X Wang, M P Chauvat, P Ruterana and T Walther (2017) Effective absorption correction for energy dispersive X-ray spectroscopy in a scanning transmission electron microscope: analyzing the indium distribution in rough samples of InGaN alloy layers. *J. Microsc*. **268**, 248-253.

Contents

1. Introduction ... 1

1.1 Brief history and applications of III-nitrides semiconductors ... 3

1.2 Physical and chemical properties of III-nitrides ... 4

1.2.1 Crystal structure of III-nitrides ... 4

1.2.2 Chemistry of ternary III-nitride semiconductors ... 6

1.2.3 Band structure of III-nitrides ... 6

1.2.4 Piezoelectric effect and spontaneous polarization effect ... 7

1.2.5 III-nitride growth techniques ... 9

1.2.6 III-nitride nano-structures ... 11

1.2.7 InGaN phase separation ... 16

2. Analytical transmission electron microscopy ... 25

2.1 Principle of analytical transmission electron microscopy (ATEM) ... 25

2.1.1 Electron interaction with matter ... 25

2.1.2 Conventional transmission electron microscope (CTEM) and scanning transmission electron microscope (STEM) ... 26

2.1.3 Spherical aberration and chromatic aberration ... 32

2.2 Energy dispersive X-ray spectroscopy ... 35

2.2.1 Principle of X-ray generation in a (S)TEM ... 35

2.2.2 Absorption of X-ray ... 36

2.2.3 Fluorescence effect ... 37

2.2.4 EDXS detector of JEOL 2010F ... 38

2.2.5 Spatial resolution of EDXS ... 40

2.2.6 Energy resolution of EDXS ... 42

2.2.7 Accuracy of X-ray intensity measurement ... 44

2.2.8 Continuum (Bremsstrahlung) X-rays ... 44

2.2.9 Cliff-Lorimer quantitative analysis of EDXS ... 45

2.2.10 Monte Carlo simulations ... 47

2.2.11 STEM elemental map processing ... 48

2.3 Electron energy-loss spectroscopy (EELS) ... 50

2.3.1 Principle of EELS ... 50

2.3.2 Collection angle set-up by using spectrometer entrance aperture and camera length ... 51

2.3.3 EELS energy drift ... 52

2.3.4 The zero-loss peak (zlp) 54
2.3.5 Spectrometer dispersion 56
2.3.6 Valence EELS 57
2.3.7 Thickness determination from EELS and EFTEM 64
2.3.8 Delocalization of inelastic scattering 65
3. Quantification of In concentration in InGaN thin film ternary alloys with variable In content 72
3.1 TEM specimen preparation 73
3.2 Monte Carlo simulation of InGaN sensitivity factor (k^* factor) based on Ga K/L ratio 82
3.3 Determination of In concentration in $In_xGa_{1-x}N$ layers from EDXS by using k^* absorption correction 92
3.4 Analysing the In distribution in rough samples of InGaN alloy layer. 101
3.4.1 EFTEM measurement of sample thickness profile and structure simulation 104
3.4.2 EDXS absorption correction method for rough samples 110
3.4.3 STEM EDXS observation of In segregation in high In content InGaN 114
4. In concentration and phase separation determination for InGaN by valence EELS 130
4.1 Plasmon energy versus In concentration from different InGaN layers 131
4.2 Quantification of phase separation from low-loss EELS in a conventional TEM 137
4.2.2 Quantification of phase separation with reconstructed GaN, InN and InGaN spectra 145
5. Determination of degree of phase separation and bandgap of an InGaN ternary alloy by an monochromated STEM 155
5.1 quantifying the degree of phase separation of InGaN thin film from a conventional STEM 157
5.2 Determination of the degree of phase separation of InGaN thin film in an monochromated STEM 164
5.3 bandgap determination from STEM mode 178
6. Quantification of In and Al concentration in InGaN/ AlGaN quantum wells in GaN nanowires 193
6.1 Monte Carlo simulation of AlGaN k^* factor as function of Ga K/L ratio 195
6.2 Comparison of nanowire and thin film absorption geometry 196
6.3 quantification of In/Al concentration from low counts element maps in an $Al_yIn_xGa_{1-x-y}N$ nanowire 198
7. Conclusion 219
7.1 Suggestion for future work 221

Chapter 1

1. Introduction

This thesis describes the application of different methods of analytical (scanning) transmission electron microscope ((S)TEM) to indium gallium nitride (InGaN) thin films and InGaN quantum wells and aluminium gallium nitride (AlGaN) barriers embedded in gallium nitride (GaN) nanowire structures. Such layers could be the foundation of next generation of visible light communication and optoelectronics devices [1-3]. The optical and electrical properties of InGaN are strongly related to the indium concentration and strain [4]. By applying Vegard's law with a bowing parameter of b=2.87±0.20 eV for relaxed InGaN layer measured by Orsal et al [5], the bandgap of bulk InGaN can be related to the indium concentration as shown in Figure 1.

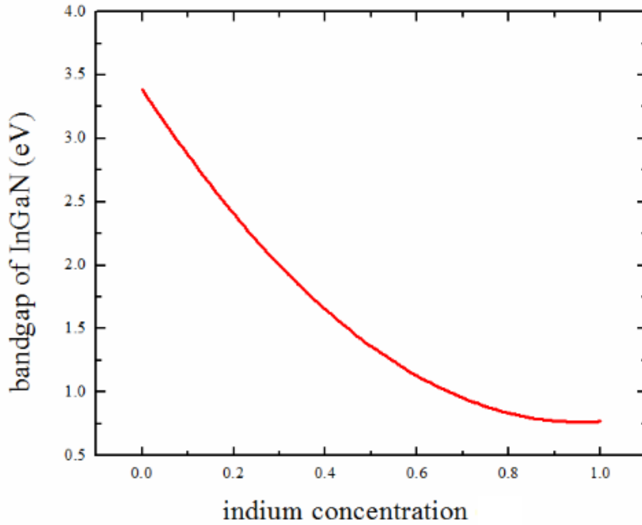

Figure 1: bandgap of unstrained bulk InGaN versus the indium concentration.

Based on Vegard's law, the differential equation for the relationship between emission wavelength shift Δλ and indium concentration change Δx can be written as

$$\Delta\lambda = -\frac{hc(-5.6+2.9x)\Delta x * e}{(3.4-5.6x+2.9x^2)^2} \quad (1)$$

where h is Planck's constant, c is the speed of light, e is the elementary charge, x is the indium concentration and Δx is the indium concentration change. The plot of In concentration as a function of emission wavelength shift is shown in Figure 2.

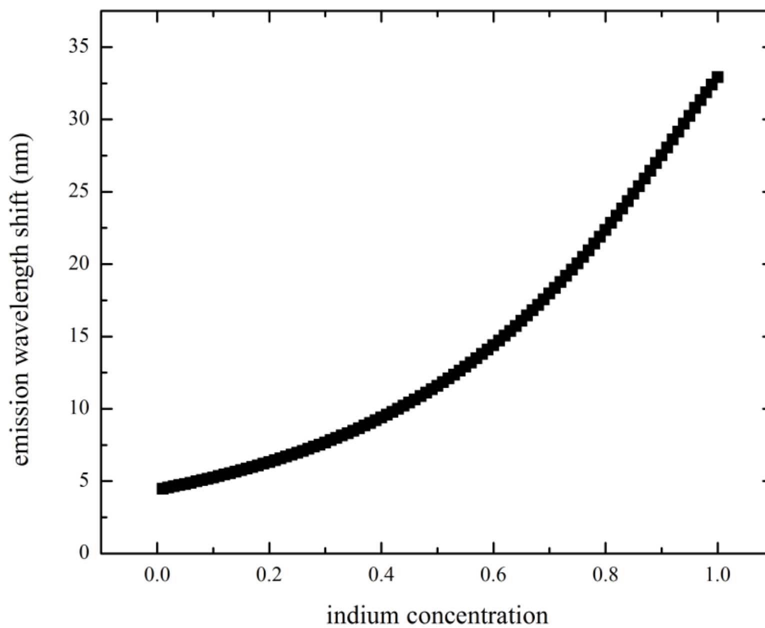

Figure 2: emission wavelength shifts versus indium concentrations

As observed from Figure 2, for low indium concentration ($x<0.5$), 1 percent of indium concentration change will lead to an emission wavelength red shift towards longer wavelength of about 5-10nm, which is not significantly changing the emission colour. On the contrary, at indium concentrations above 0.6, the emission wavelength is shifted by up to 15-35nm, towards emission at infrared wavelengths, so even 1 percent of indium concentration change may lead to a severe red shift. The nominal concentration as given by growth parameters is not always very reliable, in particular for very thin layers,

and therefore needs to be measured by independent methods, one of which, with high spatial resolution, is analytical transmission electron microscopy.

The microstructure and chemistry of a sample can be characterized by annular dark field imaging (ADF), the sample thickness measurement is conducted by energy filtered transmission electron microscopy (EFTEM), the elemental distribution is studied by self-consistent absorption corrected energy dispersive X-ray spectroscopy [6] and plasmon spectroscopy in electron energy loss spectroscopy (EELS) [7,8]. The main objective of this project is to analytically quantify the In concentration and phase separation in an InGaN ternary alloy to study regions of high In concentration in InGaN based nano-structures and help solve growth issues.

1.1 Brief history and applications of III-nitrides semiconductors

AlN GaN, InN and their ternary/quaternary alloy are commonly referred to as III-nitrides. The development of III-nitrides started when the first AlN was fabricated in 1907 [9]. The first InN and GaN crystals were produced in 1910 [10] and 1932 [11] respectively. Due to the III-nitrides being able to cover emission from ultraviolet to infrared, it is an ideal semiconductor system for the next generation of visible light communication and optoelectronics devices. Additionally, compared with traditional silicon-based electronics, GaN has superior Mohs hardness (GaN: 8 [12] compared with silicon: 7 [13]) and thermal stability (melting point of 2500ºC [12] for GaN compared with 1414ºC for Si [13]). Therefore, the III-nitrides have potential for fabrication of power electronics and electronics for harsh environments. Currently, most of the blue LED and laser diodes are fabricated from GaN. The first high brightness InGaN/GaN double heterostructure blue LED was demonstrated by Nakamura in 1994 [14]. The development of GaN based devices in early 1990s Japan can be regarded as the key evolution of modern solid-state optoelectronics. The research of GaN devices had been slowed

down for several decades since doped III-nitrides p-n junctions initially demonstrated a poor crystal quality. The first high crystal quality p-GaN based on Mg-doping was successfully fabricated in 1989 [15], which was a notable breakthrough for GaN based device fabrication. Following this, the first GaN laser action was observed in GaN [16]. A general review of physical and optical properties of III-nitrides will be provided in the following chapter sections.

1.2 Physical and chemical properties of III-nitrides

The physical and chemical properties of III-nitrides are essentially determined by the polar chemical bonds between group III and group V elements, the electronegativity difference between which is large (Al=1.18, Ga=1.13, In=0.99, N=3.0), resulting in strong polar chemical bonds in III-nitride materials [17]. Therefore, the III-nitrides are mechanically hard and chemically inert. GaN devices are frequently applied in power electronics and harsh environments because of those advantages.

The electron transitions between valence band and conduction band determine the optical properties of semiconductors. Different from indirect bandgap semiconductors such as Si, all III-nitrides have a direct bandgap [19,20]. The emission wavelength is determined by the bandgap 0.7 eV for InN and 6.4 eV for AlN [19, 20], and the emission of ternary alloys (AlGaN and InGaN) lies within this range. The wide range of the emission spectrum creates the possibility to fabricate highly efficient white LEDs and lasers with monolithically integrated devices.

1.2.1 Crystal structure of III-nitrides

The possible crystal structures of III-nitrides can be divided in three categories: zinc blende (cubic), wurtzite (hexagonal) and rock salt (NaCl) structure [21]. Mostly, epitaxial growth forms wurtzite III-nitrides, and in an ambient condition (room temperature and pressure) the thermodynamically stable crystal structure for bulk AlN, GaN and InN is wurtzite [22].

Traditionally, the epitaxial growth of III-nitrides uses sapphire as substrates (i.e. corundum, α-Al_2O_3) [17, 24, 25]; the growth of InGaN ternary alloy on sapphire substrate yields a hexagonal crystal structure. All the InGaN thin films in this work have been deposited on (0001) sapphire substrate with a GaN buffer layer, giving hexagonal structure. The GaN hexagonal crystal structure is shown in Figure 3 a). The wurtzite GaN crystal structure can be described as two hexagonal closed packed sub-lattices where the Ga sub-lattice is displaced by $5/8*c$ with respect to the N sub-lattice, where c is the lattice parameter along [0001] crystal axis [22]. The lattice parameter a has a relationship with the lattice parameter c given by c/a = 1.633 in the ideal (i.e., undistorted) wurtzite structure.

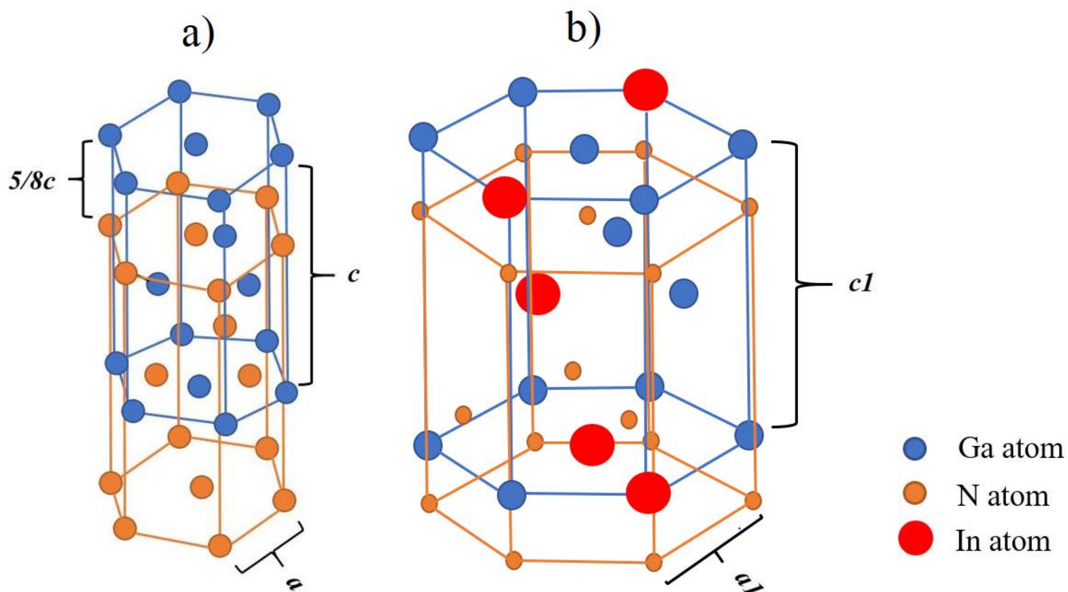

Figure 3 a) wurtzite GaN, b) wurtzite InGaN

The crystal structure of InGaN is essentially the same as that of GaN, forming an InGaN unit cell where some Ga atoms are substituted randomly by In atoms. As the In atomic radius is larger than the Ga, the lattice parameters of InGaN become bigger as more Ga atoms are replaced by In atoms. The wurtzite InGaN crystal structure is sketched in Figure 3 b).

1.2.2 Chemistry of ternary III-nitride semiconductors

Atomic percentage is used to describe the chemical composition. It determines the ratio of one element (In or Ga) to all elements (In, Ga and N) in an InGaN ternary alloy. In this thesis, we define x_{In} as concentration of indium atoms on the group III sublattice, expressed as:

$$x_{In} = \frac{N_{In}}{N_{In}+N_{Ga}} \times 100\% \quad (2)$$

where N_{In}, N_{Ga} and N_{N} are the number of In, Ga and N atoms in the unit cell of an InGaN ternary system. The total indium content in atomic% then is given by ½x_{In}. As illustrated in chapter 1.2.1, the lattice parameter is strongly related to the In concentration. The lattice parameter influences the bandgap of the semiconductor which will be described in chapter 1.2.3. Therefore, it is vital to determine the In concentration in an InGaN ternary alloy.

1.2.3 Band structure of III-nitrides

Whether the bandgap is direct or indirect is important for the application of inorganic semiconductors to photoconduction and electroluminescence [26-34] because it is one of the major factors that determine the efficiency of emission processes. III-nitrides, like most III-V semiconductors, have a direct band gap. The top of the valence band and the bottom of the conduction band are located at the centre of the Brillouin zone (Γ point). Therefore, direct transitions between the conduction band and valence band are possible. The band gap of III-nitrides material can be expressed by Vegard's law.

$$E_g(In_xGa_{1-x}N) = xE_g(InN) + (1-x)E_g(GaN) - bx(1-x) \quad (3)$$

where x is the molar fraction of In concentration (i.e. of group III sub-lattice occupancy) in InGaN. According to Figure 1, the unstrained InGaN bowing parameter has been measured as

b=2.87eV [5]. Previous experimental [5, 35] and theoretical [36] studies reported a bowing parameter of b≈1 eV for strained $In_xGa_{1-x}N$.

1.2.4 Piezoelectric effect and spontaneous polarization effect

Piezoelectricity is an effect whereby material can produce polarization in response to external stress (see Figure 4). A voltage can build up on the surface across the material. A polarization can be described macroscopically as

$$\boldsymbol{P} = \boldsymbol{D} - \varepsilon_0 \boldsymbol{E} \tag{4}$$

where $\boldsymbol{D}$ is the dielectric displacement, $\boldsymbol{E}$ is the electric field and ε_0 is the vacuum permittivity. Microscopically, the polarization vector is a vector such that:

$$\boldsymbol{P} = \boldsymbol{p} * n \tag{5}$$

where $\boldsymbol{p}$ is the (atomic or molecular) dipole moment and n is the number of charged dipoles per unit volume. The dipole moment is defined as

$$\boldsymbol{p} = q * \boldsymbol{d} \tag{6}$$

where q is the charge and $\boldsymbol{d}$ is the displacement of the charge, and points from - to + charge. Thus the polarization can be expressed as

$$\boldsymbol{P} = q * N * \boldsymbol{d} \tag{7}$$

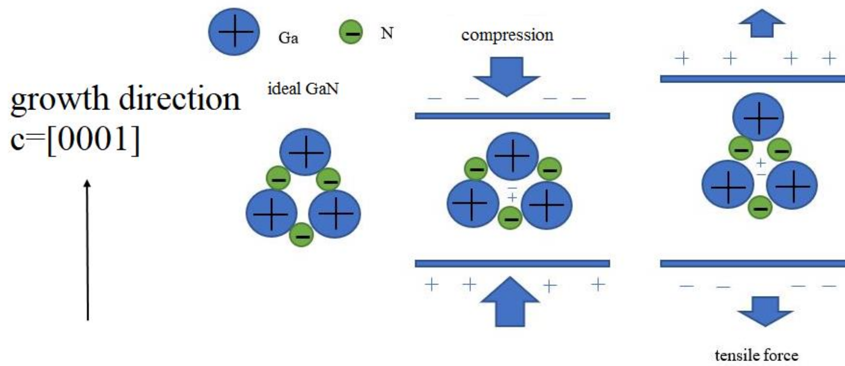

Figure 4: piezoelectric effect in GaN.

The piezoelectric effect is reversible. Polarisation can be produced when an external stress is applied, and stress is created when an electric field is applied. The piezoelectric effect was first discovered by brothers Pierre and Jacques Curie in 1880 [37]. The inverse effect was then deduced mathematically by Gabriel Lipmann in 1881 [38]. In the case of lattice misfit between substrate and semiconductor, stress can create piezoelectric effects in a semiconductor material which can affect the device performance. Spontaneous polarization is another important effect in wurtzite GaN system; a schematic of spontaneous polarization is demonstrated in Figure 5.

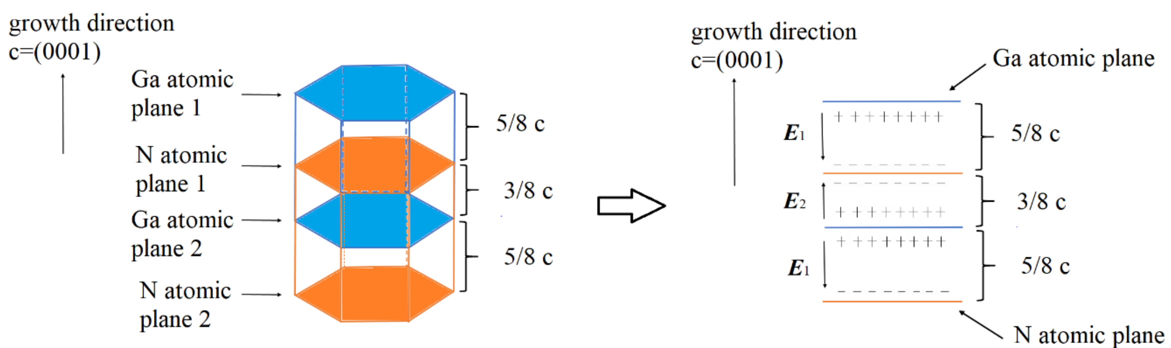

Figure 5: spontaneous polarization for GaN,

As shown in Figure 5, since the Ga atomic plane contains positive charges and N atomic plane contains negative charges, therefore, an electric field $\boldsymbol{E}_1$ can be generated between Ga atomic plane 1 and N atomic plane 1, and $\boldsymbol{E}_2$ is produced by N atomic plane 1 and Ga atomic plane 2. As demonstrated in Figure 5, since the N atomic plane 1 is displaced $5/8c$ with respect to Ga atomic plane 1, therefore, the N atomic plane 1 has a distance of $3/8c$ from the Ga atomic plane 2, leading to the $\boldsymbol{E}_1 \neq \boldsymbol{E}_2$, it is thus clear that an internal electric field cannot be totally cancelled since $\boldsymbol{E}_1 \neq \boldsymbol{E}_2$.This effect is commonly known as spontaneous polarization effect. For an InGaN/GaN heterostructure, the compressive strain induced piezoelectric field across the InGaN/GaN interface and the internal electric field produced by spontaneous polarization effect will tilt the energy bands, leading to the quantum confinement Stark effect. Less excitation energy is required to generate electron-hole pairs in a tilted band than in a flat band, which results in a red shift in the emission wavelength, in addition, as the overlap of electron and hole wavefunctions decreases, the transition probability will also decrease. Recent research confirmed the piezoelectric effect will lead to further emission wavelength red shift [39].

1.2.5 III-nitride growth techniques

The synthesis of semiconductor material can be categorized as bulk growth or epitaxial growth. The purpose of semiconductor bulk growth is mainly to produce suitable substrates for thin films, quantum wells and quantum dots. Bulk growth provides a cheap growth choice compared with epitaxial growth for wafer production. However, for GaN bulk material production is extremely difficult, due to the high pressure and temperature requirement, therefore, in current semiconductor technology, research interests are focusing on heteroepitaxial growth/deposition techniques. There are two advantages for epitaxial growth of semiconductors. Firstly, epitaxial growth has very good control of the semiconductor material's composition and nano-structure. Secondly, as the growth is usually on planar single crystalline substrates, the layer deposited can be of higher crystal quality than bulk. The

epitaxial growth techniques for III-nitride materials are metal-organic chemical vapour deposition (MOCVD), hydride vapour phase epitaxy (HVPE) and molecular beam epitaxy (MBE). In this thesis, six $In_xGa_{1-x}N$ (x from 0 to 1) thin films investigated were deposited on sapphire substrates with GaN buffer layers by using MOCVD and one $In_{0.3}Ga_{0.7}N$ thin film was grown by MBE.

1.2.5.1 Metal-organic chemical vapour deposition (MOCVD)

MOCVD is a typical chemical vapour deposition technique. MOCVD is usually used in manufacturing light-emitting diodes (LEDs), lasers, transistors, solar cells and other electronic and opto-electronic devices and is the key enabling technology for future semiconductor markets with high growth potential. In this technique, the III-nitride material is grown at high temperature either at normal atmospheric pressure or low pressure from gaseous metal-organic precursors. The precursors for InGaN can be trimethylgallium (TMGa), triethylgallium (TEGa) or trimethylindium (TMIn), and NH_3 is used for nitrogen [40]. In this work, the precursor for InGaN growth were TEGa, TMIn and NH_3. The MOCVD reaction process is:

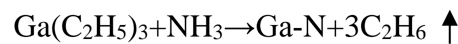

$$Ga(C_2H_5)_3+NH_3 \rightarrow Ga\text{-}N+3C_2H_6 \uparrow$$

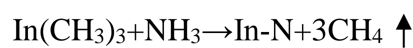

$$In(CH_3)_3+NH_3 \rightarrow In\text{-}N+3CH_4 \uparrow$$

where Ga-N and In-N represents the Ga (In) and N bonds according to Figure 3 b).

There are three important parameters that need to be monitored for the control of the growth of the III-nitride material: growth temperature, chamber total pressure and III/V ratio [40]. If the growth temperature is too high, thermodynamics can lead to the decomposition of the material. Since the In is easier to evaporate at high temperature than Ga, the evaporation of In will leave In vacancies in the material. However, when growth temperature is too low, the limited kinetics can lead to impurities incorporation, low surface mobility and structural defects. If the V/III ratio is too high, the high vapour pressure produced by group V species can result

in low surface mobility of group III atoms, and structural defects. When the III/V ratio is too high (too much group III precursor), this can lead to decomposition of InGaN or nitrogen vacancies [41]. Compared with MBE, MOCVD has a higher growth rate, typically a few μm per hour.

1.2.5.2 Molecular beam epitaxy (MBE)

Molecular Beam Epitaxy (MBE) is an typical physical deposition process. MBE is an ultra-high vacuum (UHV, with pressure p~10^{-10} torr) based technique for producing high quality epitaxial structures with monolayer (ML) control. MBE has evolved into one of the most widely used techniques for producing epitaxial layers of metals, insulators, semiconductors and superconductors, both at the research and the industrial production level. The key components of MBE are a pumping system and effusion cells. The pumping system must be efficient enough to reduce the residual impurity to a minimum, and effusion cells must provide excellent flux stability, uniformity and material purity [34]. The chemical reaction process of GaN MBE growth from gallium and nitrogen plasma is

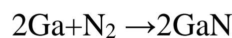

$$2Ga+N_2 \rightarrow 2GaN$$

Typical MBE growth rates for III-V type semiconductor materials are of the order of ~1ML/sec (1 μm/h).

1.2.6 III-nitride nano-structures

In the past decade, III-nitrides semiconductor have been gaining more research interest as their emission wavelength ranges from ultraviolet (200 nm for AlN [42]) to infrared (3200 nm for InN [43-45]). As the size of material decreases to nanoscale, the corresponding optical transition probability changes due to the quantum confinement. The density of states (DOS) describes the number of quantum states that are available per energy interval and per charge carrier in a system and is essential for determining the carrier concentration and energy

distribution of carriers within a semiconductor material. The number of quantum states is important in the determination of optical properties of a semiconductor.

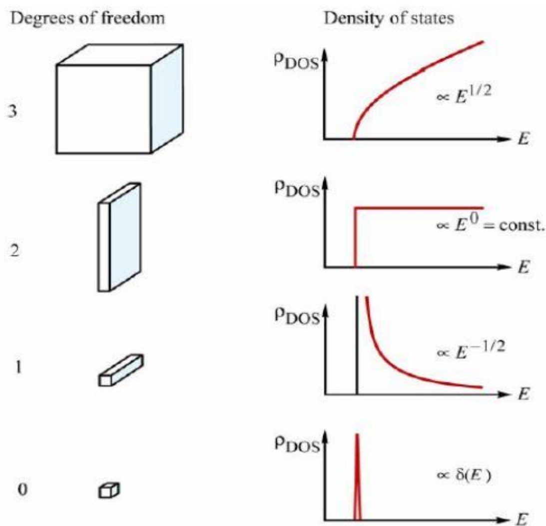

Figure 6: density of states with 3, 2, 1 and 0 degrees of freedom for electron propagation.

As shown in Figure 6, when the degree of freedom for electron propagation decreases from 3D to 0D, the number of energy levels which can be occupied by a free electron is decreased. Therefore, compared with bulk or thin film emission, quantum dots provide more coherent emission, which makes them suitable for fabricating better quality lasers [46].

1.2.6.1 Thin films

A thin film is a layer whose thickness can vary from several nanometers to micrometers (Figure 7); it can comprise both homostructures and heterostructures. A typical example is a mirror, where a silver thin film is coated on a glass plate to create a reflective surface. In semiconductor science, a very thin film is a means to providing quantum confinement depending on the layer thickness. The thin film can be deposited by either physical or chemical deposition techniques.

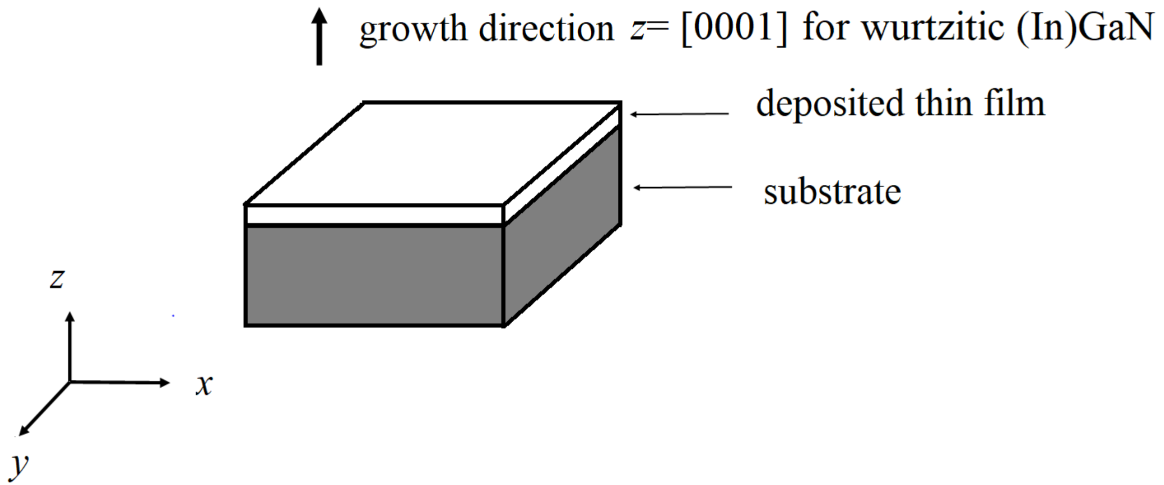

Figure 7: general thin film structure

1.2.6.2 Quantum well

Quantum wells are very thin layered semiconductor structures which exhibit quantum confinement effects. A thin "well" layer is surrounded by two "barrier" layers that confine the electron to well region. In a type-I quantum well both electrons and holes have lower energy than in the barrier layer, hence in this thin “well” both electrons and holes are confined if the well thickness L is less than the Bohr radius of the exciton. A valence electron can be pumped to conduction band by absorbing an electron or photon, and leaves a hole in the valence band. The electrons and holes can interact via the Coulomb potential, forming a quasi-particle called exciton. The model can be analogous to the hydrogen atom, with one bound electron orbiting around the single proton, therefore, the exciton radius of a semiconductor can be calculated via Bohr’s hydrogen atomic model. Because the quantum well is so thin, we cannot neglect the wave properties of the electron and hole. A typical quantum well structure is shown in Figure 8.

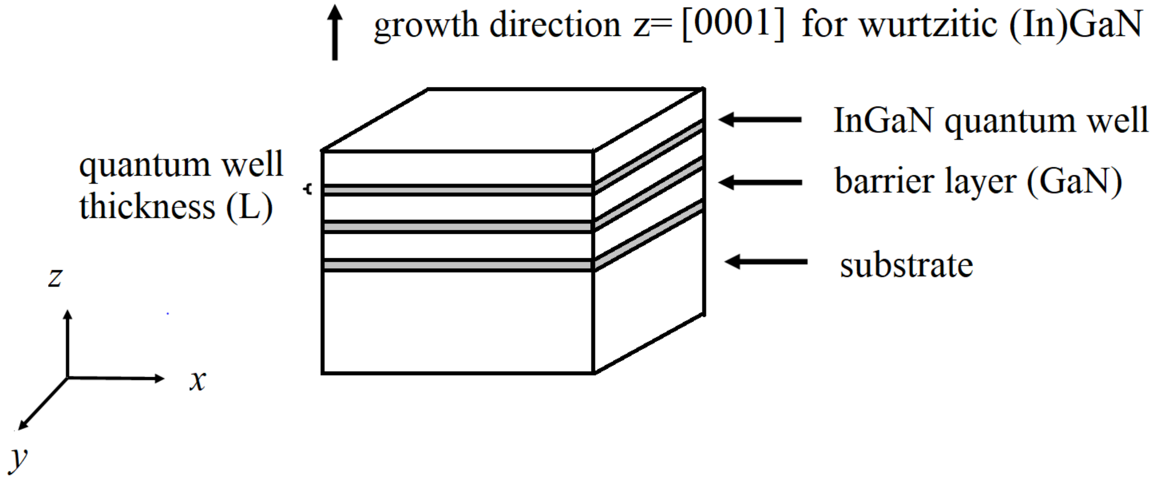

Figure 8: typical quantum well structure.

The electrons and holes are confined in the (*x*,*y*) plane perpendicular to the growth direction. For an infinite deep quantum well, the energy levels related to the quantum well width *L* can be calculated as [47]

$$E_n = \frac{\hbar^2 \pi^2 n^2}{2m^* L^2} \quad (8),$$

where $\hbar$ is the reduced Planck's constant, *n* is the quantum number associated with the energy level, m^* is the effective mass of the particle and *L* is the quantum well width. It is clear from equation (8) that the energy level spacings become larger for narrower quantum wells, resulting in a blue shift of the emission.

1.2.6.3 Nanowires

Nanowires are needle-like structures whose diameter is much smaller than their length. A typical nanowire diameter can range from 1 to 200nm with lengths of several hundred nanometers to tens of microns. The material to form a nanowire can range from electrical conductors to semiconductors and insulators [48-60]. InGaN nanowires can be fabricated by both bottom-up growth method [61] and top-down etching method [62]; in this thesis, the

investigated nanowire sample was fabricated by a top-down etching method. A SiO_2 thin film was deposited on the sample's surface of a commercial LED, then nickel islands were formed on the SiO_2 surface by thermal evaporation of Ni and annealing. Reactive ion etching was employed to create SiO_2/Ni nanorod mask. Finally, inductively coupled plasma etching was used to etch down into the InGaN, leaving behind the nanowires. The details of fabricating are described in chapter 6.

The structure of a typical InGaN multiple quantum well embedded in a GaN nanowire is shown in Figure 9.

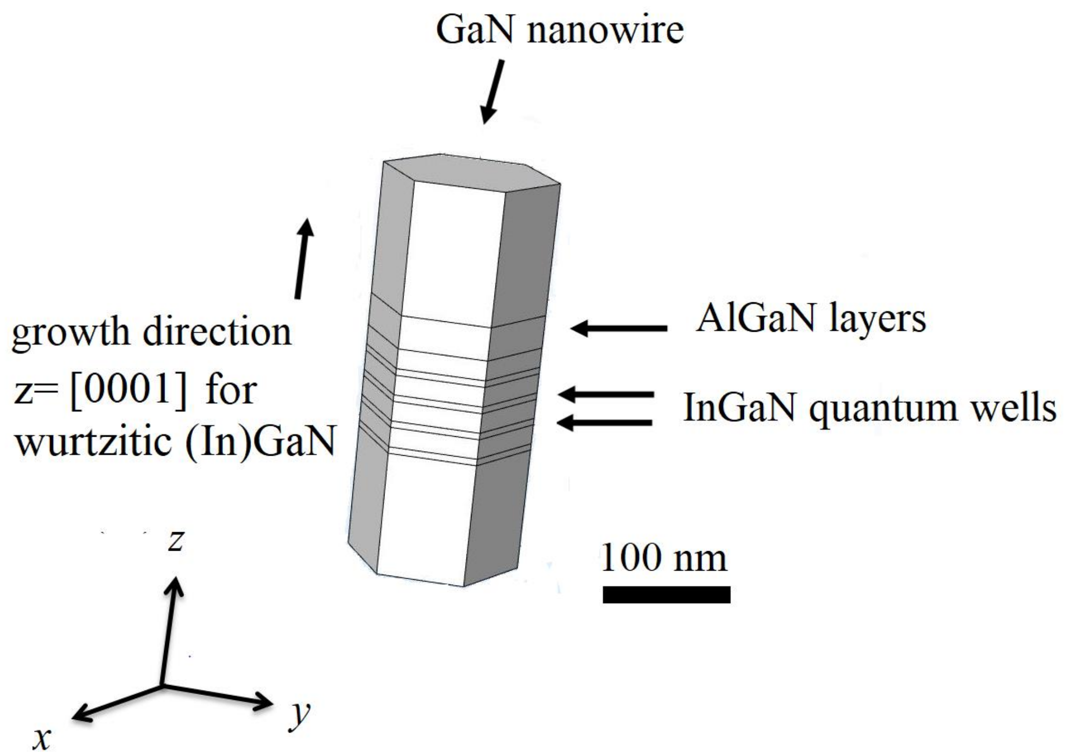

Figure 9: structure of $Al_yIn_xGa_{1-x-y}N$/GaN nanowires investigated in chapter 6.

A nanowire has the ability to confine the electron in two dimensions, x and y [63], so the electron can move freely only in z direction. The emission wavelength of the nanowire has strong dependence on its diameter [64]. Therefore, nanowires can be used as building blocks for advanced optoelectronics [65, 66]. In Figure 9, the electrons in the InGaN quantum wells

can have 0D confinement like in quantum dots if the nanowire is very thin, as the electron movement in *x* and *y* plane is confined by the extension of the GaN nanowire and, simultaneously, the InGaN quantum well provides quantum confinement in the *z* direction.

1.2.7 InGaN phase separation

If a binary mixture consists of components A and B that are immiscible, a typical phase diagram as depicted by the dotted curves in Figure 10 is obtained [67]. The homogeneous and heterogeneous phases are divided by a coexistence line in the graph. On the coexistence curve, the mixed and un-mixed states are in equilibrium with each other. Above the curve, it is only the homogeneous state. When quenched below the coexistence curve, the system is now unstable as a homogeneous mixture and will begin to separate into regions where only two pure components instead of the mixture are present. For InGaN/GaN heterostructures where compressive strain can be found at the interface of InGaN on GaN, the phase diagram should be re-calculated. The phase diagram in Figure 10 shows the result from [67] with overlaid data points for our samples.

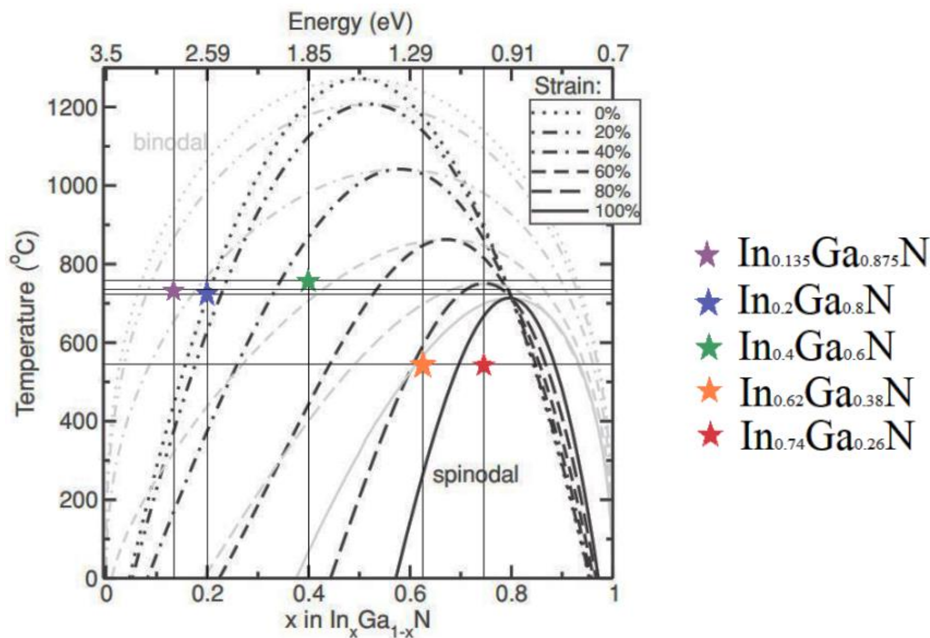

Figure 10: Spinodal (black dashed and dot-dashed curves) and binodal (light grey dashed and dot-dashed curves) curves calculated for different strain states of thin InGaN quantum wells on

a GaN substrate, as function of relative strain to that of free standing bulk InGaN [67]. Data points in colour refer to samples investigated in this thesis grown by MOCVD.

The solid black line in Figure 10 is called spinodal line. Under the spinodal curve, two pure components instead of a single mixed phase are present. Under the binodal curves alloys are meta-stable. The strain state in Figure 10 is relative to bulk InGaN. As shown, the increase of compressive strain may lead to a reduced miscibility gap but shifts it towards higher In content. At 725°C growth temperature, $In_{0.135}Ga_{0.875}N$ and $In_{0.2}Ga_{0.8}N$ are predicted to lie (just) outside the dotted curve and so can form perfect ternary alloys, whether strained or relaxed. For $In_{0.4}Ga_{0.6}N$ grown at 750 °C [or $In_{0.62}Ga_{0.38}N$ grown at 550 °C], to produce a ternary alloy, the strain should be >50% [>85%]. It is clear that for the $In_{0.74}Ga_{0.26}N$ sample grown at 550 °C, strong phase separation is expected for all strain states. In order to produce perfect alloy for $In_{0.74}Ga_{0.26}N$, the growth temperature would need to be >800 °C, at which it would be experimentally difficult to prevent In desorption, however. The lattice mismatch between InN and GaN, together with In evaporation at high growth temperature, thus affects crystal quality.

Chapter conclusion

This chapter provides a general review of InGaN and its related nano-structures, physical and chemical properties. The major obstacle for high In content InGaN growth is phase separation, particularly for thicker, partially relaxed films. Since In concentration and crystal quality are strongly related and both influence device performance, a reliable quantification method is necessary to improve the growth quality of InGaN and related nano-structures.

References

[1] J M M Santos, S Rajbhandari, D Tsonev, H Chun, B Guilhabert, A B Krysa, A E Kelly, H Haas, D C O'Brien, N Laurand, and M D Dawson (2016) Visible light communication using InGaN optical source with AlInGaP nanomembrane down-converters. *Opt. Express* **24**, 10020-10029.

[2] M Marso, M Mikulics, A Winden, Y C Arango, A Schafer, Z Sofer, D Grützmacher, H Hardtdegen (2014) InGaN nano-LEDs for energy saving optoelectronics. *The Tenth International Conference on Advanced Semiconductor Devices and Microsystems*, Smolenice, pp. 1-4.

[3] S Nakamura, M Senoh, N Iwasa and S Nagahama (1995) InGaN multi-quantum-well-structure laser diodes with cleaved mirror cavity facets. *Jpn J. Appl. Phys*, **34** (7A) L797

[4] C M Liu, Y Tai, K H Chen, L C Chen (2014) Fabrication of m-axial InGaN nanocolumn arrays on silicon substrates using triethylgallium precursor chemical vapor deposition approach. *Appl. Surf. Science.* **299**, 92–96.

[5] G Orsal, Y El Gmili, N Fressengeas, J Streque, R Djerboub, T Moudakir, S Sundaram, A Ougazzaden and J P Salvestrini (2014) Bandgap energy bowing parameter of strained and relaxed InGaN layers. *Opt. Mat. Exp.* **4**(5), 1030-1041.

[6] T Walther and X Wang (2016) Self-consistent method for quantifying indium content from X-ray spectra of thick compound semiconductor specimens in a transmission electron microscope. *J. Microsc.* **262**(2), 151-156.

[7] X Wang, M P Chauvat, P Ruterana and T Walther (2016) Investigation of phase separation in InGaN alloys by plasmon loss spectroscopy in a TEM. *MRS Advances* **1**:40, 2749-2756.

[8] T Walther, X Wang, V C Angadi, P Ruterana, P Longo and T Aoki (2017) Study of phase separation in an InGaN alloy by electron energy loss spectroscopy in an aberration

corrected monochromated scanning transmission electron microscope. *J. Mater. Res*. **32**(5), 983-995.

[9] F Fichter (1907) *Z Anorg, Chem*. **54**, 322 (in german).

[10] F Fischer and F Schroeter (1910) *Ber. Deutschen Chemischen Gesellschaft* **43** 1465 (in german).

[11] W C Johnson, J B Parsons and M C Crew (1932) Nitrogen compound of gallium. III. *J. Phys. Chem*. **36**, 2561.

[12] https://en.wikipedia.org/wiki/Silicon, access on 28/06/2018.

[13] https://en.wikipedia.org/wiki/Gallium_nitride#cite_note-b92-1, access on 28/06/2018.

[14] S Nakamura, T Mukai and M Senoh (1994) Candela‐class high‐brightness InGaN/AlGaN double‐heterostructure blue‐light‐emitting diodes. *Appl. Phys. Lett.* **64**, 1687.

[15] H Amano, M Kito, K Hiramatsu and I Akasaki (1989) p-Type Conduction in Mg-doped GaN treated with Low-Energy Electron Beam Irradiation (LEEBI). *Jpn. J. Appl. Phys*. **28**. L2112-L2114.

[16] R Dingle, K L Shaklee, R F Leheny and R B Zetterstrom (1971) Stimulated emission and laser action in gallium nitride, *Appl. Phys. Lett.* **19**, 5−7.

[17] H Amari (2011) Characterization of AlGaN and InGaN thin film and quantum wells by analytical transmission electron microscopy, PhD thesis, University of Sheffield.

[18] I Akasaki, H Amano (1997) Crystal Growth and Conductivity Control of Group III Nitride Semiconductors and Their Application to Short Wavelength Light Emitters. *Jpn. J. Appl. Phys*. **36**, 5393.

[19] V Y Davydov, A A Klochikhin, R P Seisyan, V V Emtsev, S V Ivanov, F Bechstedt, J Furthmuller, H Harima, A V Mudryi, J Aderhold, O Semchinova and J Graul (2002)

Absorption and emission of hexagonal InN. Evidence of narrow fundamental band gap. *phys. stat. sol. (b)* **229**, R1.

[20] O Madelung (1991) *Semiconductors*: *Group IV elements and III-V Compounds. Data Science and Technology*, Springer-Verlag, Berlin.

[21] S Strite and H Morkoc (1992) GaN, AlN, and InN: A review. *J. Vac. Sci. Technol*. B **10**, 1237.

[22] H Morkoc (2008) *Handbook of Nitride Semiconductors and Devices*. Vol **1**, Wiley-VCH, Weinheim.

[23] T Wang (2016) Topical review: Development of overgrown semi-polar GaN for high efficiency green/yellow emission. *Semicond. Sci & Technol*. **31**, 093003.

[24] H Sato, T Sugahara, Y Naoi and S Sakai (1998) Compositional inhomogeneity of InGaN grown on sapphire and bulk GaN substrate by metalorganic chemical vapor deposition. *Jpn. J.Appl. Phys.* **37**, 2013-2015.

[25] Q X Guo, T Yamamura, N Itoh and A Yoshida (1994) Structural properties of InN films grown on sapphire substrates by microwave-excited metalorganic vapor-phase epitaxy. *J. Appl. Phys.* **75**, 4927.

[26] J I Pankove (1971) *Optical processes in semiconductors*. Englewood Cliffs, N.J. Prentice-Hall.

[27] R H Bube (1960) Photoconductivity of solids, Wiley, New York.

[28] A L Fahrenbruch and R H Bube (1983) *Fundamentals of solar cells*. Academic Press, New York.

[29] L C Kimering, K D Kolenbrander, Michel J and Palm J (1997) Light emission from silicon. *Solid State Phys* **50** 333.

[30] L Smart and E Moore (1992) *Solid state chemistry*. Chapman & Hall, London.

[31] J A Mazer (1997) *Solar cells: an introduction to crystalline photovoltaic technology.* Kluwer, Boston.

[32] N V Joshi (1990) *Photoconductivity: art, science and technology*. Dekker, New York.

[33] R C Neville (1995) *Solar energy conversion: the solar cell.* 2nd edn. Elsevier, Amsterdam.

[34] G Biasiol and L Sorba (2001), Molecular Beam Epitaxy: Principles and Applications, *Crystal growth of materials for energy production and energy-saving applications*. R Fornari, L Sorba, Eds (Edizioni ETS, Pisa, 2001).

[35] S Nakamura (1997) III-V nitride based light-emitting devices. *Solid State Commun.* **102**, 237.

[36] A F Wright, J S Nelson (1995) First-principles calculations for zinc-blende AlInN alloys. *Appl. Phys. Lett.* **66**, 3465-.

[37] J Curie, P Curie (1880) Contractions et dilatations produites par des tensions dans les cristaux hémièdres à faces inclinées. *C R Acad. Sci. Gen*. **93**, 1137–1140.

[38] A Ledoux (2011) Theory of piezoelectric material and its application to civil engineering. Masters thesis, MIT.

[39] N I Bochkateva, A L Bogatov, R I Gorbunov, F E Latyshev, A S Zubrilov, A I Tsyuk, A V Klochkov, Y S Lelikov, Y T Rebane and Y G Shreter (2009) Effect of the electric field on the intensity and spectrum of emission from InGaN/GaN quantum wells. *Semiconductors*. **43** (11), 1499-1505.

[40] D Walker, X Zhang, A Saxler, P Kung and M Razeghi (1997) $Al_xGa_{1-x}N$ ($0<x<1$) ultraviolet photodetectors grown on sapphire by metal-organic chemical-vapor deposition. *Appl. Phys. Lett.* **70**, 949-.

[41] A Koukitu and Y Kumagai (2001) Thermodynamic analysis of group III nitrides grown by metal-organic vapour-phase epitaxy (MOVPE), hydride (or halide) vapour-phase epitaxy (HVPE) and molecular beam epitaxy (MBE). *J. Phys: Cond. Matter* **13**, 6907-.

[42] Y Taniyasu, M Kasu and T Makimoto (2006) An aluminium nitride light-emitting diode with a wavelength of 210 nanometers. *Nature* **441**, 325–328.

[43] J Wu, W Walukiewicz, K M Yu, J W Ager III, E E Haller, H Lu, W J Schaff, Y Saito and Y Nanishi (2002) Unusual properties of the fundamental band gap of InN. *Appl. Phys. Lett*. **80**, 3967

[44] G Koblmuller, C S Gallinat, S Bermardis, J S Speck, G D Cheng, E D Readinger, H Shen and M Wraback (2006) Optimization of the surface and structural quality of N-face InN grown by molecular beam epitaxy. *Appl. Phys. Lett*. **89,** 071902

[45] J Kamimura, K Kishino and A Kikuchi (2010) Dislocation reduction via selective-area growth of InN accompanied by laterial growtn by rf-plasa-assisted molecular-beam epitaxy. *Appl. Phys. Lett*. **97**, 141913.

[46] N N Ledentsov (2011) Quantum dot laser. *Semicond. Sci. Technol*. **26** (1), 014001.

[47] S M Sze and K K Ng (2007) *Physics of semiconductor devices.* John Wiley & Sons, Inc., Hoboken, New Jersey.

[48] J Hu, T W Odom and C M Lieber (1999) Chemistry and physics in one dimension: synthesis and properties of nanowires and nanotubes. *Acc. Chem. Res*, **32**, 435–445.

[49] Y Wu, H Yan, M Huang, B Messer, J H Song and P Yang (2002) Inorganic semiconductor nanowires: rational growth, assembly, and novel properties. *Chem. Eur. J.*, **8**, 1260–1268.

[50] N I Kovtyukhova and T E Mallouk (2002) Nanowires as building blocks for self - assembling logic and memory circuits. *Chem. Eur. J.*, **8**, 4354–4363.

[51] P Yang, Y Wu and R Fan (2002) Inorganic semiconductor nanowires. *Int. J. Nanosci.* **1**, 1–40.

[52] Y Xia, P Yang, Y Sun, Y Wu, B Mayers, B Gates, Y Yin, F Kim and H Yan (2003) One-dimensional nanostructures: synthesis, characterization, and applications. *Adv. Mater.* **5**, 353–389.

[53] C M Lieber (2003) Nanoscale science and technology: building a big future from small things. *MRS Bull.* **28**, 486–491.

[54] M Law, J Goldberger and P Yang (2004) Semiconductor Nanowires and Nanotubes, *Annu. Rev. Mater. Res.* **34**, 83–122.

[55] Z L Wang (2004) Zinc oxide nanostructures: growth, properties and applications. *J. Phys. Condens. Matter* **16**, R829–R858.

[56] Y Huang and C M Lieber (2004) Integrated nanoscale electronics and optoelectronics: exploring nanoscale science and technology through semiconductor nanowires, *Pure Appl. Chem.*, **76**, 2051–2068.

[57] C J Murphy, T K Sau, A M Gole, C J Orendorff, J Gao, L Gou, S E Hunyadi and T Li (2005) Anisotropic metal nanoparticles: synthesis, assembly and optical Applications. *J. Phys. Chem. B*, **109**, 13857–13870.

[58] P Yang (2005) The chemistry and physics of semiconductor nanowires. *MRS Bull.*, **30**, 85–91.

[59] J Goldberger, R Fan and P Yang (2006) Inorganic nanotubes: a novel platform for nanofluidics. *Acc. Chem. Res.*, **39**, 239–248.

[60] S J Hurst, E K Payne, L Qin and C A Mirkin (2006) Multisegmented one dimensional nanorods prepared by hard-template synthetic methods. *Angew. Chem. Int. Ed.*, **45**, 2672–2692.

[61] W Guo, A Banerjee, P Bhattacharya and B S Ooi (2011) InGaN/GaN disk-in-nanowire white light emitting diodes on (001) silicon. *Appl. Phys. Lett*. **98**, 193102.

[62] X Wang, J Bai and T Walther (2018) Self-consistent absorption correction for quantification of noisy X-ray maps of group III nitride nanowires. *submitted to J. Microsc.*

[63] J C Johnson, H J Choi, K P Knutsen, R D Schaller, P Yang and R J Saykally (2002) Single gallium nitride nanowire lasers. *Nature Materials*, **1**, 107-110.

[64] G C Yi (2012) *Semiconductor Nanostructures for Optoelectronic Devices*, *NanoScience and Technology,* Springer, Heidelberg.

[65] X Duan, Y Huang, Y Cui, J Wang, and C M Lieber (2001) Indium phosphide nanowires as building blocks for nanoscale electronic and optoelectronic devices. *Nature* **409**, 66–69.

[66] J Wang, M S Gudiksen, X Duan,., Y Cui and C M Lieber (2001) Highly polarized photoluminescence and photodetection from single indium phosphide nanowires. *Science* **293**, 1455–1457.

[67] C Tessarek, S Figge, T Aschenbrenner, S Bley, A Rosenauer, M Seyfried, J Kalden, K Sebald, J Gutowski and D Hommel (2011), Strong phase separation of strained InGaN layers due to spinodal and bimodal decomposition: formation of stable quantum dots. *Phys. Rev. B* **83,** 115316.

Chapter 2

2. Analytical transmission electron microscopy

2.1 Principle of analytical transmission electron microscopy (ATEM)

2.1.1 Electron interaction with matter

If an electron beam is incident on a material, the electron is interacting with the atoms and generates a variety of signals, as shown in Figure 11.

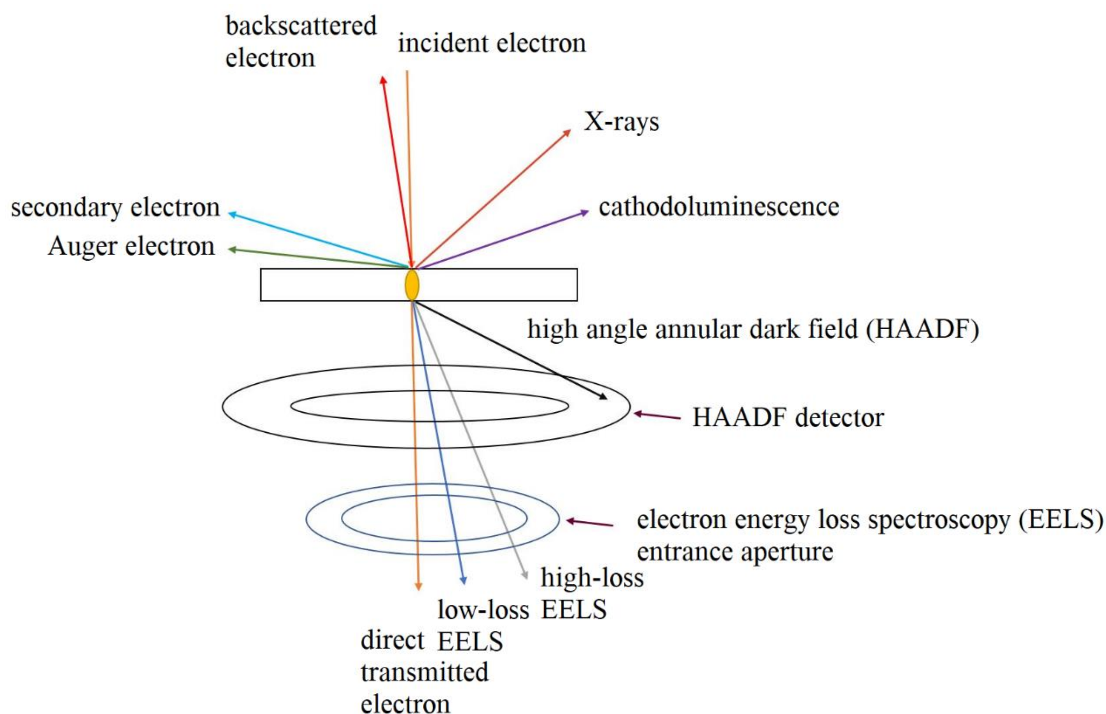

Figure 11: signals generated by the interaction of the primary electron and material

As shown in Figure 11, the interaction is producing characteristic X-rays, cathodoluminescence, Auger electrons, backscattered electrons, secondary electrons, inelastically scattered electrons, elastically scattered electrons and transmitted electrons. A bright field, dark field or high resolution TEM image can be formed by detecting the elastically diffracted electrons (where the electron Bragg diffraction angles are somewhere between the direct transmitted electrons, orange in Figure 11, and the very highly scattered ones, black in Figure 11), while the inelastically scattered electrons (usually at small electron deflection angle i.e. dark blue or grey

in Figure 11) can be used for EELS analysis. For our GIF 200 EELS spectrometer, the system provides nominal dispersions from 0.05eV/channel to 1 eV/channel. The highest dispersion, measured as 0.0502eV/channel [1] and 1 eV [2], is ideal for recording low-loss spectra. As the detector has 1024 pixels in size, to accommodate the zero-loss peak in the spectrum, the corresponding energy loss upper limit is ~50 eV for low-loss spectroscopy. The characteristic angle for inelastic scattering calculated by equation (26) for energy losses of up to 50eV is 0.13 mrad. So for a parallel illumination (TEM mode), the collection angle should be set up larger than 0.13 mrad to record all low loss EELS information. For higher core losses of InGaN, where the In $M_{4,5}$ edge is located around 443 eV, and Ga L_2 and L_3 edges lie around 1142 eV and 1115 eV respectively, to accommodate these higher core-loss edges in a single EELS spectrum, the collection angle should be larger than 2.9 mrad. The JEOL 2010F microscope used in this project has the ability to also record annular dark-field (ADF) STEM images, where the inner collection angle can be varied from 35 mrad (ADF) to 55 mrad (HAADF) and the outer collection angle is ~170 mrad, so EELS and HAADF can be acquired simultaneously.

2.1.2 Conventional transmission electron microscope (CTEM) and scanning transmission electron microscope (STEM)

The transmission electron microscope (TEM) is a powerful tool for characterization of materials. The CTEM operation method is similar to a conventional optical microscope, where the interesting area in the thin sample is illuminated by a parallel beam of high energy electrons that produce a variety of useful signals which can be studied by imaging, diffraction and spectroscopy methods [3]. By combination of these, the physics and chemistry of the material can be understood fully, which can benefit the understanding of the material. A typical TEM can be divided into three components, which are illumination system (electron gun and condenser system), image forming system (objective and projection system) and image or

spectrum recording system (detector) [correct ref]. The beam diameter and the current density are mainly determined by the upper condenser lens and aperture, while the field of view is determined by lower condenser lens and aperture. The spatial resolution of CTEM is constrained by the diffraction limit of the electrons at the aperture.

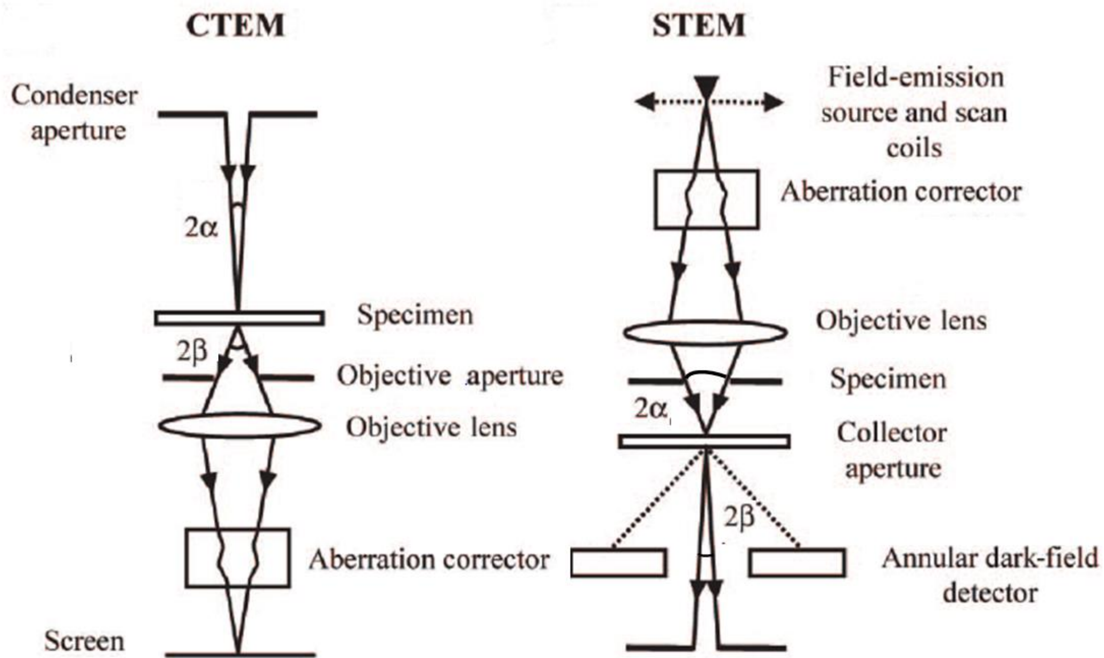

Figure 12: electron optics diagram of CTEM and STEM (corrected from top down) [4].

The STEM is essentially a mixture of a scanning electron microscope and a transmission electron microscope, where a fine and highly converged electron beam is scanned over the region of interest, each position giving individual information on the material in that small interaction volume. The STEM electron beam current is determined by the condenser lens and aperture, while the beam diameter and convergence angle are related to the condenser system and 1st objective lens. The spatial resolution in STEM of thin samples is limited mainly by the beam diameter. The optics diagram of CTEM and STEM are shown in Figure 12 [4].

2.1.2.1 Field emission gun

The electron source of a transmission electron microscope can be a thermionic or a field emitter. The typical thermionic emission gun is made of tungsten (W) or LaB_6 [5]. The Schottky field emission gun for our JEOL 2010F is made of W coated with ZrO_2. The cold field emission gun in our JEOL Z3100 R005 uses a single crystal W needle as emission source.

The brightness of the illumination can be defined as beam current density per solid angle, as demonstrated in equation (9):

$$J = \frac{i}{\pi(\frac{d_0}{2})^2 \pi(\alpha \quad)^2} \tag{9}$$

where J is the beam current density per solid angle, i is the beam current, d_0 is the diameter of the gun cross-over and α is the electron convergence semi-angle. A FEG has a higher brightness than a thermionic emitter [5]. The higher brightness can lead to higher beam current density and so smaller STEM probes or it can be used to achieve a more parallel electron beam in TEM. However, a high current can cause more beam damage to the investigated material at given accelerating voltage.

The energy spread of the electron source is important for analytical transmission electron microscopy: a smaller value of energy spread represents higher coherence of the electron beam emitted from the electron source. The measurement of the energy spread can be conducted with a spectrometer, for example, the GIF 200 in our JEOL 2010F. The energy spread determines the energy resolution and is usually represented by the full width at half maximum (FWHM) of the zero-loss peak in electron energy loss spectroscopy.

2.1.2.2 Condenser lens and aperture

The condenser lens is used to form the electron beam on the specimen. The strength of the condenser lens can limit the amount of beam current. In addition, the beam diameter can be also controlled by the condenser system. Figure 13 shows the optics diagram of an electron beam for double condenser system operations.

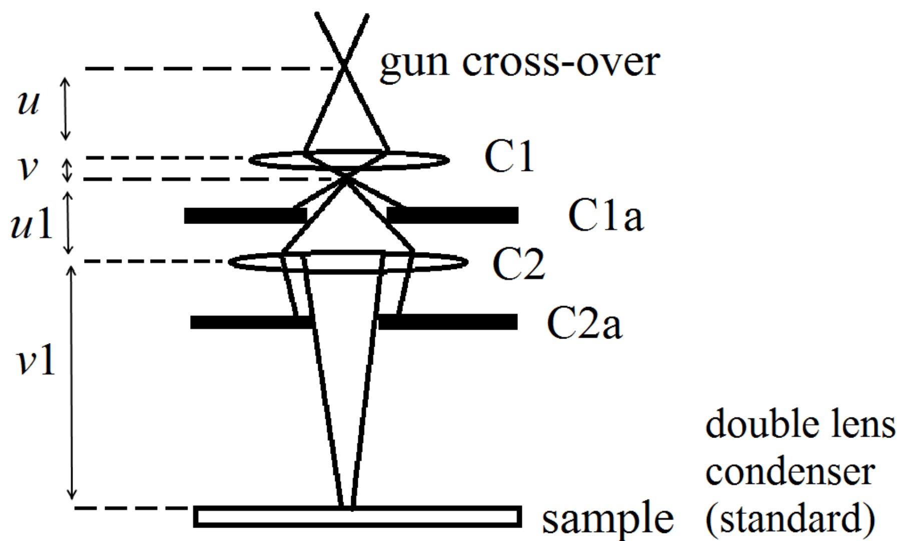

Figure 13: electron beam optics for standard double condenser systems.

If there was no condenser system to converge the electron beam, the illumination area would be huge, which is not suitable for nanoscale characterization. Therefore, a condenser system must be added to form a probe which is desired for sample investigation area. If a condenser lens C1 is placed underneath the anode, assuming the gun cross-over size for a FEG is s=0.01µm, the smallest spot size can be calculated by equation (10) [6] as

$$d_m = s\frac{v}{u} \tag{10}$$

where d_m is the smallest spot diameter, s is the size of the gun cross-over, v is the distance between gun cross-over and C1 lens, u is the distance between C1 lens to specimen. If a nano-probe is required, v should be at least 10 times smaller than u. It is hard to accommodate and

focus the sample within that distance *v*. Thus, it is possible to form a nano probe less than 1nm by further adding a C2 condenser lens, as in Figure 13. This has the additional advantage that now spot size and convergence angle can be adjusted independently.

In the condenser system, the condenser aperture plays an important role to control the beam current density and convergence angle, also the C1 aperture can avoid the generation of stray X-ray from the pole-piece. In Figure 13, if the aperture C1a is removed, the electrons deflected by a large angle will hit the pole-piece of the C2 lens or the specimen holder, which can generate stray X-rays. This is problematic for energy dispersive X-rays analysis. The aperture C2a can be used to control the beam current on the sample, where a larger aperture can provide higher electron beam intensity, however, the coherence of the electron beam will become poor. A small aperture limits the solid angle subtended by the C1 cross-over, and the coherence of the electron beam is improved at the expense of lower image intensity.

Modern microscopes are often equipped with a condenser mini-lens and objective pre-field lens acting as a third condenser lens; the optics diagram of TEM and STEM operation with condenser mini-lens and objective pre-field lens is demonstrated in Figure 14.

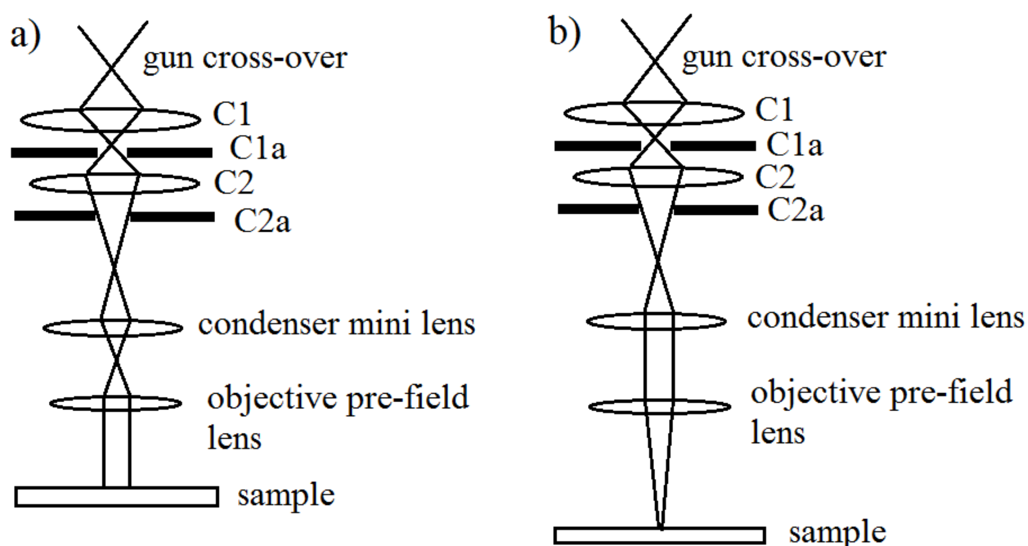

Figure 14: electron beam optics diagram with condenser mini-lens and objective pre-field lens for a) TEM mode b) STEM mode.

As shown in Figure 14 a), to form a parallel beam in TEM, the condenser mini-lens firstly takes the cross-over formed by C1 and C2 lenses and images it on the pre-focal plane of the objective pre-field lens with strong convergence of the electron beam, then a parallel beam can be formed by switching off or weakly exciting the objective pre-field lens. The parallel beam size is given by equation (11) [7].

$$d = \frac{\alpha}{M_{CL} M_{CM}} f_{obj} \tag{11}$$

where d is the beam diameter on the sample, α is the convergence semi-angle formed by condenser aperture, M_{CL} and M_{CM} are the magnifications of condenser lens and condenser mini-lens, respectively, and f_{obj} is the focal length of the objective lens. By increasing the beam diameter on the sample, the values M_{CL} and M_{CM} must be reduced, as the focal length of condenser mini-lens is fixed by the objective length, which simultaneously fixes the focal length of the condenser. Therefore, reducing M_{CL} will lead to further reduction of M_{CM}.

As demonstrated in Figure 14 b), to form a converged beam in STEM mode, the condenser mini-lens should be switched off or weakly excited in order to form a parallel beam onto the objective pre-field lens, a finely converged electron beam will then be produced by the strong objective pre-field lens excitation. As the condenser mini-lens is switched off, the beam diameter is mainly determined by the magnification of condenser lens system M_{CL}, therefore, the beam diameter d in equation (12) can be rewritten as

$$d = \frac{\alpha}{M_{CL}} f_{obj} \tag{12}$$

It is thus clear that the beam diameter can be further decreased by increasing the de-magnification of the condenser lens system.

The determination of probe size from convergence angle in STEM is useful for both EDXS and EELS mapping. The probe size should ideally correspond to the pixel size in each elemental map or spectrum image, which defines the spatial sampling of the elemental map

and EELS spectrum image. Optimizing the convergence angle can also limit the spherical aberration to the spectrum image in EELS, which will be discussed in the next chapter.

2.1.3 Spherical aberration and chromatic aberration

The spherical aberration is caused by inhomogeneity of the magnetic strength of the lens system, resulting in the off-axis rays failing to converge at the same point [8]. A ray diagram of spherical aberration is shown in Figure 15.

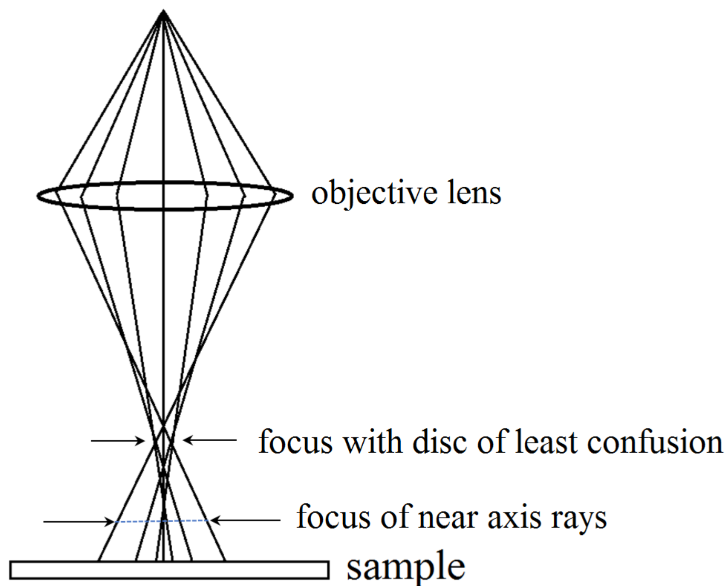

Figure 15: spherical aberration

From Figure 15 it is clear that a point object is imaged as a disc of finite size, which decreases the spatial resolution of the image. As Reimer implied [9], at small convergence semi-angle, the diffraction limitation (d_d=0.61λ/α) dominates the probe size, while at large convergence semi-angle, the probe size is mainly determined by spherical aberration (d_s=0.5C_sα^3).

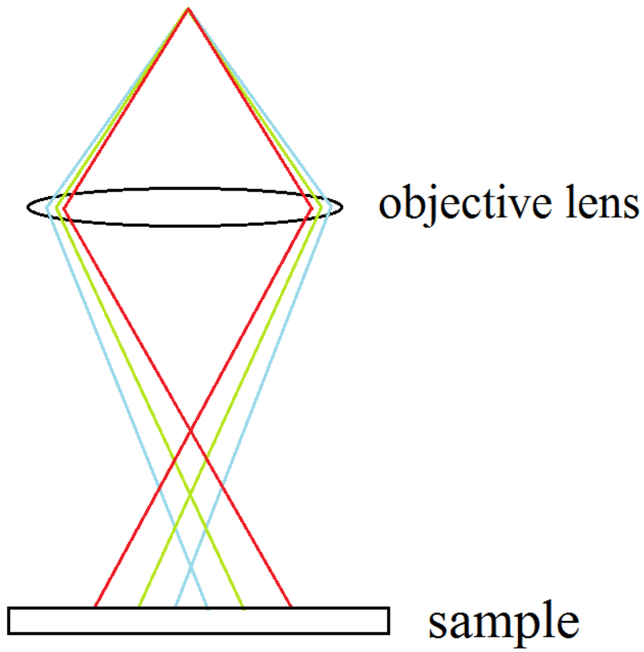

Figure 16: chromatic aberration

The electrons emitted from the electron source are not monochromatic. After bending the electron optical path by the objective lens, a lower energy electron is more strongly deflected than a high energy electron (red line compared with blue line), which forms an electron beam disc rather than a point; this effect is known as chromatic aberration (Figure 16) [10]. The radius of the disc can be expressed as equation (13).

$$\mathrm{r}_{chromatic} = C_c \frac{\Delta E}{E} \beta \tag{13}$$

where $r_{\text{chromatic}}$ is the radius of the disk, C_c is the chromatic aberration constant, ΔE is the energy loss of the electron, E is the incident electron energy and β is the collection angle. For a thick sample with low atomic weight, the dominating inelastic scattering will enhance the chromatic aberration. The chromatic aberration can be improved by using a small entrance aperture (smaller β), a monochromator (C_c corrector) and an ideally thin sample.

2.1.4 JEOL 2010F and NION ultra STEM 100 microscope

In this project, two types of analytical transmission electron microscope were used to analyse InGaN thin films and related nano structures. The JEOL 2010F is a conventional FEG (S)TEM, without aberration corrector or monochromator. In order to get best performance of the EELS spectra, as described in chapter 2.1.3, the smallest EELS spectrometer entrance aperture should be used to reduce the chromatic aberration. In our system, the GIF 200 EELS spectrometer has a smallest entrance aperture of 0.6 mm, the best energy resolution we can achieve is ~0.75 eV (FWHM of zero loss peak) at 200kV. However, this resolution is not sufficient to analyse high In content InGaN, whose bandgap value is close to 0.75 eV.

To improve the EELS spectra quality, in this project, the NION Ultra STEM 100 was used to record high quality EELS spectra. The NION Ultra STEM 100 is a high brightness CFEG STEM equipped with aberration corrector and monochromator, therefore, the smallest spectrometer entrance aperture is no longer needed to obtain good spectrum quality. The energy resolution is much better than 0.15 eV, down to 0.02eV at 60kV, after monochromation of the electron beam, which is ideal for extrapolating InGaN bandgap in VEELS. It is thus clear that the NION Ultra STEM 100 can provide better quality EELS spectra than JEOL 2010F.

For the spherical aberration, the spatial resolution of JEOL 2010F is limited to 0.19 nm due to the spherical aberration. With a spherical aberration corrector, the NION Ultra STEM 100 can easily reach a spatial resolution smaller than 0.1 nm. Compare to the JEOL 2010F, NION Ultra STEM 100 is more suitable for EELS mapping than JEOL 2010F.

Finally, compared with the JEOL 2010F operating at 200 kV, the NION Ultra STEM 100 has the ability to collect good EELS at 60 kV. It is important to protect the sample during spectrum acquisition. the lower acceleration voltage will reduce the possibility of electron knock-on damage, especially for electron beam sensitive materials (most III-V nitrides). This advantage makes the NION Ultra STEM 100 perfect for recording high quality EELS without considering

electron beam damage too much (Thomas Walther used the microscope to record InGaN low EELS map demonstrated in chapter 5 at Arizona state university on 2016).

Overall, to analyse the plasmon loss in a single EELS spectrum, the JEOL 2010F is sufficient, but bandgap measurements can be only achieved by NION Ultra STEM 100

2.2 Energy dispersive X-ray spectroscopy

2.2.1 Principle of X-ray generation in a (S)TEM

One process of electron interaction with matter is called inelastic scattering. This can lead to X-ray emission as shown in Figure 17 [11].

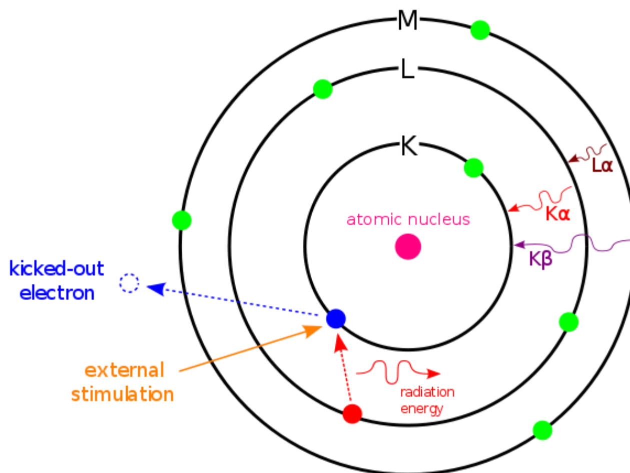

Figure 17 X-ray emission process [11]

As seen in Figure 17, an incident electron beam can eject an electron from an inner shell (K) of a sample atom. Then the vacancy can be filled by an electron from a higher-energy shell (L). The transition of an electron from L to K shell will either generate electromagnetic radiation or an emitted Auger electron. Since this energy difference is fairly large for inner shells, radiation will appear as X-rays.

The most useful rule for characteristic X-rays is Moseley's law, which is described by

$$E=c_1(Z-c_2)^2 \tag{14}$$

where E is the energy of the X-ray, Z is the atomic number and c_1, c_2 refer to given X-ray line types. As shown in Figure 18 [12], the energy of the X-rays increases with atomic number.

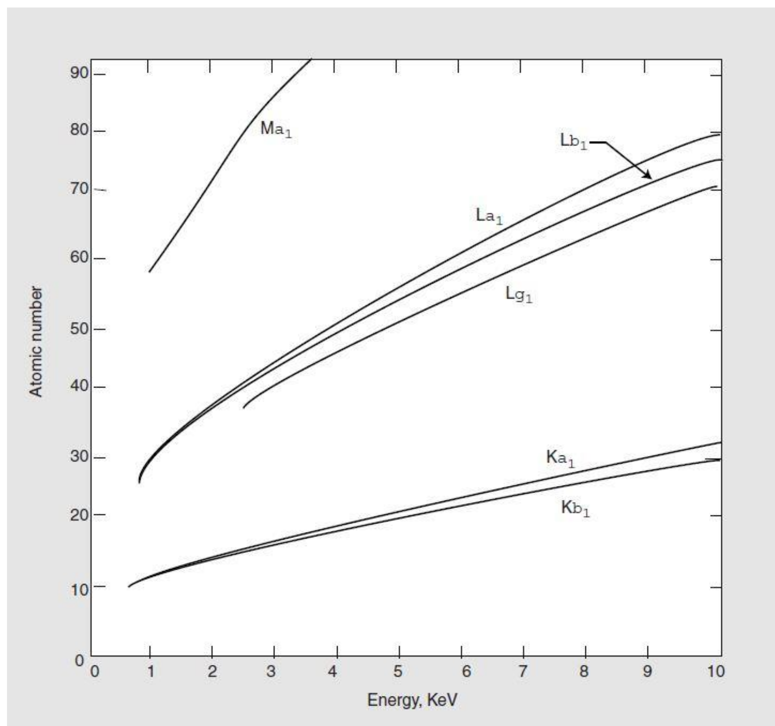

Figure 18: plot of the energies of major X-ray emission lines observed below 10 keV [12].

2.2.2 Absorption of X-ray

As an X-ray travels through the sample, it may be absorbed, giving up its energy entirely to an electron and ejecting the electron from its orbital. The absorption process is strongly related to electron bond energy and X-ray energy. If the X-ray energy is greater than the bond energy, the absorption possibility is increased.

The probability of X-ray absorption follows Beer's law

$$\frac{I}{I_0} = \exp(-\mu_m \rho d) < 1 \qquad (15)$$

where I/I_0 is the fraction of X-rays transmitted through a thickness d of a material of density ρ. It is clear the absorption effect is enhanced by increasing the sample thickness d. The parameter μ_m is called the mass absorption coefficient. Its units are m^2/kg or cm^2/kg. Creagh

and Hubbell (1987) [13] have shown that the mass attenuation coefficient μ_m can be expressed as

$$\mu_m = \frac{\sigma_{total}}{uA} \tag{16}$$

where σ_{total} is the total photon interaction cross-section, u is the atomic mass unit (u= 1.660 540 2 × 10^{-24} g), A is the atomic mass. The total photon interaction cross-section is the sum of photoelectric absorption cross-section (σ_{pe}), Compton scattering cross-section (σ_c), Laue-Bragg scattering cross-section (σ_{LB}) and thermal diffuse scattering cross-section (σ_{TD}) , The summation of σ_{LB} and σ_{TD} is usually called Rayleigh scattering cross section [13]. For GaN, the Ga L and Ga K attenuation coefficient is calculated by J H Hubble et al and published on the National Institute of Standards and Technology website (NIST) [https://www.nist.gov/pml/x-ray-mass-attenuation-coefficients], where the Ga L has attenuation coefficient of 1697 cm^2/g and 63.02 cm^2/g for Ga K X-ray, it is thus clear, the higher X-ray energy will lead to the lower absorption in the material.

The absorption effect is important for EDXS measurements, because absorption will decrease the X-ray count rate measured.

2.2.3 Fluorescence effect

A typical X-ray fluorescence effect can be sketched in Figure 19.

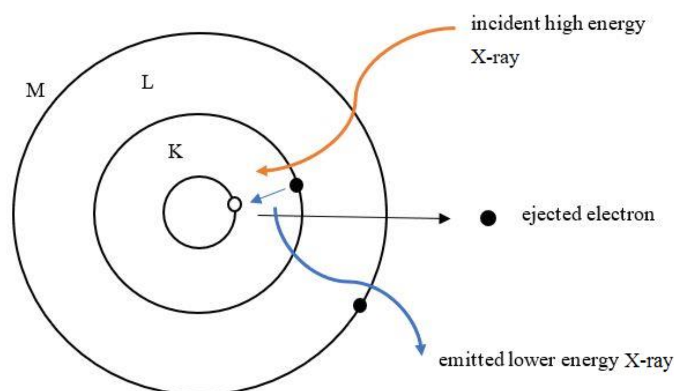

Figure 19: X-ray fluorescence

For a high energy X-ray interaction with material, the ionization process may take place by ejecting an inner electron, the recombination of the outer-shell electron with the hole left by the ejected electron, resulting in a lower energy X-ray photon generated. In element quantification the fluorescence effect should always be considered. For example, for an $In_{0.5}Ga_{0.5}N$ ternary alloy, the In_L and Ga_L can be excited by Ga_K X-ray. Therefore, for absolutely quantification, the fluorescence effect should be taken into account.

2.2.4 EDXS detector of JEOL 2010F

Almost all the energy-dispersive spectrometers have in common a solid-state detector. The EDXS detector is manufactured from a single crystal of either silicon or germanium; our JEOL 2010F is equipped with a lithium-drifted silicon (Si:Li) detector from Oxford Instrument. Ideally, only X-ray can create electron hole pairs in the intrinsic region in the detector (Figure 20), those electron and hole pairs may serves as charge carriers under the influence of an applied electric field, any free charge carrier produced by point defect or dislocations will generate dark current in the detector, which will create noise in the spectrum. Therefore, an ideal detector should be fabricated from perfect single crystalline semiconductor. A schematic of a Si (Li) detector is shown in Figure 20 [15].

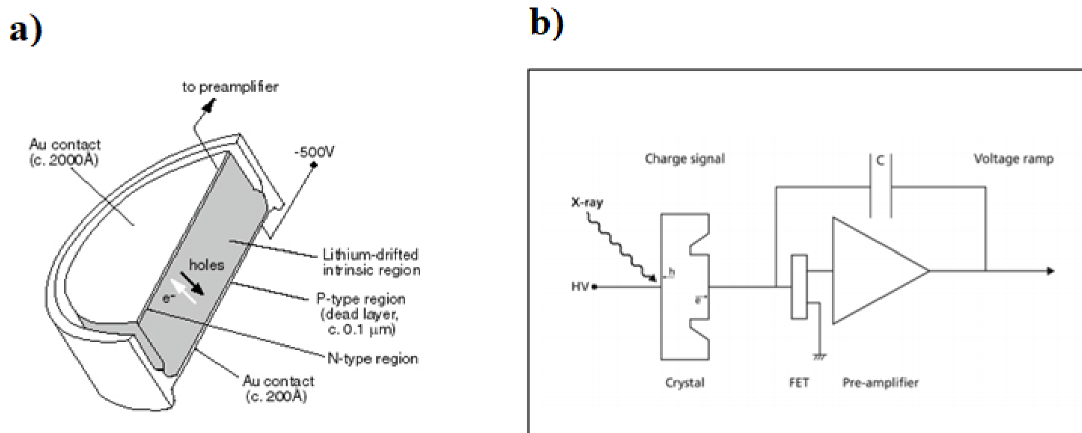

Figure 20: a) cross-section of a typical lithium-drifted silicon detector [15], b) the schematic of circuit diagram of detector [41].

As depicted in Figure 20, the X-ray creates electron-hole pairs in the intrinsic region of the semiconductor. These charge carriers then migrate to the electrode under the influence of an applied bias. The leakage current and thermal excitation of electrons are two main issues limiting detector efficiency. To avoid thermal excitation, the detector should be operated at low temperature. The leakage current which is mainly created by impurities can be reduced by drifting Si with Li atoms to remove point defects. The Li atoms are mainly used for removing point defects in the intrinsic region of the p-i-n junction in Figure 20. so that no free charge exists in the intrinsic region. Then electron-hole pairs can be only generated by X-rays. If the detector was not cooled by liquid nitrogen, the Li atoms could easily diffuse from the stable site, create some doping of the previously intrinsic region, therefore, the X-ray spectrum would become extremely noise and not possible to process.

There is a polymer window before our EDXS detector in JEOL 2010F, which serve as a barrier to maintain the vacuum condition of the detector. However, it also acts as an absorber of low energy X-rays traveling to the detector.

The pulse processor is another important component of the EDXS detector. The main role of the pulse processor is to measure the incident X-ray energy, by converting the number of electron and hole pairs per time unit into a voltage signal by using a field effect transistor (FET). The conversion of electron hole pairs into a voltage signal is shown in Figure 20 b) [41]. As demonstrated in Figure 20 b), when an electron and hole pair is generated by an X-ray photon, the capacitor is charged by the electron. Then the capacitor is discharged and creates a voltage signal by FET, the signal is then amplified by a pre-amplifier in the diagram.

The multiple channel analyser adds a digital count to the corresponding energy channel in the spectrum. Goldstein et al [14] showed that when an X-ray hits the Si:Li detector, the detector will shut down for a certain time during which the pulse processor can convert the X-ray signal into a digital count in the spectrum. A fast acquisition time will lead to a poor energy resolution of the spectrum, while a longer recording time will result in better energy resolution. The relationship between pulse processing time and energy resolution will be explained in detail in chapter 2.2.6.

2.2.5 Spatial resolution of EDXS

The spatial resolution is governed by the electron beam size, its penetration and spreading of the electron beam in the specimen. An overview of spatial resolution for an $In_{0.79}Ga_{0.21}N$ sample simulated by CASINO software at 200kV accelerating voltage with 10 nm initial electron beam radius is shown in Figure 21 [16]. Although the CASINO software was initially programmed to simulate X-ray generation in SEMs operated at 1-30kV, it now uses relativistically corrected cross-sections and can hence also be used for simulation of X-ray generation in higher voltage TEMs and STEMs, e.g. at 200kV [42].

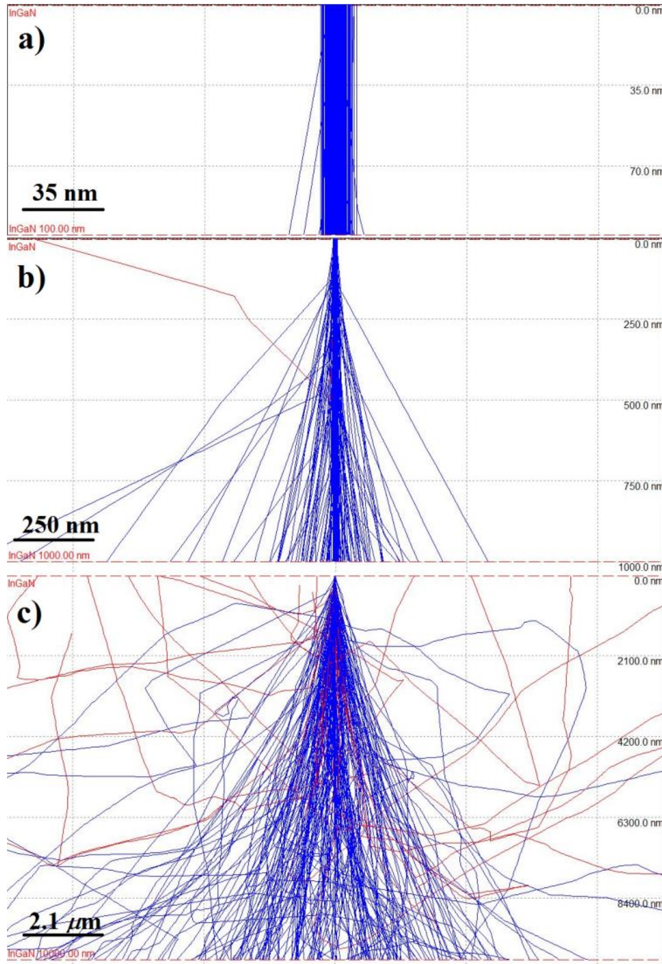

Figure 21: the interaction volume for a) 100 nm thick $In_{0.79}Ga_{0.21}N$ sample (thin foil), b) 1000 nm thick $In_{0.79}Ga_{0.21}N$ sample (thick film), c) 10000nm $In_{0.79}Ga_{0.21}N$ (almost bulk) sample.

As shown in Figure 21, as the sample thickness increases, this leads to strong spreading of the electron beam in the sample, resulting in the increase of interaction volume. The interaction volume in X-ray analysis is strongly related to three important factors: initial beam diameter, beam spreading and the X-ray take-off angle. The beam spreading is mainly caused by elastic scattering of the incident electron beam. A single scattering model was first proposed by Goldstein [17] and then re-defined by Reed [18], giving a beam spreading of

$$\mathrm{b} = 7.21 \times 10^5 Z/E_0(\rho/A)^{1/2} t^{3/2} \tag{17}$$

where Z is the atomic number, ρ is the density of the material, E_0 is the incident beam energy in keV, A is the atomic weight. b is the beam spreading in nanometer. The expression indicates that the generation volume for X-rays increases faster than thickness.

When X-rays travel towards the detector, they can be absorbed or re-emitted (fluoresce) in the sample, in this case the take-off angle adjustment is important to minimize those effects.

An approximation of the X-ray spatial resolution was first given by Michael [19], where the beam radius R midway through the thin foil is a combination of spot radius incident on sample surface (d) and radius of electron beam exit at the bottom of the sample (R_{max}).

$$R = \frac{d+R_{max}}{2} \tag{18}$$

where d is the spot diameter and R is the resolution. The parameter R_{max} is given by

$$R_{max}=(b^2+d^2)^{1/2} \tag{19}$$

Because the specimen geometry can be complicated (surface roughness), electron diffraction and channelling in crystalline structures have led to many different definitions.

2.2.6 Energy resolution of EDXS

The EDX spectrum is presented in digitized form. The x-axis is depicting the X-ray energy (usually the dispersion of EDXS ranges from 5eV to 40eV per channel), while the y-axis represents the number of counts per channel. A typical InGaN EDXS spectrum is shown in Figure 22.

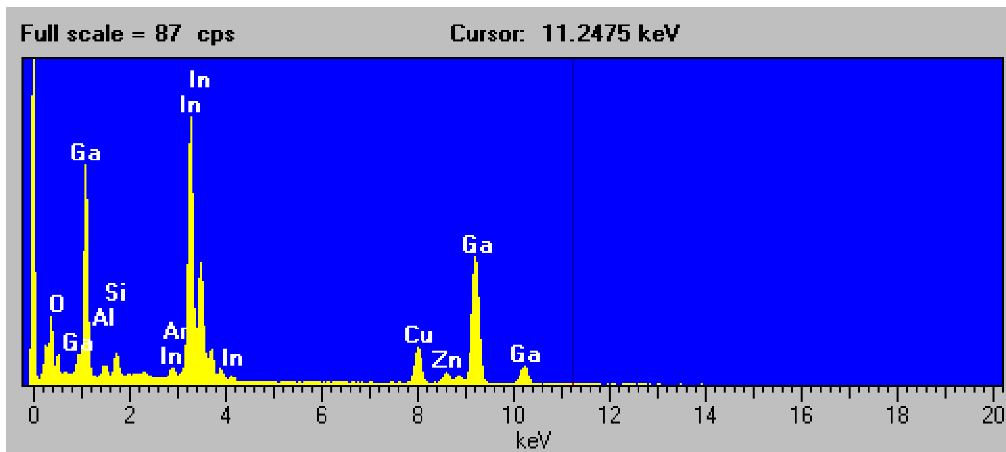

Figure 22: typical $In_{0.54}Ga_{0.46}N$ EDXS spectrum

An X-ray line is usually presented as a Gaussian profile. The energy resolution of EDXS is defined by the full width of the peak at half maximum height (FWHM). Conventionally, the FWHM is specified for the Mn Kα peak at 5.89 keV. A typical Si:Li detector can reach a resolution in the range of 130eV to 150eV, while a Ge detector can achieve 115eV. For the strobe at 0 keV, a FWHM of <60eV can be obtained, so even B_K (0.183keV) and C_K (0.277keV) can be distinguished if they are roughly at equal height. As our EDXS detector is equipped with a polymer window before the Si:Li crystal, most of the low energy X-rays are absorbed by the polymer window, only a few low-energy X-rays will reach the Si: Li crystal and generate electron-hole pairs. The resolution of EDXS is worse than wavelength dispersive spectroscopy (WDS) but gives a good separation of K lines for neighbouring elements if Z>8 (oxygen). The energy resolution is strongly depending on the pulse processor time. While a longer processing time can decrease the noise and improve the energy resolution of each peak, making it easier to separate neighbouring X-ray peaks, the longer processing time for each X-ray will lead to fewer events be measured by the detector, therefore, the total counts for each X-ray peak will decrease. If the total X-ray intensity is decreased, the statistical error will be enhanced, which will be discussed in chapter 2.2.7.

2.2.7 Accuracy of X-ray intensity measurement

In principle, the X-ray intensity is given by counting X-ray photons and thus the precision of the count number is limited by statistical errors (usually defined as 2σ intervals [5]). The statistical error of X-ray peak intensity can be expressed as $(N)^{0.5}$, where N is the total counts measured by peak integration. In ISIS system, the background subtraction produces almost same statistic error ($(N)^{0.5}$), which indicates the peak intensity after background subtraction will have $2\times(N)^{0.5}$ in statistic error. In chapter 2.2.6, the increasing of processing time in the pulse processor can enhance the energy resolution of the EDXS spectrum, however, the X-ray total counts will be decreased, and the relative error thus increases and results in a larger error in quantification of elemental concentration. Overall, it is a trade-off between energy resolution and measured X-ray intensity accuracy.

The X-ray intensity can also be enhanced by using a larger probe size with more beam current, the number of scattering events will then be increased. Unfortunately, for beam sensitive material, a large beam current may create beam damage to the sample or even before it can be analysed. Additionally, the enhancement of continuum (Bremsstrahlung) X-rays can occur by increasing the incident beam current, resulting in the increase of the X-ray spectrum background, illustrated in chapter 2.2.8.

2.2.8 Continuum (Bremsstrahlung) X-rays

When an electron interacts with material, the electron's gradual energy losses along the beam direction can generate an X-ray photon called continuum X-ray. The closer the electron beam strikes the nucleus of the atom, the stronger the Coulomb interaction between them, thus more continuum X-rays can be generated. The continuum X-ray spectrum is continuous and independent of the characteristic X-ray lines that depend on atomic number. Since the continuum X-rays give no information about sample chemistry, they should be excluded from

quantitative analysis. For low energy X-rays, the strong absorption provided by material and polymer window of the detector will lead to a low detector efficiency. For high energy X-rays with weak absorption, the background in the spectrum also has low intensity. Therefore, the continuum background from a polymer window detector appears like a 'whale' structure due to the superposition of the detector efficiency and Bremsstrahlung X-rays. An example EDXS spectrum with background model is shown in Figure 23.

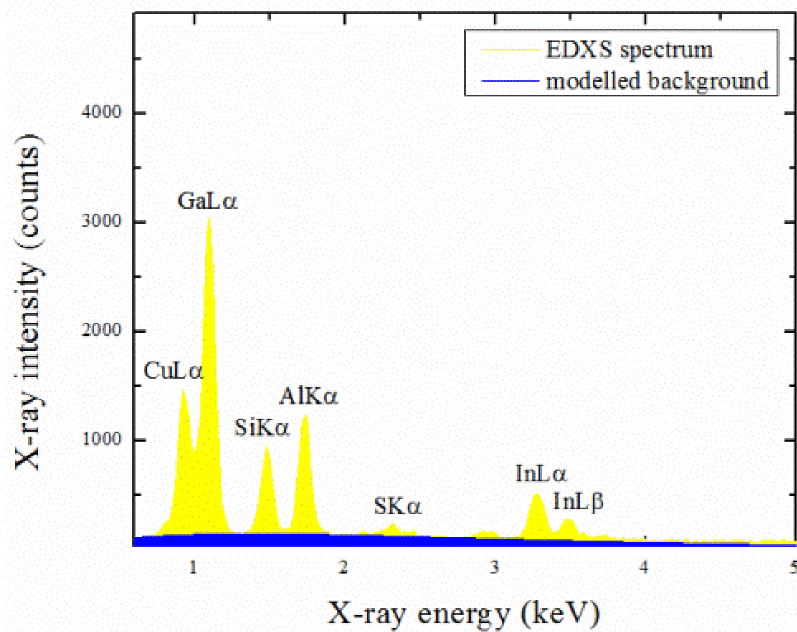

Figure 23: recorded EDXS spectrum with background model

As shown in Figure 23, the background influence on the high energy characteristic X-rays peak is small, it is thus important to apply a good background subtraction model mainly for low energy X-ray peaks to obtain precise counts for further quantification.

2.2.9 Cliff-Lorimer quantitative analysis of EDXS

Qualitative analysis is the process of identifying which elements are present in a sample. Quantitative analysis measures their abundance. Considering a binary material with elements A and B only, the quantification of an EDXS spectrum is based on the Cliff-Lorimer equation.

$$\frac{C_A}{C_B} = k_{AB} \frac{I_A}{I_B} \tag{20}$$

where I_A and I_B are the X-ray intensities for elements A and B, C_A and C_B are the concentrations (%) of the elements A and B in binary material, k_{AB} is a sensitivity factor.

Assuming the specimen is thin enough so that absorption and fluorescence can be neglected, the ratio of the elements is proportional to the intensity of the EDXS peaks [5]. For historical reasons, most *k*-factors tabulated as function of *Z* and kV refer to weight % (mostly used in metallurgy).

The k_{AB} in equation (20) is called Cliff-Lorimer factor, which is often referred to as 'the' *k* factor. It is sensitive to the voltage of the TEM and the detector efficiency of the EDXS instrument. k_{AB} is the *k* factor of element A with respect to element B. In practice, the ISIS 300 routine can only provide the *k* factor of elements with respect to silicon (Si). Therefore, the k_{AB} can be expressed as

$$k_{AB} = \frac{k_{A\,Si}}{k_{B\,Si}} \tag{21}$$

In order to calculate the C_A and C_B, a second equation is needed. For binary material, the specimen only contains elements A and B, thus the sum of weight ratios should be 100%.

$$C_A + C_B = 100\% \tag{22}$$

For ternary or higher order material systems, additional equations should be applied in order to obtain the different element concentrations. Considering a ternary material with elements A, B and C. the equations for calculating the elemental concentrations can be expressed as

$$\frac{C_A}{C_B} = k_{AB}\frac{I_A}{I_B},$$

$$\frac{C_B}{C_C} = k_{BC}\frac{I_B}{I_C},$$

$$k_{AC}/k_{BC} = k_{AB} \text{ and } C_A + C_B + C_C = 100\% \tag{23}$$

In GaN and related alloy systems, since most nitrogen X-rays will not penetrate our polymer window, the measured nitrogen /gallium ratio will usually be lower than unity, thus the quantification process is often restricted to the group III-element sub-lattice [20]. The Cliff-Lorimer sensitivity factor (k) can be affected by three important effects [5], illustrated in chapter 2.2.1 to 2.3.3: the atomic number Z, the absorption of X-rays in the specimen (A) and fluorescence of X-rays (F). For a sufficiently thin TEM sample, the A and F effects are relative low and may be neglected. For very thin TEM samples we should mainly consider the effect of the atomic number Z. For thicker samples, all three parameters should be considered in the k factor correction, which is common known as ZAF model.

In STEM EDXS quantification, a thick sample will give high X-ray intensity at each pixel, resulting in small relative errors obtained for each X-ray peak. However, as the beam broadening effect in a thick sample is stronger than in a thin sample, this leads to a decrease of spatial resolution. On the other side, a thin sample provides better spatial resolution but at a higher quantification error due to poorer statistics.

2.2.10 Monte Carlo simulations

The name Monte Carlo originates from a famous casino in Monaco. In modelling, it is an important mathematical approach since it applies random numbers to solve problems numerically. A Monte Carlo simulation is essentially a probability related method to predict the outcome of individual events in a system. The Monte Carlo method is based on a law of large numbers, which can give the expected outcome by averaging all results. The Monte Carlo method was first described by Metropolis and Ulam in 1949 [21]. In their paper, they illustrated a model of a particle hitting the atmosphere and starting a series of nuclear events, similar to our electron interaction with matter, when an electron passes through the sample. Several scattering events will take place and generate sub-particles. All events obey particle scattering probability. Mathematically, it can be called a Markov chain, which can be solved by Monte

Carlo method. Therefore, the probability of producing a specific sub-particle with a given energy in any given collision can be predicted.

In this thesis, we applied the CASINO software [16] to calculate the X-ray counts generated by an electron beam and extrapolate the theoretical EDXS sensitivity factor (k). The CASINO software is a Monte Carlo based modelling tool, which includes absorption and fluorescence effect for electrons and photons travelling in a material. Therefore, the theoretical k factor provided by CASINO software can be treated as a ZAF corrected k factor. This is called k^* factor in the following.

2.2.11 STEM elemental map processing

The elemental distribution in a material can be measured by STEM. Modern EDXS systems can store all spectra for each point using a 3D spectrum similar to STEM EELS, and each pixel contains a full X-ray spectrum. Unlike the modern EDXS system, our ISIS 300 software only stores elemental maps with related X-ray intensity at each pixel. The X-ray intensity is integrated over an energy window selected in the reference spectrum for each element, and if two elements have emitted X-rays of similar energy, the overlap region will only contribute to that element whose energy window was selected first and lead to an overestimation of its X-ray counts. The example for Ga L_α and Cu L_α is demonstrated in Figure 24.

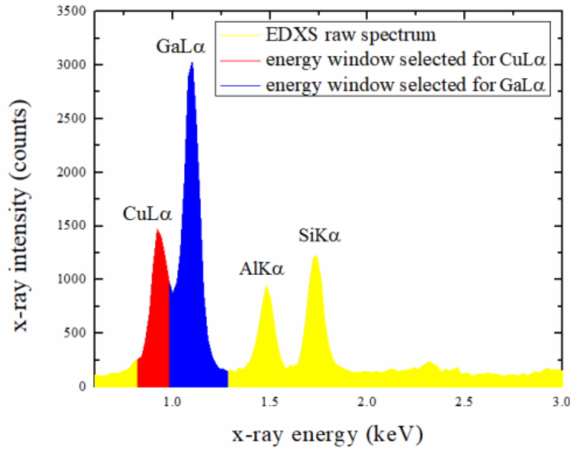

Figure 24: energy windows selected by ISIS for X-ray counts integration (blue: Ga L_α, red: Cu L_α)

As shown in Figure 24, the energy window for Ga L_α was selected first in the reference spectrum, and it is thus clear the Ga L_α intensity extrapolated from the spectrum is higher than its proper value, which leads to an underestimation of the Cu L_α X-ray counts. To solve this problem, a proper background subtraction should be applied to the spectrum, where the Cu L_α and Ga L_α peaks in the background subtracted spectrum should be fitted with Gaussian functions, then a better measurement of the intensity of Ga L_α and Cu L_α can be obtained. The proportion of overlap area with respect to the Ga L_α intensity recorded from ISIS 300 system can be expressed as

$$P = \frac{I_{GaL\alpha ISIS} - I_{GaL\alpha real}}{I_{GaL\alpha ISIS}} \tag{24}$$

where $I_{GaL\alpha,ISIS}$ is the intensity recorded from ISIS 300 system with the energy window selected, P is the proportion of overlap area and background intensity for the Ga L_α intensity measured by ISIS 300 system. Therefore, the X-ray intensity at each pixel should be processed before quantification.

2.3 Electron energy-loss spectroscopy (EELS)

2.3.1 Principle of EELS

Considering an electron beam with a small range of kinetic energies projected on the sample, the electrons will undergo elastic and inelastic interaction with the sample. The primary electron will lose energy if an inelastic scattering has taken place. The electron beam can be deflected by a magnetic prism and projected onto a charge coupled device (CCD) detector. As shown in Figure 25 [22], electrons of different energies will be deflected differently in the vertical direction and be dispersed onto a thin scintillator screen.

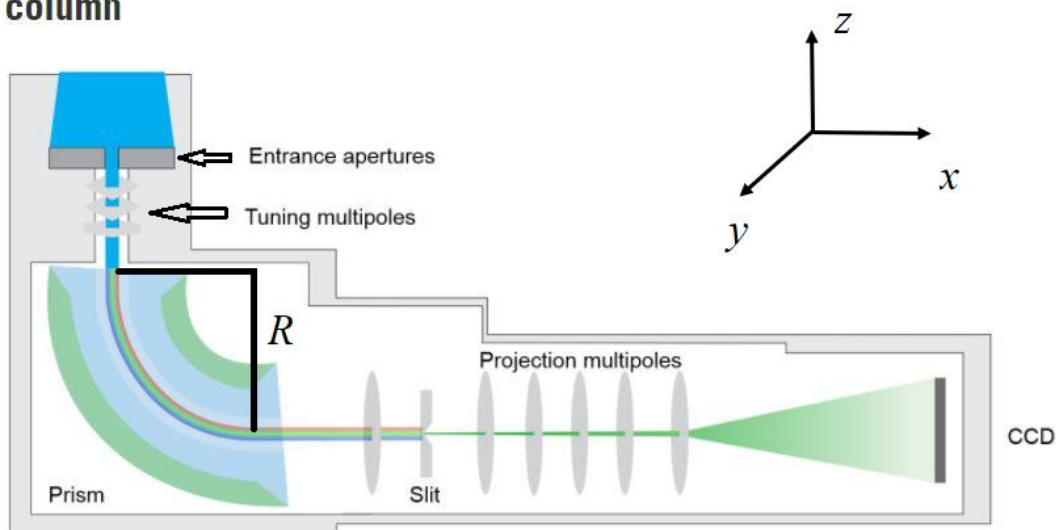

Figure 25: structure of Gatan image filter (GIF); the slit must be retracted for EELS measurements [22].

A selection of electrons at certain deflection angles entering the spectrometer can be achieved by the entrance aperture, or by using an objective aperture.

The multipole system is essentially a complex system containing deflectors, quadrupoles and sextupoles, and is used to deflect and focus the electron beam. The calibration of multipoles system is fully automated via the *tune GIF* function in Gatan Digital Micrograph software.

After tuning the electron beam by GIF function, the maximum electron beam intensity will directly enter the prism with the least aberrations for the largest (3mm) entrance aperture.

The prism is the heart of the spectrometer; it generates a magnetic field which can bend the electron beam by a certain angle and vertically project the dispersed electron beam onto the CCD. Within the magnetic field provided by prism, the electrons travel in a circular orbit, and the radius of curvature *R* in Figure 25 can be expressed as

$$R = \frac{m_0 v\sqrt{1-\frac{v^2}{c^2}}}{eB} \tag{25}$$

where m_0 is the rest mass of the electron, *B* is the magnetic induction provided by prism, *v* is the speed of the electron, *c* is the speed of the light and *e* is the electron charge. As shown in equation (25), for a constant magnetic field provided by the prism, the electrons which have lost energy will have a smaller *v*, resulting in a smaller *R*. Therefore, the electrons with energy loss will leave the magnetic prism with a slightly larger deflection angle than zero-loss electrons.

2.3.2 Collection angle set-up by using spectrometer entrance aperture and camera length

After the electron undergoes inelastic scattering, its optical path will have effective scattering angle for inelastic scattering calculated by Egerton [23] as follows

$$\theta_E = \frac{E}{E_0}\left(\frac{E_0+m_0c^2}{E_0+2m_0c^2}\right) \tag{26}$$

where θ_E is the effective scattering angle for inelastic scattering, E_0 is the kinetic energy of an electron, m_0 is the electron mass, *c* is the speed of the light and *E* is the energy loss during the scattering. It is clear the electron scattering angle is strongly related with the electron's kinetic energy and energy loss. θ_E is an important parameter for EELS experimental set-up. Consider recording a low-loss and high-loss spectrum at a certain camera length: for the low-loss EELS spectrum, since the *E* is relatively low value, a smaller entrance angle is needed to record all

information from low-loss scattered electrons. On the contrary, a high loss spectrum must be recorded by using a larger aperture. A ray diagram for both set-ups is shown in Figure 26.

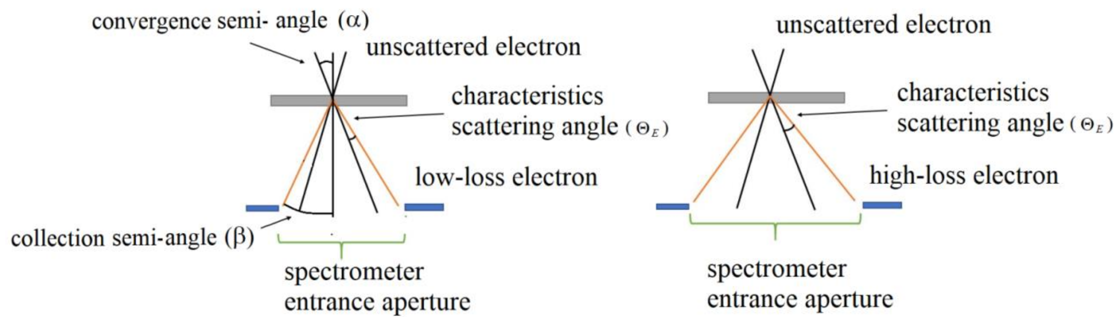

Figure 26 ray diagram of low loss and high loss electron trajectories.

As shown in Figure 26, the black straight lines present the unscattered electron optical paths, while the orange lines demonstrate that of inelastically scattered electrons. It is clear the collection angle β has a relation with the convergence angle α formed by condenser system and characteristic scattering angle θ_E ($\beta>\alpha+\theta_E$). In a transmission electron microscope, the collection angle of EELS measurement is defined by the smallest angle formed by objective aperture and entrance aperture of spectrometer, which can be expressed as β=min($\beta_{\text{objective}}$, β_{entrance}).

2.3.3 EELS energy drift

EELS energy drift is mainly caused by primary instability of the energy of the incident electron beam [24]. This instability is mainly caused by a continuous drift and random ripple of the high tension. It is an unavoidable factor for any accumulated EEL spectrum with large frame number recorded in TEM or in STEM mode. As addressed by Popatov et al. [24], the zero-loss peak cannot be easily accommodated in a high loss EEL spectrum with high dispersion, for example, for recording the Ga L_2 edge (1142eV) with our GIF 200 spectrometer, the detector has 1024 pixel with 1 eV dispersion per channel, therefore, if the spectrum collection started at 0 eV, the

spectrum upper limit will end up at 1024 eV, which is below the Ga L_2 edge in the spectrum, therefore, at 1 eV dispersion, it is not possible to simultaneously accommodate the zero loss peak and Ga L_2 edge in the same spectrum. If the zero-loss peak is not observed in the spectrum, there is no direct calibration point for accurately measuring the edge onset energy. Therefore, high-tension instability may lead to an apparent chemical shift of the ionization edge, resulting in inaccurate measurement of the element edge onset. For low loss EEL spectra, energy drift is not a problem since the zero-loss peak is usually recorded within the spectra and serves as reference. However, in the accumulative EEL spectrum recording routine provided by Gatan Digital Micrograph, spectra recorded individually by single exposures can be added together to obtain an accumulative EELS, and if a high-tension instability drifts the EEL spectrum, this will lead to an increase of the FWHM of the zero-loss peak in accumulative EELS. The problem can be solved by manually recording lots of single frame EEL spectra repeatedly, calibrate all the zero-loss peaks in each and align all spectra before summation [25].

To demonstrate the primary energy instability of incident electrons, we have recorded a 56×56 pixels spectrum image of an InGaN/GaN sample with 7.1 nm per pixel. The exposure time for each pixel was 0.2s, and our detector is a CCD with 1024 channels. The measured dispersion was 0.0502(5) eV/channel. The recorded spectrum image and two extracted EEL spectra are shown in Figure 27.

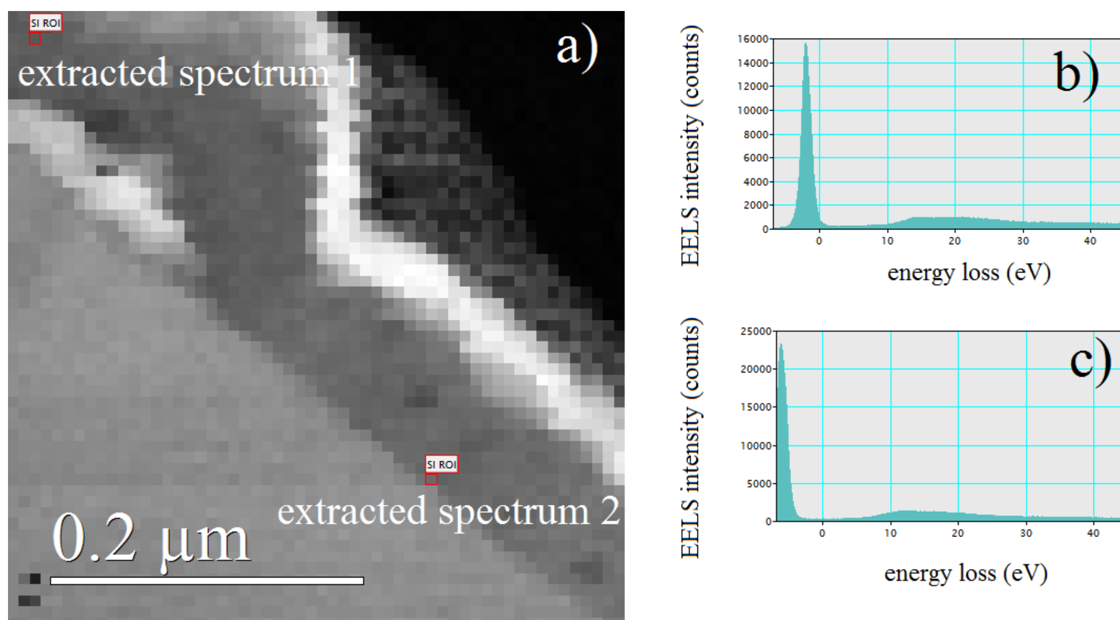

Figure 27: a) InGaN spectrum image, b) extracted spectrum 1, c) extracted spectrum 2.

As shown in Figure 27, the zero loss peak drifted from -2.0eV at pixel (1,1) to -5.4eV at pixel (41,10), which demonstrates energy drift in STEM EELS mapping. A fluctuation of the high-tension voltage together with the chromatic error in GIF 200 will lead to a range of electrons of different velocity entering the spectrometer. A correction of the acceleration voltage can be achieved by using the drift tube voltage function in GIF. This drift tube voltage temporarily accelerates/decelerates the electrons travelling through the prism, which makes the zero loss peak fully stable in the spectrum. However, in current Gatan EELS system, the drift tube function is only useful in Duel EELS option in the GIF Quantum model system, our GIF 200 and GIF Tridium in JEOL 2010 F and JEOL 3100z R005 are far too slow to operate. The drift tube voltage can be adjusted in the range of 1-2kV, depending on the hardware option.

2.3.4 The zero-loss peak (zlp)

Considering a thin sample, the predominant feature in the EEL spectrum is called the zero-loss peak (zlp). As the name implies, this peak is generated by electrons without energy loss during

the interaction with the sample, but also phonon losses that cannot be resolved will contribute towards it. Therefore, the zero-loss peak is essentially formed by the elastically scattered electrons and phonon scattered electrons (direct transmitted electron beam) in Figure 26.

The spectrometer resolution can be defined by the FWHM of zero-loss peak [5]. In principle, an ideal zero-loss peak measured by an ideal spectrometer would be a delta function, however, there are various parameters that can contribute to broadening the FWHM of the zero-loss peak. Firstly, the electrons emitted from the electron gun are not monochromatic in energy; the distribution for a FEG follows the Fowler-Nordheim distribution [24], which leads to an asymmetry and broadens the zero-loss peak. The energy distribution of the electron source can be improved by a monochromator directly below the electron source.

The energy resolution can be degraded by introducing a too large spectrometer entrance aperture, so spectrometer aberrations broaden the EELS.

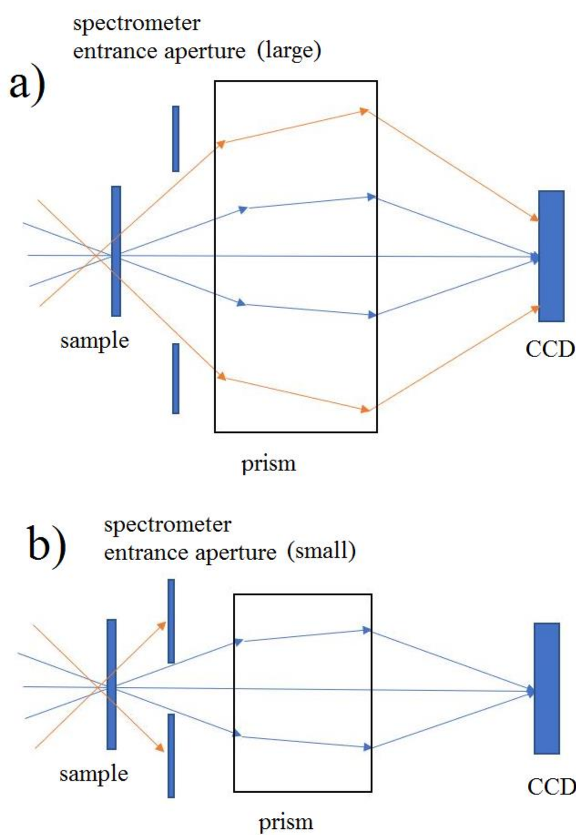

Figure 28: ray diagram for different spectrometer entrance apertures: a) large, b) small.

As demonstrated in Figure 28, the aberrated ray (orange) can enter the spectrometer and degrade the energy resolution of the spectrum if a large entrance aperture is used. A small entrance aperture can block these, so only the in-focus rays (blue) can form the zero-loss peak, therefore, the energy resolution is improved by using a small entrance aperture.

The point spread function of a detector can also degrade the apparent energy resolution of the spectrum; it can be measured by decreasing the dispersion to ensure the zero-loss is focused within one channel, however, as all the electron beam intensity is going into one channel, the high intensity will burn the detector, therefore, it is necessary to reduce beam intensity before focusing the beam into one channel. the intensity appearing outside that channel can be treated as artefact from the detector, and the recorded intensity profile can be treated as the point spread function.

2.3.5 Spectrometer dispersion

The spectrometer dispersion can be defined as the distance in the spectrum between the positions of electrons differing by a certain amount of energy. The dispersion can be calculated for electron path curvature R (equation (25)), incident electron energy (E_0 in equation (26)) and size of each channel in detector. For our JEOL 2010F operating at 197kV, if the radius of the curvature is 200mm, the dispersion can be calculated as 1μm/eV; for a channel (pixel) size of 24 μm, an electron energy range of 25eV will cover a single pixel channel, therefore, the dispersion plane should be magnified 25× to obtain 1eV/channel. For a low-loss EEL spectrum at 0.05eV/channel, the dispersion plane should be magnified 500×. The magnification of the dispersion in the GIF can be adjusted by quadrupoles in the post-spectrometer lenses.

For absolute measurement of the plasmon peak position or core loss edge onset, the dispersion should be calibrated accurately. The measurement process contains two steps. First of all, a

zero-loss peak should be recorded with drift tube voltage of 0 ($V_{original}$), then by changing the drift tube voltage to another value (in this experiment $V_{drift\ tube}$), the zero-loss peak will shift by certain number of channels ($N_{channel}$), then the dispersion can be calculated as $e(V_{drift\ tube}-V_{original})/N_{channel}$. Figure 29 shows a zero-loss spectrum image and integrated spectrum (green square) recorded with 10V and -30V drift tube voltage.

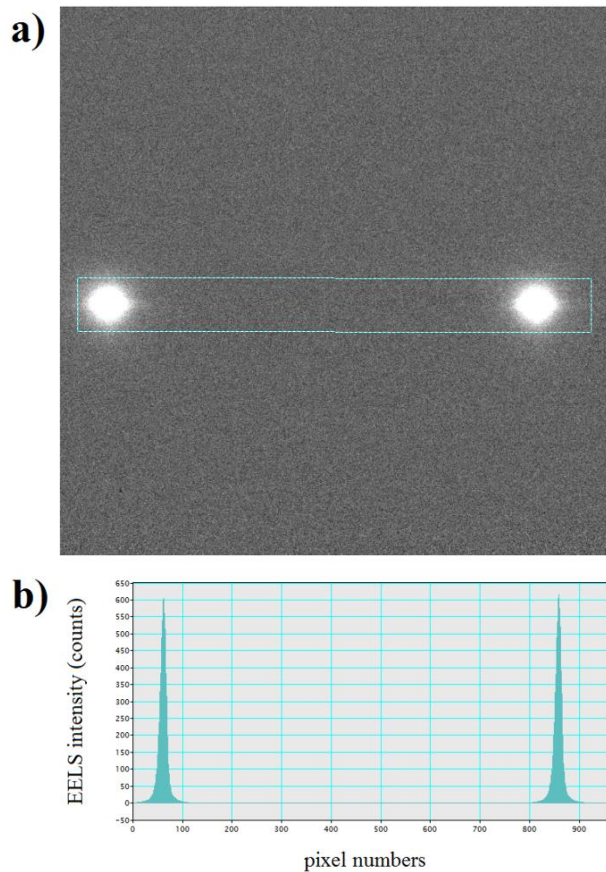

Figure 29: a) zero-loss spectrum image recorded at 10V and -30V drift tube voltage, b) vertical integrated spectrum from the dotted rectangle in a).

As shown in Figure 29, the zero-loss peak shifts 796 channels if a 40V drift tube offset is applied. Then the dispersion can be calibrated as 0.0502(5) eV per channel.

2.3.6 Valence EELS

In principle, low electron energy losses happen if the high energy electron beam is inelastically scattered by bound (valence) electrons in the specimen. It is a powerful technique for

determining the bandgap [26]. The VEELS region of 0-50eV [27-29] also contains bulk and surface plasmon losses and inter/intra-band transitions [30]. A measurement of bandgap by using VEELS can be affected by three main factors: zero-loss peak tails [31], resolution of the (non-)monochromatic instrument [31] and Cerenkov radiation [32].

The zero-loss peak is defined by the elastic interaction with the material and phonon scattering (<<1eV). In principle, the transmitted electrons of the ZLP have suffered no significant energy loss during the interaction with material, However, in practice, the field-emission tip and quality of monochromatic instrument contribute to the broadening of the zero-loss peak as does phonon scattering [30]. The onset of the bandgap of small bandgap semiconductors in a VEEL spectrum is covered by the tails of the zero-loss, which makes it impossible to detect. The improvement of monochromatic instruments to an energy resolution under 100meV has created the possibility to interpret VEELS data more reliably [33-35].

Cerenkov radiation was first studied by Pavel Alekseyevich Cherenkov, who was the winner of 1958 Nobel Prize [36]. Cerenkov radiation is emitted if a charged particle moves faster than the light in a certain medium. In order to satisfy the condition for Cerenkov radiation in a material, equation (27) must be fulfilled [32]

$$v \geq \frac{c}{\sqrt{\varepsilon}} \tag{27}$$

where v is the speed of the electron, c is the speed of the light in vacuum and ε is the real part of the dielectric function. For many semiconductor materials, ε is large enough to observe Cerenkov radiation between ZLP and plasmon peak [32, 23]. The minimum accelerating voltage to prevent the Cerenkov radiation in GaN will be described in chapter 5.3.

Surface/interface plasmons can also affect the measured value of the bandgap, and extended Lorentz tails can shift the apparent onset of the band-edge position. Therefore, the surface and interface plasmons should be subtracted before fitting the onset of the bandedge.

Due to the high energy of the projected electron beam, a valence electron can also be pumped to higher energy states, which can lead to intra-band transitions when this electron relaxes to the bottom of the conduction band. Such intra-band transitions can also affect the precision of the determined direct bandgap value.

2.3.6.1 Plasmon loss spectroscopy

As shown in Figure 30, if the electron beam goes through or passes a specimen at high energy, the incident electron can exert an electric force on the free electron gas (or bound electrons) of the material. Since the nucleus has much higher mass, it can be seen as stationary. The electrons of the electron gas interact with each other and the incident electron beam, and the repulsive electrostatic force from the incident beam renders a displacement from equilibrium position. When the fast electron has passed, the electrostatic force from the nucleus attracts the electron gas back to its equilibrium position, leading to an electron gas oscillation. It is called plasma oscillation. The quantization of the plasma oscillation is defined as plasmon.

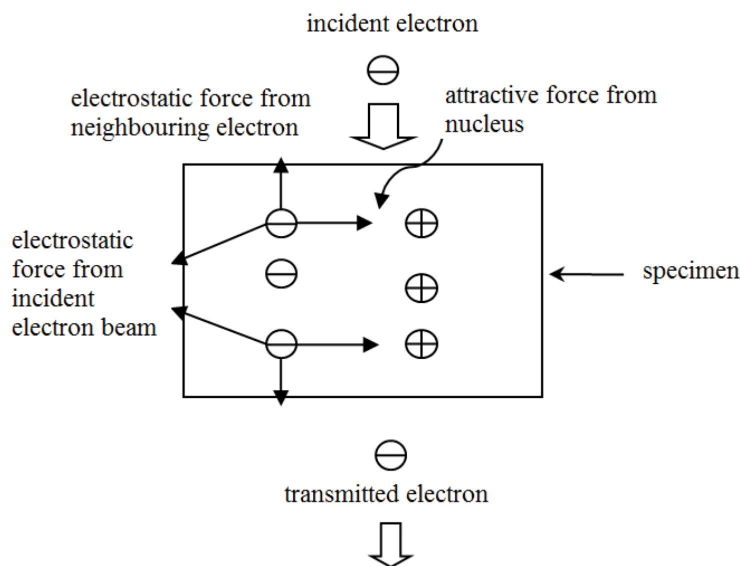

Figure 30: schematic of plasmon oscillation.

The plasmon can be explained by a so-called jellium model [23], where the displacement x of a quasi-free electron is mathematically related to the local electric field E, and can be expressed as

$$m\frac{d^2\boldsymbol{x}}{dt^2} + m\Gamma\frac{dx}{dt} = -e|\boldsymbol{E}| \tag{28}$$

where m is the electron mass, $\boldsymbol{x}$ is the displacement vector of a quasi-free electron, Γ is the damping constant, e is the electron charge and $\boldsymbol{E}$ is the vector of oscillation field.

For an oscillation of $\boldsymbol{E}=\boldsymbol{E}_0$*exp($-i\omega t$), equation 28 can be solved as

$$\boldsymbol{x} = \frac{e/m}{\omega^2+i\Gamma\omega} \tag{29}$$

The quasi-free electron displacement will introduce a polarization $\boldsymbol{P}=-en\boldsymbol{x}=\varepsilon_0\chi\boldsymbol{E}$,

where χ is the electronic susceptibility and n is the number of electrons per unit volume. The dielectric function $\varepsilon(\omega)=1+\chi$ can then be expressed as

$$\varepsilon(\omega) = \varepsilon_1 + i\varepsilon_2 = 1 - \frac{\omega_p^2}{\omega^2+\Gamma^2} + \frac{i\Gamma\omega_p^2}{\omega(\omega^2+\Gamma^2)} \tag{30}$$

ω is the angular frequency of the forced oscillation and ω_p is the resonance frequency for plasma oscillation. ω_p can be expressed as $\omega_p=[ne^2/V(x)(\varepsilon_0 m)]^{1/2}$, where $V(x)$ is the concentration dependent volume of unit cell. The energy loss function is then

$$Im\left(\frac{-1}{\varepsilon(\omega)}\right) = \frac{\omega\Gamma\omega_p^2}{\left(\omega^2-\omega_p^2\right)^2+(\omega\Gamma)^2} \tag{31}$$

By combining the plasmon energy $E_p=\hbar\omega_p$ and energy loss $E=\hbar\omega$, the angular frequency in energy loss function can be replaced by energy loss and plasmon energy, which gives equation (32).

$$Im\left(\frac{-1}{\varepsilon(\omega)}\right) = \frac{E(\Delta E_p)E_p^2}{\left(E^2-E_p^2\right)^2+(E\Delta E_p)^2} \tag{32}$$

where ΔE_p is the full width at half maximum (FWHM) of the plasmon loss peak, therefore, it is clear the plasmon loss peak in EELS can be modelled by a Lorentzian function, since the E_p and ΔE_p are constants. The theoretical bulk plasmon loss energy for GaN, InN and AlN can be calculated as 19.21 eV, 16.36 eV and 19.92 eV respectively from $E=\hbar\,[ne^2/V(x)(\varepsilon_0 m)]^{1/2}$ [23]. During the electron beam passing the sample, it transfers kinetic energy to give the displacement of the electron gas. Due to the energy conservation law, the primary electron loses the same amount of energy in order to create the plasma oscillation. Since the electron beam has been accelerated with high voltage, the energy loss is small, yielding a plasmon loss peak somewhere between 1eV (conductor) to 30eV (insulator). For many semiconductors, the plasmon loss is located at around 15eV.

Plural plasmon scattering is an unwanted effect, as plural scattering distorts the shape of the higher energy-loss spectrum [26]. The reduction of the sample thickness under the mean-free path of the inelastic scattering process can minimize the plural scattering effect, unfortunately, the control of thickness during sample preparation is difficult. By using deconvolution one can remove plural scattering effectively [26]. The Ga 3d transition is another issue during plasmon measurements of GaN and its ternary alloys [37], as it partially overlaps with the plasmon, creating a shoulder on the high-energy side, which leads to an apparent asymmetry of the plasmon peak. The shift of the plasmon peak position can affect the measurement precision of the In concentration in InGaN ternary alloy.

2.3.6.2 Core losses

When a high energy electron beam transfers sufficient energy to K, L, M, N or O shell electrons in order to eject them from the nucleus, the atom is ionized. The decay of the ionized atom back to its ground state can lead to emission of an X-ray photon or an Auger electron. Therefore,

the core-loss EELS and EDXS can be described as different aspects of the same excitation mechanism.

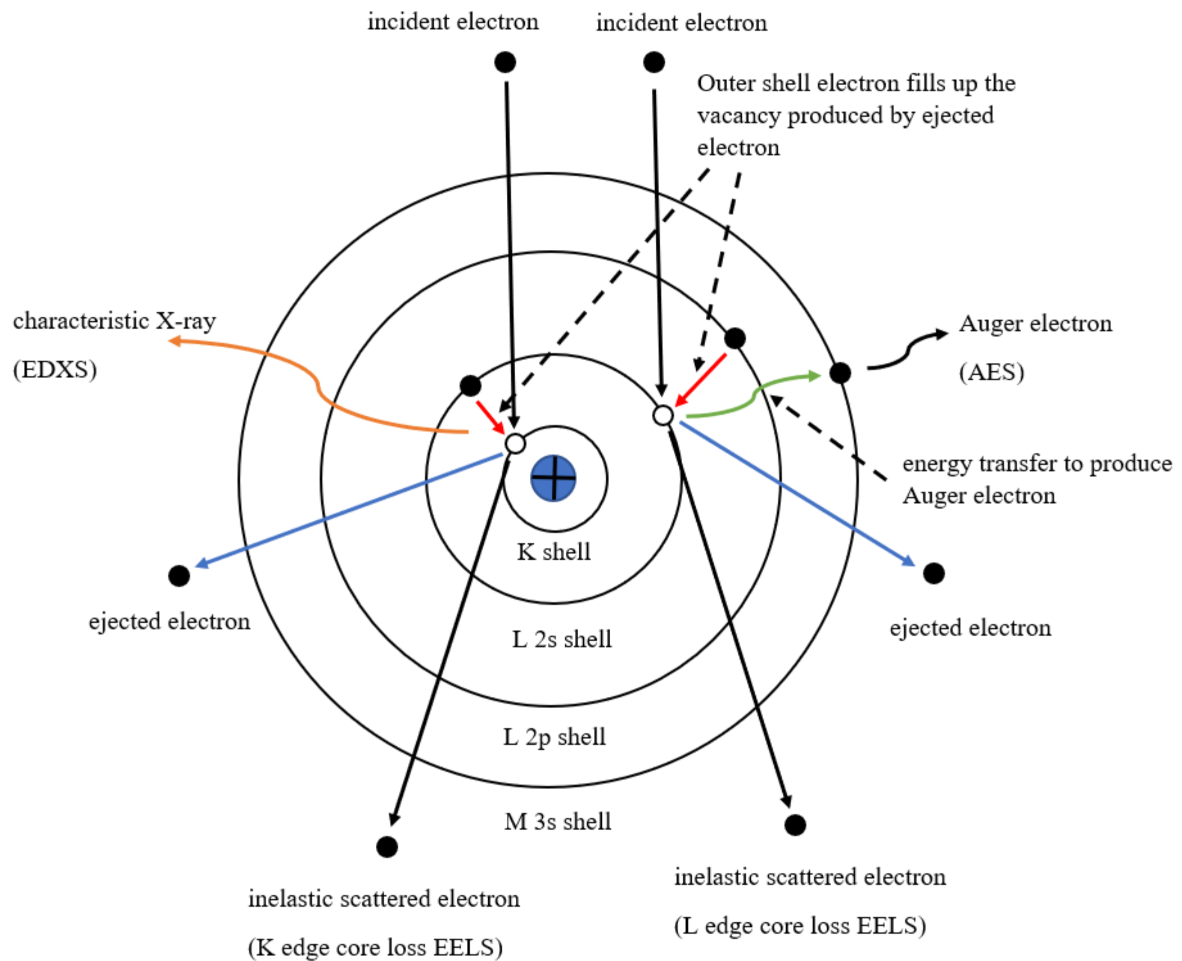

Figure 31: range of possible edges due to inner shell ionization associated with the energy dispersive X-ray spectroscopy (EDXS) and Auger electron spectroscopy (AES).

Due to the loss of the electron beam energy during inelastic scattering, the core-loss edge is at higher energy loss than the plasmon loss peak, the valence electron binding energy is small compared to the ionisation energy under consideration. A small collection aperture can act as enhancement tool for improving the edge/background ratio [23]. However, reducing the collection aperture will result in a weaker core loss signal [23], therefore, a selection of

optimized collection aperture and proper background subtraction may result in a relatively good spectrum.

In principle, the K ionization edge of a free atom shows a sawtooth-shaped profile, while the L core loss represents a more rounded profile. In crystals the profiles can be further modified in detail. Due to their relatively low intensity, overlap with the background can make them hard to observe. A good understanding of the background can render a good background subtraction to the spectrum, creating a possibility to measure the edge profile and position [38].

For low-loss EELS of InGaN, the Ga 3d and In 4d can be observed after its plasmon peak. The low energetic core losses of GaN are the Ga 3d transitions and yield $M_{4,5}$ edges at 23.8 and 28.5eV [39]. For InN these are In 4d transitions that yield $N_{4,5}$ edges at 20.0 and 25.9eV [39]. The low energetic core losses combined with plasmon losses are an important tool for quantifying phase separation in InGaN ternary alloys.

2.3.6.3 Band edge onset of III-nitride semiconductors

The density of states (DOS) describes the number of quantum states that are available per energy interval and volume in a system and is essential for determining the carrier concentration and energy distribution of carriers within a semiconductor material.

For a TEM cross-sectional sample with 100 nm thickness, no significant quantum confinement effect is expected in the electron beam propagation direction. When attempting to fit the band edge onset in valence EELS, the expected profile would have a behaviour of intensity$\propto$ $(E-E_g)^{0.5}$ for a bulk semiconductor with a direct bandgap, E_g, such as InGaN.

In order to accurately determine the band edge onset, three main issues should be considered in the analysis.

1. The energy resolution of spectrum should be high enough to separate the bandgap from the zero-loss peak, for example, our JEOL 2010F can achieve an energy resolution of ~0.8 eV, which is not sufficient to determine the bandgap of the pure InN or high In content InGaN

ternary alloy (<0.8 eV). To absolutely determine the band edge onset, the influence from the zero-loss tail should be as small as possible. therefore, the zero-loss tail should be modelled and subtracted from the raw spectrum, which ensures the band edge onset can be observed.

2. For many semiconductor materials, their dielectric constant (ε) is large enough to observe Cerenkov radiation between the ZLP and plasmon peak [31,35]. The band edge onset cannot be accurately determined unless the Cerenkov radiation is properly modelled and subtracted from the EEL spectrum.

3. Since the plasmon peak can be modelled by a Lorentz function which has pronounced tails, therefore, the plasmon peak intensity will never drop to 0 in the preceding energy loss interval. To determine the band edge onset, the plasmon peak should be properly modelled and subtracted from the spectrum.

In our experiment, we have used an aberration corrected STEM equipped with monochromator to improve the energy resolution of the spectrum. An energy resolution of ~0.15eV could be achieved, which is sufficient for measuring the InGaN band edge onset. To minimize the Cerenkov radiation in the sample, the microscope was operated at low accelerating voltage to reduce the electron speed travelling in the sample. The zero-loss tail and plasmon loss tail should be subtracted from the recorded high-quality spectrum before fitting the bandgap intensity by a square root function.

2.3.7 Thickness determination from EELS and EFTEM

The determination of sample thickness is sometimes necessary for material analysis. The thickness can be measured by both EELS and EFTEM. The relative thickness can be expressed as [23]

$$\frac{t}{\lambda} = \ln\left(\frac{I_t}{I_0}\right) \tag{33}$$

where t is sample thickness, λ is the total inelastic mean free path for all inelastic scattering, I_t is the total integral intensity under the whole spectrum and I_0 is the integral intensity under the zero-loss peak. The relative amount of elastic scattering compared to the total scattering thus determines the sample thickness. The inelastic mean free path can be approximated by equation (34)

$$\lambda = \frac{106F(E_0/E_m)}{\ln(2\beta E_0/E_m)} \tag{34}$$

□here β is the collection angle in mrad, E_0 is the incident electron energy in keV, F is the relativistic factor defined as F=(1+E_0/1022)/(1+E_0/511)^2 E_m is called mean energy loss, measured in eV and an approximate formula for E_m was first approximately proposed by Malis et al. (1988) as E_m=0.76$Z^{0.36}$, where Z is the effective atomic number. The effective atomic number can be expressed as

$$Z = \frac{\sum_i f_i Z_i^{1.3}}{\sum_i f_i Z_i^{0.3}} \tag{35}$$

where f_i is the atomic fraction of each element with atomic number Z_i.

In the combination of equations (33), (34) and (35), the investigated material thickness t can be estimated. The estimation usually has 10% error.

2.3.8 Delocalization of inelastic scattering

The spatial resolution in EELS is limited by the interaction width of inelastic scattering [23]. The delocalization of inelastic scattering is defined as width of the real-space distribution of scattering probability, which gives an object size function [40]. As observed from Rutherford's scattering model in Figure 32, the impact parameter m determines the scattering angle of an electron, where a small m value implies a strong electrostatic interaction, resulting in a large scattering angle. The large inelastic scattering angle indicates a localized electron-atom scattering.

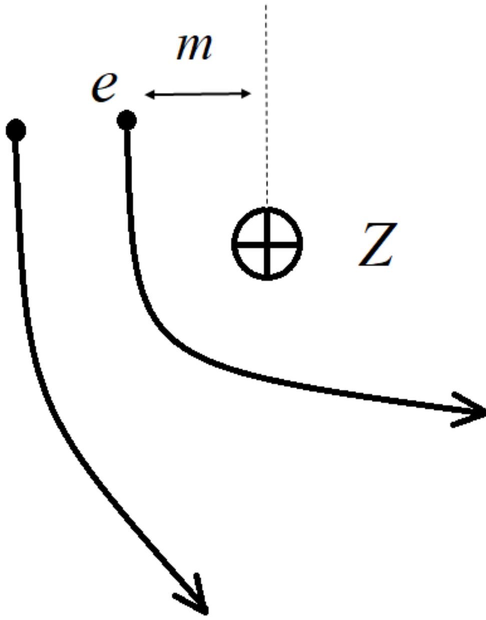

Figure 32: schematic of Rutherford scattering

For high energy loss, the inelastic scattering angle is large and the scattered electron fills the collection aperture of semi-angle β. Therefore, the resolution is limited by diffraction of the electron to $0.6\lambda/\beta$. At low energy loss, the scattered electron does not fill the aperture since the scattering angle is smaller than the collection aperture. The spatial resolution can be defined as the diameter d_{50} that contains 50% of the intensity from a Fourier transform of the finite energy and thus also finite momentum transfer based on mean scattering angles and finite collection aperture. d_{50} can be calculated as [23]

$$(d_{50})^2 = (0.5\lambda/\theta_E^{3/4})^2 + (0.6\lambda/\beta)^2 \quad (36)$$

The delocalization is important in plasmon and bandgap EELS mapping, where the delocalization can directly be used to measure the extent of a plasmon. The sampling in a spectrum image should be set large enough to make sure each pixel contains local sample information.

2.4 Chapter conclusion

In this chapter, the main analytical methods for InGaN research in chapters 3-6 are introduced. For EDXS measurement, the spatial resolution is limited by (multiple elastic) electron beam broadening in the material, and the interaction volume is determined by sample thickness, material geometry of sample and take-off angle. A thinner sample provides better spatial resolution, however, the lower counts in the spectrum will lead to larger statistical errors in quantification. A thicker sample gives large X-ray intensity from which more accurate quantification can be obtained, while the strong beam broadening in the sample will decrease the spatial resolution. For low-loss EELS quantification, the spatial resolution is limited by aberrations and scattering delocalization, the spherical and chromatic aberration can be improved by using an aberration corrector and monochromator. The delocalization can be also improved by reducing the accelerating voltage of the microscope, therefore, in STEM EELS measurement, the sampling size should be bigger than the delocalization width to make sure the EEL spectra in each pixel are independent. The energy resolution of an EEL spectrum can be improved by monochromation. A smaller spectrometer entrance aperture can be used to limit induced aberrations if no monochromator is available.

References

[1] X Wang, M P Chauvat, P Ruternana and T Walther (2015). Combination of electron energy-loss spectroscopy and energy-dispersive X-ray spectroscopy to determine indium concentration in InGaN thin film structures. *Semicond. Sci. Technol.* **30** (11), 114011.

[2] V C Angadi, C Abhayaratne and T Walther (2016). Automated background subtraction technique for electron energy-loss spectroscopy and application to semiconductor heterostructures. *J. Microsc.* **262** (2)**,** 157-166.

[3] H Amari (2011). Characterization of AlGaN and InGaN thin film and quantum wells by analytical transmission electron microscopy, PhD thesis, University of Sheffield.

[4] S J Pennycook, M Varela, C J D Hetherington and A I Kirkland (2006). Material advances through aberration-corrected electron microscopy. *MRS Bulletin*, **31**(1), pp 36-43.

[5] D B Williams and C B Carter (1996). *Transmission Electron Microscopy*. Springer, New York, 1st edition.

[6] M D Graef (2003). *Introduction to conventional transmission electron microscopy*. Cambridge University Press, Cambridge. ISBN: 0521629950.

[7] J M Zuo and J C H Spence (2017). *Advanced transmission electron microscopy*. Springer, New York, ISBN: 978-4939-6607-3.

[8] C Hetherington (2004). Aberration correction for TEM, *Material Today* **7**(12), pp 50-55.

[9] L Reimer (1989) Transmission Electron Microscopy - Physics of Image Formation and Microanalysis. Springer Series in Optical Sciences, 2nd ed., Berlin.

[10] R F Klie (2009). Viewpoint: reaching a new resolution standard with electron microscopy. *Physics* **2**, 85.

[11] http://en.wikipedia.org/wiki/Energy-dispersive_X-ray_spectroscopy#/media/File:EDX-scheme.svg, accessed on 18/01/2018.

[12] NORAN Instruments, Energy-Dispersive X-ray Microanalysis, An Introduction. Wisconsin, Copyright 1983, 1988, 1989 Kevex Instruments, Inc., 1999 NORAN Instruments.

[13] D C Creagh and J H Hubbell (1987). Problems associated with the measurement of X-ray attenuation coefficients. I. silicon report on the International UNION of Crystallography X-ray Attenuation Project. *Acta. Cryst* **A43**, 102-112.

[14] https://www.nist.gov/pml/x-ray-mass-attenuation-coefficients, access on 28/06/2018.

[15] https://nau.edu/CEFNS/Labs/Electron-Microprobe/GLG-510-Class-Notes/Detection-of-Signals/, accessed on 18/01/2018.

[16] Hovington P, Drouin D and Gauvin R, (1997) CASINO: A new Monte Carlo code in C language for electron beam interaction .1. Description of the program. *Scanning* **19** (1997) 1-14.

[17] J I Goldstein, J L Costley, G W Lorimer and S J B Reed (1977). Quantitative X-ray Analysis in the Electron Microscope Scanning Electr. Microsc. *Proc. Workshop Anal. Electron Microsc*. (IIT Research Institute, Chicago, IL, USA, March 1977, **1**) ed O Johari, p 315

[18] S J B Reed (1982). The single-scattering model and spatial resolution in X –ray analysis of thin foils. *Ultramicrosc.* **7,** 405-410.

[19] J R Michael, D B Williams, C F Klein and R Ayer (1990). The measurement and calculation of the X-ray spatial resolution obtained in the analytical electron microscope. *J. Microsc.* **160,** 41

[20] T Walther and X Wang (2016) Self-consistent method for quantifying indium content from X-ray spectra of thick compound semiconductor specimens in a transmission electron microscope. *J. Microsc*. **262**, 151-156.

[21] N Metropolis and S Ulam (1949). The Monte Carlo method. *J. Am. Stat. Assoc*. **44**, 335-341.

[22] http://www.eels.info/products/gatan-imaging-filter-gif, accessed on 29/01/2018.

[23] RF Egerton (1996). *Electron Energy-loss Spectroscopy in the Electron Microscope*, 2nd ed. Plenum Press, New York.

[24] P L Potapov and D Schryvers (2004). Measuring the absolute position of EELS ionisation edges in a TEM. *Ultramicrosc.* **99** 73–85.

[25] Y Wang, M R S Huang, U Salzberger, K Hahn, W Sigle and P A Van Alken (2018) Towards atomically resolved EELS elemental and fine structure mapping via multi-frame and energy-offset correction spectroscopy. *Ultramicrosc*. **184**, 98-105.

[26] P E Batson, K L Kavanagh, J M Woodall and J.W Mayer (1986). Electron-energy-loss scattering near a single misfit dislocation at the GaAs/GaInAs interface. *Phys. Rev. Lett.* **57** 2729.

[27] Z L Wang (1996). Valence electron excitations and plasmon oscillations in thin films, surfaces, interfaces and small particles, *Micron* **27**, 265.

[28] M Stöger-Pollach (2008). Optical properties and bandgaps from low loss EELS: pitfalls and solutions. *Micron* **39**, 1092.

[29] K A Mkhoyan, T. Babinec, S. E. Maccagnano, E. J. Kirkland and J. Silcox (2007). Separation of bulk- and surface-losses in low-loss EELS measurements in STEM. *Ultramicrosc.* **107**, 345.

[30] H Raether (1980). *Excitations of plasmons and interband transitions by electrons.* Springer, Berlin.

[31] B Rafferty, S J Pennycook and L M Brown (2000), Zero loss peak deconvolution for bandgap EEL spectra. *J. Electron Microsc.* **49**(4), 517-524.

[32] R Erni, N D Browning (2008). The impact of surface and retardation losses on valence electron energy-loss spectroscopy. *Ultramicrosc.* **108,** 84–99

[33] K. Kimoto, G. Kothleitner, W. Grogger, Y. Matsui, F. Hofer (2005). Advantages of a monochromator for bandgap measurements using electron energy-loss spectroscopy. *Micron* **36**, 185.

[34] R Erni, N D Browning (2005). Valence electron energy-loss spectroscopy in monochromated scanning transmission electron microscopy. *Ultramicrosc.* **104,** 176.

[35] L Gu, V Srot, W Sigle, C Koch and P A van Aken (2008). VEELS band gap measurements using monochromated Electrons, *Proc Electron Microscopy and Analysis Group Conference* 2007 (EMAG 2007) Journal of Physics: Conference Series **126**, 012005.

[36] P A Cherenkov, (1934). Visible emission of clean liquids by action of γ radiation. *Doklady Akademii Nauk SSSR* **2**: 451.Reprinted in Selected Papers of Soviet Physicists, *Usp. Fiz. Nauk* 93 (1967) 385. V sbornike: Pavel Alekseyevich Čerenkov: Chelovek i Otkrytie pod redaktsiej A. N. Gorbunova i E. P. Čerenkovoj, M.,"Nauka, *1999, s. 149-153.*

[37] X Kong, S Albert, A Bengoechea-Encabo, M A Scanchez-Garcia, E Calleja and A Trampert (2012). Plasmon excitation in electron energy-loss spectroscopy for determination of indium concentration in (In,Ga)N/GaN nanowires. *Nanotechnology.* **23** 485701.

[38] V C Angadi and T Walther (2014). Core-Loss Edge Detection and Background Subtraction Techniques for EELS, *Hyperspectral Imaging and Applications Conference, Sheffield.*

[39] X Wang, M P Chauvat, P Rutherana and T Walther (2016). Investigation of phase separation in InGaN alloys by plasmon loss spectroscopy in a TEM, *MRS Advances* **1**: 40, pp 2749-2756.

[40] S J Pennycook, D E Jesson and N D Browning (1995) Atomic-resolution electron energy loss spectroscopy in crystalline solids. *Nucl. Instrum. Methods B*. **96**, 575-582.

[41] Oxford Instrument (2006). An introduction to energy-dispersive and wavelength-dispersive X-ray microanalysis, *Microscopy and Analysis* **20**(4): S5-S8 (UK).

[42] private communication from R. Gauvin to T. Walther by email on 19 July 2014.

Chapter 3

3. Quantification of In concentration in InGaN thin film ternary alloys with variable In content

Cliff and Lorimer 1975 [1] applied a standard sensitivity factor (k_{AB} factor in equation (20)) to determine chemical composition in a thin specimen where their *k*-factor depends on primary voltage (V_0), take-off angle (θ) and detector efficiency (ζ). The absorption and fluorescence effect are ignored in this thin film approach. A *ZAF* correction is essentially needed on top of the standard Cliff-Lorimer equation to quantify the element concentration in thicker samples, where the absolute thickness and density is difficult to measure. Three methods have been developed previously by some research groups that try to avoid the difficulties of thickness and density determination.

1) determination the absorption correction by extrapolating the X-ray intensity ratio to zero thickness [2-5];
2) extrapolating relative absorption difference between two X-ray emission lines (K, L lines or L M lines) from a single element to estimate mass attenuation factors, called K-L ratio method or differential X-ray absorption method [6,7].
3) The zeta factor absorption correction method proposed by Watanabe [9-11].

Both methods have their own limitations. For the first method, many of the X-ray measurements must come from the same area with multiple tilting angles [8] or different areas with exactly identical surface structure so the extrapolated absorption correction factor is only thickness dependent. In addition, the absorption correction extrapolated from a planar TEM specimen cannot be directly transferred to a wedge sample, since the X-ray absorption lengths in the samples are different for the two kinds of specimens. In the K-L ratio method, sinceboth of the X-ray lines are required from single elements, therefore, the absorption correction is only applicable if an element has $Z>20$ (Ca).

The third absorption correction method called zeta-factor correction (ζ_A)was developed by Watanabe et al. [9-11]. The ζ_A factor can be independent from thickness and density, however, an accurate measurement of beam current and X-ray take-off angle is required. Also, if a major element is missing from the quantification, this will result in an over/under-estimation of element concentration, thickness and density. Therefore, all major elements should be qualitatively analysed before zeta-factor correction iteration process is applied [12].

In this chapter, the *k** absorption correction method developed in Sheffield is applied to quantify the In concentration in InGaN specimens. The quantification process consists of two parts. Firstly, the Monte Carlo simulation is introduced to derive an effective sensitivity factor (*k** factor) for different $In_xGa_{1-x}N$ ternary alloys as function of Ga K/L ratio, wherein the fluorescence and absorption effects are taking into account during the simulation. Then for the measured Ga K/L in a spectrum a *k** factor is iteratively determined that gives a consistent In content for quantification with both Ga K and Ga L. lines. With this approach the In concentration in different $In_xGa_{1-x}N$ specimens (nominal x values from 0.14 to 0.84) are calculated by using *k** absorption correction. Finally, the absorption corrected method is applied to analyse the In distribution in rough InGaN samples to evaluate the growth mechanism of high In content InGaN islands.

3.1 TEM specimen preparation

The specimen preparation is very important for TEM characterization because the sample thickness strongly influences the quality of spectroscopy. As shown by equations (33), (34) and (35), the ideal plasmon loss can be recorded from a region where the relative thickness is equal to 1 ($t=\lambda$, where t is the sample thickness and λ is the inelastic mean free path). As calculated by equation (34) and (35) in section 2.3.7, GaN has an inelastic mean path of 112 nm at 200 kV (JEOL 2010F with 9.5 mrad collection angle) and 45 nm at 60 kV (NION Ultra

STEM 100 with 35 mrad collection angle). For core-loss spectroscopy the ideal sample should be even thinner (t/λ=0.2-0.3) so multiple plasmon scattering does not influence the edge shape and deconvolution is not necessary. Such thin specimens can be prepared by several TEM sample preparation methods; in this work, we have used tripod polishing and argon ion milling to produce TEM specimens.

The reason for preparing cross-sectional TEM specimen for our InGaN thin films is that the interfaces of InGaN thin film and GaN buffer layer can be directly analysed if viewed edge-on. The procedure of making InGaN TEM specimen can be divided into the following steps:

1) preparing the InGaN blocks,
2) cleaning,
3) face-to-face glueing the cleaned InGaN blocks,
4) sawing the sandwiched sample,
5) mechanical grinding and polishing by using tripod polisher,
6) glueing the polished sample on copper ring,
7) ion milling for final reduction of thickness and surface polishing.

Firstly, two blocks need to be cut from the raw sample, each block having a length of 10 mm and width of 2-3 mm.

Secondly, the blocks need to be cleaned before glueing, as the glue line width can be minimized by a good cleaning process and will thus be stronger. The cleaning the InGaN blocks involves three steps of cleaning. A swipe with n-butyl acetate at room temperature is the first step and removes most of the contamination. After cleaning with n-butyl acetate, acetone is heated to 50°C to further clean the sample. The residual contamination from n-butyl acetate remains will be dissolved by acetone. Finally, the sample is cleaned by ethanol at 70 ^{o}C to dissolve the final

residual from the acetone clean. All the cleaning steps should be checked under a light microscope to make sure all the contaminations are removed from sample surface. The ethanol on the cleaned InGaN blocks will be removed by a dry nitrogen blower. It is notable that the longer the sample surfaces are exposed to air, the larger the possibility the InGaN blocks will again be contaminated by particles from the environment.

Third, Gatan G1 epoxy glue is then used to glue together two parts face-to-face; the epoxy glue has two components, epoxy resin and hardener, and to mix a good glue for TEM sample, the proportion of epoxy resin (yellow in colour) and hardener (transparent) should be 1:10. After carefully mixing the two components, the glue is ready to be used on the prepared InGaN sandwich blocks. The glued InGaN blocks are clamped mechanically to ensure the glue line will be as narrow as possible. The glue is then cured at 100 ^{o}C for ½ to 1 hour.

In the fourth step, after the glue is cured, the sandwiched block is cut by a diamond blade saw perpendicular to the sandwiched InGaN/GaN layers. The cutting thickness is ~1 mm to obtain a cross-sectional cut of the sandwiched sample.

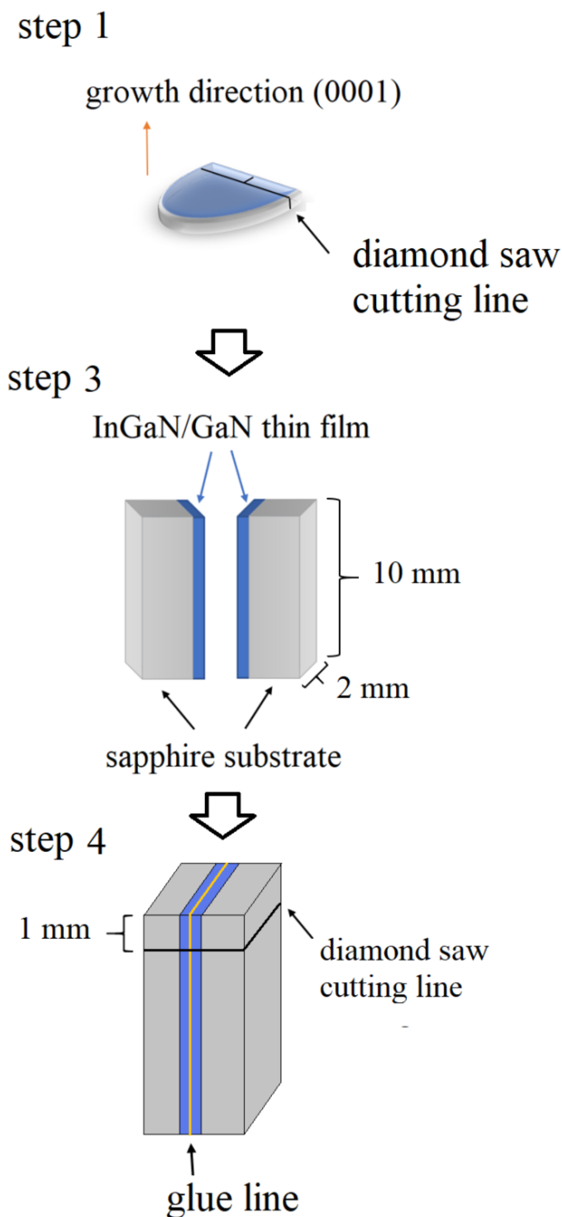

Figure 33: steps 1, 3 & 4 to prepare InGaN sandwiched sample.

Fifth, we have used a South Bay Technology tripod polisher Model 590 to mechanically grind and polish the InGaN sandwich until electron transparency. The structure of the tripod polisher is shown in Figure 34.

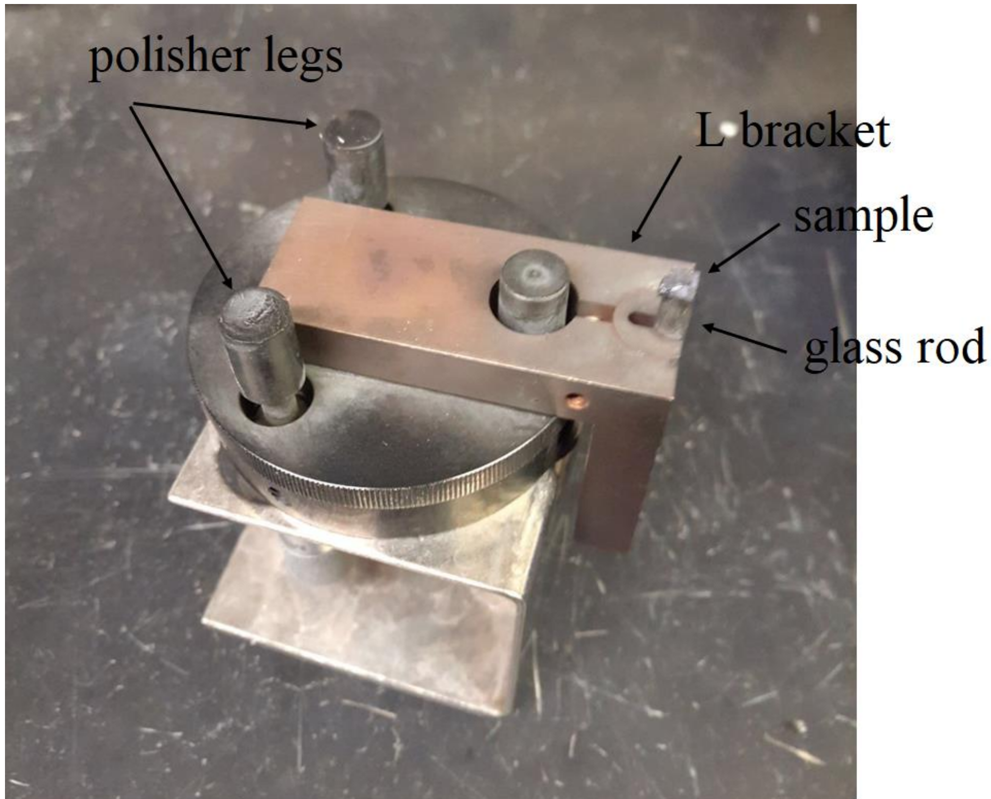

Figure 34: tripod polisher

As shown in Figure 34 an L-formed bracket is attached to the tripod polisher, wherein a glass rod can be inserted. Wax is then used to glue the sample onto the glass rod. Before grinding the sample, two front polisher legs and the sample should be exactly in the same polishing plane; a big metal block is used to calibrate and adjust the three polishing legs. Figure 35 demonstrates the misaligned and aligned tripod polisher before grinding and polishing.

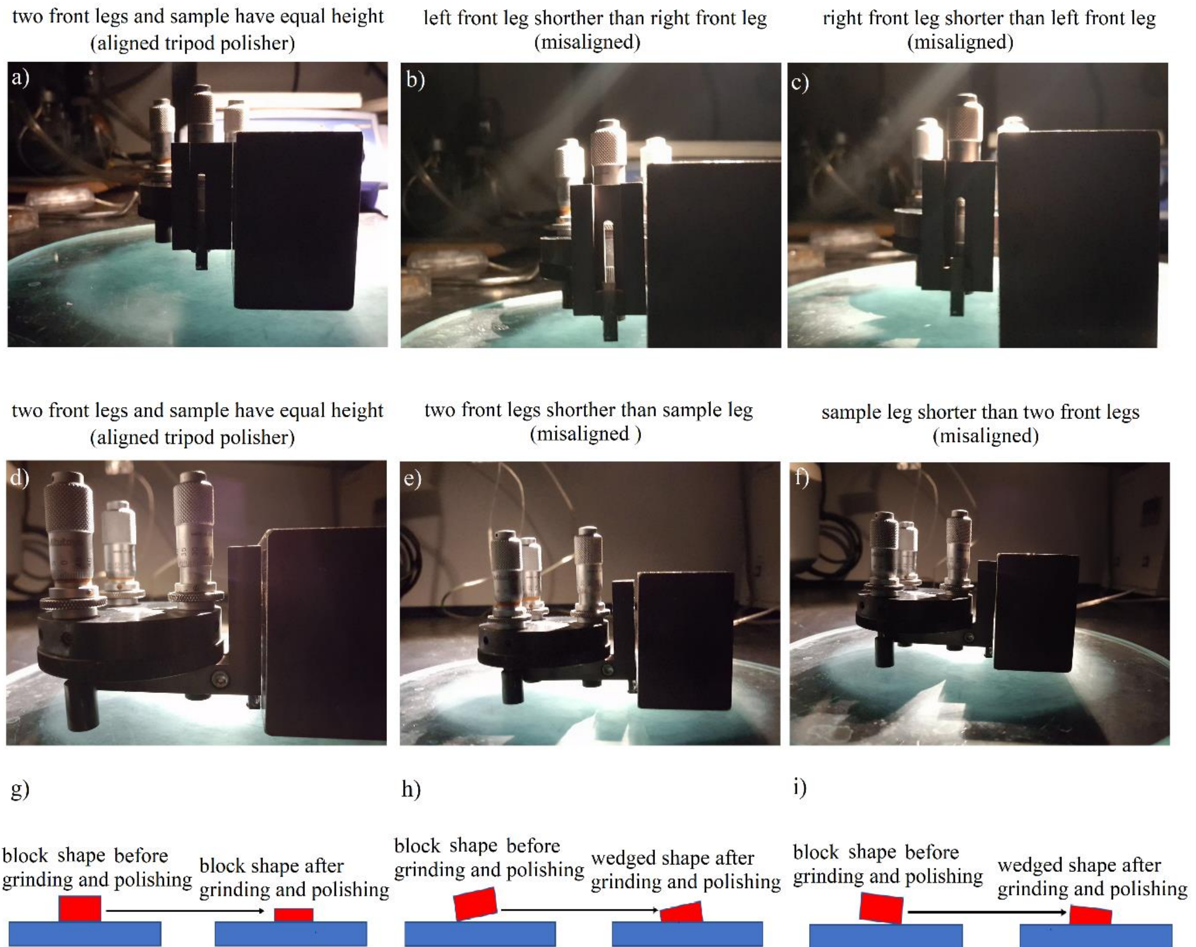

Figure 35: aligned and misaligned tripod polisher

For first side grinding and polishing, the sample shape should remain in the form of a rectangular block but only decrease in thickness. The tripod polisher has 3 legs with micrometre screws that can be adjusted and define the polishing plane and an additional leg with the sample to be polished. As demonstrated in Figure 35 a) and d), the tripod polisher should be calibrated so the three legs with micrometre screws and the sample leg should have equal height, Therefore, during the mechanical grinding and polishing, material will always be removed evenly so the sample retains its block shape (Figure 35 g)). Any misalignments (Figure 35 b) c) e) and f)) will lead to the sample shape transform from block to wedge shape Figure 35 h) and i)). The misaligned tripod polisher can be adjusted by two front legs. After the tripod polisher calibration, 15 μm, 6 μm, 3 μm, 1 μm and 0.6 μm diamond covered polishing cloths

are used to grind and polish the first face of the sample until ~500 μm thin. After every 10 min of grinding and polishing, the tripod polisher should be recalibrated to ensure all legs and sample are still in the same polishing plane.

After finished processing of the first side, the sample is detached from the glass rod, glued with the polished side on a silicon piece by using wax, and then the silicon piece is directly glued on the glass rod. By repeating the calibration of the tripod polisher, the sample is then ground until ~100 μm thin. The final step for mechanical processing of the sample is setting the wedge to roughly 2° for making a wedged sample; the schematic of wedge setting is shown in Figure 36.

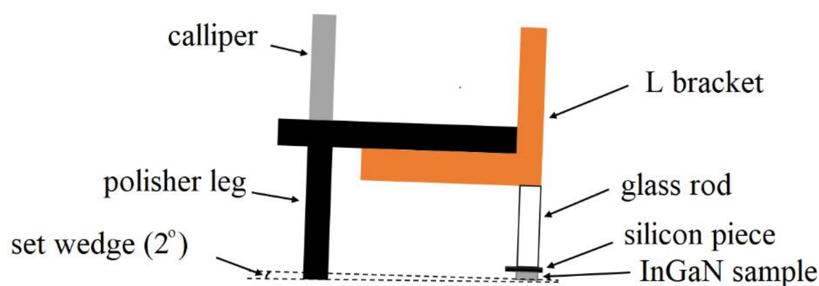

Figure 36: schematic of wedge setting

After the wedge is set, the 0.6 μm diamond cloth is used to polish the sample tip as thin as possible. The tip thickness can be roughly determined by observing the polished region on the silicon piece under a light microscope, as shown in Figure 37.

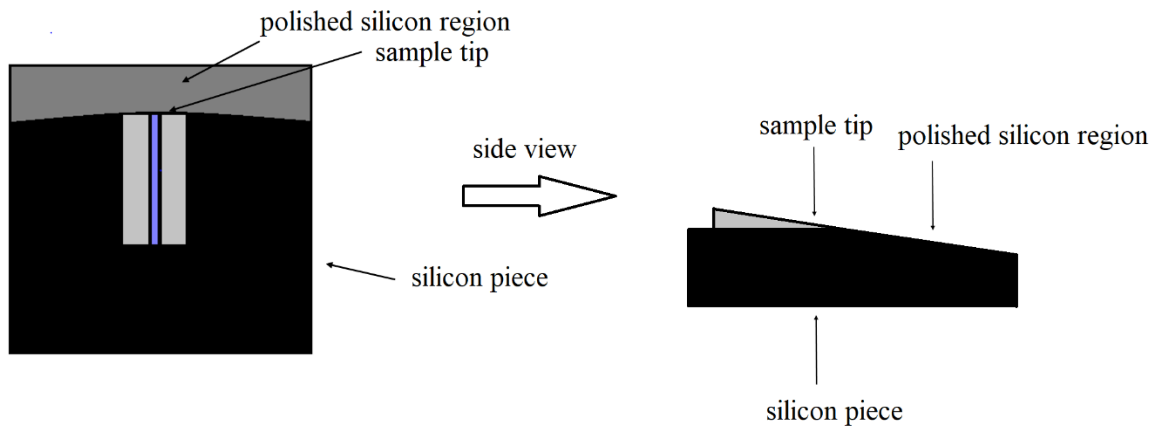

Figure 37: final structure when mechanical polishing has been stopped

As shown in Figure 37, the polishing process can be finished when the polished silicon region reaches the sample's tip; the thickness near the tip then is roughly 1 μm and ideal for ion milling.

Sixth step: as the sample edge is too thin for handling, a copper (Cu) ring is first glued on the sample by G1 epoxy glue, the tip should be placed at the middle of the copper ring, as depicted in Figure 38 a). The sample parts outside the copper ring can be easily removed by cutting with a thin blade. Since the wax is dissolved in acetone much faster than G1 epoxy glue, the sample can be then detached safely from the silicon piece by using acetone. As the G1 epoxy glue is not electrically conductive glue, in Figure 38 b), silver (Ag) paste is used to form a good electrical contact between sample and copper ring.

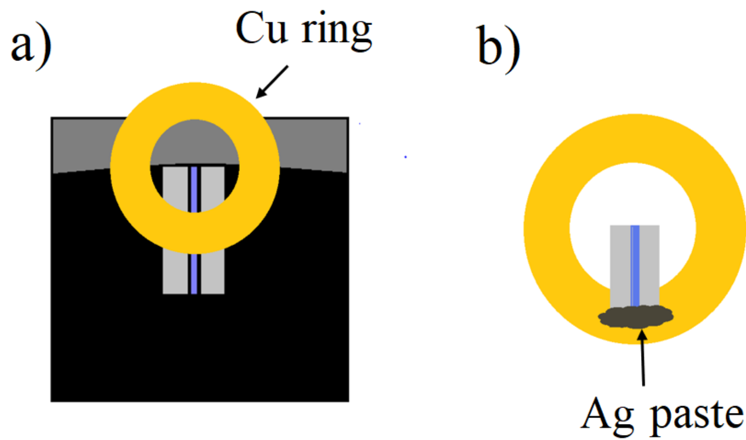

Figure 38: a) positioning of Cu ring glued onto the sample; b) Ag paste position after detaching the sample from silicon piece.

The final step for preparing the TEM sample is argon ion (Ar^+) milling. In this work, a Gatan precision ion polishing system (PIPS) was used to mill and polish the InGaN sample. The starting ion energy for ion milling is set at 5 kV with 10° incident angle. Since the tip is at the middle of the cooper ring, most of the ions are bombarding the tip of the sample. As the tip is roughly 1 μm thick, the maximum milling time at this stage should be less than 10 min. The ion energy is then decreased to 3 kV with 6° incident angle to finely remove the material the sample until thickness fringes are observed under the optical microscope as shown in Figure 39.

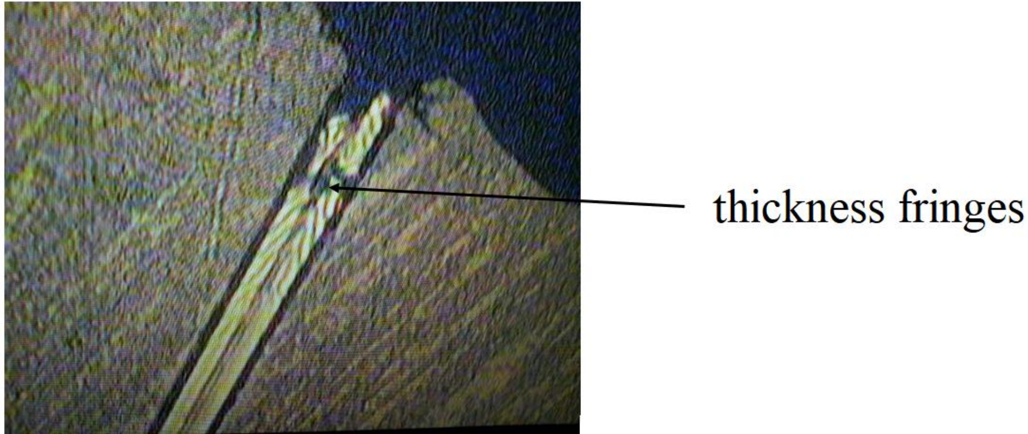

Figure 39: thickness fringes on sample tip

As shown in Figure 39, when thickness fringes are observed under the PIPS in-situ optical microscope, the specimen can be seen as ideally thin near the tip for TEM investigation. To remove damage on the sample surface due to high energy ion bombardment, the final step is ion polishing the sample, the polishing energy is set at 0.6 kV with 3° incident angle; several minutes should be enough.

3.2 Monte Carlo simulation of InGaN sensitivity factor (*k** factor) based on Ga K/L ratio

Based on the Monte Carlo simulations in chapter 2.2.10, as the CASINO software uses relativistically corrected cross-sections and can hence also be used for simulation of X-ray generation in higher voltage TEMs and STEMs, e.g. at 200kV [27]. Casino V 2.4.8.1 [13] is employed to calculate the X-ray intensity generated by fast electrons for different specimen thicknesses. The general set-up of the microscope and detector is for our JEOL 2010F microscope. The accelerating voltage of the microscope is 197 kV and the nominal detector take-off angle is 25°. The diameter of the electron beam in the simulations is assumed to be 50 nm and at least 100,000 electron trajectories are used for the simulation.

The specimen set-up is given by the nominal x value of $In_xGa_{1-x}N$, material thickness and its corresponding density, ρ. □this can be estimated by equation (36).

$$\rho_{In_xGa_{1-x}N}=x\times \rho_{InN}+(1-x)\times \rho_{GaN} \tag{36}$$

where the density of wurtzite GaN and InN can be set as ρ_{GaN}=6.15g/cm^3 [14] and ρ_{InN} 6.81g/cm^3 [14], and x is the In concentration.

Figure 40 demonstrates an example of electron trajectories in $In_{0.5}Ga_{0.5}N$ for a thickness from 10 nm to 2000 nm.

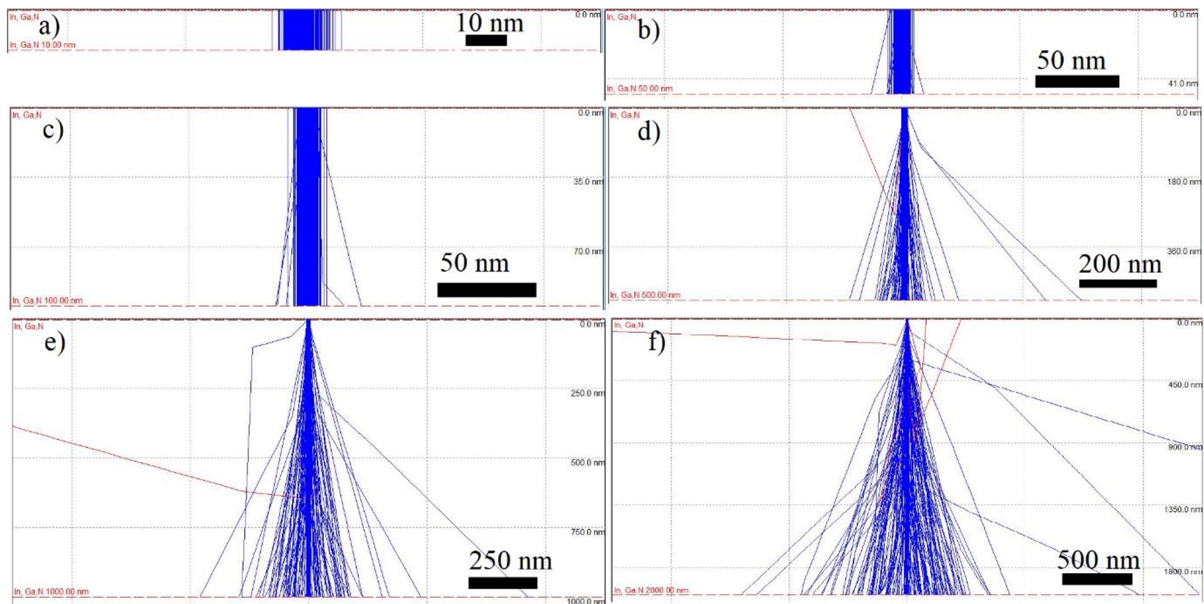

Figure 40: electron trajectories in $In_{0.5}Ga_{0.5}N$ thin film sample of thickness a) 10nm, b) 50nm, c) 100 nm, d) 500nm, e) 1000nm, f) 2000nm.

In Figure 40, each line represents an electron scattering path inside the sample, where elastic and inelastic scattering will take place along those electron trajectories. As fluorescence and absorption effects of characteristic X-rays are considered in Casino V 2.4.8.1, the X-ray intensity after considering the self-absorption effect of In L, Ga K and Ga L can be determined and is listed in Table 1.

Thickness (nm)	Ga_K intensity	Ga_L intensity	Ga K/L ratio	In_L intensity
10	2.36	1.84	1.28	2.10
50	11.77	8.10	1.45	10.36
100	23.49	13.92	1.69	20.36
500	115.84	28.06	4.13	89.29
1000	226.19	29.37	7.70	152.11
2000	433.90	29.86	14.53	229.23

Table 1: I_{GaK} and I_{GaL} and I_{InL} for different thicknesses (x=0.5).

For InGaAs or InGaSb, the heavy element of the group-V sub-lattice (arsenic or antimony) can be used for reference of a known concentration (50at%), and it has recently been shown that plots of an effective k-factor, $k^*_{\mathrm{In,As}}$, as function of As K/L ratio, yields unique calibration curves that can provide the indium concentration in a precise and self-consistent way for InGaAs using the As L or the As K line as reference [15].

Unlike InGaAs, nitrogen has no L line and so for $In_xGa_{1-x}N$ alloys only the Ga X-ray lines can serve as internal reference. The same in principle applies to InGaP, where phosphorus has only very weak and low-energy L-lines (0.13-0.18keV) that are difficult to detect and almost impossible to quantify, even for a windowless X-ray detector. For $In_xGa_{1-x}N$ we can neglect C_N and assume $C_{In}+C_{Ga}$=50 at% for the group III atoms, therefore, $k^*_{InL\,GaK}/k^*_{InL\,GaL}$ is required to calculate the In concentration with respect to Ga concentration. The k^* factor can be written as follows

$$k^*_{\mathrm{InL,GaL}}=x_{In}\, I_{\mathrm{GaL}}\, A_{\mathrm{In}}/[(1-x_{in})I_{\mathrm{InL}}\, A_{\mathrm{Ga}}]$$
$$k^*_{\mathrm{InL,GaK}}=x_{In}\, I_{\mathrm{GaK}}\, A_{\mathrm{In}}/[(1-x_{in})I_{\mathrm{InL}}\, A_{\mathrm{Ga}}] \quad (37)$$

where x_{In} is the In concentration value for the simulation, I_{GaL}, I_{GaK} and I_{InL} are the X-ray intensities of Ga L, Ga K and In L lines, and A_{Ga} and A_{In} are the atomic weights of Ga and In. The theoretical curve of k^* factor including absorption and fluorescence effect as a function of Ga K/L ratio for $In_{0.5}Ga_{0.5}N$ sample is shown in Figure 41.

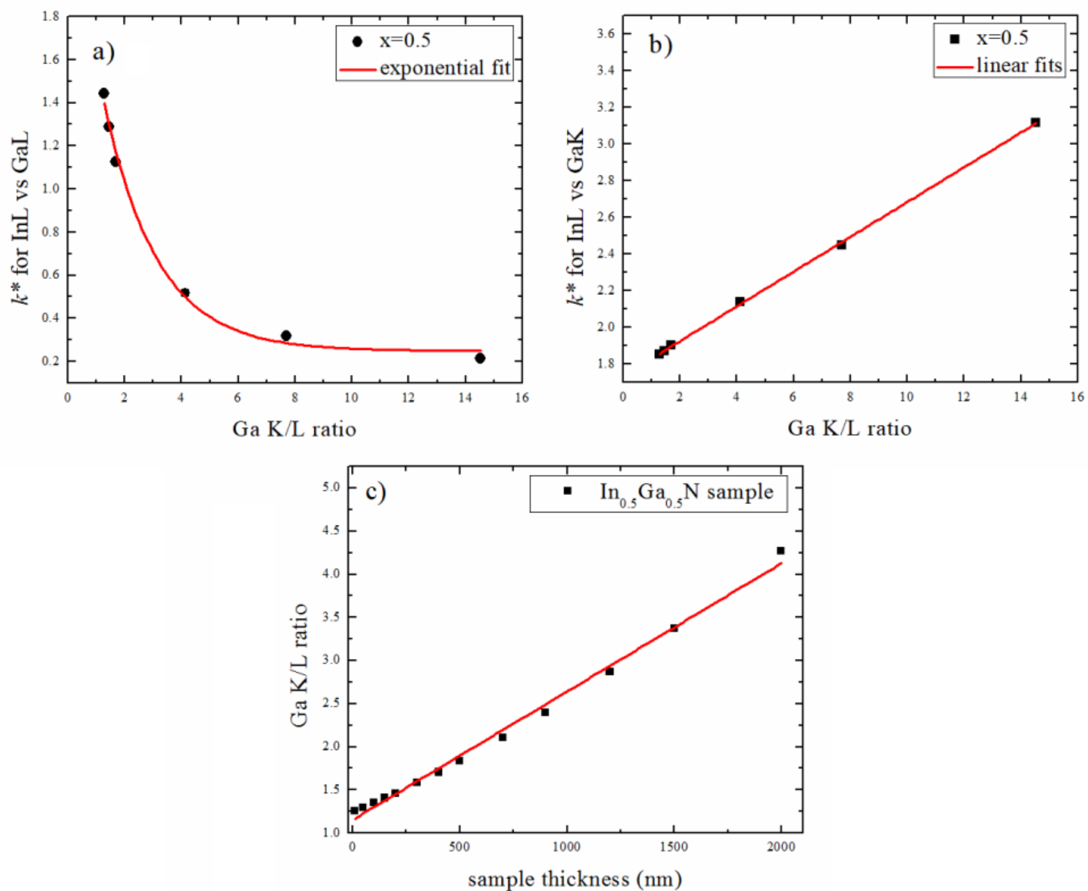

Figure 41: Casino simulation of a) $k^*_{InL,GaL}$, b) $k^*_{InL,GaK}$, c) sample thickness for $In_{0.5}Ga_{0.5}N$ as function of Ga K/L ratio for 25° X-ray take-off angle.

As shown in Figure 41, $k^*_{InL\ GaL}$ decreases exponentially as a function of Ga K/L ratio, while the $k^*_{InL\ GaK}$ increases almost linearly with Ga K/L ratio. The reason for the different curvatures of $k^*_{InL\ GaL}$ and $k^*_{InL\ GaK}$ are that the Ga_L X-ray (soft X-ray) is suffering greater absorption than Ga_K X-ray (hard X-ray) when it passes through the material and polymer window of the detector. The detection efficiency of our Si:Li detector has been calculated by M C Parri [16],

based on estimated X-ray absorption in the polymer window, top electrode and electric dead space below. In the sample, lower detection efficiency means fewer X-rays are recorded. As the X-ray energy for Ga L line is lower than In L line, it is more strongly absorbed than the In L line, while the Ga K suffers less absorption than In L. Meanwhile, the X-ray mutual fluorescence of X-ray lines in InGaN is of minor importance as the line energies are sufficiently wide apart. Therefore, the k^* factor profile is mainly dominated by the X-ray difference in absorption coefficients.

For $In_{0.5}Ga_{0.5}N$ specimen, since fluorescence effects are negligible, the intensity ratios I_{GaK}/I_{InL} and I_{GaL}/I_{InL} are only related to the corresponding X-ray generation rates, detector efficiencies and absorption coefficients. As the value of x_{In}, A_{In} and A_{Ga} in equation (1) are constant for a given material, by using the Beer-Lambert law, the $k^*_{InL,GaL(K)}$ factor function can be determined by exp $[(\alpha_{InL}-\alpha_{GaL(K)})d/\sin\theta]$, where $\alpha_{GaL(K)}$ is the absorption coefficient of Ga L (K) lines, α_{InL} is the absorption coefficient for In L line, d is the sample thickness and θ represents the X-ray take off angle. As the thickness of the $In_{0.5}Ga_{0.5}N$ sample has an almost linear relation with the Ga K/L ratio, as depicted in Figure 41 c), the exponential decay of $k^*_{InL,GaL}$ can be explained as large absorption difference ($\alpha_{InL}-\alpha_{GaL}$) between In L and Ga L lines, while the absorption of In L and Ga K is more similar, therefore, the profile of $k^*_{InL,GaK}$ shows a only a very weak curvature function of Ga K/L ratio.

By repeating the same approach for $In_xGa_{1-x}N$ samples with different x, the k^* factor plot for both Ga K and Ga L lines in Figure 42 can be computed.

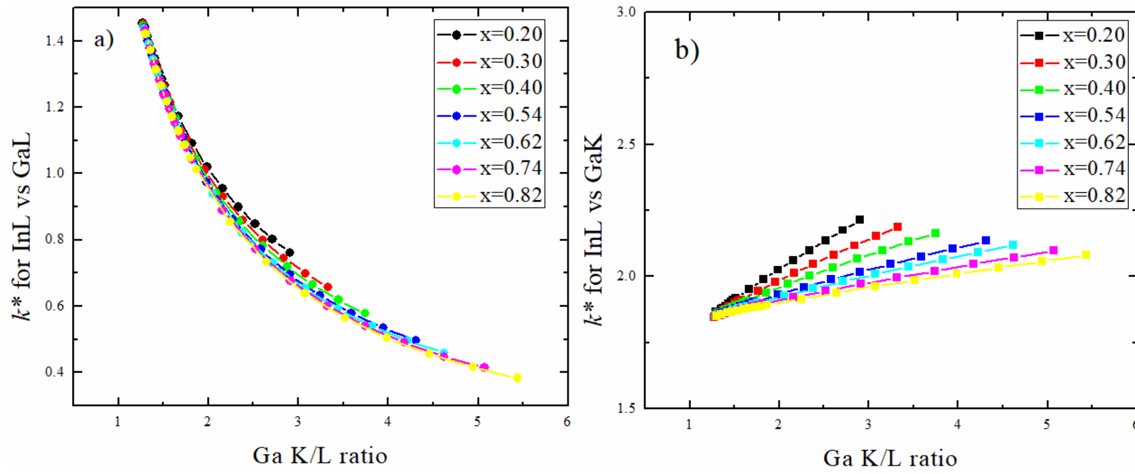

Figure 42: CASINO simulations of a) $k^*_{InL,GaL}$ and b) $k^*_{InL,GaK}$ with different x of $In_xGa_{1-x}N$

Again, we can fit the $k^*_{InL,GaL}$ curve with exponential functions and $k^*_{InL,GaK}$ curve with linear functions, which can be used as the k^* factors in equation (4) to quantify the In concentration in an InGaN ternary alloy. As shown in Figure 42, the end points of the curves for different In concentrations are different. The simulations were run from 50 nm to 1000 nm for pure GaN, $In_{0.25}Ga_{0.75}N$, $In_{0.5}Ga_{0.5}N$ and $In_{0.8}Ga_{0.2}N$ for calculating the intensity of Ga K and Ga L as a function of thickness, however, for different x values of $In_xGa_{1-x}N$, the densities and hence self-absorption are different, so the same physical thickness corresponds to different Ga K/L intensity ratios in the plots. The result is depicted in Figure 43.

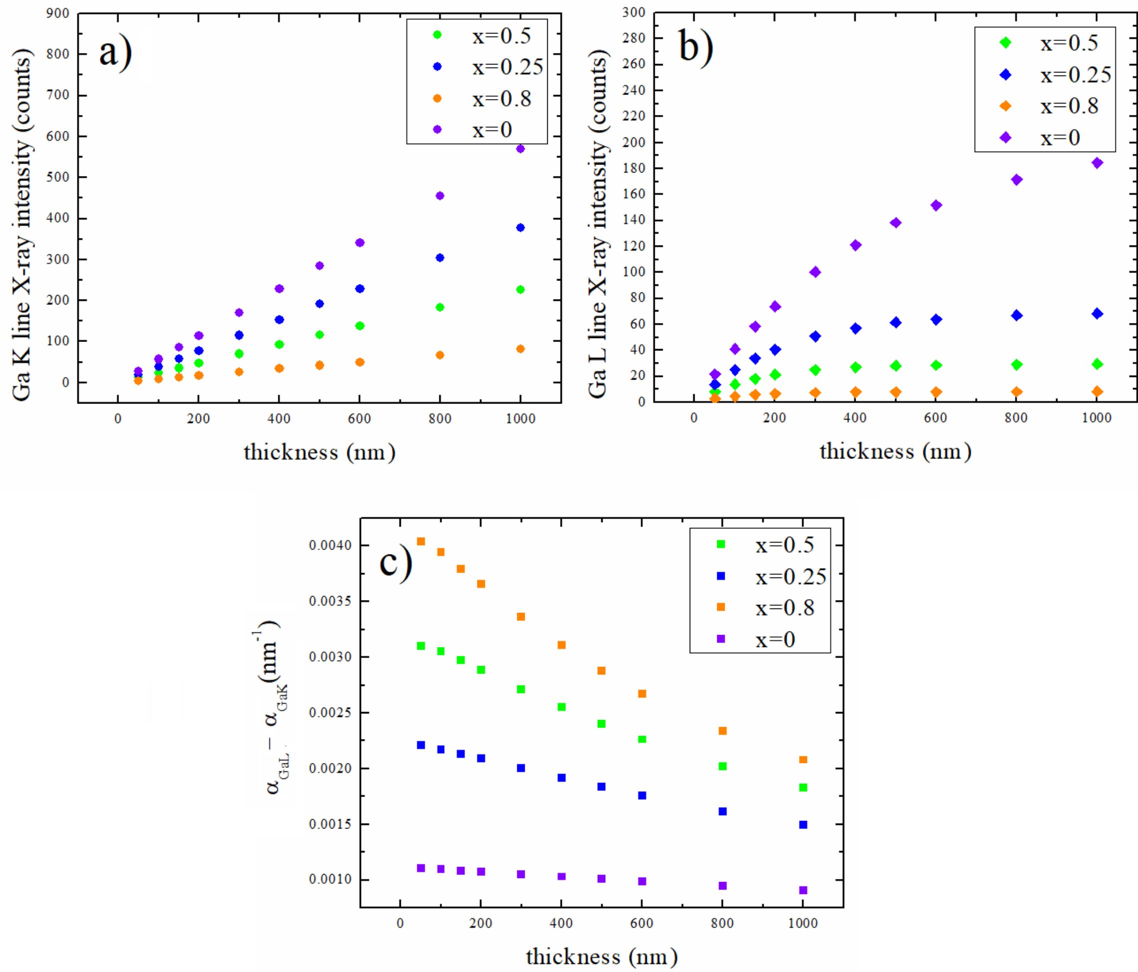

Figure 43: simulation of a) Ga_K X-ray intensity, b) Ga_L X-ray intensity and c) difference of absorption coefficient of Ga_L and Ga_K lines (α_{GaL}-α_{GaK}) as function of sample thickness for $In_xGa_{1-x}N$.

As shown in Figures 43 a) and b), the Ga L intensity increases sub-linearly as thickness increases, while the Ga K intensity has a near-linear relation with thickness. The result indicates Ga L suffers stronger absorption than Ga K X-ray. For high In content InGaN, an increasing amount of gallium atoms is replaced by indium atoms, which systematically decreases the yield of X-ray intensity of both Ga K and Ga L lines. The Ga K/L ratio can be determined from the difference of attenuation coefficients of Ga K and Ga L X-rays ($\alpha_{GaL}-\alpha_{GaK}$), by using Beer's law in chapter 2.2.2 in form of equation (15), and the Ga K/L ratio can be expressed as

$$\frac{I_{GaK}}{I_{GaL}} = \frac{I_{GaK0}}{I_{GaL0}} \exp(\alpha_{GaL-}\alpha_{GaK})\ d/sin\theta \qquad (38)$$

where I_{GaK} and I_{GaL} are the measured X-ray intensity, I_{GaK_0} and I_{GaL_0} are the intensities generated by X-ray fluorescence, d is the sample thickness and θ corresponds to the X-ray take off angle. By using the data in appendix 1, the difference $\alpha_{GaL}-\alpha_{GaK}$ can be plotted as a function of thickness in Figure 43 c). As shown in Figure 43 c), for a given thickness, the largest value of $\alpha_{GaL}-\alpha_{GaK}$ can be found in the InGaN sample of highest indium content; it is thus clear that $\alpha_{GaL}-\alpha_{GaK}$ increases as the In concentration increases, therefore, in the k* factor curves for high In content InGaN a large thickness will always correlate with a large Ga K /L ratio.

3.1 Information on investigated samples

The InGaN samples investigated in this project were grown by both MOCVD and MBE. The nominal $In_{0.3}Ga_{0.7}N$ and InN sample was grown by plasma assisted molecular beam epitaxy (PAMBE) in a chamber equipped with standard effusion cells for Ga, In, Si and Mg, and a radio-frequency nitrogen plasma cell. For $In_{0.3}Ga_{0.7}N$ sample, the active nitrogen flux was fixed at $F_N = 0.38$ monolayers per second (ML/s). Substrates consisted of 4-μm-thick GaN-on-sapphire MOVPE templates. The InGaN growth temperature was 610°C, calibrated with a pyrometer. The growth was monitored *in situ* by reflection high-energy electron diffraction (RHEED). The InN was grown in the same PAMBE system, the substrate temperature was set as 450°C, the N-limited growth rate was measured as 280 nm/h (0.8 ML/s).

The nominal $In_{0.135}Ga_{0.865}N$ (L533), $In_{0.2}Ga_{0.8}N$ (L604), $In_{0.4}Ga_{0.6}N$ (L648), $In_{0.54}Ga_{0.46}N$ (L656), $In_{0.62}Ga_{0.38}N$ (L645), $In_{0.74}Ga_{0.26}N$ (L644) and $In_{0.82}Ga_{0.18}N$ (L587) samples were all grown by MOCVD. The L656 sample is grown by using trimethylgallium (TMGa) and trimethylindium (TMIn) as Ga and In source. Unfortunately, the growth parameters are lost for this sample, which is depicted as not applicable (NA) in the following table. The rest of the

sample are grown by using triethylgallium (TEGa) and TMIn as Ga and In source, for all the samples NH_3 was used as nitrogen precursor. The growth parameters provided by grower are listed in Table 2.

sample number	growth pressure (mbar)	growth temperature (ºC)	growth time (sec)	NH_3 flow (µmol/min)	TEGa flow (µmol/min)	TMIn flow (µmol/min)	V/III ratio	average layer thickness measured by TEM (nm)
L533	800	725	6750	133	1.3	3.9	25.4K	59
L604	400	715	5400	178.6	1.8	6.5	43.7	400
L648	200	755	7200	223.2	.87	0.46	167K	92
L645	200	550	7200	223.2	.87	1.2	110.3K	87
L644	200	550	7200	223.2	.87	2.3	70.3K	202
L587	600	550	7200	223.2	.87	3.5	51.5	NA
sample number	growth pressure (mbar)	growth temperature (ºC)	growth time (sec)	NH_3 flow (µmol/min)	TMGa flow (µmol/min)	TMIn flow (µmol/min)	V/III ratio	average thickness measured by TEM (nm)
L656	NA	NA	NA	NA	NA	NA	NA	NA

Table 2: data of InGaN samples grown by MOCVD

In this project, we have aimed to analyse those InGaN samples by using analytical transmission electron microscope to explore the influence of growth condition on the thin film structure and chemistry. The result will benefit the material growers to improve and optimize the growth conditions of InGaN. The thin film thicknesses were initially measured by using **g**=[0002] weak beam dark field images in TEM, the images shown were provided by Pierre Rutherana and the results have been published [25]. The measured layer thicknesses are listed in Table 2 and some of the weak beam dark field images are presented in Figure 44.

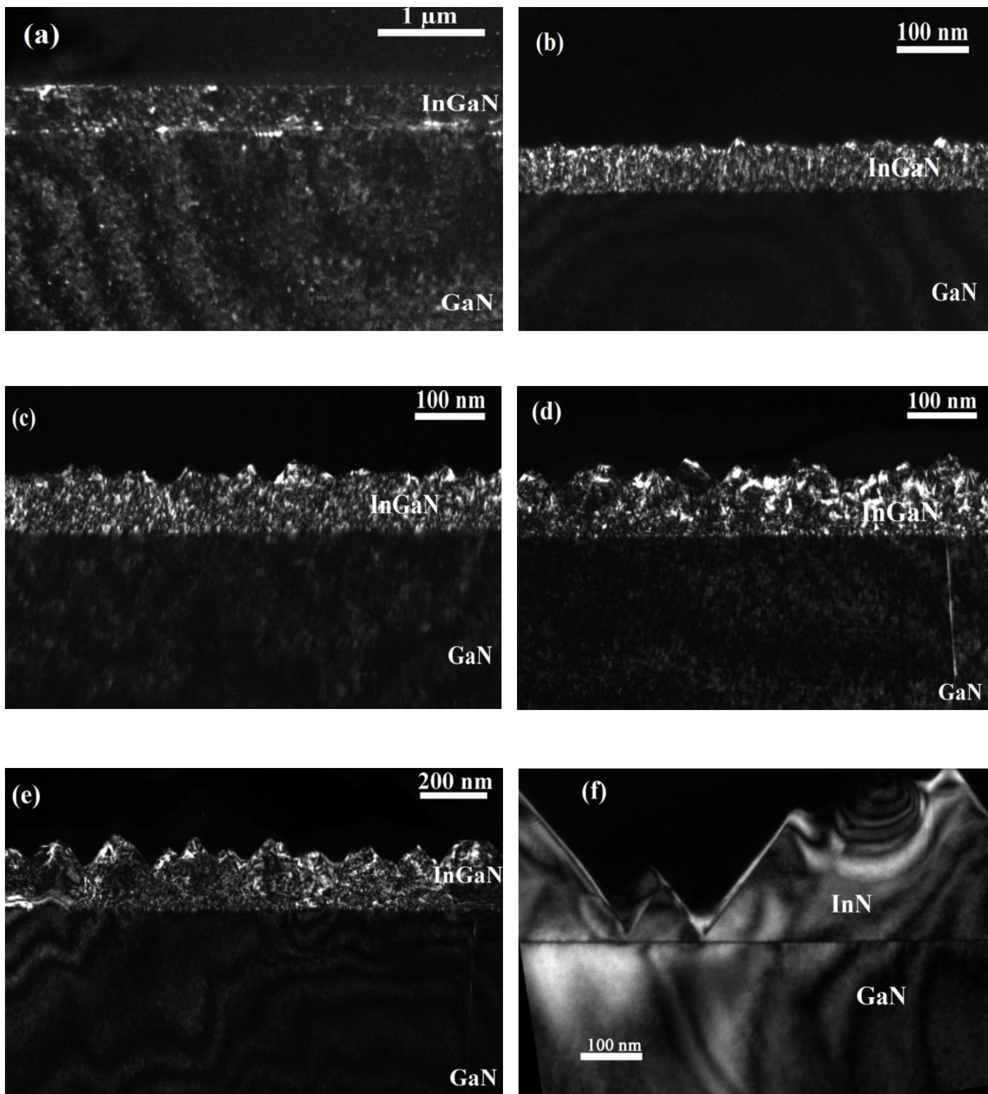

Figure 44: **g**=0002 weak beam image of (a) In0.34Ga0.66N, (b) In0.42Ga0.58N, (c) In0.59Ga0.41N, (d) In0.64Ga0.36N, (e) In0.78Ga0.22N, (f) In0.92Ga0.08N (InN); all images provided by Pierre Rutherana.

As shown in Figure 44, for low In content InGaN sample (L604), even 400 nm thick films of InGaN have a smooth surface (Figure 44 a)). When the indium concentration increases, the surface roughness increases dramatically, and layer crystalline quality degrades as shown in Figures 35 (b)–(e). However, for pure InN growth on GaN, the thin film is approximately 100–300 nm thick and consists of facetted islands of pyramidal forms, as shown in Figure 44 (f), but it exhibits a perfect crystalline quality, in contrast to the In rich ternary alloys. It is thus

clear that as the In concentration increases the growth mode transforms from Frank Van der Merwe (flat layer growth) to Vollmer Webber growth mode (3D island growth).

3.3 Determination of In concentration in $In_xGa_{1-x}N$ layers from EDXS by using *k** absorption correction

In order to calculate the In concentration in InGaN samples from equation (4), the intensities of X-rays and the corresponding *k** factors are needed. As the *k** factor is simulated by Monte Carlo simulation in chapter 3.1, only X-ray intensities need to be measured.

X-ray spectroscopy and mapping was performed using our JEOL 2010F field emission TEM operated at 197 kV, which is equipped with an Oxford Instrument Si:Li ultra-thin polymer window detector. The nominal take-off angle is 25°. The sample has been tilted a few degrees off the zone axis of the cross-section sample to avoid the strong diffraction which can influence the X-ray yield [17]. The quantification of In content was performed by using the normal *k* factor provided by the ISIS 300 software as well as our absorption corrected *k** factor.

To avoid preferential indium loss by electron beam sputtering, the beam current density should be low. To measure beam damage we have used ~5 nA beam current with a 10 nm beam diameter to illuminate the InGaN sample at the same position, and the experiment was conducted over 10 min with a spectrum recorded every 1 min. The measured In/Ga ratios of $In_{0.63}Ga_{0.27}N$ sample are shown in Figure 45.

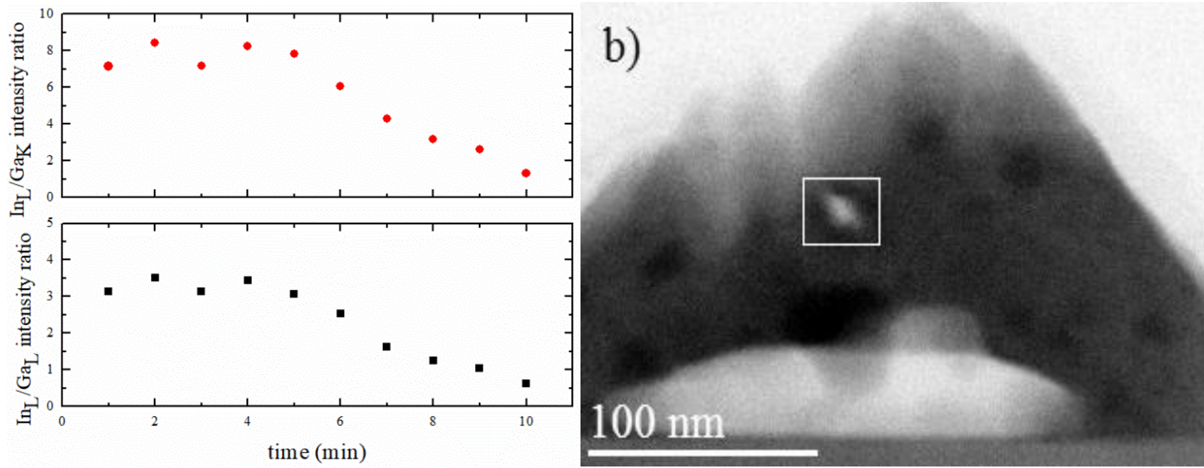

Figure 45: a) Measured I_{InL}/I_{GaK} for the $In_{0.63}Ga_{0.37}N$ specimen with beam focused to ~10nm diameter b) electron beam induced material loss (inside white square) from bright field image.

As shown in Figure 45, after ~5 min, the measured I_{InL}/I_{GaK} ratio starts to decrease, which indicates preferential indium loss in the specimen. In Figure 45 b), the bright field image taken after the experiment indicates a thin regionproduced by the electron beam after illumination for 10 min. The diameter of the locally sputtered area is measured as 12 nm, which correlates with the illuminating electron beam diameter. The corresponding electron beam dose after 5 minutes, which is the point from which the In/Ga ratio starts to change, is 1.91×10^{10} C/m^2. Therefore, the electron beam induced damage on material chemistry property can be minimized if the dose is $< 2\times10^{10}$ C/m^2.

In our next experiments, we have increased the beam diameter from 10 nm to 50 nm. The livetime for all spectra varied from 114 s to 608 s, the corresponding deadtime decreased from 51% to 8%. The effective total illumination time can be calculated by applying equation (3) [12].

$$deadtime(\%) = \frac{clocktime - livetime}{livetime} \times 100\% \qquad (39)$$

The clocktime for the experiment varied from 228 s to 659 s, so the corresponding total electron beam dose ranges from 5.87×10^{8} C/m^2 to 1.68×10^{9} C/m^2. This experimental electron beam

current is too small to cause material loss due to sputtering. It may still produce damage in the form of local atomic re-arrangements but these will not change the chemical composition integrated over larger volumes as measured by EDXS.

The experimental EDXS intensity of Ga K, Ga L and In L for different nominal indium concentrations are listed in appendix 2. For each InGaN sample, we have taken X-ray spectra from different positions, the related thickness being expressed in percentage of deadtime. As Goldstein et al (1992) [18] explained, if an X-ray pulse arrives at the detector, the detector is switched off for a certain period (deadtime) while the pulse processor analyses the pulse. For a thick material yielding more X-rays, the detector will switch off quite often for processing the X-ray pulses [12], therefore the thickness of the sample can be roughly determined by percentage of the deadtime. In appendix 2 the nominal $In_{0.135}Ga_{0.865}N$ sample has Ga K/L ratios <1.24, while CASINO predicts Ga K/L ratio values >1.24 for all InGaN samples of thickness above 1nm, therefore, I could not quantify the absolutely In concentration from the $In_{0.135}Ga_{0.865}N$ sample EDXS spectrum from our absorption correction method. Here, only the standard *k* factor provided by ISIS 300 software has therefore been used to quantify the In concentration from $In_{0.135}Ga_{0.865}N$ spectra.

From appendix 2, to select the proper k^* factor for Ga K and Ga L lines, the Ga K/L ratio should be evaluated for each EDXS spectrum. Any calibrated k^* factor curve for any x_{in} value can be used as a starting point. By applying the measured I_{InL}, I_{GaK}, I_{GaL} and equation (4), an estimate of x_{out} can be obtained.

$$x_{out} = \begin{cases} I_{\text{InL}}\, k^*_{\text{InL, GaL}} / \left(I_{\text{InL}}\, k^*_{\text{InL, GaL}} + I_{\text{GaL}}\, A_{\text{In}}/A_{\text{Ga}} \right) \\ I_{\text{InL}}\, k^*_{\text{InL, GaK}} / \left(I_{\text{InL}}\, k^*_{\text{InL, GaK}} + I_{\text{GaK}}\, A_{\text{In}}/A_{\text{Ga}} \right) \end{cases} \tag{40}$$

As the first x_{in} value can be randomly selected, therefore, an iterative process is needed to obtain a convergence of x_{in} towards a result x_{out}. The flow chart in Figure 46 illustrates the iteration procedure.

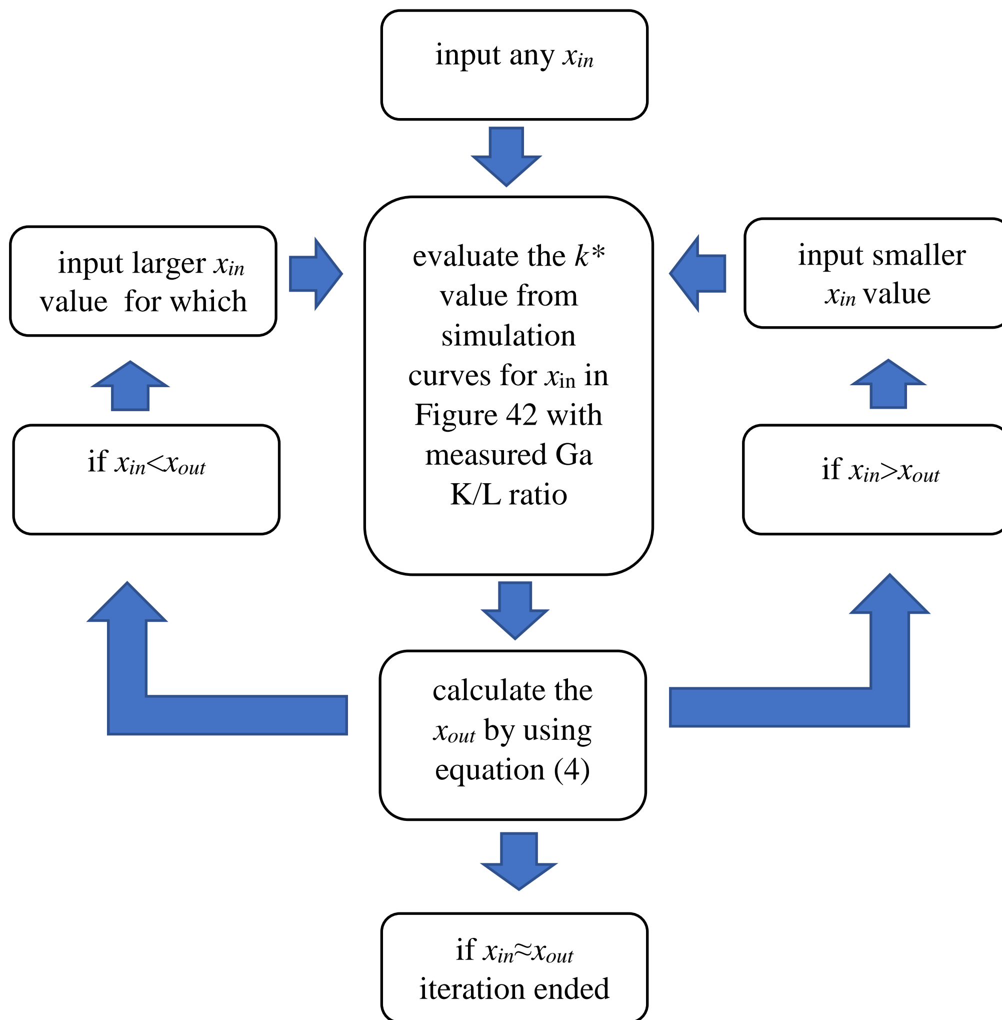

Figure 46: flow chart of iteration process for x value determination for both Ga K and Ga L lines.

As demonstrated in Figure 46, if $x_{in}\approx x_{out}$ within a certain error bar, then the x value can be considered as an indium concentration x_{In} for which all X-ray spectra are self-consistent, however, if $x_{in}<x_{out}$, the selection of k^* factor is too big so a larger x_{in} should be applied to reduce k^* factor value. On the contrary, if $x_{in}> x_{out}$, a smaller x_{in} should be used to increase the k^* factor value. The iteration process stops when $x_{in}\approx x_{out}$ is satisfied. Convergence is guaranteed because smaller x values yield larger k^* factors in Figure 42.

In chapter 2.2.7, the characteristic X-ray peaks have Gaussian line profiles, and the uncertainty of X-ray intensity is obeying counting statistics [12]. The relative statistical error for quantification of the chemical composition can be expressed by simply introducing the error in X-ray intensity in *k** iteration process and equation (4). The *x* value calculated from absorption correction with *k** is depicted in appendix 2.

As shown in appendix 2, different In concentrations were observed at different probing positions within the $In_{0.2}Ga_{0.8}N$ sample. Since the X-ray intensity of In L, Ga K and Ga L is relatively large, therefore, the calculated statistical error bar of the In L, Ga K and Ga L X-ray intensities for $In_{0.2}Ga_{0.8}N$ sample is rather small, as demonstrated in Table 3.

nominal *x*=0.2				
X-ray deadtime	Ga K	Ga L	In L	Ga K/L ratio
0.08	28900±340	11720±217	4660±137	2.46587
0.14	25214±3184	12254±221	8342±183	2.05761
0.15	54422±467	25680±320	17239±263	2.11924
0.19	150702±776	70917±533	50457±449	2.12505
0.26	133661±731	57629±480	78941±562	2.31934
0.3	117983±687	53141±461	68448±523	2.22019
0.4	168892±822	74104±544	74212±545	2.27912
0.43	97526±625	41776±409	68532±524	2.3345
0.5	132523±728	53790±464	71238±534	2.46371

Table 3: measured X-ray intensities and their statistical error bars (~2√N including background fitting) for sample number L604

As the statistical error bar for all X-ray intensity is less than 1.5% (error of the counts/total counts), the quantified x value will have an error bar within 2.1 at%. The indium concentration measured for sample position of different thickness is displayed in Figure 47.

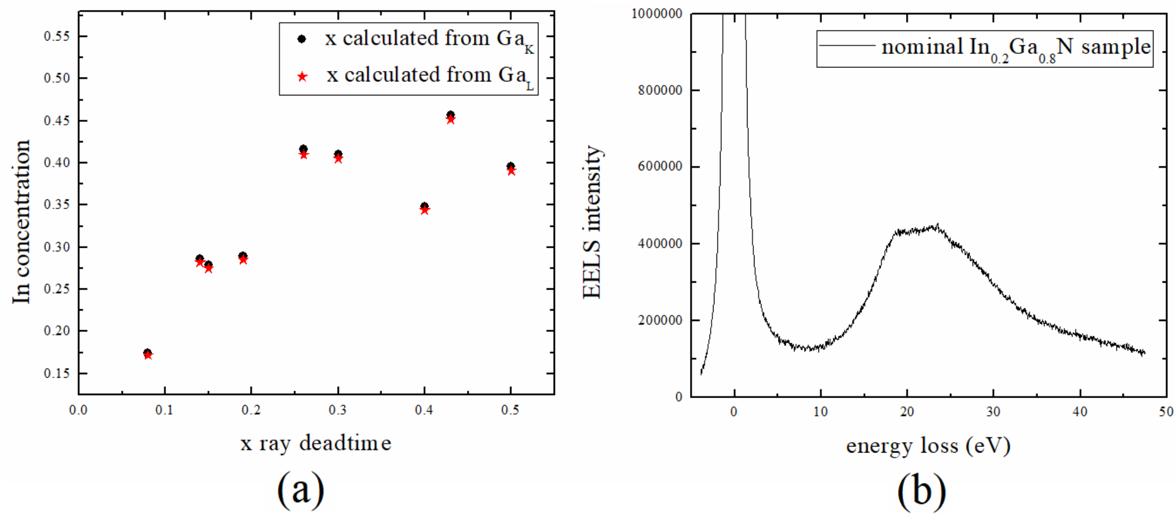

Figure 47: (a) In concentration measured at different positions for $In_{0.2}Ga_{0.8}N$ sample from EDXS, (b) EELS spectrum of the same $In_{0.2}Ga_{0.8}N$ sample

It is clear that the fraction of In content in the thinner sample (smaller percentage of deadtime) appears to be lower than in the thicker region, indicating a preferential In depletion in the thinner area. However, whether the In depletion could be attributed to the growth process of InGaN or to preferential sputtering by Ar^+ ion milling during the sample preparation process is presently unclear. A varying In distribution could be also attributed to phase separation in high In content InGaN samples, but [19,20,21] indicate phase separation was only observed for $In_xGa_{1-x}N$ thin films and quantum well samples with x>0.3. However, as demonstrated in Figure 47 b), no clear plasmon and core loss peaks are observed in EELS, so the spectrum probably contains spectral contributions by GaN, InN and InGaN, which could be explained as

phase separation in our $In_{0.2}Ga_{0.8}N$ sample. The quantification of phase separation will be described in chapter 4.

As shown in Table 3, the smallest percentage of deadtime is correlated with the largest value of Ga K/L ratio. As a thinner sample is expected to have smaller percentage of deadtime and thus smaller Ga K/L ratio, the estimation of sample thickness from Ga K/L ratio and percentage of deadtime is not completely consistent. As observed by Qiu et al. (2013) [22], a heavy carbon contaminated SiGe sample showed a larger Ge K/L ratio at small percentage of deadtime, the carbon contamination increasing the apparent Ge K/L ratio without changing the deadtime. By applying the same approach to our InGaN sample, the relationship between Ga K/L ratio and relative deadtime plotted in Figure 48 can be explained in the same way.

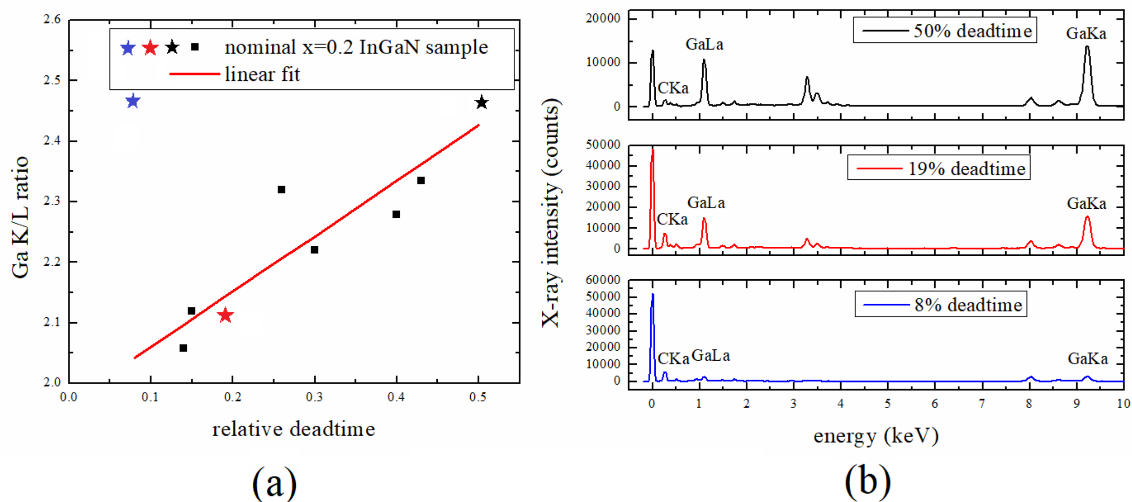

Figure 48: (a) plot of Ga K/L ratio vs detector deadtime of $In_{0.2}Ga_{0.8}N$ sample, (b) three selected EDXS spectra of $In_{0.2}Ga_{0.8}N$ sample (depicted in corresponding colour stars in Figure 48 a)), the one with the smallest deadtime showing carbon peak stronger than the gallium peaks.

As observed in Figure 48 (b), for 8% deadtime sample, the C Kα signal is similar to the Ga Kα, which indicates the strong carbon contamination of the thin sample. On the contrary, the 50% deadtime sample shows pronounced Ga Kα and Ga Lα peaks, while the C Kα is almost

vanishing. Since the carbon contamination deposited on the InGaN material increases the absorption of the Ga L line, the decrease of Ga L intensity will in turn increase the Ga K/L ratio. Therefore, the reason for 8% deadtime showing the largest Ga K/L ratio is most probably carbon contamination. However, whether the low In content observed in this thin area is attributed to phase separation or argon ion milling induced indium sputtering is currently still unclear.

For determining the average In concentration of each $In_xGa_{1-x}N$ thin layer sample, one needs to calculate average values and root-mean-square (RMS) deviations. These are listed in Table 4.

nominal In content, x_{nom}	x from Ga K	x from Ga L
0.2	0.34±0.09	0.34±0.09
0.3	0.30±0.06	0.29±0.06
0.4	0.45±0.09	0.44±0.09
0.54	0.58±0.10	0.58±0.10
0.62	0.65±0.08	0.65±0.08
0.74	0.77±0.04	0.77±0.04
0.82-0.86	0.82±0.07	0.82±0.07

Table 4: average In concentrations of different InGaN samples

The ISIS 300 software-based quantification has been compared with our absorption correction method. The system can apply a *ZAF* based correction if a precise sample thickness and density is put in, which is only approximately applicable to ternary InGaN due to the density of the probed region being unknown if the indium content is assumed to be unknown. Hence, also the determination of the absolute thickness of the material from Ga K/L ratio is difficult since the density of the probed region is unknown [16]. Furthermore, if the geometry of the surface is

rough this will make the thickness determination even more complicated. Here, we use a sample thickness of 0 nm as a starting point, which yields a standard *k* factor selection without absorption or fluorescence effects considered. The input density of the material is based on the nominal indium concentration provided by the grower. By using the nominal concentration provided by the grower and the measured Ga K/L ratio, the thickness determined for each probed area can be estimated by Ga K/L ratio correspondent with its simulation thickness at specific In concentration (like Figure 42 c)). The determined thickness and nominal density is then put in the ISIS 300 software for obtaining an absorption correction. The *x* value can then be calculated by the absorption correction applied within ISIS. The comparison of ISIS 300 quantification method (with and without absorption correction) and our absorption corrected approach is shown in Figure 49.

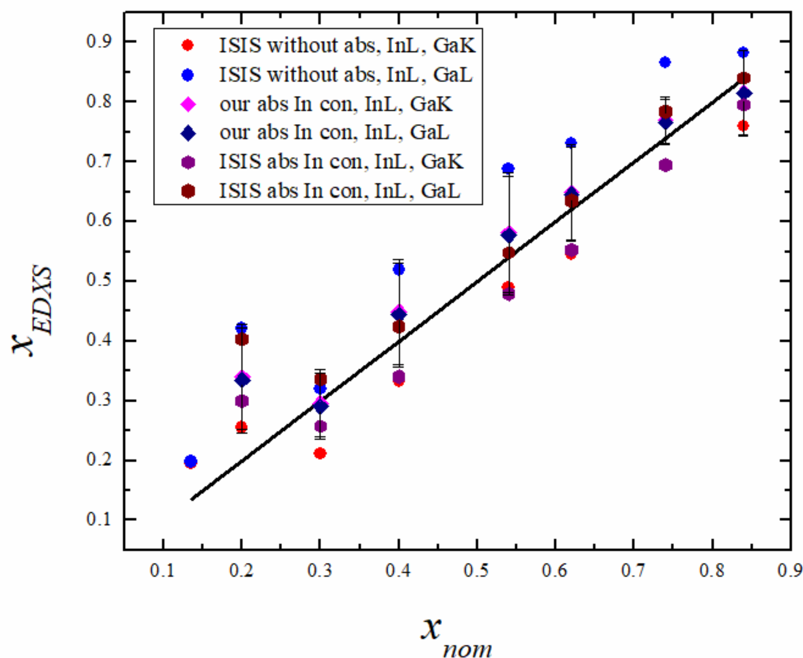

Figure 49: quantification of indium concentration from our absorption corrected k* factor approach and ISIS 300 software versus nominal indium concentration provided by grower.

As shown in Figure 49, the quantification from ISIS 300 system (with or without absorption correction) demonstrates a difference of x values calculated from Ga K or from Ga L lines, which can be attributed to an incorrect k factor or density of the material. By using the absorption correction provided by ISIS 300 system with nominal density, the consistency of x value determined from Ga K and Ga L is improved somewhat. However, the x value differences are still too large to evaluate the true In concentration, which directly indicates the accuracy of the absorption correction built into ISIS is not sufficient to obtain consistent In quantification for InGaN. This could confuse a user having to decide which result is believed to be more reliable. However, our absorption correction method demonstrates a self-consistent result of x evaluated from Ga K and Ga L lines. This yields a more reliable quantification result compared with standard software. The main advantage of the k^* absorption correction method is that neither absolute sample thickness nor material density need to be known. As the absorption correction only depends on the measured Ga K/L ratio, this serves as an inherent absorption calibration for each spectrum. Our iteration method is shown as a robust approach for quantification of In content.

3.4 Analysing the In distribution in rough samples of InGaN alloy layer.

In section 3.2, the absorption correction method was developed and tested in TEM mode, where the evaluation of In concentration averaged over a wide illumination area, however, as illustrated in section 3.2, to investigate In distribution and phase separation locally, the self-consistent X-ray absorption method can be applied in STEM mode to calculate the In concentration for each pixel in an elemental map. The *ZAF* correction (Goldstein & Williams 1981 [23]; Tixier, Thomas & Bourgeot 1981[24]), which is the standard thin film absorption correction, multiplies the specimen thickness by the *cosec* function of the take-off angle. If the sample surface is very rough and the take-off angle low, the X-ray may pass through the

material several times before reaching the detector (Figure 54), which would give a larger Ga K/L value compared to a planar geometry, thus the standard *ZAF* correction is invalid because it only takes into account the specimen thickness rather than the actual X-ray optical path. In this chapter, we will apply our self-consistent absorption correction method in STEM mode to study fluctuations in the indium concentration in nominal $In_{0.62}Ga_{0.38}N$ samples with rough sample geometry.

For the $In_{0.62}Ga_{0.38}N$ sample, 7 spectra were recorded at different thicknesses to extrapolate the In concentration. The In concentration measured versus the Ga K/L ratio is plotted in Figure 50.

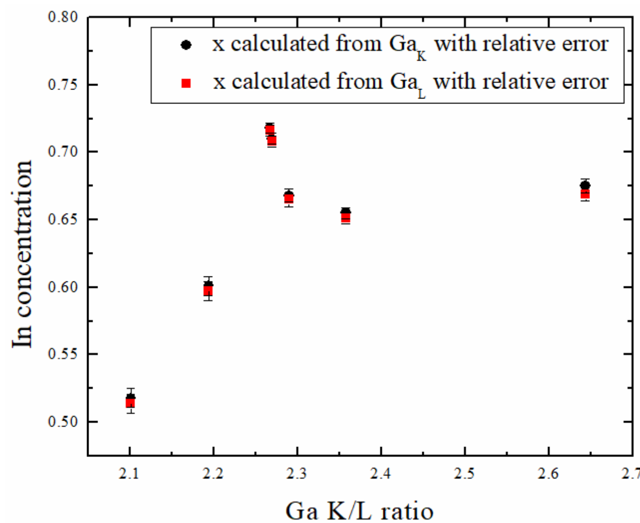

Figure 50: In concentration measured at different positions for $In_{0.62}Ga_{0.38}N$ sample

It is clear that for Ga K/L ratios from 2.2 to 2.3, the In concentration scatters from x~0.6 to 0.7. As observed earlier, a reduced In content in InGaN thin areas may be due to preferential In sputtering during Ar^+ ion milling, therefore, we exclude from further analysis the In concentration calculated for the thinnest area in Figure 50 (Ga K/L=2.1) since the low In content may be attributed to the ion milling. From appendix 2, the count rates of In L, Ga K and Ga L are higher than 39000, the relative statistic error can thus be calculated and is shown in Figure 50 as error bar. Since the relative error is less than $\Delta x=\pm0.007$, the scattering of the

In concentration evaluated from the same sample could be attributed to indium segregation in this InGaN sample. It is worth analysing the In distribution by calculating the x map from recorded X-ray elemental maps.

In our previous publication [25, 26], the high In content $In_{0.62}Ga_{0.38}N$ thin film exhibited island structures rather than forming a flat film. A secondary electron microscope image was taken of the topography by using a FEI Helios SEM to reveal the surface structure of $In_{0.62}Ga_{0.38}N$ sample. The accelerating voltage is 5 kV and the magnification 80kX, the probing spot size is 3 with a 10.3 mm working distance. The recorded SE image is shown in Figure 51.

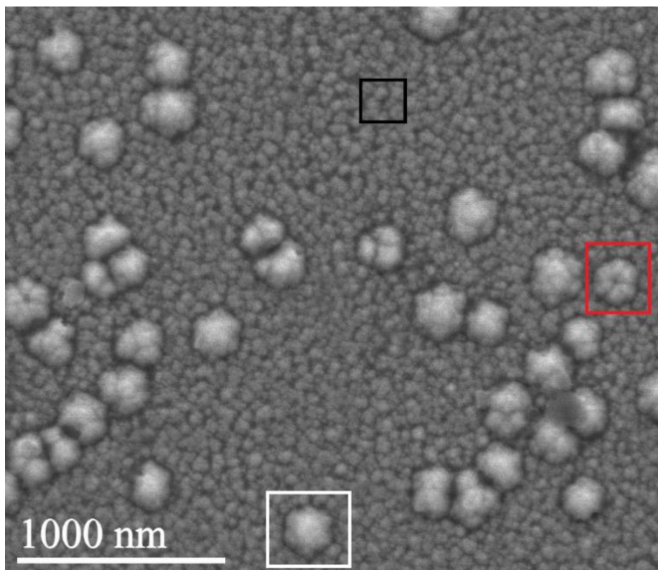

Figure 51: SEM topography of $In_{0.68}Ga_{0.32}N$ thin film (the SEM image was recorded with the help of Dr Peng Zeng)

The SEM image clearly shows Vollmer-Weber growth (3D island growth). Three different island types are observed:

1. small and homogenous islands (as indicated inside the black square),

2. big islands with a possible hollow structure in the middle (red square),

3. big pyramid-like island structures (white square).

To identify these characteristic structures in cross-sectional TEM, the combination of EFTEM thickness determination and analytical TEM with correlated structure simulations has been used.

3.4.1 EFTEM measurement of sample thickness profile and structure simulation

The $In_{0.62}Ga_{0.38}N$ cross-section STEM ADF images below have been taken using the JEOL 2010F FEGTEM under the same experimental conditions as the EDXS elemental maps. 70μm condenser aperture is used to record the STEM images, yielding a 16.6 mrad semi-angle of electron beam convergence, resulting in a ~1 nm diameter probe size. We have recorded both 128×100 and 256×200 pixels maps, with the same sampling of 4.72 nm pixel. ADF images are shown in Figure 52.

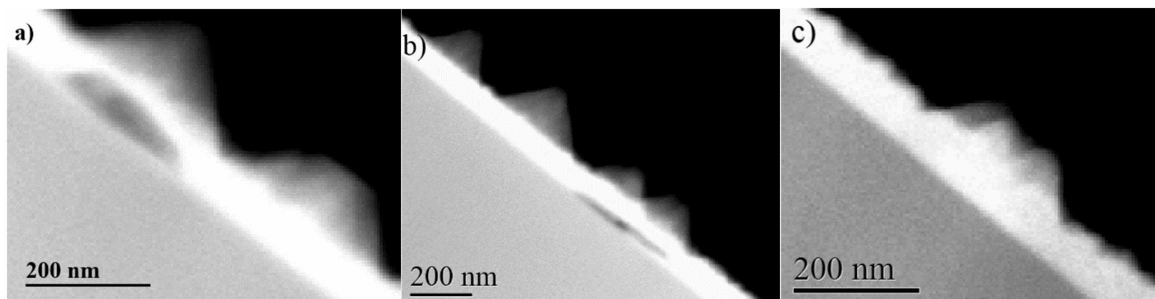

Figure 52: ADF images of $In_{0.62}Ga_{0.38}N$ sample with cross-section through different types of islands.

As shown in Figure 52 a) underneath one island the ADF intensity is much reduced. In the ADF images, the intensity is approximately proportional to the square of atomic number and to the sample thickness ($I\sim tZ^2$), i.e. lower In content and thinner regions show as darker contrast in the image. In order to verify the region is In poor or thinner, an additional thickness

determination by EFTEM is used. The corresponding EFTEM relative thickness maps are shown in Figure 53.

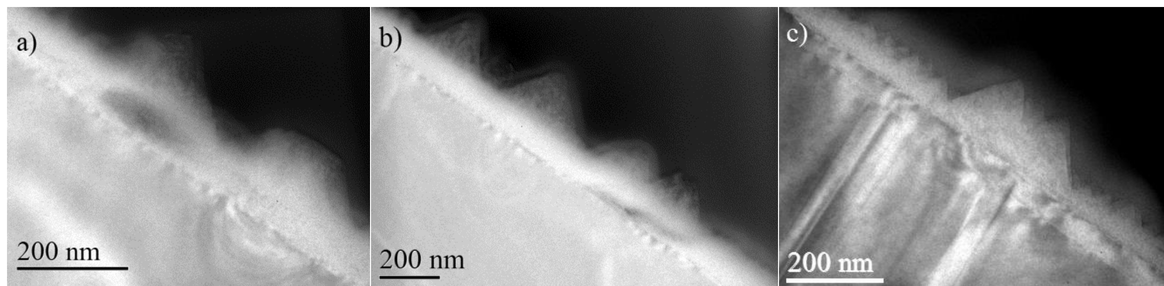

Figure 53: EFTEM t/λ maps of the same areas as in Figure 52 a) max: 3.4, min: 0; b) max: 3.15, min: 0; c) max: 2.41, min: 0.

The EFTEM relative thickness maps were recorded in our c-FEG JEOL R005 3100Z TEM equipped with an aberration corrector operating at 300 kV. The EFTEM image acquisition was performed in a Gatan Tridium865 imaging energy filter with an Ultrascan2k charge-coupled device (CCD) camera system. A 5mm entrance aperture with a 24.9 mrad collection semi-angle from a 120μm objective aperture was used to record the EFTEM images from which relative thickness maps were calculated.

The relative thickness maps in Figure 53 a) shows underneath the large island clearly a high degree of local thickness change. Before calculating the absolute thickness of the InGaN sample, the carbon contamination deposited during scanning needs to be subtracted. This can be achieved from the area which contains only GaN or only glue. The absolute thickness of the sample can then be calculated by using equations in chapter 2.3.7. The inelastic mean free path for $In_{0.62}Ga_{0.38}N$ is calculated as 99 nm. The possible thickness profiles along line AB in Figure 54 a) are shown in Figures 54 b), c) and d) for given specimen of the same thickness but different surface roughness.

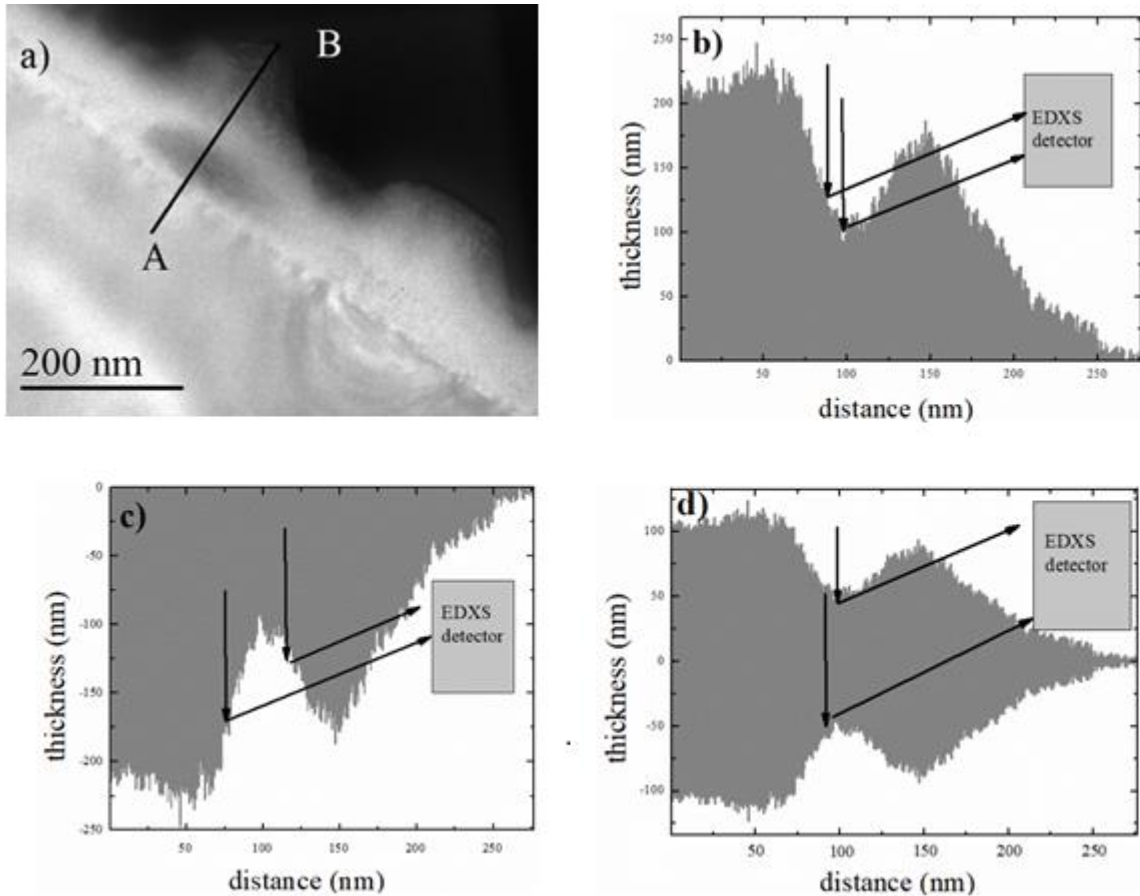

Figure 54: a) line profile position in relative thickness map corresponding to Figure 53 a) (max:2.28, min:0); X-ray path sketches for b) case of top surface roughness only; c) bottom surface roughness only; d) symmetrical surface roughness on both top and bottom surfaces.

Since EFTEM can only measure the projected sample thickness change in two dimensions (laterally), the actual thickness profile of the sample is unknown. Therefore, in Figure 54, we have sketched three possible thickness profiles with the corresponding X-ray paths to the X-ray detector position in side view. For each of these three conditions, an X-ray generated in the centre of the dark area in Figure 54a) must pass through extra InGaN material before it reaches the detector, which increases the absorption. Therefore, the Ga K/L ratio measured no longer only depends on the sample thickness but the total X-ray optical path length inside the sample where the absorption can be estimated from the Ga K/L ratio.

Figure 53 c) shows an island with a clear dip in the middle, which could be the type 2 island in Figure 51. In order to exclude that Figure 53 c) could be due to two pyramidal islands overlapping in projection, COMSOL MULITIPHYSICS software has been used to model different island structures in 3D as a function of cutting direction as shown in Figure 55.

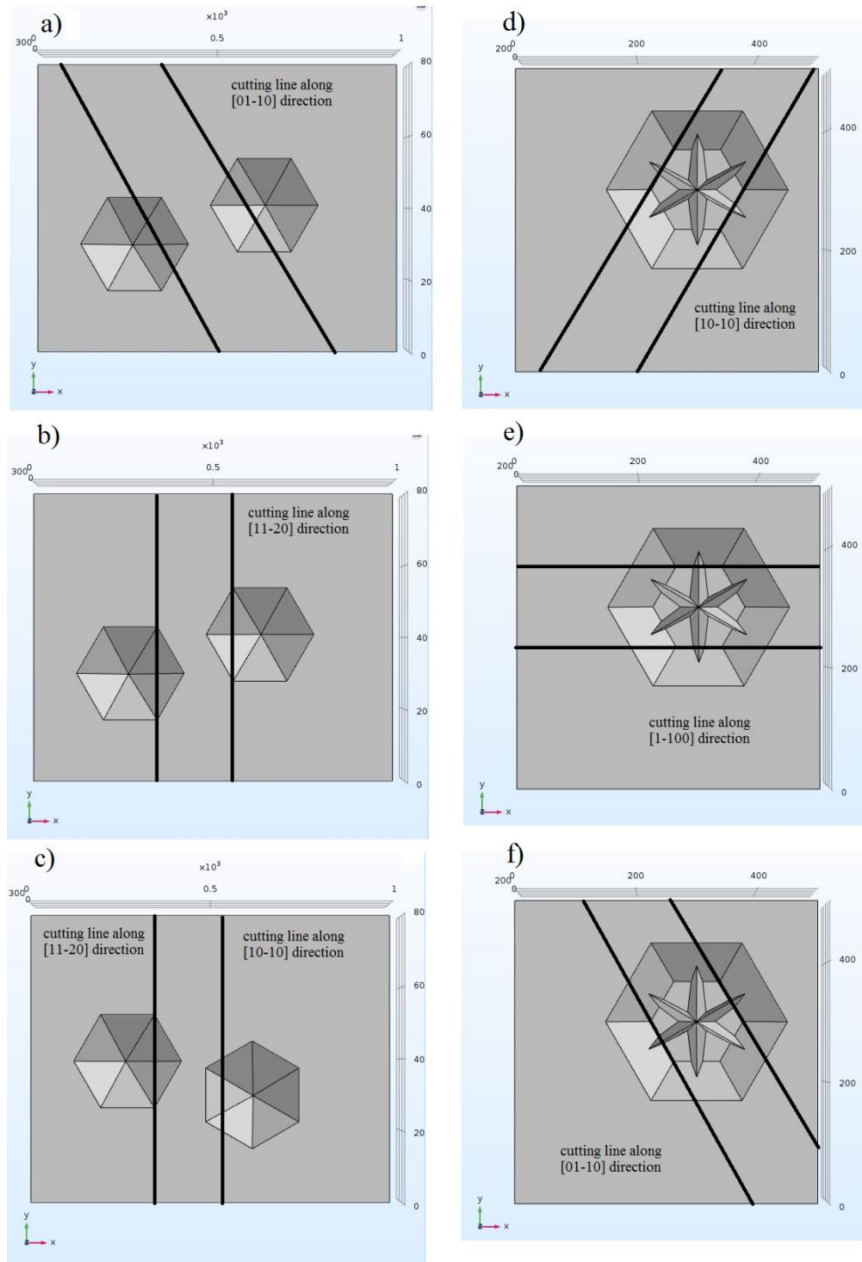

Figure 55: simulations of different sample cutting geometries. The islands in a), b) and c) correlate with the island structure in the white square of Figure 51, whiles the island in d), e) and f) corresponds to the island structure in Figure 51, red square.

The six cutting approaches shown in Figure 55 are satisfying two conditions:

1. a clear dip can be observed in the projected island outline in a cross-sectional sample,

2. the total width of the two overlapping islands or of the island with hollow crater in the middle can be correlated with the ADF width measurement.

The cross-sectional ADF images for those six cutting approaches are expected to be identical to their thickness profile. Their TEM sample cross-section and thickness profile can then be obtained as shown in Figure 56.

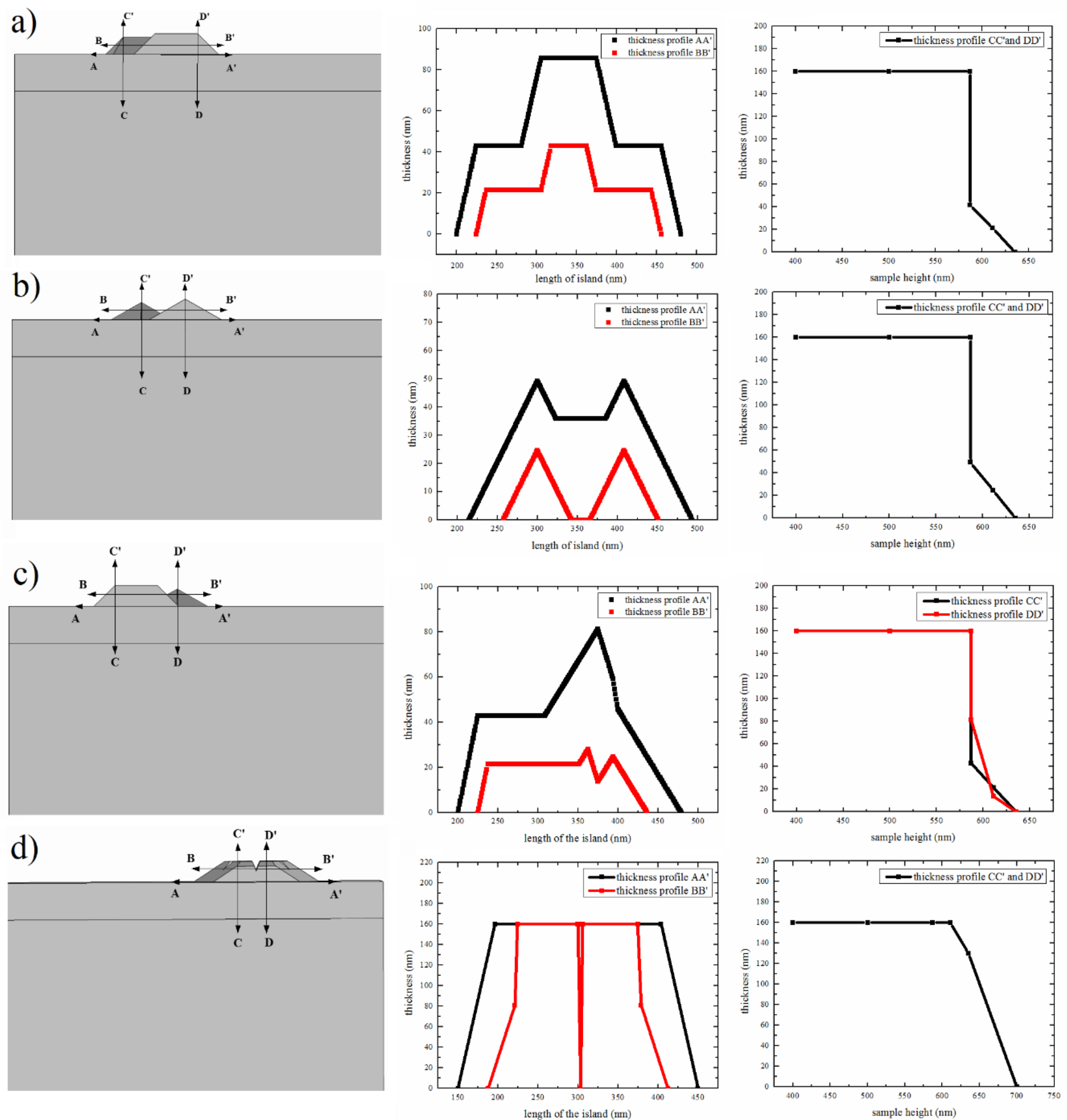

Figure 56: structural simulation of possible TEM sample geometries representing cross sections through the islands: top row corresponding to Figure 55 a), second row corresponding to Figure 55 b), third row corresponding to Figure 55 c) last row corresponding to Figure 55 d)-f).

The profiles of the experimental thickness map from Figure 53 c) along AA', BB', CC' are plotted in Figure 57 for comparison. The thickness profiles in Figure 57 correlate well with that in Figure 56 d) from which it is conducted that the actual structure in Figure 52 c) is similar to that of type 2 island in Figure 51.

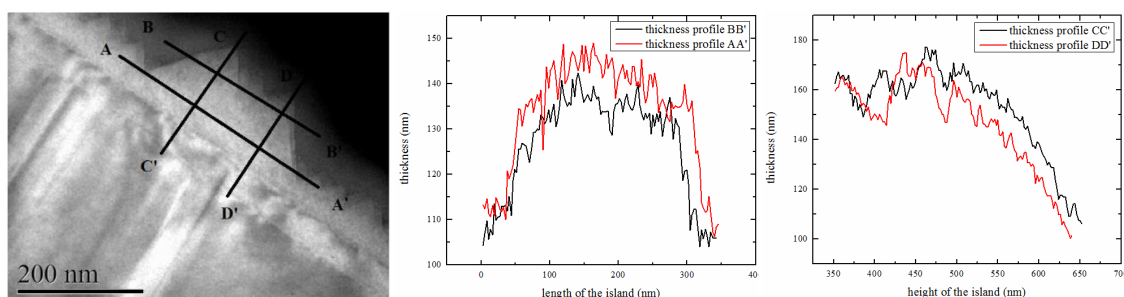

Figure 57: experimental thickness profiles along lines AA', BB', CC' and DD' corresponding to Figure 56.

3.4.2 EDXS absorption correction method for rough samples

The EDXS measurement was undertaken under the same condition as for the ADF imaging (Figure 52). The nominal take-off angle of the Oxford Instruments Si:Li detector with ultra-thin polymer window is 25 degrees [15], the energy resolution various from 60 eV (FWHM of strobe) to 136 eV (FWHM of Mn Kα peak at 5895eV).

In chapter 2.2.8, it has been shown that the background of the X-ray spectra will influence the quantification result, especially for low energy X-rays. Therefore, we have also recorded elemental maps of some elements whose characteristic peak positions are close to the In and Ga X-ray peaks but that are not contained in the specimen. Our approximation of background X-ray intensities are for windows around $Cu_{L\alpha}$ for Ga_L and $S_{K\alpha}$ for In_L lines, respectively. The recorded elemental maps for InL, GaK and GaL after background subtraction are depicted in Figure 58.

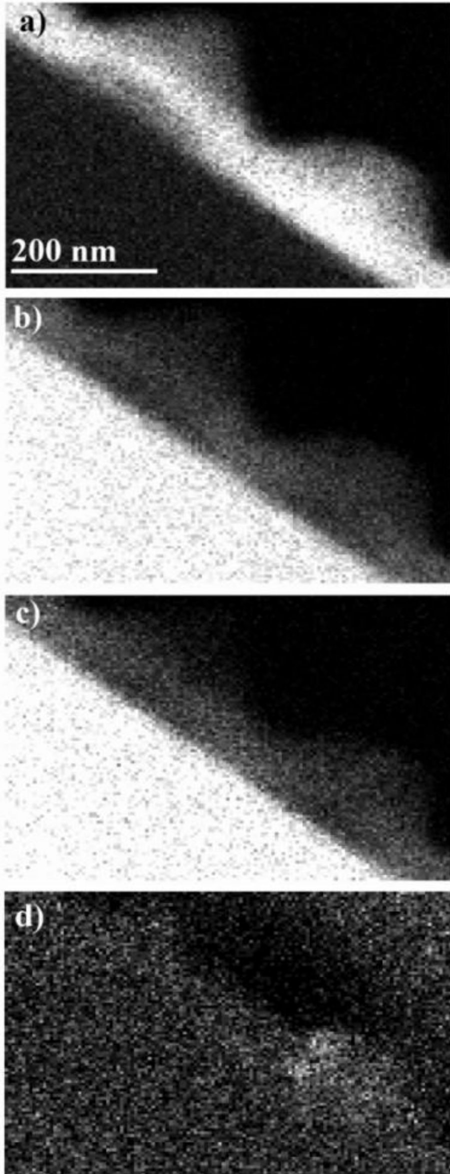

Figure 58. elemental maps of a) In_L (In_L^{max}=60 counts); b) Ga_K (Ga_K^{max}=70 counts), c) Ga_L (Ga_L^{max}=40 counts), d) N_K (N_K^{max}=11 counts).

Since EDXS with a polymer window in front of the Si:Li detector is not very sensitive to light elements as illustrated in chapter 2.2.8 [12], the N_K map in Figure 58 d) is very noisy and cannot be quantified. From Figures 49 a)- c), the thickness reduced area in Figure 54 a) gives lower counts for In_L, Ga_L and Ga_K X-ray lines. After background subtraction of In_L and Ga_L, the absorption correction method is applied, calculating step by step the Ga K/L ratio effective *k**

factor, x value and difference map Δx from Ga_K and Ga_L lines for each pixel in the map. The result is displayed in Figure 59.

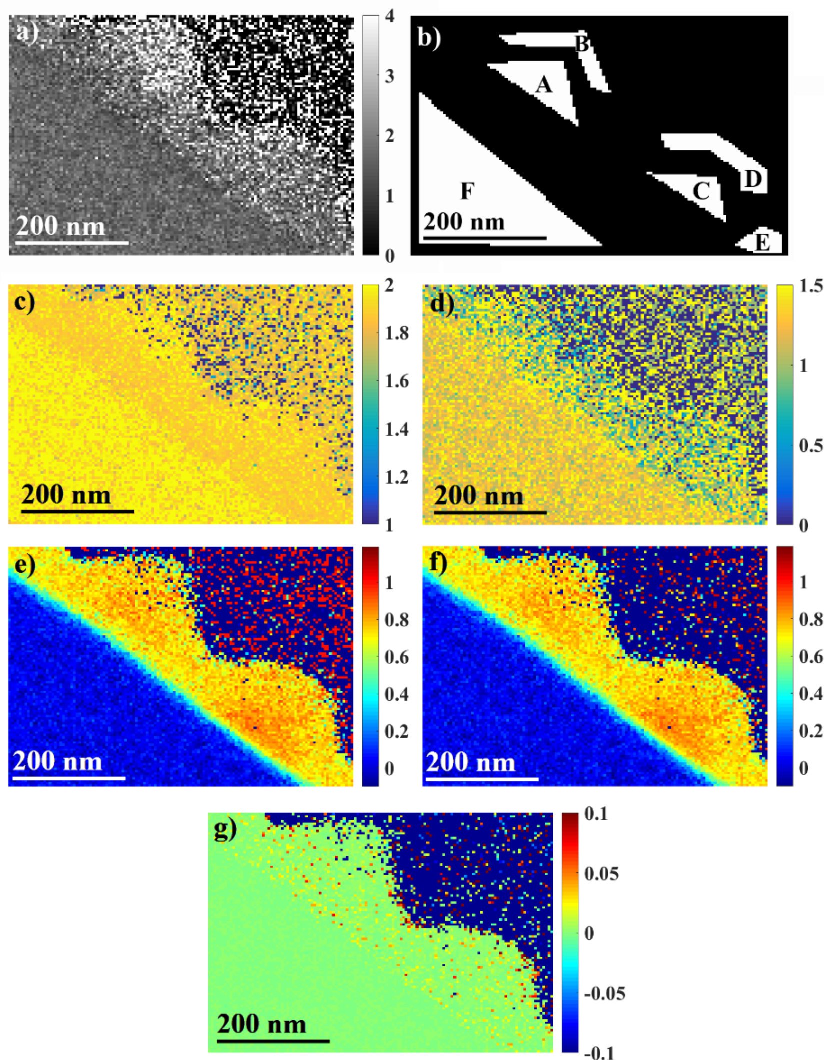

Figure 59: a) Ga K/L ratio map; b) definition of regions masked for histogram analysis; c) map of $k^*_{InL,GaK;}$ d) map of $k^*_{InL,GaL}$; e) x map calculated from Ga_K; f) x map calculated from Ga_L; g)=e)−f) difference map Δx from Ga_K and Ga_L lines.

In the k^* factor maps in Figures 59 c) and d), the thinner area in Figure 54 a) is no longer observed. Figures 59 e) and f) demonstrate the x maps calculated based on the k^* factors from Figures 59 c), d) are very similar and indicate the thinned area is not a hole in the specimen but

just thinner InGaN. The difference map Δx from Ga_K and Ga_L lines in Figure 59 g) has a mean value of 0 with standard deviation of ±0.036 (rms), which indicates consistency of the x maps calculated from Ga_K and Ga_L.

For further analysis of the indium distribution in the InGaN thin film, an analytical mask is introduced in Figure 59 b). The histograms of the In distribution in these five areas are presented in Figure 60.

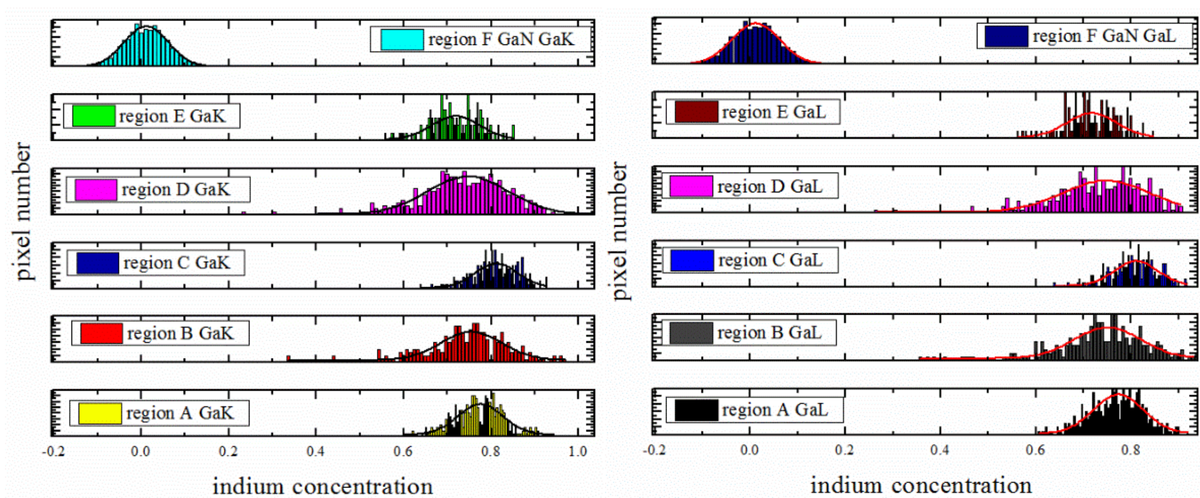

Figure 60: histograms of x-values calculated from regions A-F in Figure 59 b) from Ga_K (left column) and Ga_L lines (right column).

The histograms taken from 6 regions in Figure 59 b) are fitted with Gaussians to find the mean value and standard deviation for each region. Region F is the GaN buffer layer [25], which can be used as a reference point for the x quantification. As shown in Figure 60, the region F histograms give x_{mean}=0.011 and have FWHM values of 0.10, which corresponds to ±0.04 standard deviation (rms). The result indicates the quantification of the x value for each pixel in region F is highly reliable, which means our absorption correction method has been

successfully applied to GaN in STEM mode. The fitting parameters in Figure 60 are listed in Table 5.

region	peak for Ga_K	peak for Ga_L	standard deviation of Ga_K	standard deviation of Ga_L
A	0.793	0.786	0.055	0.051
B	0.751	0.745	0.093	0.093
C	0.810	0.812	0.047	0.051
D	0.740	0.736	0.072	0.072
E	0.717	0.719	0.055	0.055
F	0.011	0.013	0.036	0.036

Table 5: fitting parameters for x-value from all regions A-F defined in Figure 59 b)

As shown in Table 5, the In concentration $x \approx 0.8$ for regions A and C, which can be regarded as In rich. Regions B, D and E have a slightly lower In concentration of $x \approx 0.7$. The EDXS result was independently verified by EELS in chapter 4, which indicates our absorption correction quantification result is independent of sample geometry.

3.4.3 STEM EDXS observation of In segregation in high In content InGaN

As illustrated in chapter 1.2.7, phase separation is a major issue for fabricating high In content InGaN of reasonable quality. The mapping of In distribution in a thin film is vital for directly observing phase separation taking place in a thin film. Due to grinding and Ar^+ ion milling during sample preparation for TEM, the specimen surface cannot be perfectly flat (as

demonstrated by the thickness fluctuation in chapter 3.3.2), therefore, to quantify the indium concentration for each position one needs either a relative flat surface or the use of an appropriate absorption correction method. Here, we have applied our k^* absorption correction method to analyse two different areas depicted in Figure 52b) and c). The experimental condition are the same as in chapter 3.3.2, only that Figure 52 b) has been recorded with a larger field of view (256×200 pixels with 4.72 nm pixel) than Figures 52 a) and c).

In chapter 3.3.1, the island in Figure 52 c) has been identified as a type 2 island in Figure 51. Figure 52 b) demonstrates a similar local thickness reduction as Figure 52 a) and relative thickness map in Figure 53 b) proved this.

To further investigate the In distribution, the elemental maps for the structures in Figure 52 b) and c) are shown in Figure 61 including the related background maps for Cu Lα and S Kα.

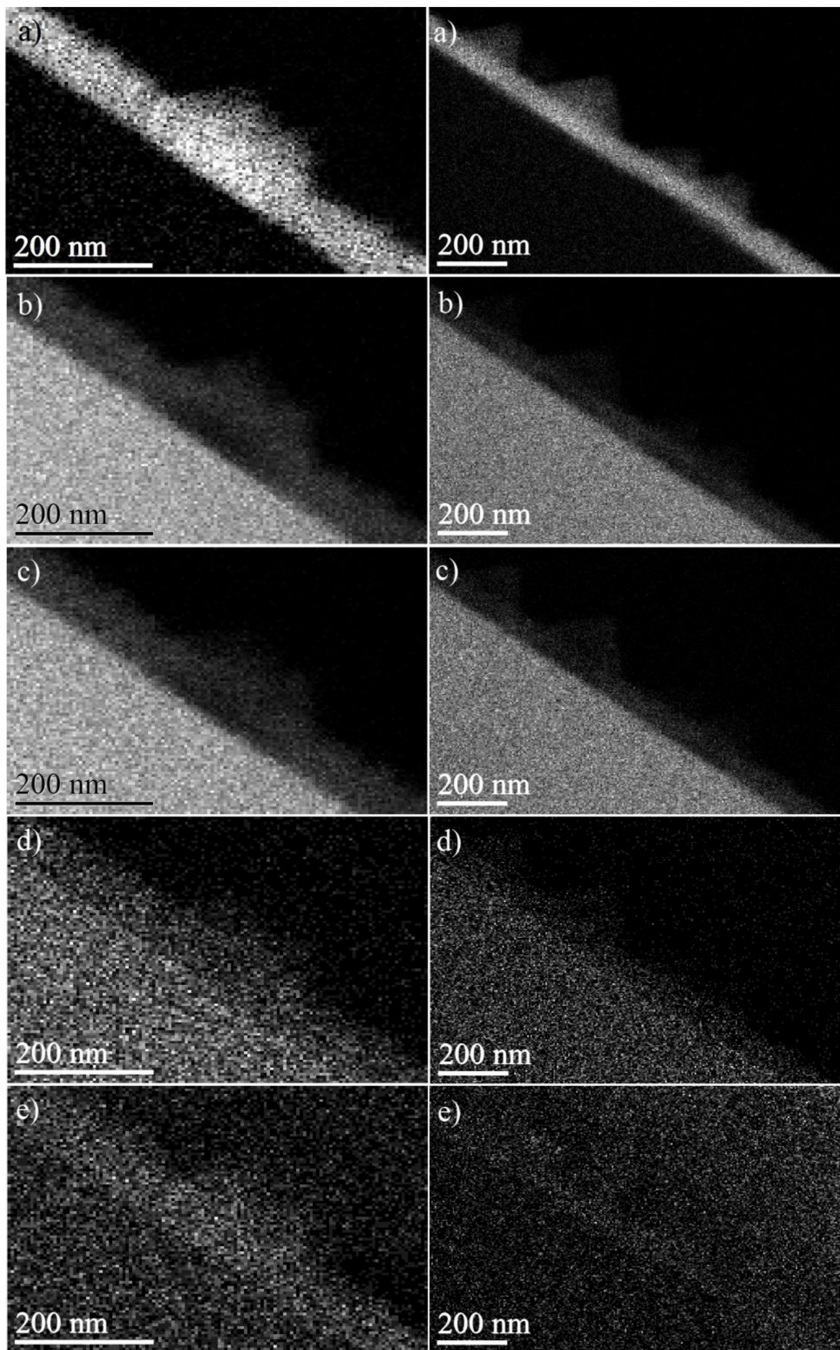

Figure 61: left column: elemental maps of a) In L (max=76), b) Ga K (max=86), c) Ga L (max=60), d) Cu La (max=15), e) S Kα (max=9) corresponding to Figure 52 c); right column: elemental maps of a) In L (max=35), b) Ga K (max=46), c) Ga L (max=26), d) Cu La (max=6), e) S Kα (max=6) corresponding to Figure 52 b).

After the background subtraction, the *k**absorption correction method is applied to the background subtracted In L, Ga K and Ga L maps to calculate the In distribution in the island

structures from both series of X-ray maps in Figure 61. The Ga K/L ratio, effective k^* factors and x maps calculated from Figure 61 are shown in Figure 62.

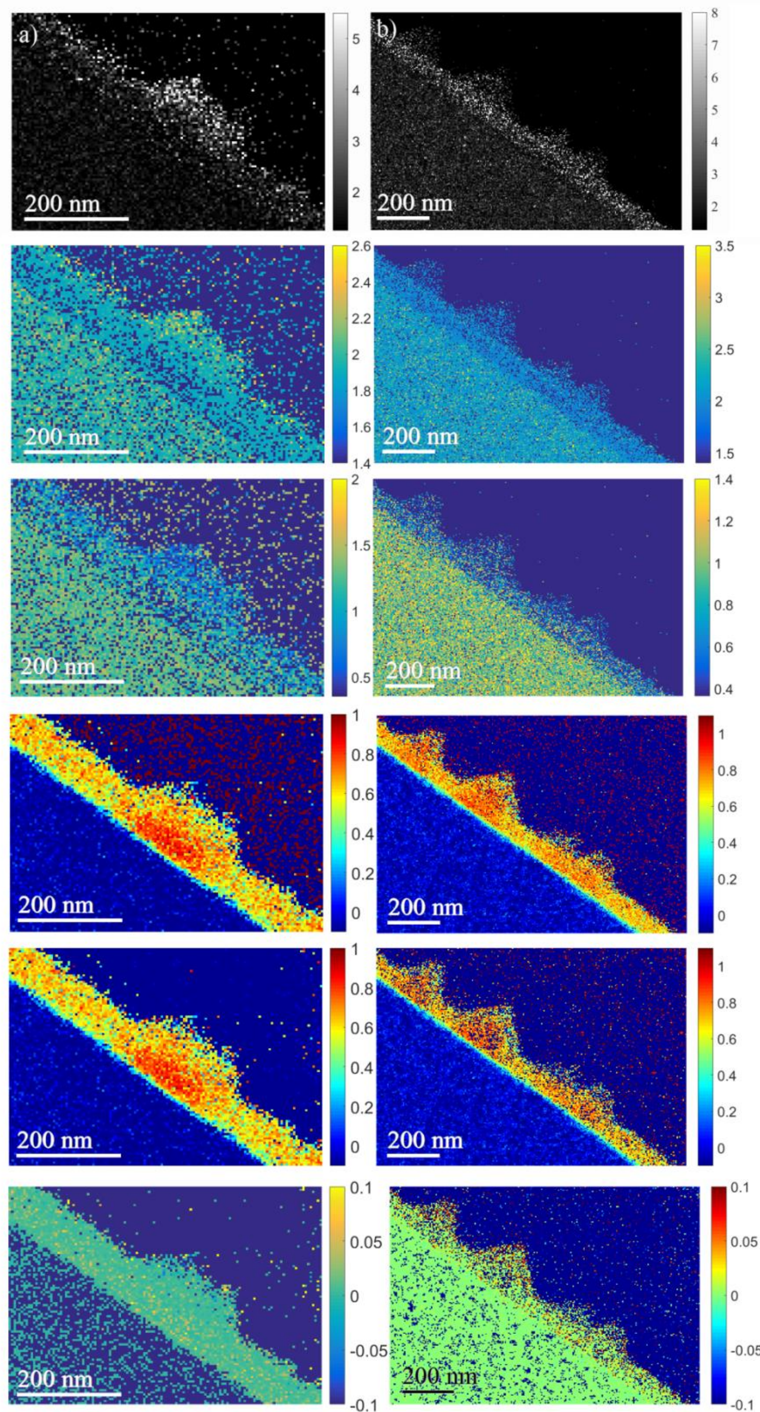

Figure 62: a) top to bottom Ga K/L ratio, $k^*_{\mathrm{GaK\ InL}}$ map, $k^*_{\mathrm{GaL\ InL}}$ map, $x_{\mathrm{InL\ GaK}}$ map, $x_{\mathrm{InL\ GaL}}$ map calculated from Figure 61 left column, b) top to bottom Ga K/L ratio, $k^*_{\mathrm{GaK\ InL}}$ map, $k^*_{\mathrm{GaL\ InL}}$ map, $x_{\mathrm{InL\ GaK}}$ map, $x_{\mathrm{InL\ GaL}}$ map calculated from Figure 61 right column group

Similar to k^* and x maps calculated in chapter 3.3.2, the thickness reduced area in Figure 52 b) is a high In content area. Such high In content areas are observed underneath all large islands. In order to evaluate the growth mechanism, we have summed the number of pixels in all x maps where $x>0.8$. The 2D fraction of the islands with $x>0.8$ can then be calculated by simply dividing this by the total pixel number of the island. As observed from maps of x, the high In content areas have shape similar to the island outline, so the In rich areas will likely have 3D shapes similar to the islands. For converting the 2D fraction into a 3D fraction, the height and width of the In rich region and island need to be measured in cross-section, then the In rich region and island structure can be simulated in 3D using the same geometry but with the measured height and width. One simulation example is demonstrated in Figure 63. The approximate 3D volume ratio with $x>0.8$ has been calculated for each island and is plotted versus island height in Figure 63 b).

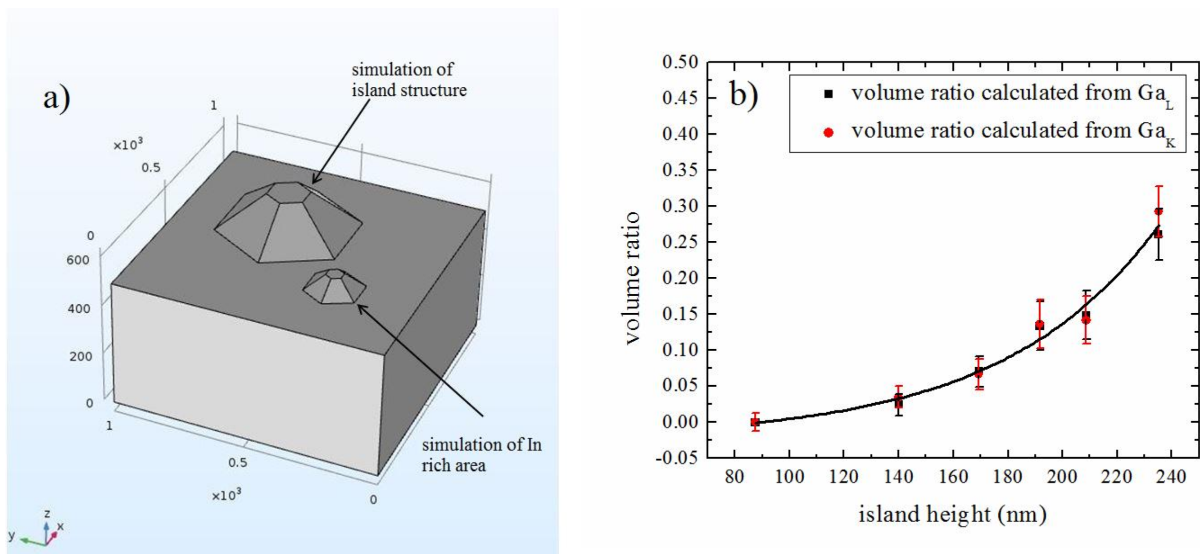

Figure 63: a) simulation of island and In rich area structure where both are displaced for visualisation, b) approximate 3D volume ratio of regions with $x>0.8$ from Ga_K or Ga_L as function of island.

The 3D volume ratio as function of the island height can be fitted with an exponential function, as shown in Figure 63 b). In the EDXS mapping, we assumed the sample drift error was ±1 pixel, thus the 2D outline of the In rich region will have an error of ±1 pixel in both width and height, from which the error for the 3D volume ratio can be calculated as reported in Table 6.

island height (nm)	relative volume error from Ga_L	relative volume error from Ga_K
87.5	0.013	0.013
140	0.015	0.014
169.4	0.021	0.021
191.7	0.034	0.034
208.7	0.034	0.033
235.2	0.036	0.035

Table 6: error bars of the volume ratio $\Delta V/V$ from Ga_K and Ga_L versus island height.

It is clear that the high indium content regions expand with island height, from small islands to large pyramidal islands. It is clear from the maps that indium accumulates in the bottom parts of the islands, and from Figure 63 that the high In content area produced by In segregation correlates with and is probably responsible for the formation of the larger islands.

Chapter conclusion

In this chapter, we started from the simulation of the sensitivity factor (k^* factor) of In L line with respect to Ga K/L lines by using Monte Carlo simulations (CASINO V 2.4.2). The X-ray photon absorption and fluorescence effects are included in the simulation. The calculated k^* factor is then applied to series of experimental spectra from $In_xGa_{1-x}N$ samples with different nominal x values. The results obtained from absorption correction method are consistent, while the ISIS 300 software demonstrates inconsistent quantification from Ga K and Ga L lines. In

Figure 49 a), the different electron beam probing positions for one sample (x_{nom}=0.2) gave different average In concentrations, which implies a non-uniformity of In distribution in the sample. STEM EDXS is used to record elemental maps of InL, Ga K and Ga L with their corresponding background. The absorption correction method is then applied to calculate the x value for each pixel in the maps. The result shows that even with a rough geometry of the sample surface, our quantification still works properly, and quantification demonstrates InGaN phase separation where indium accumulates in the bottom parts of the islands and is probably responsible for the formation of the large island structures for high In content.

Appendix

Appendix 1 simulation of Ga K and Ga L X-ray intensities for different In concentration InGaN samples (25° nominal X-ray take off angle, the incident energy is 200 kV and a default cross-sections and ionisation potentials from Casino are used to calculate the emitted X-ray intensity, emitted X-ray=generated X-ray-absorbed X-ray).

x=0				
sample thickness	Ga K generated	Ga L generated	Ga K emitted	Ga L emitted
50	28.45	21.65	28.48	22.9
100	56.9	41.01	57.05	45.87
150	85.32	58.32	85.66	68.88
200	113.72	73.8	114.33	91.93
300	170.88	100.27	172.25	138.5
400	227.57	121.3	230.01	184.95
500	284.78	138.41	288.59	232.06
600	341.06	151.68	346.55	278.68

x=0.25				
sample thickness	Ga K generated	Ga L generated	Ga K emitted	Ga L emitted
50	19.29	13.89	19.34	15.55
100	38.52	24.93	38.73	31.14
150	57.76	33.74	58.24	46.83
200	76.88	40.71	77.75	62.51
300	115.17	50.83	117.11	94.17
400	153.01	57.19	156.46	125.81
500	190.89	61.36	196.28	157.84
600	228.43	64.02	236.19	189.93

x=0.5				
sample thickness	Ga K generated	Ga L generated	Ga K emitted	Ga L emitted
50	11.77	8.1	11.82	9.5
100	23.51	13.93	23.7	19.05
150	35.21	18.13	35.64	28.66
200	46.86	21.15	47.62	38.29
300	69.88	24.9	71.58	57.56
400	92.81	26.92	95.83	77.06
500	115.45	28	120.17	96.63
600	138.04	28.58	144.82	116.46

x=0.8				
sample thickness	Ga K generated	Ga L generated	Ga K emitted	Ga L emitted
50	4.31	2.83	4.33	3.48
100	8.58	4.65	8.67	6.97
150	12.83	5.84	13.03	10.48
200	17.07	6.61	17.43	14.02
300	25.43	7.45	26.25	21.1
400	33.66	7.81	35.1	28.23
500	41.79	7.97	44.04	35.41
600	49.91	8.07	53.15	42.74

Appendix 2 experimentally measured X-ray intensity of Ga K, Ga L and In L for different nominal In concentration InGaN samples (acm represents our k^* factor absorption correction method and ISIS is correspond to the absorption corrected method provided by ISIS 300 software).

nominal x=0.135							
X-ray deadtime	Ga K	Ga L	In L	x_{InLGaK} acm	x_{InLGaL} acm	x_{InLGaK} ISIS	x_{InLGaL} ISIS
0.15	34491	38861	14246	NA	NA	0.163	0.149
0.18	34461	37521	14438	NA	NA	0.166	0.155
0.21	28837	31823	11638	NA	NA	0.157	0.146
0.36	30424	29720	13212	NA	NA	0.178	0.178
0.37	61028	59888	26806	NA	NA	0.176	0.175
0.44	44400	39752	19142	NA	NA	0.191	0.201
0.48	50542	43057	21289	NA	NA	0.221	0.244
0.58	38087	34054	16107	NA	NA	0.309	0.338

nominal x=0.2							
X-ray deadtime	Ga K	Ga L	In L	x_{InLGaK} acm	x_{InLGaL} acm	x_{InLGaK} ISIS	x_{InLGaL} ISIS
0.08	28900	11720	4660	0.174	0.172	0.137	0.1898
0.14	25214	12254	8342	0.286	0.282	0.100	0.2101
0.15	54422	25680	17239	0.279	0.275	0.185	0.3129
0.19	150702	70917	50457	0.289	0.285	0.179	0.3099
0.26	133661	57629	78941	0.416	0.410	0.187	0.3225
0.3	117983	53141	68448	0.410	0.405	0.289	0.4782
0.4	168892	74104	74212	0.348	0.344	0.285	0.4629
0.43	97526	41776	68532	0.457	0.452	0.232	0.4012
0.5	132523	53790	71238	0.396	0.391	0.326	0.4767

nominal x=0.3							
X-ray deadtime	Ga K	Ga L	In L	x_{InLGaK} acm	x_{InLGaL} acm	x_{InLGaK} ISIS	x_{InLGaL} ISIS
0.12	11687	5063	2059	0.184	0.181	0.107	0.213
0.2	106031	51866	28029	0.244	0.240	0.153	0.265
0.24	23419	11271	11221	0.364	0.359	0.247	0.399
0.45	35324	16285	17026	0.367	0.362	0.248	0.411
0.51	189392	82392	72324	0.319	0.314	0.207	0.250

nominal x=0.4							
X-ray deadtime	Ga K	Ga L	In L	x_{InLGaK} acm	x_{InLGaL} acm	x_{InLGaK} ISIS	x_{InLGaL} ISIS
0.11	19160	9068	10470	0.395	0.390	0.130	0.232
0.16	54591	26339	32709	0.416	0.411	0.273	0.436
0.19	32953	15479	23506	0.458	0.453	0.292	0.454
0.2	54574	26362	29395	0.391	0.386	0.329	0.504
0.26	47576	21968	38101	0.487	0.482	0.270	0.427
0.33	52114	22839	41958	0.490	0.484	0.355	0.537
0.49	57086	22531	49102	0.509	0.502	0.356	0.551

nominal x=0.54							
X-ray deadtime	Ga K	Ga L	In L	x_{InLGaK} acm	x_{InLGaL} acm	x_{InLGaK} ISIS	x_{InLGaL} ISIS
0.08	24224	11470	11176	0.356	0.352	0.241	0.395
0.1	53227	25877	39932	0.469	0.465	0.340	0.508
0.15	53159	25587	67658	0.598	0.595	0.467	0.639
0.2	40800	19513	53751	0.606	0.603	0.475	0.649
0.285	53066	23824	83209	0.647	0.644	0.519	0.701
0.31	53998	23758	74149	0.618	0.614	0.486	0.677
0.36	49506	20778	67127	0.616	0.611	0.483	0.685
0.39	67648	28114	107507	0.652	0.648	0.522	0.720
0.45	66512	25996	114159	0.670	0.665	0.541	0.747

nominal x=0.62							
X-ray deadtime	Ga K	Ga L	In L	x_{InLGaK} acm	x_{InLGaL} acm	x_{InLGaK} ISIS	x_{InLGaL} ISIS
0.09	41028	19527	37469	0.518	0.514	0.360	0.537
0.18	35083	15992	44990	0.601	0.597	0.386	0.562
0.25	52074	22741	89422	0.668	0.665	0.469	0.653
0.28	54906	24194	114827	0.710	0.708	0.542	0.725
0.34	50920	22461	111036	0.718	0.716	0.590	0.761
0.4	65106	27613	105142	0.655	0.651	0.600	0.768
0.43	46930	17752	81888	0.675	0.669	0.526	0.718

nominal x=0.74							
X-ray deadtime	Ga K	Ga L	In L	x_{InLGaK} acm	x_{InLGaL} acm	x_{InLGaK} ISIS	x_{InLGaL} ISIS
0.12	21358	8574	39372	0.685	0.681	0.559	0.754
0.19	20894	8022	52751	0.749	0.745	0.635	0.815
0.26	22878	8320	80075	0.805	0.802	0.707	0.866
0.3	21666	8222	74050	0.801	0.798	0.702	0.858
0.37	22707	8278	72077	0.790	0.786	0.686	0.854
0.41	21604	7077	69056	0.792	0.787	0.687	0.867

nominal x=0.84							
X-ray deadtime	Ga K	Ga L	In L	x_{InLGaK} acm	x_{InLGaL} acm	x_{InLGaK} ISIS	x_{InLGaL} ISIS
0.08	29865	13886	44420	0.635	0.632	0.505	0.682
0.14	10756	4754	39842	0.812	0.811	0.718	0.849
0.15	20645	9601	65590	0.787	0.787	0.686	0.821
0.17	11734	5776	50845	0.833	0.834	0.749	0.861
0.19	17575	8067	84948	0.849	0.849	0.768	0.876
0.22	13594	5745	74315	0.864	0.864	0.790	0.896
0.4	11502	4224	83373	0.895	0.894	0.833	0.930
0.51	25458	8119	123411	0.852	0.849	0.770	0.911

References

[1] G Cliff and G W Lorimer (1975) Quantitative analysis of thin specimens. *J. Microscopy* **103**, 203-207.

[2] D A Porter and H Westengen (1981) STEM microanalysis of intermetallic phases in an Al-Fe-Si alloy. *Quantitative Microanalysis with High Spatial Resolution* (ed. by G. W. Lorimer, M. H. Jacobs and P. Doig), pp. 94–100. The Metals Society, London.

[3] Z Horita, T Sano and M Nemoto (1987) Simplification of X-ray absorption correction in thin-sample quantitative microanalysis. *Ultramicroscopy*. **21**, 271–276.

[4] E V Cappellen (1990) The parameterless correction method in X-ray microanalysis. *Microsc. Microanal. Microstruct*. **1**, 1–22.

[5] O Eibl (1993) New method for absorption correction in high-accuracy, quantitative EDX microanalysis in the TEM including low-energy X-ray lines. *Ultramicrosc*. **50**, 179–188.

[6] P L Morris, M D Ball, and P J Statham (1980) The correction of thin foil microanalysis data for X-ray absorption effect. *Developments in Electron Microscopy and Analysis* (ed. by T. Mulvey), pp. 413–416. The Institute of Physics, London.

[7] Z Horita, K Ichitani, T Sano, and M Nemoto (1989) Application of the differential X-ray absorption method to the determinations of foil thickness and local composition in the analytical electron microscope. *Phil. Mag. A*, **59**, 939–952.

[8] P J Statham and M D Ball (1980) An indirect method for determining mass thickness for absorption corrections in the microanalysis of thin foils. *Microbeam Analysis − 1980* (ed. by D B Wittry). San Francisco Press, San Francisco, CA.

[9] M Watanabe, Z Horita, and M Nemoto (1996) Absorption correction and thickness determination using ζ-factor in quantitative X-ray microanalysis. *Ultramicrosc*. **65**, 187–198.

[10] M Watanabe and D B Williams (1999a) The new form of the ζ-factor method for quantitative microanalysis in AEM-XEDS and its evaluation. *Microsc. Microanal.* 5 (Suppl. 2) (ed. by G. W. Bailey, W. G. Jerome, S. McKernan, J. F. Mansfield and R. L. Price). Springer, New York.

[11] M Watanabe and D B Williams (2006) The quantitative analysis of thin specimens: a review of progress from the Cliff-Lorimer to the new ζ-factor methods. *J. Microsc.* **221** (2) 89–109.

[12] D B Williams and C B Carter (1996) *Transmission Electron Microscopy.* Springer, New York.

[13] P Hovington, D Drouin and R Gauvin (1997) CASINO: A new Monte Carlo code in C language for electron beam interaction.1. Description of the program. *Scanning* **19** (1997) 1-14.

[14] H Morkoc (2008) Handbook of Nitride semiconductor and devices. Wiley, Weinheim. Vol **1**, ISBN:978-3-527-40837-5.

[15] M C Parri, Y Qiu and T Walther (2015) New pathways for improved quantification of energydispersive X-ray spectra of semiconductors with multiple X-ray lines from thin foils investigated in transmission electron microscopy. *J. Microscopy* **260**, 427-441.

[16] M C Parri (2014) New method for quantifying x-ray spectra in a transmission electron microscope. PhD thesis, University of Sheffield.

[17] T Walther and C J Humphreys (1999) A quantitative study of compositional profiles of chemical vapour-deposited strained silicon–germanium/silicon layers by transmission electron microscopy. *J. Cryst. Growth* **197**, 113–28

[18] J I Goldstein, D E Newbury, P Echlin, D C Joy, A D Jr Romig, C E Lyman, C E Fiori and E Lifshin (1992) *Scanning electron microscopy and X-ray microscopy*, Plenum press, New York. 2nd ed

[19] A Rosenauer, T Mehrtens, K Muller, K Gries, M Schowalter, P V Satyam, S Bley, C Tessarek, D Hommel, K Sebasld, M Seyfried, J Gutowski, A Avramescu, K Engl and S Lutgen (2011) Composition mapping in InGaN by scanning transmission electron microscopy. *Ultramicroscopy* **111**, 1316-1327.

[20] S R Meher, K P Biju and M K Jain (2011) Raman spectroscopic investigation of phase separation and compositional fluctuations in nanocrystalline $In_xGa_{1-x}N$ thin films prepared by modified activated reactive evaporation. *phys. stat. sol. (a)* **208**, 2655-2660.

[21] F A Ponce, S Srinivasan, A Bell, L Geng, R Liu, M Stevens, J Cai, H Omiya, H Marui and S Tanaka (2003) Microstructure and electronic properties of InGaN alloys. *phys. stat. sol (b)* **240**(2), 273-284.

[22] Y Qiu, V H Nguyen, A Dobbie, M Myronov and T Walther (2013) Calibration of thickness-dependent k-factor for germanium X-ray lines to improve energy-dispersive

X-ray spectroscopy of SiGe layers in analytical transmission electron microscopy. *Journal of physics: Conference Series* **471**, 012031.

[23] J I Goldstein and D B Williams (1981) X-ray microanalysis of thin specimens. In: *Proc. Quantitative Microanalysis with High Spatial Resolution*. The Metals Society, London, UK. pp. 5-14.

[24] R Tixier, B Thomas and J Bourgeot (1981) Principles, limits and statistical evaluation of quantitative X-ray analysis. In: *Proc. Quantitative Microanalysis with High Spatial Resolution*, The Metals Society, London, UK. pp. 15-22.

[25] X Wang, M P Chauvat, P Ruterana and T Walther (2015) Combination of electron energy-loss spectroscopy and energy-dispersive X-ray spectroscopy to determine indium concentration in InGaN thin film structures. *Semicond. Sci. Technol.* **30**(11), 114011.

[26] T Walther, X Wang, V C Angadi, P Ruterana, P Longo and T Aoki (2017) Study of phase separation in an InGaN alloy by electron energy loss spectroscopy in an aberration corrected monochromated scanning transmission electron microscope. *J. Mater. Res.* **32**(5), 983-995.

[27] private communication from R. Gauvin to T. Walther by email on 19 July 2014.

Chapter 4

4. In concentration and phase separation determination for InGaN by valence EELS

Quantification of In concentration in InGaN is difficult by conventional TEM due to the projection effect averaging through the thickness of the sample. Low-loss EELS in a TEM has been demonstrated a powerful technique to determine the local chemical composition of InGaN on the order of nanometers [3-7]. In EDXS, to produce enough X-rays, the beam current must be relatively high, which can possibly produce In-rich clusters due to the induced electron beam damage [8]. Low-loss EELS offers an improvement due to the large scattering cross-section of the plasmon [9], which allows to record signals at low probe intensity and therefore is effectively decreasing the possibility to form In-rich. So low loss EELS is able to measure the In composition of an InGaN sample without inducing damage.

As Kong et al [10] have shown, the plasmon peak position in low-loss EELS has a linear relation with the In concentration, however, they performed experiment only up to 50% of In concentration, therefore, general validity of relationship the linear proposed therein could be questioned. In this chapter, we have used our series of InGaN samples, EDXS measurements of which have been described in chapter 3, to measure the plasmon loss, where the nominal In concentration is varies from 0% to 100%, the InGaN plasmon peak position for In content in the range of 50% to 100% can be obtained. The result is an improvement of the fitting of the In concentration as a function of plasmon energy loss peak position.

Phase separation of an InGaN ternary alloy into Ga-rich and In-rich areas was first predicted by Ho and Stringfellow [11] and later observed by several research groups. In chapter 3.3, In-rich and Ga-rich region are clearly displayed by EDXS quantification. Since our EDXS detector is not sensitive to light elements like nitrogen, the statistics for N counts is not reliable. an In rich area must either consist of a high degree of InN binary alloy or metallic In. Previously

the degree of phase separation in InGaN could only be reliably quantified by Rutherford Back Scattering (RBS) [12]. In this chapter, we develop a novel approach to quantify the degree of phase separation from a low-loss EELS recorded in a conventional TEM.

4.1 Plasmon energy versus In concentration from different InGaN layers

The recording of low loss EELS spectra is undertaken in our FEG JEOL 2010F TEM equipped with a Gatan Imaging Filter (GIF 200). The energy resolution as measured by the FWHM of the zero-loss peak was ~0.8eV. The spectra were collected in diffraction mode (image coupled mode) to allow enough electrons to enter the spectrometer. The collection semi-angle was ~20mrad using a dispersion of 0.0502(5) eV per channel. 5 nA beam current with a probe size of 50 nm was used to avoid electron beam damage of the samples. Several spectra were recorded for different thicknesses for each sample. Drift of high tension and magnetic strength of the prism are not a problem since the zero-loss peak is recorded for each spectrum and serves as an internal calibration for zero energy-loss offset.

The collected low-loss EELS spectra were first normalized to observe the plasmon peak shift for different InGaN samples are depicted in Figure 64.

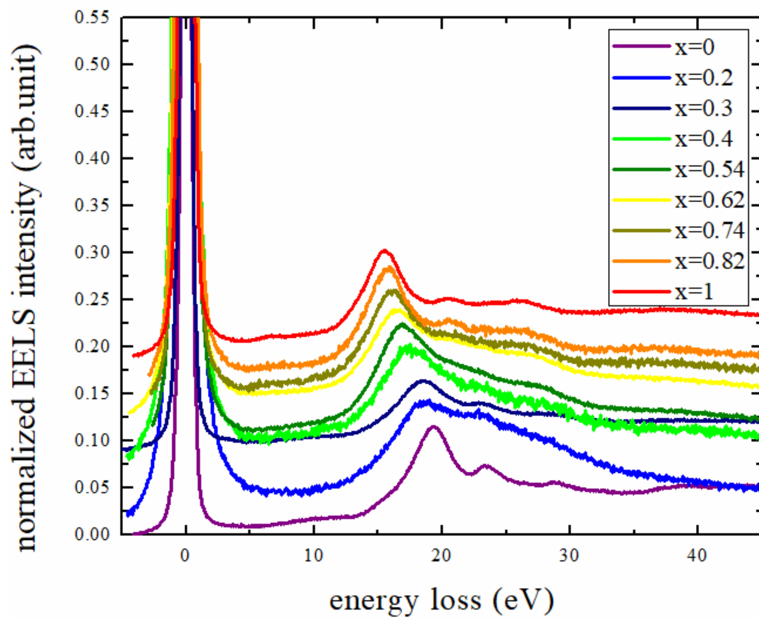

Figure 64 normalized low loss EELS spectra for different $In_xGa_{1-x}N$ samples of nominal In content x.

As shown in Figure 64, InN has the lowest plasmon energy. It is clear that the plasmon peak position is red shifted as the In concentration increases. In order to determine the plasmon peak position to high accuracy, Fourier log devolution is applied to remove the plural scattering effect. A comparison of original spectra and deconvoluted spectra for the $In_{0.54}Ga_{0.46}N$ sample is shown in Figure 65.

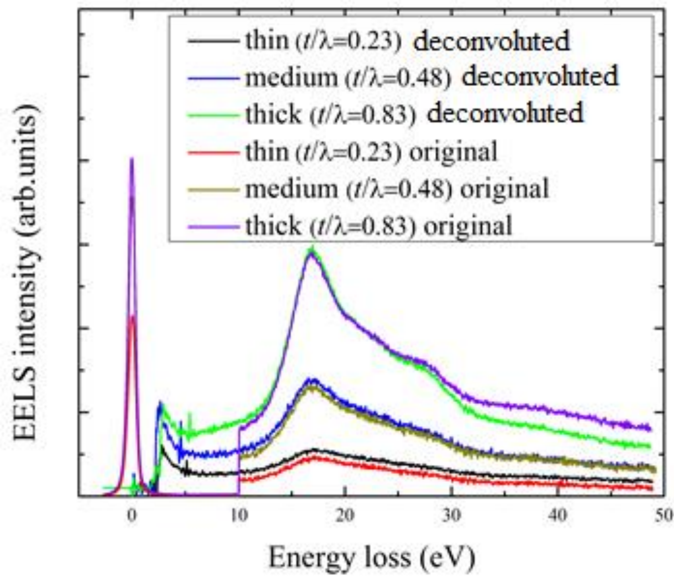

Figure 65 original and deconvoluted spectra from the $In_{0.54}Ga_{0.46}N$ sample

As shown in Figure 65, the deconvolution changes the height of the plasmon peaks, but no peak position shifted is observed, thus deconvolution is not deemed necessary for determination of plasmon loss energies.

The original and deconvolved spectra demonstrate a high noise level. In chapter 2.3.6.1, the plasmon excitation has been described by a Jellium model, which a Lorentz function fit well. By using the spectrum of $In_{0.54}Ga_{0.46}N$ sample as an example, a Lorentzian fit based on least-squares regression analysis can be applied to fit the plasmon peak. The result is demonstrated in Figure 66.

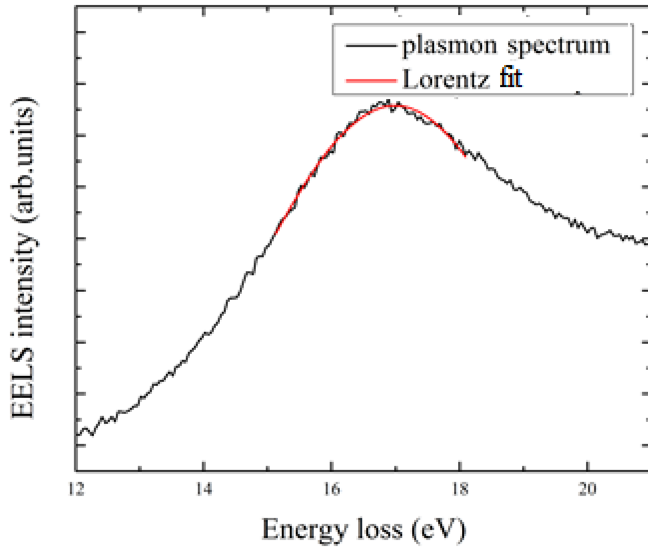

Figure 66 Lorentz curve fitted to the central part (15eV-18eV) of a plasmon peak for $In_{0.54}Ga_{0.46}N$ sample with t/λ=0.83.

From Figure 66, the plasmon peak position E_{max} can be determined by fitting the peak by a Lorentz function. The fitting approach is then applied to different InGaN thin films to observe the evolution of the plasmon peak position. The evaluated plasmon peak position for different InGaN samples is presented in Table 7. Three spectra have been recorded for each sample at different thicknesses, therefore, a weighted average energy was calculated for each sample. The ideal thickness for plasmon EELS is t/λ=1, where λ denotes the inelastic mean free path and t associate the sample thickness. The result was also presented in Table 7 with the corresponding RMS error.

nominal indium concentration, $x_{nominal}$	weighted average plasmon peak energy (eV)
0	19.33±0.01
0.135	18.69±0.04
0.20	18.42±0.01
0.30	18.27±0.01
0.40	17.66±0.05
0.54	17.00±0.02
0.62	16.76±0.04
0.74	16.14±0.03
0.84	15.88±0.02
1	15.52±0.01

Table 7 weighted average value of plasmon peak energy as function of nominal indium concentration for three measurements for each sample.

It is notable the error bar in Table 7 is pure fitting error from the spectra. As the calibrated dispersion is 0.0502(5), if the dispersion error is range from 0.00001~0.00009, for the measurement plasmon loss at 19.33, the measurement plasmon peak position uncertainty can be varied from 0.004eV to 0.035eV. Therefore, the accuracy of plasmon energy determination from EELS is really depending on the knowledge of dispersion from spectrometer.

The plasmon peak position of 15.8-16.9eV in a biaxially strained $In_{0.185}Ga_{0.815}N$ quantum well has been reported by Keast V J et al [14], which cannot be explained by bulk plasmon theory. However, as our thin film are of the order of 100 nm thick, the InGaN is only strained for a few nanometers around the InGaN/GaN interface, while the illuminated area is located away from the InGaN/GaN interfaces, therefore our samples can be treated as strain free and it is almost impossible to observe a strain effect in our EELS spectra.

In chapter 3.2, the measured In concentration from EDXS for each InGaN sample were obtained by averaging In concentration calculated from our absorption correction method at different probe positions (chapter 3.2 Figure 39), which can be served as a calibrated In concentration for each InGaN sample. In order to explore the plasmon energy and In concentration relationship, here, we plot the measured plasmon energy for each InGaN samples respect to their averaged In concentration calibrated by EDXS absorption correction method. By taking the others measurement of plasmon peak position [15-19] as supplementary data, the relationship of plasmon peak position and In concentration is shown in Figure 67.

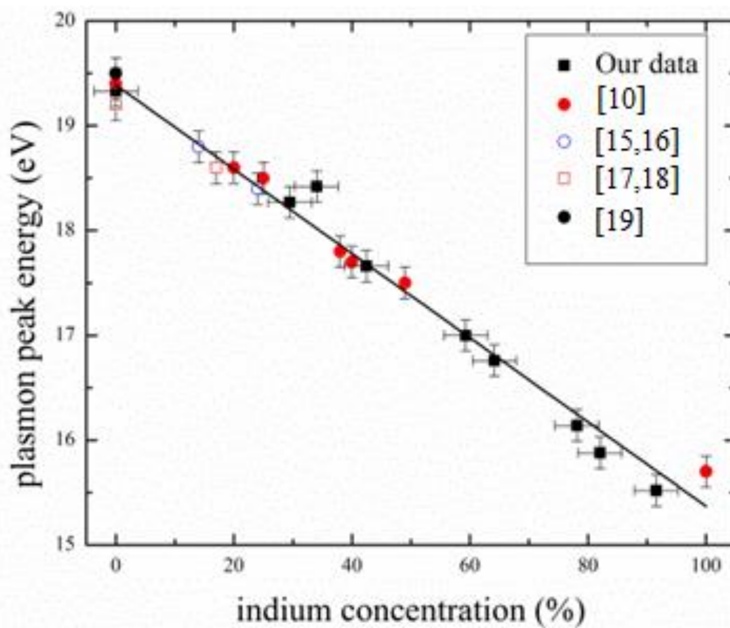

Figure 67 dependence of plasmon peak position on measured indium concentration in InGaN, including our data as well as data from other groups. The black line is the linear least-squares regression fit to all data.

As shown in Figure 67, the relationship between indium concentration and plasmon peak position is linear and can be expressed as

$$E_{max}[eV] = (19.39 \pm 0.06) - (4.02 \pm 0.11)x \quad (41)$$

where x is the In concentration, E_{max} is the plasmon peak energy. The adjusted R^2 value (R^2=0.9845) confirms the plasmon peak energy versus calibrated indium concentration is linear over the complete compositional range $0<x<1$, with an uncertainty in the indium concentration (random mean-square error from linear regression) of $\Delta x=\pm0.037$, which indicates an improved accuracy in the determination of indium concentration of InGaN compared to previous studies [10].

4.2 Quantification of phase separation from low-loss EELS in a conventional TEM

Matsuoka et al. [21] suggested that for growth of InGaN by metalorganic chemical vapour deposition (MOCVD) at 500°C, a maximum In concentration for a perfect ternary InGaN alloy could reach 42%. Several studies indicate the growth of InGaN heterostructures by MOCVD at higher growth temperature (700 °C ~800 °C) may only achieve a perfect ternary alloy for x<0.3 [22-25]. In this chapter, we investigated $In_{0.3}Ga_{0.7}N$, $In_{0.59}Ga_{0.41}N$ and $In_{0.68}Ga_{0.32}N$ samples, where phase separation may probably take place. The low-loss EELS for phase separation analysis were recorded under the same microscope (JEOL 2010F FEG TEM) and recording conditions as in chapter 4.1.

The collected low-loss EELS spectra were fitted with reference GaN, InN and InGaN reference spectra by using multiple linear least-squares fitting (MLLS), the weighting of each components representing the degree of phase separation in the InGaN. The construction process of $In_xGa_{1-x}N$ (x=0~1) reference spectra are detailed explained in chapter 4.2.1. the examples of phase separation analysis are demonstrated in chapter 4.2.2.

4.2.1 Construction of artificial Ga 3d (In 4d) core loss transition spectral and quantification of degree of phase separation in TEM mode

To construct spectra for InGaN ternary alloys, the GaN and InN binary compound spectra are used as references. The plasmon loss is smoothed and modelled by using Lorentz function. The raw spectra and modelled plasmon losses for GaN and InN are shown in Figure 68.

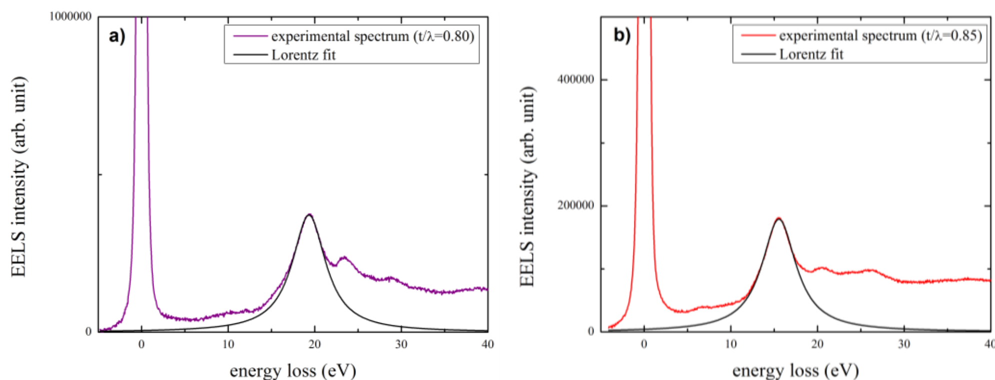

Figure 68 Lorentzian fits for a) GaN spectrum and b) InN spectrum.

The selection of reference spectra depends on the relative thickness of the probed area. in principle, the ideal reference spectra should be taken at $t/\lambda=1$, where λ is the inelastic mean free path under the specific experimental conditions, as the first plasmon peak has maximial intensity at $t/\lambda=1$[26], unfortunately, to record a spectrum from an area where the relative thickness exactly equal to 1 is difficult. From Figure 68, we have recorded spectra collected from regions where $t/\lambda=0.8$ and $t/\lambda=0.85$ for GaN and InN respectively. The Lorentz fitting window is opened 4eV wide centred around the plasmon peak position, which can provide a good modelling of the plasmon peak without influence by Cherenkov radiation or scattering in the low-loss range (0-10eV).

The FWHM of the plasmon peaks can be extracted from the fitted Lorentz function for each spectrum of InGaN ternary alloy. The In concentration can be quantified by using the relationship of plasmon energy position and In concentration in chapter 4.1. The relationship

of fitted spectra FWHM of plasmon peaks for all InGaN samples is plotted as function of In concentration in Figure 69.

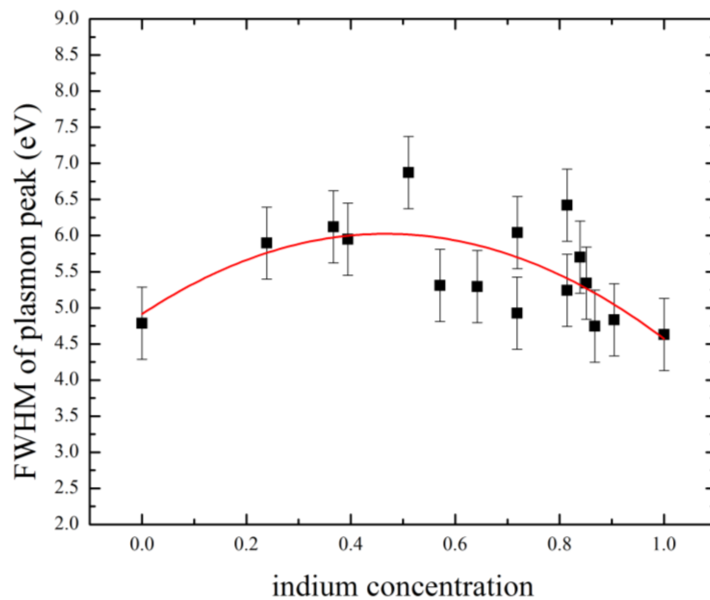

Figure 69 plot of FWHM of plasmon peak as function of indium concentration

The experimental FWHM of the plasmon loss shows a parabolic behaviour across the range from x=0 to 1. In order to reconstruct the pure core loss of GaN and InN (Ga 3d $M_{4,5}$ edge and In 4d $N_{4,5}$ edge), the modelled plasmon peaks should be subtracted from the raw spectrum. The Ga 3d $M_{4,5}$ transitions located at 23.8 and 28.5eV and the In 4d $N_{4,5}$ transition at 20.0 and 25.9eV are shown in Figure 70 a).

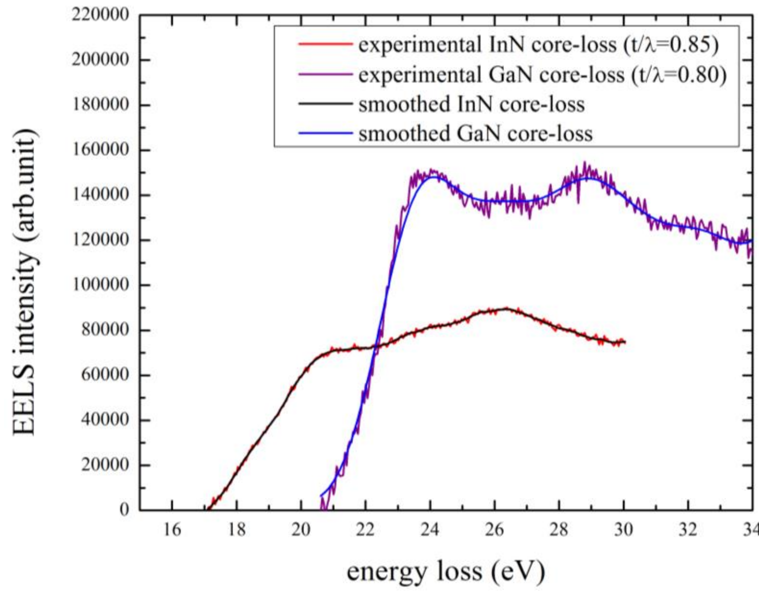

Figure 70 smoothed InN and GaN core-loss contributions after zero loss peak and plasmon subtraction

The Fast Fourier Transform (FFT) method is used to smooth the raw core loss spectra in Figure 70. The smoothing window is 18 channels wide which is roughly the energy resolution of the spectrometer (ZLP FWHM~0.9eV), so high frequency shot noise can be removed. The processed Ga 3d and In 4d spectra are also depicted in Figure 70.

To construct the reference core loss spectra of a perfect InGaN ternary alloy, the reference Ga 3d and In 4d core loss spectra in Figure 70 need to be normalized with respect to the relative thickness and experimental intensity. The normalization equation is provided in equation (42)

$$S_{Normalized\ coreloss} = \frac{S_{coreloss}}{\left(\frac{t}{\lambda}\right) * \int I(E)_{total} dE} \quad (42)$$

where $S_{coreloss}$ is the experimental core-loss spectrum profile, t/λ is the relative thickness of the specimen and $\int I(E)_{total}\, dE$ is the integral of total EELS intensity of the spectrum. The normalized reference core-losses for InN and GaN are shown in Figure 71.

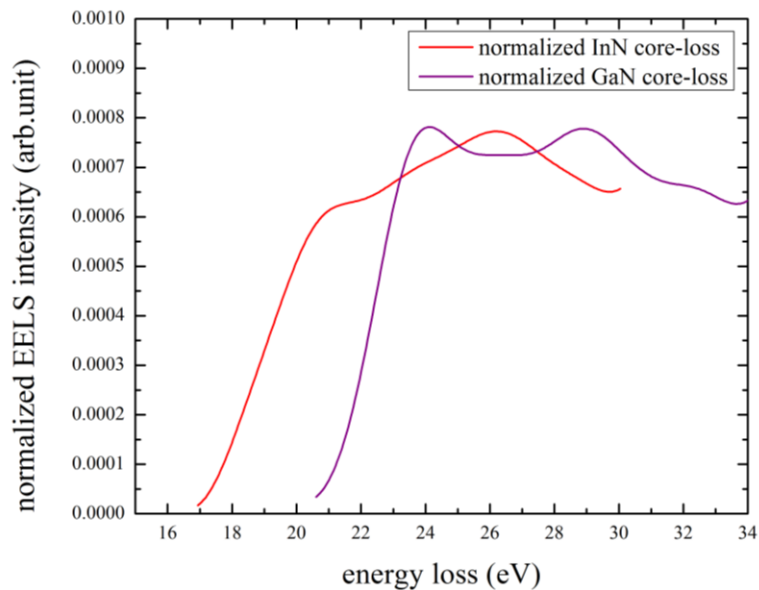

Figure 71 smoothed and normalized core-loss references spectra for InN and GaN.

Two methods are used to model InGaN core loss spectra by using normalized core loss spectra of InN and GaN in Figure 71:

1, the InGaN reference core loss is directly obtained by superimposing the weighted Ga 3d and In 4d transition with weights of (1-x) and x, respectively in Figure 71, where x is the indium concentration evaluated from the plasmon peak position.

2, the edge onset for In 4 d and Ga 3d are first brought to the same onset energy, weighting the Ga 3d core losses with weight (1-x) and the one for In 4d core losses with weight x. This merged core loss is then shifted back to an energy level given by the distance from the corresponding plasmon loss from Figure 74.

The reference $In_{0.3}Ga_{0.7}N$ modelled spectra from the two methods are compared with the smoothed and normalized experimental core loss spectrum of an $In_{0.3}Ga_{0.7}N$ sample, the result of which is shown in Figure 72

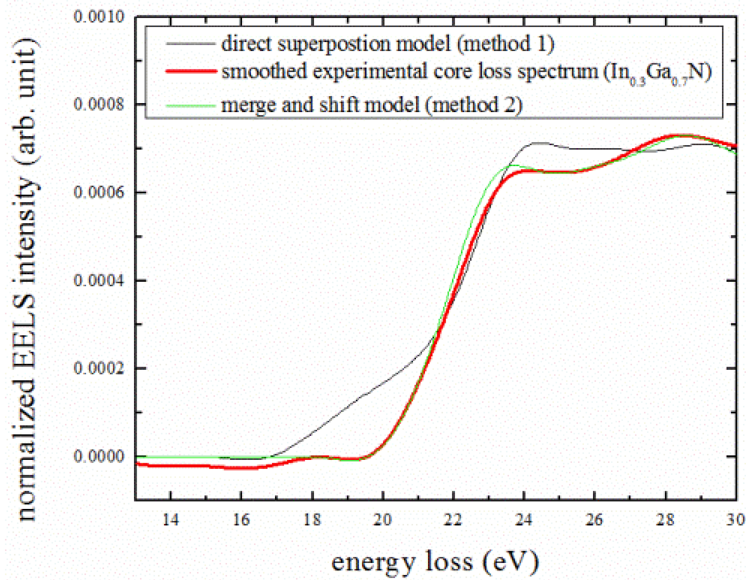

Figure 72 comparison of smoothed experimental core loss spectrum for $In_{0.3}Ga_{0.7}N$ with reference core loss spectra modelled by method 1 and method 2.

As observed in Figure 72, it is clear the reference core loss for $In_{0.3}Ga_{0.7}N$ modelled by method 2 fits better the experimental $In_{0.3}Ga_{0.7}N$ spectrum than the reference $In_{0.3}Ga_{0.7}N$ spectrum constructed by method 1. This indicates method 2 seems to be more suitable for modelling the core loss of $In_xGa_{1-x}N$ ternary alloys (x=0 to 1).

By applying the method 2 to construct reference InGaN core loss spectra. The resulting calculated evolution of InGaN core loss spectra profile for $t/\lambda=1$ is shown in Figure 73.

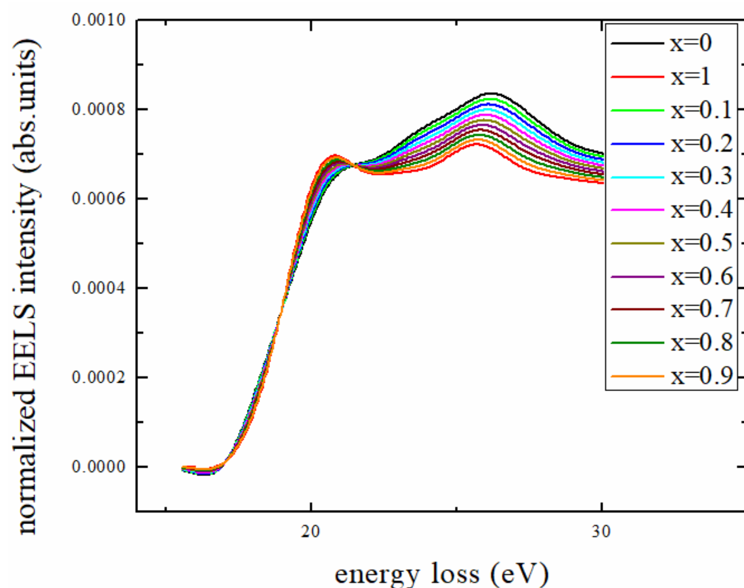

Figure 73 evolution of core loss spectra for InGaN of different In content (t/λ=1 for plasmon and core loss intensity)

As shown in Figure 64, the onset position of InGaN core loss changes with respect to the plasmon energy peak position. The investigated samples were two binary alloys (GaN and InN) one sample with *x*=0.3 grown by molecular beam epitaxy (MBE), and one sample with x=0.84 grown by MOCVD, as for these samples the spectra showed distinct core loss peaks. We have applied the previous strategy to smooth the core loss spectra and therefore accurately measure the separation of the first core loss from the plasmon loss for 4 different samples. The distance between the plasmon loss and first core loss varies from 4.5eV to 5eV, increasing nonlinearly with the In concentration. Applying a 2nd order polynomial fitting to the four data points, the fit shown in Figure 74 is obtained.

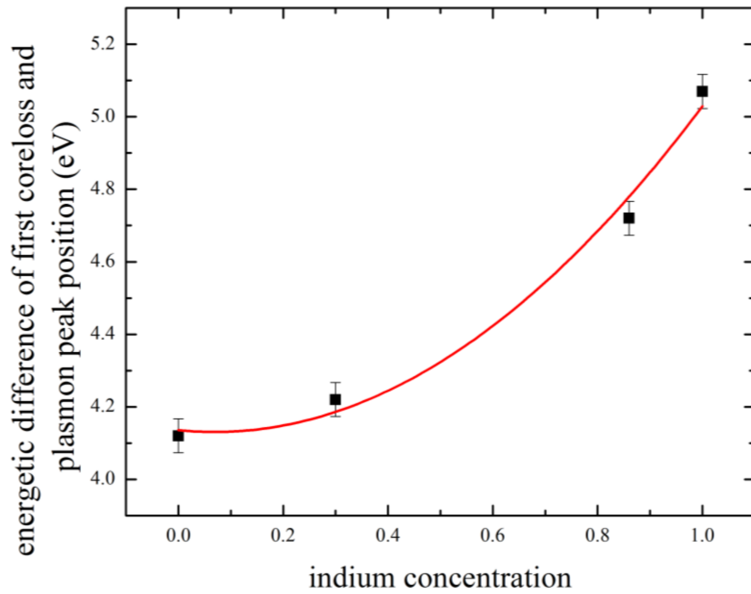

Figure 74 energetic difference measured between first core-losses (Ga M_5, In N_5) and corresponding plasmon peak positions in different InGaN samples.

The bowing factor in Figure 74 is determined as 1.04±0.46 eV. The bowing reflects that the core loss shifts similar to the bandgap with indium concentration, which follows Vegard's law with a bowing factor of 1.3-1.4eV for $In_xGa_{1-x}N$ [29]. The artificial core loss spectra generated for each InGaN alloy therefore need to be systematically shifted to the specific distance from the plasmon to satisfy the above energetic spacing. The core-loss spectrum of $In_xGa_{1-x}N$ for a specific thickness t and a total integral spectral intensity can then be constructed from the normalized reference spectra by multiplication with the factor $t/\lambda * \int I_{total}(E)dE$. By simply multiply with their corresponding plasmon loss spectra. The reference InGaN alloy low loss spectra for $t/\lambda = 1$ are shown in Figure 75.

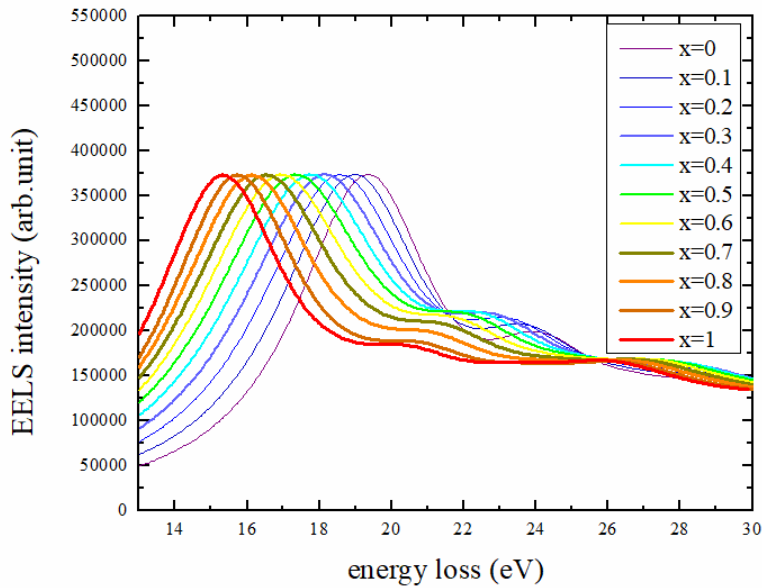

Figure 75 Comparison of InGaN alloy reference spectra for *x*=0 to 1.

4.2.2 Quantification of phase separation with reconstructed GaN, InN and InGaN spectra

The quantification of phase separation is to provide the percentage of perfect InGaN alloy in the sample relative to the sum of binary GaN and InN, by using MLLS regression for each alloy component contributing to the spectrum.

MLLS regression has been applied to fit experimental $In_{0.3}Ga_{0.7}N$ (MBE growth), $In_{0.3}Ga_{0.7}N$ (MOCVD growth), $In_{0.59}Ga_{0.41}N$ (medium thick) and $In_{0.86}Ga_{0.14}N$ EELS in the range of 13-30 eV. These spectra contain two core loss edge onset, which appear to be pure ternary alloy. This is shown in Figure 76.

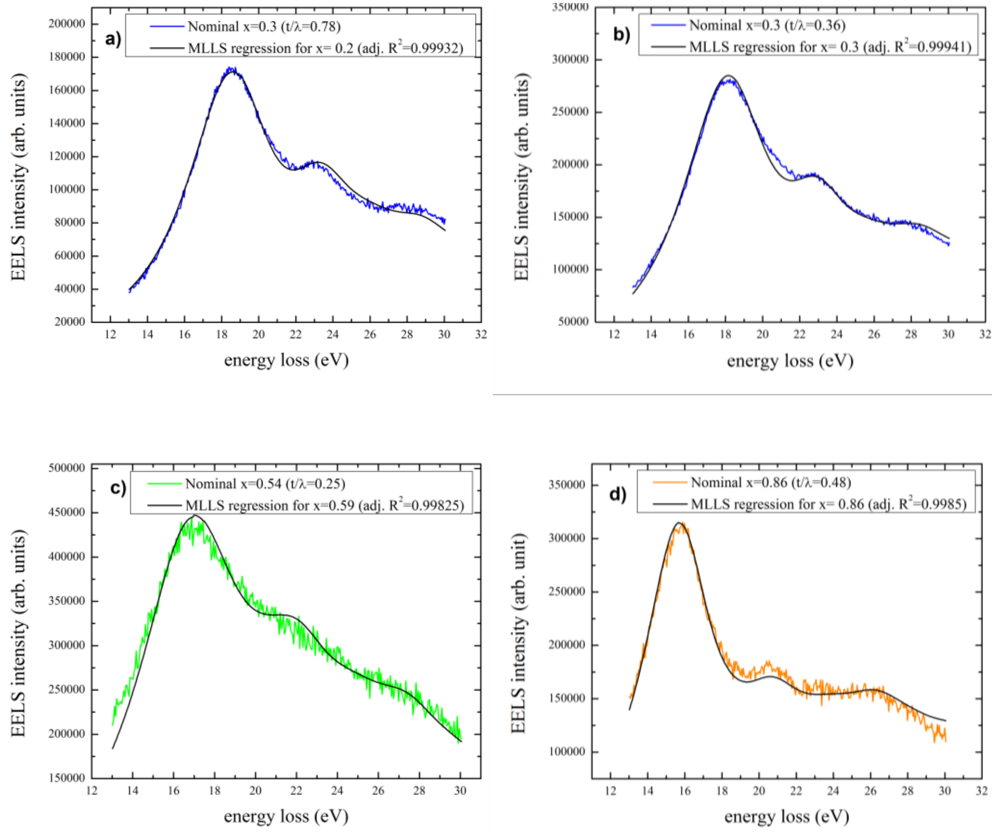

Figure 76 MLLS regression for a) $In_{0.3}Ga_{0.7}N$ (MBE), b) $In_{0.3}Ga_{0.7}N$ (MOCVD), c) $In_{0.59}Ga_{0.41}N$, and d) $In_{0.86}Ga_{0.14}N$. These spectra appear to be pure ternary alloy.

The adjust R^2 for each fitted spectrum in Figure 75 is >0.998, which indicates good fits. Some EELS spectra, presumed to have been collected from a phase separated region, present a much broader plasmon and core loss, sometimes without distinct edge features. An explanation may be the superposition of GaN, InN and InGaN along the electron beam direction. For any spectrum the average In concentration determined from plasmon loss and core loss should be consistent. In addition, the weight (*W* in Figure 77) of each alloy component calculated from plasmons and core losses needs to produce the same average In concentration. MLLS regression was applied to fit EELS spectra from possibly phase separated $In_{0.59}Ga_{0.41}N$ (thin and thick) and $In_{0.68}Ga_{0.32}N$ (Figure 77), where the actual average indium content has been verified by EDXS in chapter 3.2.

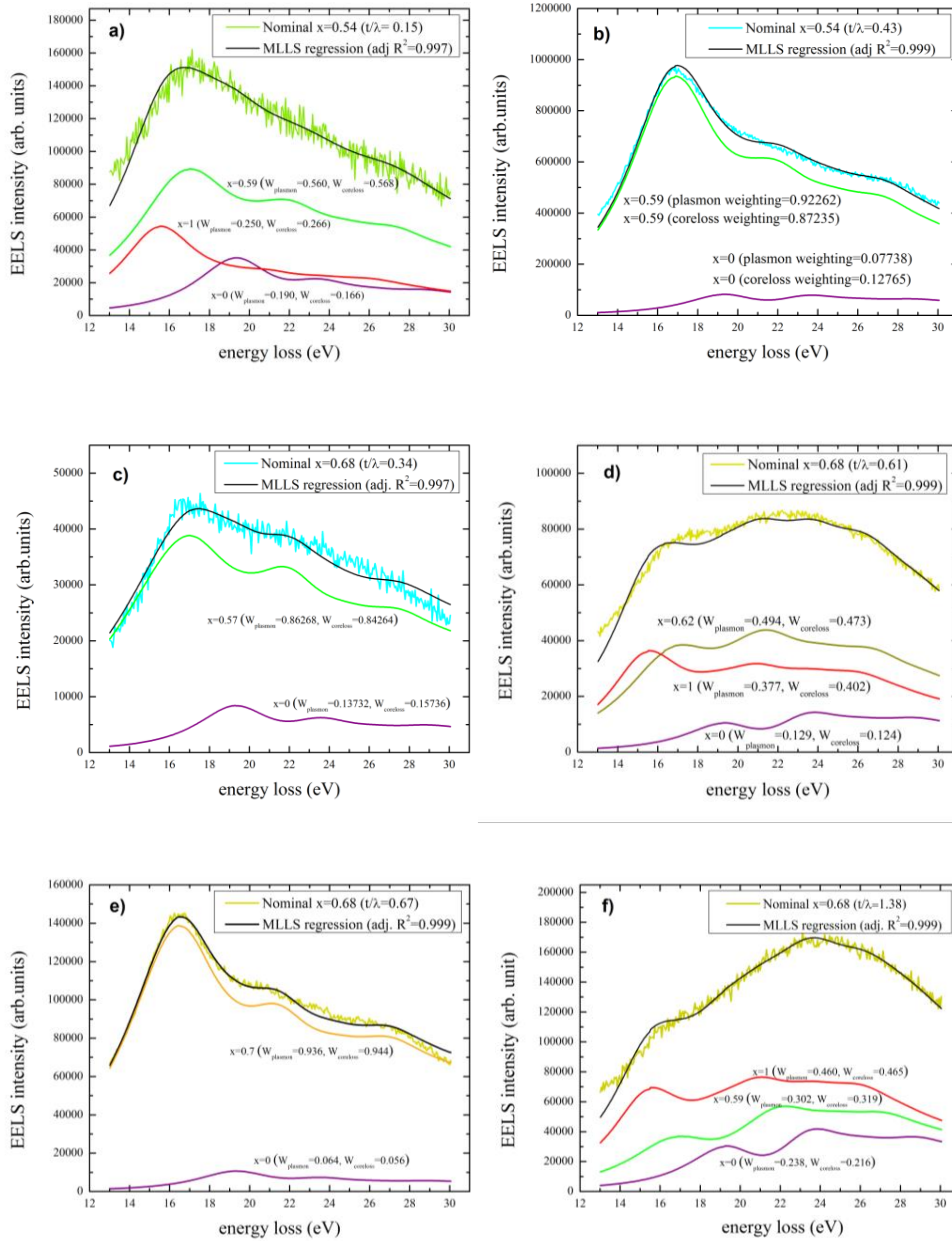

Figure 77 MLLS regression fits for a) $In_{0.59}Ga_{0.41}N$ thin sample (t/λ=0.15, nominal: x=0.54, EDXS: x=0.59), b) $In_{0.59}Ga_{0.41}N$ thick sample (t/λ=0.43), c) $In_{0.68}Ga_{0.32}N$ (t/λ=0.34), d) $In_{0.68}Ga_{0.32}N$ (t/λ=0.61), e) $In_{0.68}Ga_{0.32}N$ (t/λ=0.67), f) $In_{0.68}Ga_{0.32}N$ (t/λ=1.38).

The quantification of degree of phase separation is given by the calculated relative weghts W of GaN and InN, which represents the percentage of binary alloys in the illuminated area. As defined in equation (43).

$$D = W_{GaN} + W_{InN} \tag{43}$$

The average In concentration can be also quantified with the W parameters for binary and ternary alloy components. Equation (44) expresses the In concentration x calculated from these.

$$x_{average} = W_{GaN} \times 0 + W_{In_{xfit}Ga_{1-xfit}N} \times x_{fit} + W_{InN} \times 1 \tag{44}$$

where $x_{average}$ is the average In content, W_{GaN}, W_{InN} and $W_{In_{xfit}Ga_{1-xfit}N}$ are the weighting parameters calculated from fitted curve, the x_{fit} is the single x value used to fit the ternary InGaN spectral component. After quantifying W parameters for each alloy components, the degree of phase separation and average In concentration have been determined and are listed in Table 8.

EDXS indium concentration (measured from EDXS in chapter 3.2)	degree of phase separation	average indium concentration from plasmon and core-loss
0.59 (t/λ=0.15)	$D_{plasmon}$=44% $D_{core\text{-}loss}$=43.2%	$x_{plasmon}$= 0.58 $x_{core\text{-}loss}$= 0.60
0.59 (t/λ=0.43)	$D_{plasmon}$= 13.6% $D_{core\text{-}loss}$= 17.9%	$x_{plasmon}$= 0.574 $x_{core\text{-}loss}$= 0.543
0.68 (t/λ=0.34)	$D_{plasmon}$=13.1% $D_{core\text{-}loss}$=14.7%	$x_{plasmon}$= 0.502 $x_{core\text{-}loss}$= 0.499
0.68 (t/λ=0.61)	$D_{plasmon}$=50.6% $D_{core\text{-}loss}$=52.6%	$x_{plasmon}$= 0.68 $x_{core\text{-}loss}$= 0.70
0.68 (t/λ=0.67)	$D_{plasmon}$=6.4% $D_{core\text{-}loss}$=5.6%	$x_{plasmon}$= 0.66 $x_{core\text{-}loss}$= 0.66
0.68 (t/λ=1.38)	$D_{plasmon}$=54% $D_{core\text{-}loss}$=53.5%	$x_{plasmon}$= 0.64 $x_{core\text{-}loss}$= 0.65

Table 8 degree of phase separation and average indium concentration for $In_{0.59}Ga_{0.41}N$ and $In_{0.68}Ga_{0.32}N$ samples of different relative thicknesses that showed broadened peaks in EELS.

As shown in Table 8, the quantification of average In concentration from plasmon and core loss spectra demonstrate consistent results (within Δx= 1.7% standard deviation calculated from difference between plasmons and core losses). The D parameters quantified from plasmon loss and core loss also show consistent results for individual spectra, yielding a standard deviation of ΔD= 1.4% calculated from difference between plasmons and core losses. However, results from different positions within the same sample can differ a lot, indicating the degree

of phase separation varies a lot locally. From the EDXS measurements in chapter 3.2, the calibrated In concentration for nominal $In_{0.54}Ga_{0.46}N$ and $In_{0.62}Ga_{0.38}N$ samples were x=0.59 and x=0.68 respectively, which correlates well with our MLLS quantification approach except for the very thin area (t/λ=0.34) in $In_{0.68}Ga_{0.32}N$ sample. As observed from Figures 33 c), e) fitting of the $In_{0.68}Ga_{0.32}N$ spectra can sometimes be achieved without any InN spectra contribution, and the unique quantification result for t/λ=0.34 may be explained by the illumination region containing only InGaN ternary alloy and pure GaN.

In this chapter, we have developed a novel approach to quantify the phase separation in InGaN, the adjusted R^2 in Figure 77 representing a high quality of MLLS fitting. The quantification result in Table 8 and relative error bars indicate the degree of phase separation determined from plasmon and core-loss is consistent, and the average In concentration calculated from the degree of phase separation is confirmed independently by the EDXS quantification in chapter 3.2. Therefore, the developed MLLS quantification method seems to be reliable.

Chapter conclusion

In this chapter, we have successfully quantified the In concentration by using plasmon energy loss spectra. The plasmon energy shifts linearly with the In concentration in the InGaN samples. Phase separation was observed in $In_{0.59}Ga_{0.41}N$ and $In_{0.68}Ga_{0.32}N$ samples. Reference spectrum for GaN, InN and InGaN were constructed and the experimental spectrum was then fitted with three components to quantify the degree of phase separation the area probed by the electron beam. it is clear some measured InGaN samples have a strong phase separation around x~0.5, which can be attributed to thermodynamics instability [30] or strain [31]. The quantification of average In concentration from low-loss EELS is in good agreement with absorption corrected EDXS quantification, therefore the quantified degree of phase separation seems reliable as well.

References

[1] Y Narukawa, Y Kawakami, M Funato, S Fujita and S Nakamura (1997), Role of self-formed InGaN quantum dots for exciton localization in the purple laser diode emitting at 420 nm. *Appl. Phys. Lett* **70** 981–3.

[2] K Watanabe, N Nakanishi, J R Yang, K Inoke, J T Hsu and M Shiojiri (2003), Atomic-scale strain field and In atom distribution in multiple quantum wells of InGaN/GaN. *Appl. Phys. Lett* **82** 715–7

[3] X Kong, A Trampert, E Tournie and K H Ploog (2005), Decomposition in as-grown (Ga, In) (N, As) quantum wells. *Appl. Phys. Lett* **87** 171901

[4] X Kong, A Trampert and K H Ploog (2006), Composition fluctuations in dilute nitride (Ga, In) (N, As)/GaAs heterostructures measured by low-loss electron energy-loss spectroscopy. *Micron* **37** 465-72.

[5] D B Williams and J W Edington (1974), Microanalysis of Al-Li alloys containing fine 6' precipitates. *Phil. Mag* **30**(5) 1147-1153.

[6] A M Sanchez, R Beanland, M H Gass, A J Papworth, P J Goodhew and M Hopkinson (2005), Mapping quantum dot-in-well structures on the nano-scale using the plasmon peak in electron energy loss spectra. *Phys. Rev.* ***B*** **72** 075339.

[7] N Jiang, D Su, J C H Spence and A Howie (2009), Valence electron energy-loss spectroscopy of nanoporous MgO. *Appl. Phys. Lett* **94** 253105

[8] T M Smeeton, C J Humphreys, J S Barnard and M J Kappers (2006), the impact of electron beam damage on the detection of indium-rich localisation centres in InGaN quantum wells using transmission electron microscopy. *J. Mater. Sci* **41** 2729.

[9] X Wang, M P Chauvat, P Ruternana and T Walther (2015), Combination of electron energy-loss spectroscopy and energy-dispersive X-ray spectroscopy to determine indium concentration in InGaN thin film structures. *Semicond. Sci. Technol.* **30**(11), 114011.

[10] X Kong, S Albert, A Bengoechea-Encabo, M A Scanchez-Garcia, E Calleja and A Trampert (2012), Plasmon excitation in electron energy-loss spectroscopy for determination of indium concentration in (In, Ga)N/GaN nanowires. *Nanotechnology* **23** 485701

[11] I Ho and G B Stringfellow (1996), Solid phase immiscibility in GaInN. *Appl. Phys. Lett* **69**, 2701.

[12] M D Mccluskey, L T Romano, B S Krusor, D P Bour, C Chua, N M Johnson and K M Yu (1998), Phase separation in InGaN/GaN multiple quantum wells. *Mat. Res. Soc. Symp. Proc*. **482** 985-9.

[13] P L Potapov and D Schryvers (2004), Measuring the absolute position of EELS ionisation edges in a TEM. *Ultramicroscopy* **99** 73–85.

[14] V J Keast, N Sharma and C J Humphreys (2001), Energy-loss spectroscopy of GaN alloys and quantum wells. *Proc. 12th Microscopy of Semiconducting Materials Conf. (Oxford) Inst. Phys. Conf. Ser.* **169** *pp* 259–62.

[15] J R Jinschek, R Erni, N F Gardner, A Y Kim and C Kisielowski (2006), Local indium segregation and band gap variations in high efficiency green light emitting InGaN/ GaN diodes. *Solid State Commun* **137** 230–4.

[16] M Bosman, L J Tang, J D Ye, S T Tan, Y Zhang and V J Keast (2009), Nanoscale band gap spectroscopy on ZnO and GaNbased compounds with a monochromatic electron microscope. *Appl. Phys. Lett* **95** 101110

[17] Egerton R F (2009), Electron energy-loss spectroscopy in the TEM. *Rep. Prog. Phys* **72** 016502

[18] P Specht, J C Ho, X Xu, R Armitage, E R Weber, R Erni and C Kisielowski (2006), Zincblende and wurtzite phases in InN epilayers and their respective band transitions. *J. Cryst. Growth* **288** 225–9.

[19] P Specht, X Xu, R Armitage, E R Weber, R Erni and C Kisielowski (2006), Local band and defect transitions in InGaN observed by valence electron energy loss spectroscopy. *Physica* ***B*** **376/377** 552–5.

[20] T Walther, F Wolf, A Recnik and W Mader (2006), Quantitative microstructural and spectroscopic investigation of inversion domain boundaries in zinc oxide ceramics sintered with iron oxide. *Int. J. Mater. Res* **97**, 934.

[21] T Matsuoka, T Sasaki and A Katsui (1990), Growth and properties of a wide-gap semiconductor indium gallium nitride. *Optoelectronics Dev. Technol* **5 (1)**, 53.

[22] T Matsuoka, N Yoshimoto, T Sasaki and A Katsui (1992), Wide-gap semiconductor InGaN and InGaAlN grown by MOVPE. *J. Electron. Mater* **21**, 157.

[23] S. Nakamura (1994), Growth of InxGa(1-x)N compound semiconductors and high-power InGaN/AlGaN double heterostructure violet-light-emitting diodes. *Microelectron. J* **25**, 651.

[24] M Shimizu, K Hiramatsu and N Sawaki (1994), Metalorganic vapor phase epitaxy of $(In_xGa_{1-x}N/GaN)^n$ layered structures and reduction of indium droplets. *J. Cryst. Growth.* **145**, 209.

[25] S Nakamura, T Mukai, M Senoh, S Nagahama and N Iwasa (1993), $In_xGa_{1-x}N$/ $In_yGa_{1-y}N$ superlattices grown on GaN films. *J. Appl. Phys.* **74**, 3911.

[26] R.F. Egerton (1996), Electron Energy-Loss Spectroscopy in the Electron Microscope, Plenum Press, New York, 2nd ed.

[29] R R Pelá, C Caetano, M Marques, L G Ferreira, J Furthmüller and L K Teles (2011), Accurate band gaps of AlGaN, InGaN, and AlInN alloys calculations based on LDA-1/2 approach. *J. Appl. Phys.* **98**, 151907.

[30] Steffi Y. Woo, Matthieu Bugnet, Hieu P. T. Nguyen, Zetian Mi, and Gianluigi A. Botton (2015), Atomic ordering in InGaN alloys within nanowire heterostructures. *Nano Lett.* **15**, 6413−6418

[31] Il-Kyu Park, Min-Ki Kwon, Sung-Ho Baek, Young-Woo Ok, Tae-Yeon Seong, and Seong-Ju Park (2005), Enhancement of phase separation in the InGaN layer for self-assembled In-rich quantum dots. Appl. Phys. Lett. **87**, 061906

Chapter 5

5. Determination of degree of phase separation and bandgap of an InGaN ternary alloy by an monochromated STEM

In chapter 4, the degree of phase separation has been quantified by EELS using conventional TEM integrating over relatively large region. The critical thickness for dislocation nucleation decreases with the increase of In content [1], and for partial relaxation the starting of the InGaN/GaN interface unrelaxed, the strain may increase towards the top of the InGaN layer, which could lead to an enhancement of phase separation [2]. Several groups observed the critical thickness decreasing as In concentration increasing [3-5]. Coulon et al suggested faster growth along [11-20] InGaN could incorporate large In atoms with less lattice dilation [6], and several research groups found that by changing the NH_3, H_2, and TMIn flow rate or the growth temperature, the amount of In incorporation in the material could be increased [7-9]. By using HRSTEM Z-contrast imaging [2] or EDXS mapping in chapter 3, chemical fluctuations in the sample could be directly observed, however, phase separation on a nanoscale cannot be identified by EDXS mapping or Z-contrast imaging. The mapping of phase separation on the nano-scale is important for directly observing and understanding the components of phase separated InGaN.

Rutherford Back Scattering (RBS) [10-12] is a promising technique to quantify phase separation with relatively high reliability, but since the illuminated area is relative large, the quantification can only render an average degree of phase separation in the probed area. InN and GaN in a phase separated InGaN ternary alloy can be properly identified by X-ray diffraction (XRD) [13-15] or reflection high energy electron diffraction (RHEED) based on the splitting of diffraction spots [16-18]. Because of the lower crystal quality of high In content InGaN ternary alloys than InN and GaN binary alloys, XRD quantification is usually restricted to at low In content ($x<0.3$) InGaN sample [19]. Also as XRD has a relative large beam

diameter compared to electron beams in TEM, it is clearly not suitable for analysing phase separation on the nanoscale. Several groups reported InGaN phase separation by using atom probe tomography (ATP) [20, 21], which offers atomic spatial resolution in 3D, however, problems related to preferential ionization during laser-pumped desorption limit the quantification. Therefore, InGaN phase separation induced chemical fluctuations can be observed by ATP, but whether InN or high In content InGaN makes up to the In rich area remains unknown, unless the detection ratio of the individual atomic species is determined. Raman spectroscopy of InGaN phase separation was reported by Reiley et al [22], where the quantification of phase separation has been possible, but the spatial resolution (35nm) was larger than in EELS due to the diffraction limit of the excitation source (laser).

Here, we introduce our novel method to determine the degree of phase separation in STEM, where the phase separation can be directly observed in the InGaN thin film of the nano-scale.

For our JEOL 2010F, the recorded spectrum quality is suffering from chromatic aberrations. Therefore, to precisely analysis the phase separation along the InGaN thin film growth direction, a monochromated STEM operating at low accelerating voltage is needed to collect high-quality EELS spectrum image.

The bandgap of a semiconductor is important for optoelectronics and photonics device design. Conventional photoluminescence can measure the bandgap of bulk semiconductors, but due to the diffraction limitation of light, the probe size is of the laser beam is in the range of micrometers, which limits the spatial resolution, therefore, PL will not be able to provide a bandgap mapping on the nanometer scale. Cathodoluminescence (CL) is an improved technique to analysis the bandgap of a semiconductor, but similar to EDXS, the CL suffers from electron beam broadening within the sample and surface recombination effects, which decreases the spatial resolution. In this chapter, we have measured the bandgap of the nominal

$In_{0.62}Ga_{0.38}N$ sample with valence EELS in STEM, where beam broadening and absorption effect is not a problem, only EELS delocalization is an issue.

In this chapter, our JEOL 2010F and an aberration corrected NION Super STEM with monochromator is used to record spectrum images; our novel method to quantify the degree of phase separation is applied to both. Simultaneously, the bandgap fitting is applied to analyse the high-quality EELS spectrum image. The analysis result can reveal the distribution of phases and bandgap in an InGaN thin film on the nano meter scale.

5.1 quantifying the degree of phase separation of InGaN thin film from a conventional STEM

The STEM spectrum images for $In_{0.62}Ga_{0.38}N$ sample were collected in our JEOL 2010 F FEG TEM equipped with a Gatan image filter (GIF200) and in a c-FEG NION Ultra STEM 100 with Gatan Enfinium ER energy-loss spectrometer, aberration corrector and monochromator [23]. The JEOL 2010 F was operated at 197kV (this voltage allows the user to increase the high tension by up to 3kV for energy-filtered imaging, cf. [24]). A 40 µm condenser aperture was used to reduce the aberration generated from condenser lens, yielding a 9.5 mrad convergence semi-angle and ~0.5 nm probe size. A 3mm GIF entrance aperture was used to allow enough electrons to be collected by the spectrometer. The probe current is roughly 1nA, 84×51 pixels spectrum image was recorded with a sampling size of 3 nm at 200kX magnification. The dispersion was calibrated as 0.0502(5) eV per channel (calibrated by drift tube offsetting). The energy resolution of the spectrum image is measured as ~1.7eV (FWHM of zero loss peak).

Figure 78 shows spectra and ADF image collected from our JEOL 2010 F with the spectrum iamge extracted from the green rectangle in a).

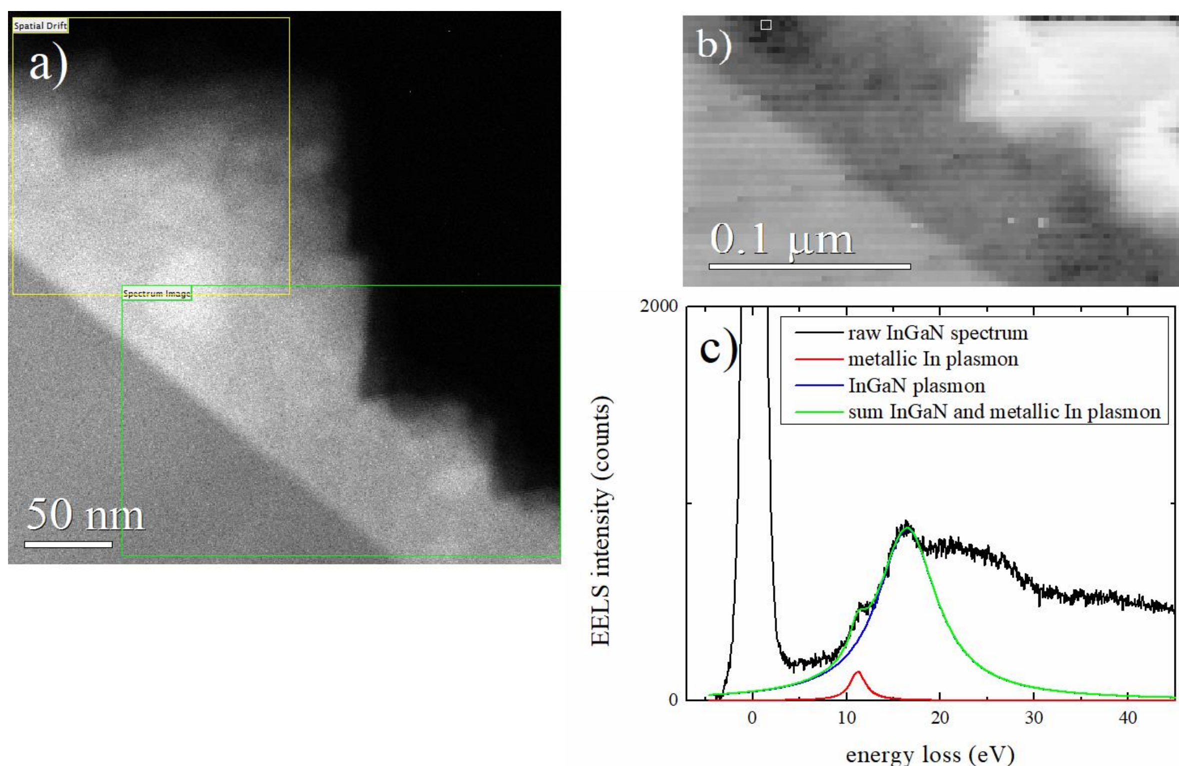

Figure 78 a) ADF image showing the region for spectrum image (green) and drift correction (yellow), b) spectrum image c) spectrum extracted from small white square in Figure 78 b), with fitting of plasmons

As observed in Figure 78 the spectrum image shows some residual drift due to sample and scan coil drift. The sample drift is mainly due to the temperature difference between the sample stage inside the column and outside, the scan coil drift is attributed to the temperature change when the microscope is switched from TEM to STEM mode. At the top left corner, the spectrum image displays a darker region, while the ADF image gives a brighter contrast (whether In rich or thicker region in chapter 3). The spectrum was then extracted from the white square in Figure 78 b) and plotted in Figure 78 c). An additional plasmon peak is observed at 11.3eV which corresponds well with plasmon resonance energy of metallic indium [25, 26]. Lorentz fitting was then applied to both InGaN and metallic In plasmon peaks; the integral intensity of the plasmon peak attributed to metallic In is 5868 compared with 184807 for InGaN,

which indicates metallic In in the InGaN amount to only roughly 3 percent along the projection direction. As measured from Figure 78 a), the diameter of the brighter region is roughly 50 nm, which correlates well with the previous EDXS measurement. In-rich cluster formation by electron beam induced damage was observed previously by Smeeton et al and O'Neill et al [27, 28]. From [27], the electron beam induced damage was observed when illuminating an $In_{0.22}Ga_{0.78}N$ sample with 200kV accelerating voltage with 14000 C/cm^2 electron beam dose, resulting in chemical fluctuations in the sample. As the In-N bond energy (7.72eV/atom) is smaller than the Ga-N bond energy (8.92eV/atom) [29], it is easier to produce beam induced damage in high In content InGaN since the sample contains more In-N bonds than Ga-N bonds. As our previous EDXS measurements were conducted under the dose from 1.6×10^5 C/cm^2 to 4.7×10^5 C/cm^2, metallic In could likely be formed by breaking In-N bonds by the high energy electron beam and knock-on evaporating the N atoms from the sample surface.

Compared with the low-loss EELS spectra recorded in TEM mode in chapter 4, the energy resolution for spectrum imaging was significantly worse (FWHM of zlp of ~1.7eV for STEM mode compared to ~0.8 eV for TEM mode), because we used 3 mm entrance aperture into our Gatan image filter to maximise collection efficiency, however, the aberrations of the spectrometer are higher under these conditions. The GaN spectra recorded in STEM mode with 3mm entrance aperture and TEM mode with 0.6 mm aperture are compared in Figure 79.

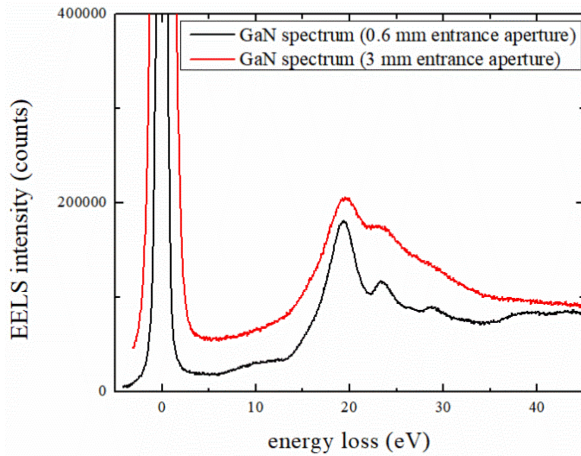

Figure 79 comparison of low-loss EELS spectrum collected from 0.6 mm and 3 mm entrance aperture. JEOL 2010 F, 197kV.

As shown in Figure 79, both plasmon and core-loss recorded with 3mm entrance aperture are broader than with the 0.6 mm entrance aperture, which can be attributed to spectrometer aberrations. As the plasmon loss peak is quite broad, the decrease of energy resolution will only weakly affect its FWHM, eg: if the plasmon loss FWHM is 4.5-5.5eV in TEM mode, in STEM mode the FWHM will only increase as 4.7-5.7eV, therefore, the decrease of energy resolution influences sharp core loss stronger than broader plasmon losses. It is thus difficult to obtain a consistent quantification result from plasmon and core loss in STEM mode by using reference spectra recorded from TEM mode. The MLLS fitting method is still applied to the spectrum image to quantify the degree of phase separation at each pixel, where the GaN, InN and one InGaN reference spectra should be selected to achieve best fitting quality (best R^2 value). The increment of InGaN reference spectra selection is set as Δx=0.05. The quantification result is shown in Figure 80.

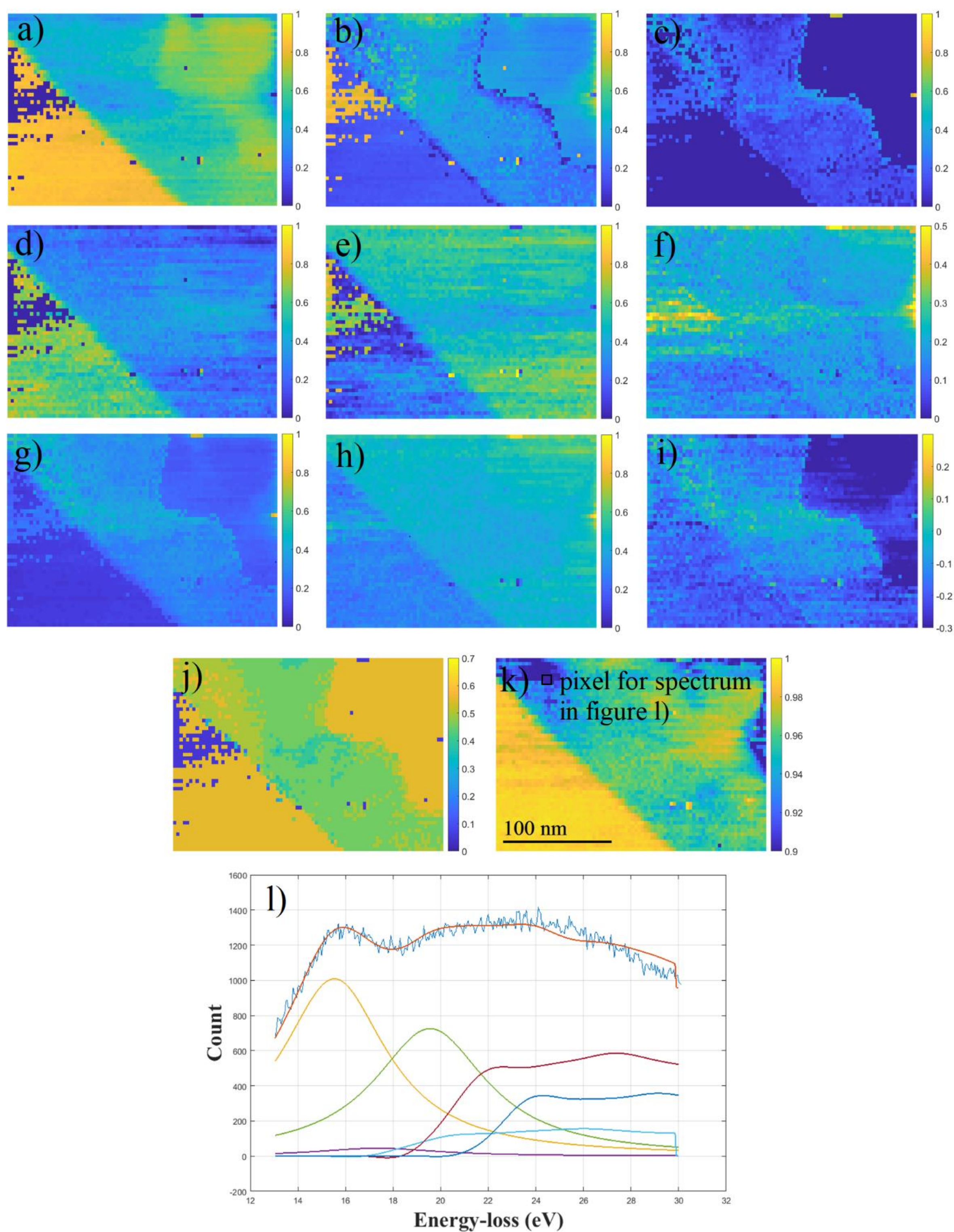

Figure 80 results from fitting each spectrum from the spectrum image in Figure 78 b) by a linear superposition of GaN, InGaN and InN reference spectra recorded in TEM mode. a) weight parameters for GaN calculated from plasmon loss (W_{GaN} plasmon), b) W_{InGaN} plasmon,

c) W_{InN} plasmon. d) weight parameters for GaN calculated from core loss (W_{GaN} core loss), e) W_{InGaN} core loss, f) W_{InN} core loss, g) x map calculated from plasmon loss, h) x map calculated from core loss, i) difference map [i)=g)-h)], j) the best fitting x value of the ternary component only, k) R^2 map, l) fitted spectrum extracted from Figure k) white square.

In Figure 80, The difference of x maps in i) gives a mean value of Δx=0.22, which indicates the weight maps calculated from plasmon and core loss are not quite consistent. Also, the metallic In region observed in Figure 78 is expected to provide extra In 4d core loss intensity, which should lead to the InN weight value quantified from core loss being slightly higher than the value determined by plasmon loss. However, from our quantification result, it is lower, indicating the reference plasmon and core loss spectra need to be modified to obtain a more consistent quantification result.

Since the zero-loss peak is broadening by increased spectrometers aberrations, the reference plasmon and core loss spectra for different InGaN should be reconstructed by convolving the reference spectra recorded with 0.6 mm entrance aperture with the zero-loss peak recorded with 3 mm entrance aperture. The reconstructed plasmon and core loss spectra are then introduced to process the experimental spectrum image recorded with 3 mm entrance aperture. The quantification results are shown in Figure 81.

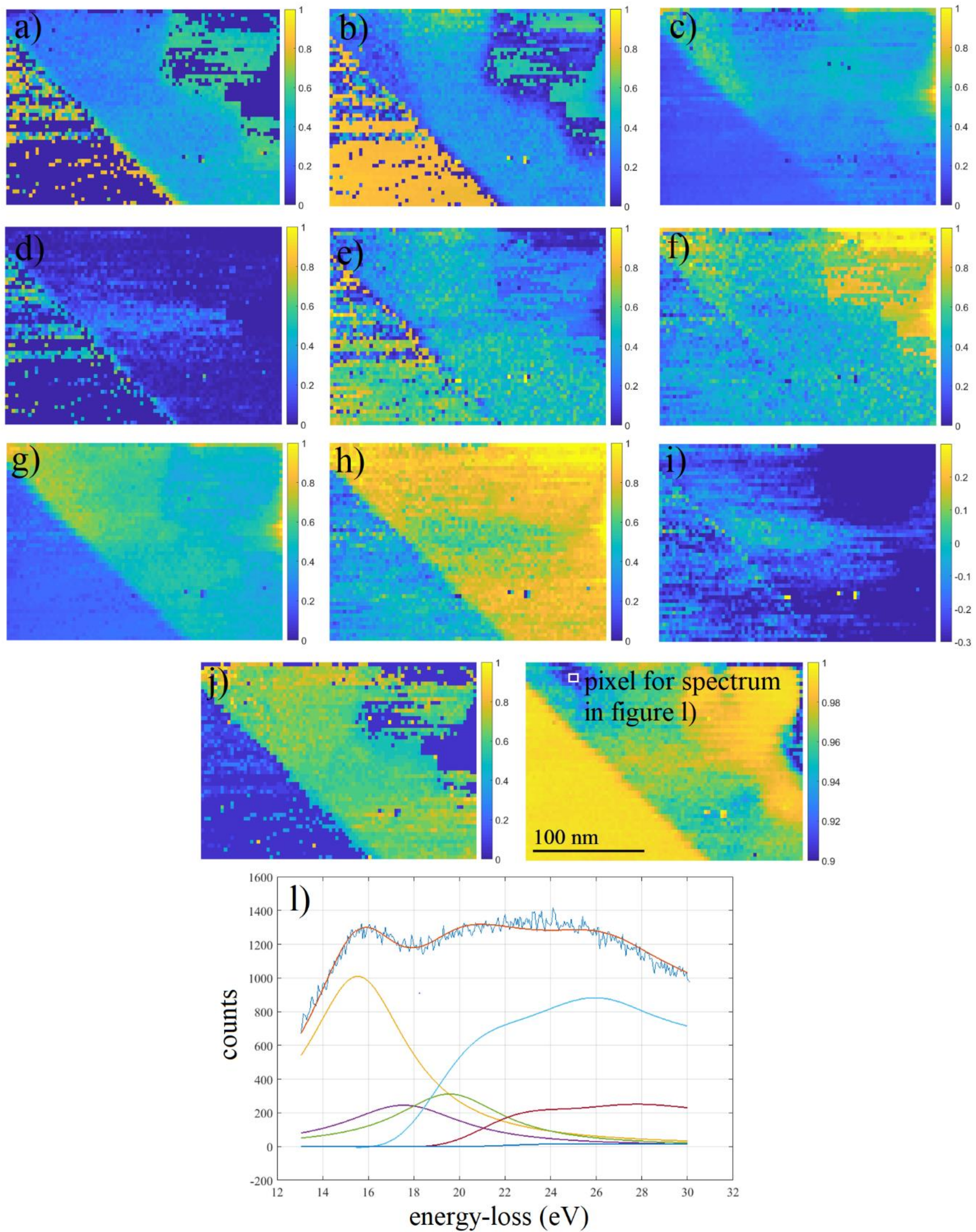

Figure 81 results from fitting each spectrum from the spectrum image in Figure 78 b) by a linear superposition of GaN, InGaN and InN reference spectra from convolving the core loss reference spectra with the measured STEM zlp. a) weight parameters for GaN calculated from plasmon loss (W_{GaN} plasmon), b) W_{InGaN} plasmon, c) W_{InN} plasmon, d) weight parameters for

GaN calculated from core loss (W_{GaN} coreloss), e) W_{InGaN} core loss, f) W_{InN} core loss, g) x map calculated from plasmon loss, h) x map calculated from core loss, i) difference map [i)=g)-h)], j) the best fitting x value of the ternary component only, k) R^2 map, l) example of fitted spectrum extracted from Figure k) white square.

As shown in Figure 81, a large fraction of InN is observed underneath the upper big island from both plasmon and core loss weight maps, which correlates well with the STEM EDXS measurement. The mean value of difference map x improves from Δx=0.22 to Δx=0.15, indicating the convolution with zero-loss peak recorded with 3 mm entrance aperture has an improvement on spectrum analysis. However, the reconstructed plasmon and core loss spectra are still inadequate although clearly better as shown by the improved Figure in l) and in the R^2 map, the metallic In region demonstrates a poor fit quality (~0.8), as the fitting interval is conducted from 13eV to 30eV, so that the metallic In plasmon loss peak at 11.3 eV is not included in the fitting. The metallic In area demonstrated in the $W_{InN\ core\ loss}$ map has a higher value than $W_{InN\ plasmon}$ map, which would be expected.
To conclude an accurate analysis of phase separation in EEL spectrum imaging by using aberration induced poor energy resolution and a partially beam damaged sample is difficult. Therefore, it will be necessary to apply the quantification approach to a spectrum image recorded from a lower kV monochromated STEM, which is described in the next section.

5.2 Determination of the degree of phase separation of InGaN thin film in an monochromated STEM

As pointed out in chapter 5.1, the optimal EEL spectrum image can be obtained by using an aberration corrected low kV STEM equipped with a monochromator.

The ADF image and spectrum image data in Figure 82 was collected by using a c-FEG NION Ultra STEM 100. The set up accelerating voltage for low-loss EELS is 60kV, the collection semi-angle 45 mrad with a 2mm entrance aperture for low loss EELS (at 60kV), A ~0.12nm probe size with ~300pA beam current (20-30 pA after monochromation) was set up and spectra were acquired with the charge-coupled device (CCD) detector in single read-out vertical integration mode and binning for fast acquisition to avoid electron beam-induced damage of the sample. Only the combination of monochromator with aberration corrector enabled the formation of a small electron beam of sufficient current suitable for high-quality VEELS for both bandgap extraction and plasmon fitting. The low-loss spectrum image was monochromated, yielding a dispersion of 0.015eV per channel and energy resolution of 0.15eV. A 60×30 pixels spectrum image was collected with a real space sampling size of 2.1 nm/pixel.

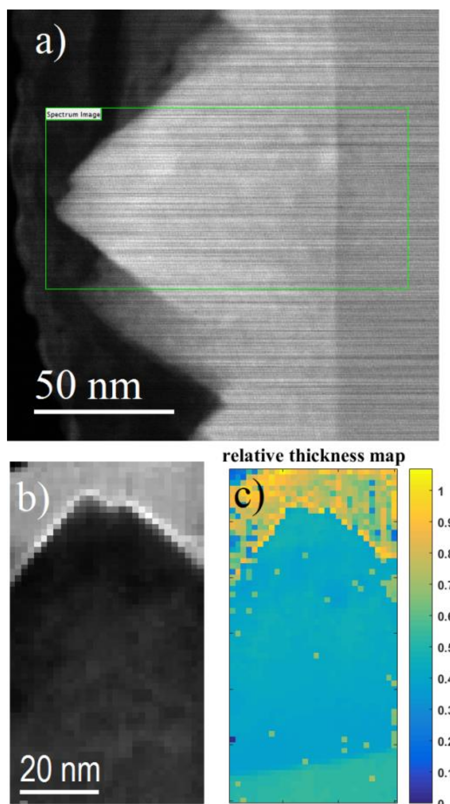

Figure 82 a) ADF image with the region for spectrum imaging indicated, b) spectrum image from the green rectangle in a), turned by 90° for display c) t/λ map calculated from spectrum image in b).

The spectrum imaging was undertaken in the marked area of the ADF image; the spectrum image has then been rotated for further processing. A t/λ map was first derived from the spectrum image. The t/λ map is shown in Figure 82 c).

As shown in Figure 82 b), no electron beam knock-on damage was observed and no metallic In plasmon peak was presented in the spectrum image. The slightly incline of the InGaN/GaN interface in Figure 82 c) indicates the sample drifting during spectrum image acquisition. The *t/λ* mean values are evaluated as *t/λ*= 0.43±0.02 in the InGaN layer and 0.59±0.13 in the GaN buffer. By calculating the inelastic mean free path (λ) in chapter 2.3.7 for GaN, C and $In_{0.68}Ga_{0.38}N$, the thickness of three regions can be estimated as 27 ±6 nm for GaN and 18±1 nm for $In_{0.68}Ga_{0.38}N$, and 34±8 nm for carbon. The result indicates the scanning region of InGaN/GaN heterostructure has a wedged sample geometry.
The CCD of the NION Ultra STEM 100 has a dimension of 2048×2048 pixels. The calibrated dispersion is 0.015eV, the investigated spectrum at each point reaches up to 27eV. For the spectra recorded in the JEOL 2010F, the CCD has a dimension of 1024×1024 pixels with a dispersion of 0.05025eV, the recorded spectrum energy is up to 40eV. Since the energy resolution of the NION STEM is significantly better than of the JEOL 2010F, we should compare the reference GaN spectrum recorded from two systems to determine whether the reference spectra need to be re-recorded at higher resolution or not. The GaN reference spectra from NION Super STEM and JEOL 2010F are shown in Figure 83.

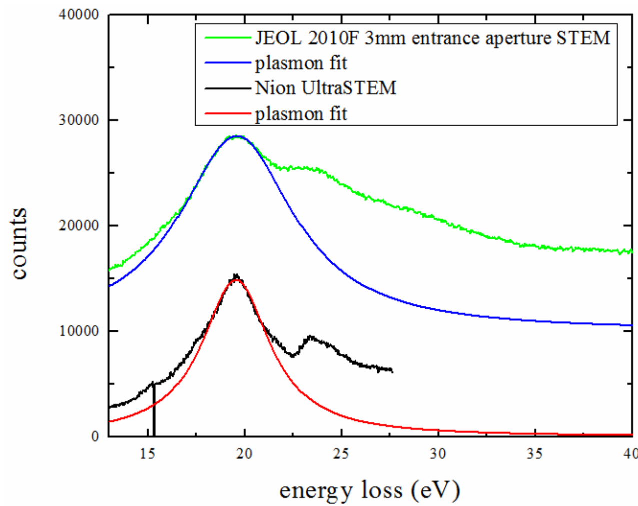

Figure 83 Comparison of low-loss EELS from GaN recorded at 197 kV in the JEOL 2010F (green line, with blue fit to plasmon) and at 60kV in the NION UltraSTEM (black line, with red fit to plasmon).

Lorentz fitting of the plasmon has been applied to both spectra. The plasmon and core loss for JEOL 2010F are broader than in the NION Super STEM. The main reason could be explained by the lower energy resolution in the JEOL 2010F leading to a broadening of both plasmon and core loss profile, however, as the two machine operated under different acceleration voltage with different spectrum collection angle, the absolute effect on plasmon and core loss broadening is currently unknown. The modelled plasmon loss has then been subtracted from the raw spectra and remaining core-loss are smoothed according the method in chapter 4.2.1, the results are compared in Figure 84.

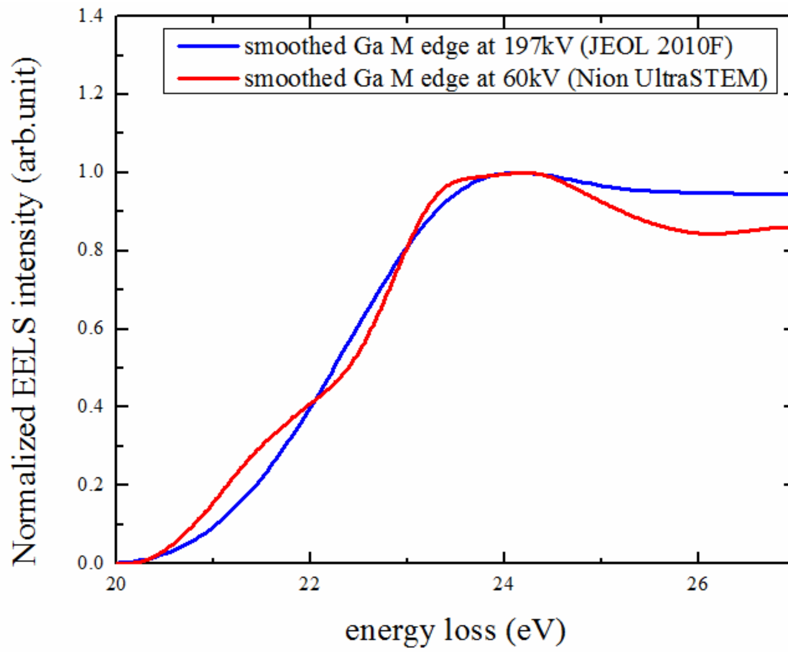

Figure 84 Comparison of smoothed Ga M-edge core loss components from JEOL 2010F and NION ultra STEM.

The profiles of the core loss for both spectra are clearly different. With the better energy resolution, lower accelerating voltage and larger collection angle provided by the NION Ultra STEM, partial structure of $M_{5,4}$ edge can be resolved indicated by the two stronger peaks observed. The difference between the core loss profiles recorded from both TEMs means that our database of InGaN reference spectra previously acquired at 197kV in the JEOL microscope need to be refreshed and replaced by monochromated reference InGaN spectra for processing the spectrum image collected at 60kV.

With the GaN core-loss spectrum being obtainable from the buffer region but no InN region present, we have extracted one InGaN spectrum from the spectrum image to reconstruct the InN core loss, by eliminating the Ga 3d component from it, which should work under two conditions:

1. the two corresponding core loss edges of InGaN ternary alloy should be observed clearly in the spectrum, which indicates the spectrum was possibly recorded from a perfect InGaN ternary alloy region.

2. the FWHM and peak position should follow the relationship plotted in chapter 4.2.1, indicating a perfect InGaN ternary alloy plasmon characteristic.

The InGaN and GaN core losses can be obtained by subtracting the fitted plasmon peak. The obtained core loss is then smoothed and normalized by using the process illustrated in chapter 4.2.1. By simply subtracting the Ga 3d core loss from the InGaN core loss, the In 4d core loss for InN can then be obtained. Underneath the island a high degree of phase separation is observed in Figure 80, which is believed to be constituted by large fraction of InN and small portion of GaN. The selected InGaN spectrum position should be within this region, where the GaN plasmon and core loss influence on the spectrum can be minimized. By following the two conditions above, a sharp plasmon peak with clear core-loss onset should be observed in the selected spectrum. The selected spectrum has been shown in Figure 85 a), the plasmon energy is located at 15.76eV, corresponding to x=0.94. the fitted plasmon loss has a FWHM of 4.75eV, which correlates well with the relationship between plasmon peak position and FWHM. Also, two core loss edges are observed in the spectrum. Therefore, it can be seen as a ideal spectrum for reconstructing the InN core loss.

The core-loss spectra for InGaN of different In concentrations are constructed as described in the approach demonstrated in chapter 4.2.1. and are shown in Figure 85.

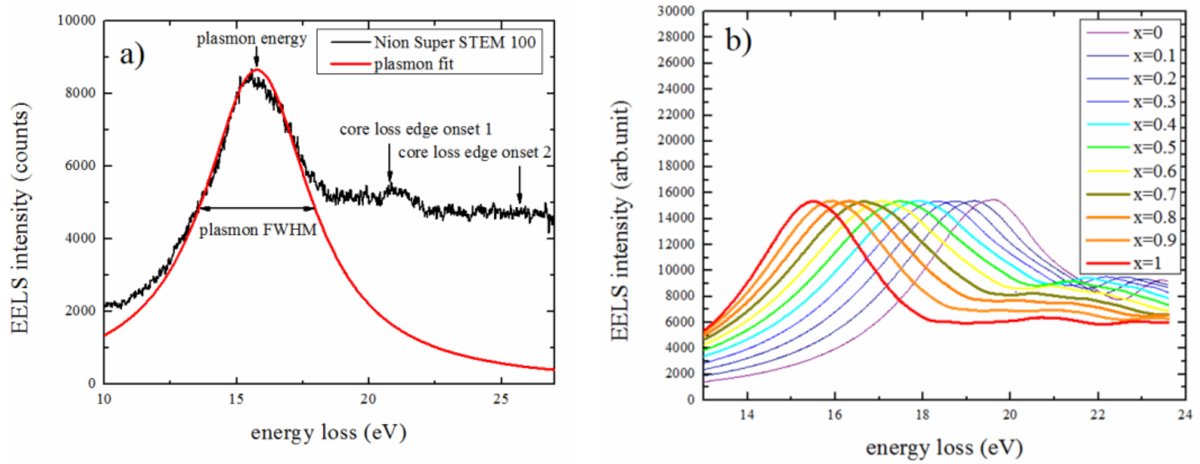

Figure 85 a) extracted spectrum for reconstructed InN core loss, b) $In_xGa_{1-x}N$ reference spectra from x=0 to x=1 for monochromated STEM at 60kV.

The reference GaN, InN and InGaN spectra are applied to fit spectra in Figure 82 to quantify the degree of phase separation at each pixel. The paramters W, x for ternary alloy fitting and R^2 maps are shown in Figure 86.

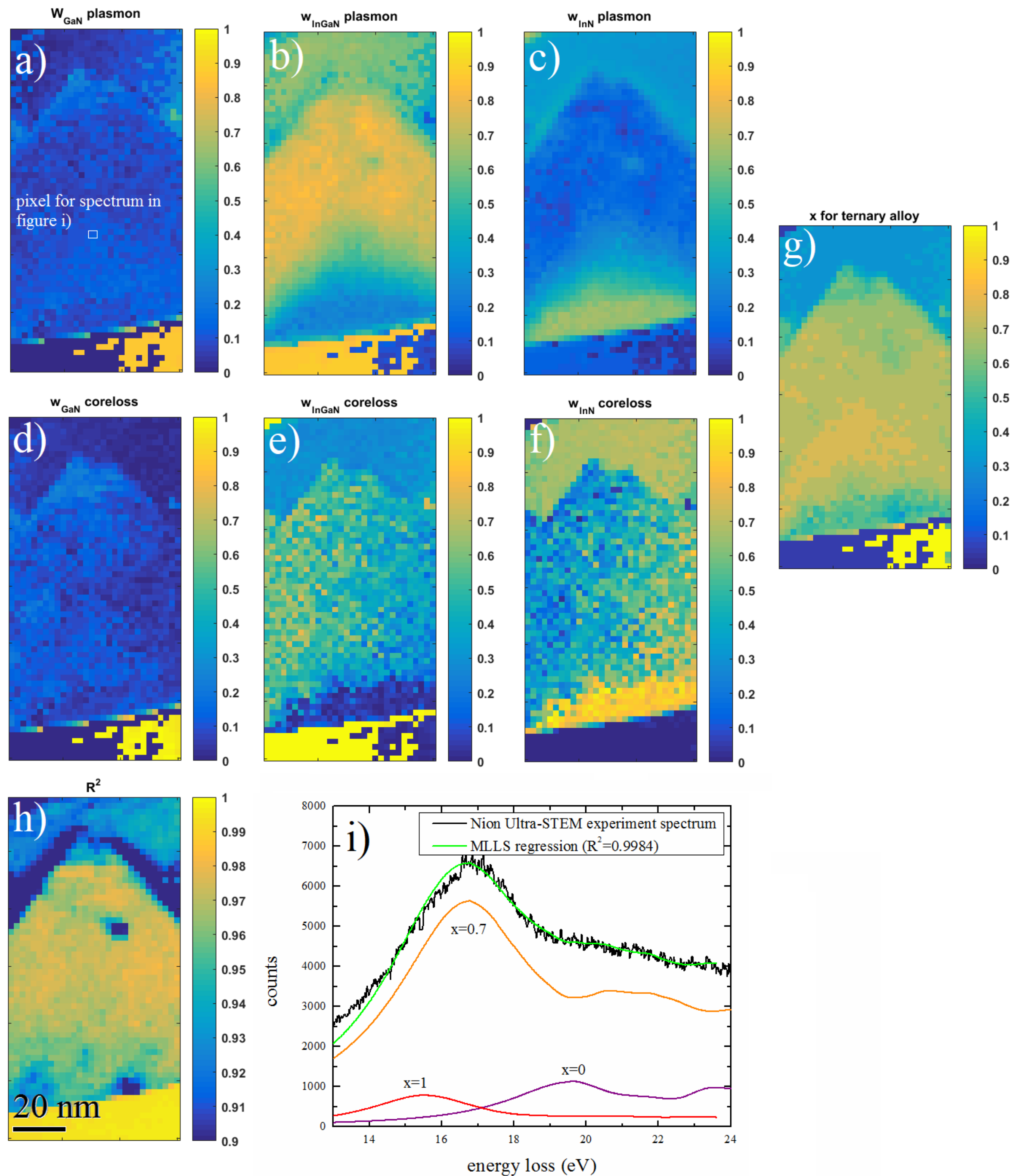

Figure 86 results from fitting each spectrum from the spectrum image in Figure 78 b) by a linear superposition of GaN, InGaN and InN reference spectra constructed from the spectrum image itself. a) weighting parameter calculated from GaN plasmon loss (W_{GaN} plasmon), b) W_{InGaN} plasmon, c) W_{InN} plasmon, d)) weighting parameter calculated from GaN core loss (W_{GaN} coreloss), e) W_{InGaN} coreloss, f) W_{InN} coreloss, g) the best fitting x value of the ternary component only, h) R^2 map, i) example of fitted spectrum extracted from white square in a).

All value of the weight maps in Figure 86 lie between 0 and 1 without applying any constraints, hence they are physically meaningful. The quantification results from plasmon and core losses are relatively consistent, both weight maps demonstrating a high degree of phase separation underneath the island, where most of the InGaN is phase separated into InN and GaN. The result is in a good agreement with the observation in chapter 5.1. The R^2 map indicates most of the region in the InGaN thin film and GaN buffer layer can be properly analysed by our MLLS regression method, all regions show $R^2>0.9$ and most have $R^2>0.98$. One pronounced spot with $R^2<0.9$ value is observed in Figure 86 h), which not observed in Figure 82 a), therefore, beam induced damage can probably be excluded. The main reason could be carbon contamination, which decreases the fitting quality.

The difference of the x maps from plasmon and core loss fitting is then shown in Figure 87.

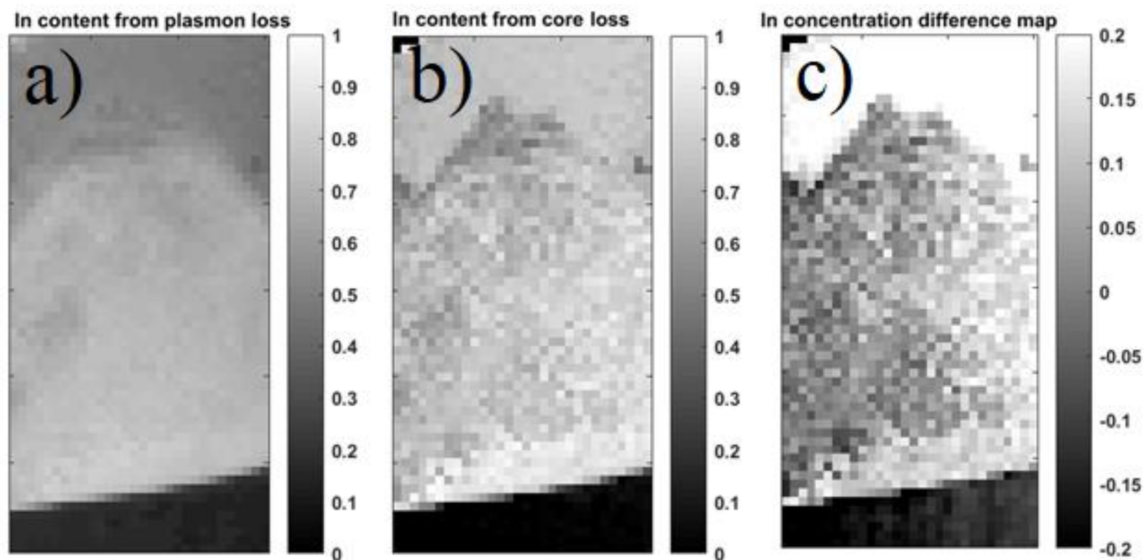

Figure 87 maps of indium content, x, calculated for data from Figure 86 from weights of fitting a) plasmon losses, b) low core-losses, c) difference map [c)=b) - a)].

As shown in Figure 87 a) and b), the map from core-loss has higher contrast of a high noise levels. The plasmon map appears smoother but lower in overall contrast. Both quantification indicate In rich area located within the first 15 nm of InGaN grown on the GaN buffer, the core-loss fitting indicates almost pure InN (x~0.9), while the plasmon loss fitting suggests an In concentration maximum of around x~0.8.

The inconsistent quantification result can be attributed to two reasons. Firstly, as the increment of InGaN modelled spectra is Δx=0.05, the expected error at energy single pixel in the spectrum image will be ±0.05 for In concentration quantification. The Δx map in Figure 87 c) has a mean value of Δx=0.11±0.06 which somewhat larger. Secondly, as demonstrated in Figure 86 i), only the first Ga 3d core loss edge from GaN spectrum was observed, while for InN and InGaN presents both core loss edges have been fitted, therefore, the integral intensity of Ga 3d core loss is lower than it should be. It is thus clear W_{GaN} will be underestimated while W_{InN} will be overestimated.

Since plasmon loss and core loss are not located at the same energy, the spatial delocalization will differ and should be calculated to verify the reliability of both quantification methods. The delocalization of EELS is usually an issue for low loss EELS. As in chapter 2.3.8, for our experiment, the delocalization of plasmon loss and core-loss onset can be calculated as to d_{50} which presents the diameter that contains 50% of the intensity calculated from a Fourier transform of the finite momentum transfer based on mean scattering angles and finite collection aperture. To directly observe the transition between the GaN buffer layer to the InGaN thin film, a line scan from GaN to InGaN region was applied to the weight maps in Figure 86. The line scan position and extracted weight values for each binary alloy component are shown in Figure 88. The extracted data is fitted with a simple model which estimates the transition width for 20% to 80%.

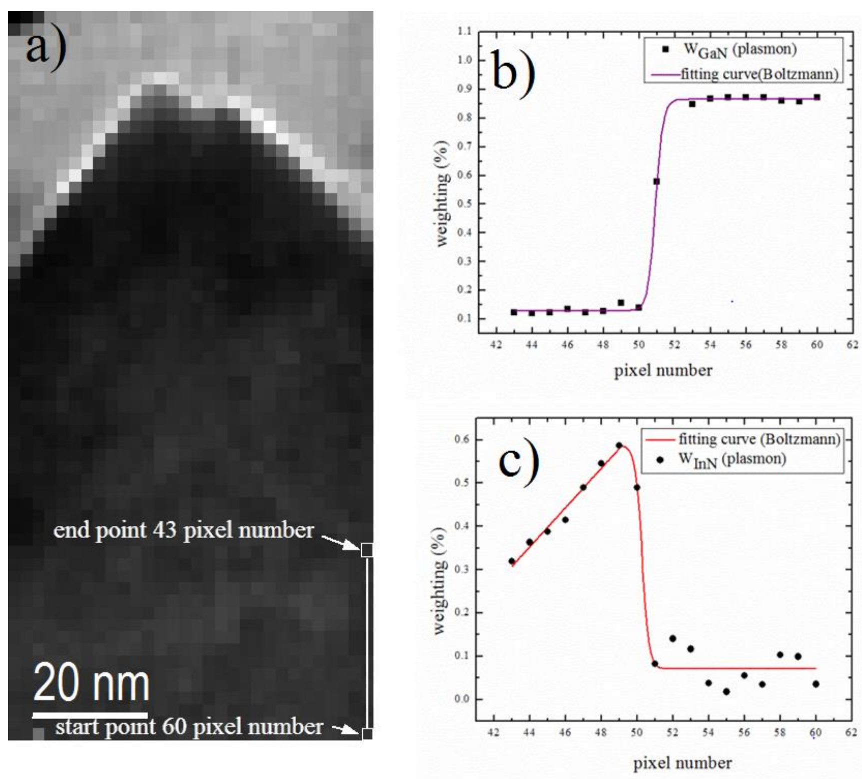

Figure 88 a) spectrum image with line width indications region for profile extraction, b) plots of the weight parameters from the least-squares fitting for the GaN plasmon and c) plots of the weight parameters from the least-squares fitting for the InN plasmon,

The fitted data directly indicate the plasmon losses of GaN and InN may be regarded as local within the sampling limit of a few nanometres (here: 1-2 pixels, i.e. 2-4nm), while the core-loss is local within 1 pixel. The result indicates the quantification from core-loss is somewhat slightly more localized than quantification from plasmon loss.

Compared with the quantification result from JEOL 2010F in chapter 5.1, the NION UltraSTEM 100 provides higher quality EEL spectra, and the mean value of the difference x map from plasmon and core loss decreases from Δx=0.15 (JEOL 2010F) to Δx=0.11 (NION Ultra STEM 100), which indicates that a more consistent quantification can be obtained by monochromation and low-kV operation. To further improve the quantification reliability and accuracy, the reference InN, GaN and InGaN spectra should be recorded at slightly lower

dispersion, eg: 0.02eV/channel so that the energy level of the Ga 3d M_4 edge can also be included in the quantification.

By reducing the channel dispersion to 0.05eV/channel and the sampling size to 5 nm/pixel where delocalization is not a problem, fast acquisition was used to further reduce the electron beam damage to the sample, then the MLLS fitting approach was applied to the spectrum image, and results for NION UltraSTEM 100 are shown in Figure 89.

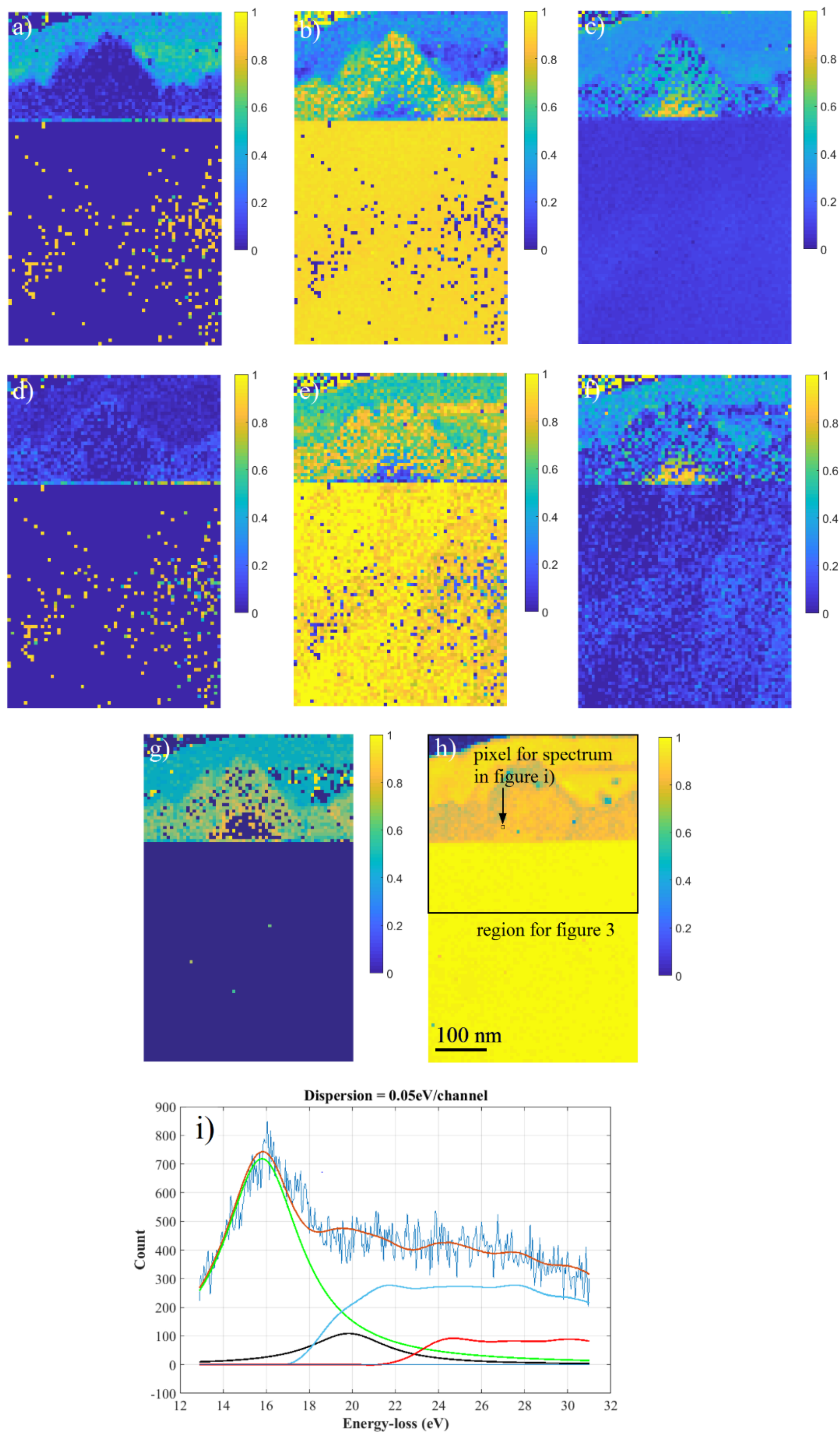

Figure 89 results from fitting each spectrum from the spectrum image in Figure 78 by a linear superposition of GaN, InGaN and InN reference spectra constructed from spectrum image itself a) weight parameter for GaN calculated from plasmon loss (W_{GaN} plasmon), b) W_{InGaN} plasmon,

c) W_{InN} plasmon, d)) weight parameter for GaN calculated from core loss (W_{GaN} core loss), e) W_{InGaN} core loss, f) W_{InN} core loss, g) x map calculated from plasmon loss, h) x map calculated from coreloss, i) difference map g)-h), j) the best fitting x value of the ternary component only, k) R^2 map, l) fitted spectrum extracted from black square in Figure k).

As shown in Figure 89, the weight maps from plasmon and core loss for each component are more consistent compared with Figure 86, and the difference map given a mean value of Δx=0.024, which indicates a consistent quantification result from plasmon and core loss. The high In content region with x>0.8 in both x maps correlates well with the EDXS quantification result in chapter 3. Since the spectrum image has been recorded under fast scanning, the increased noise level slightly decreases the fitting quality compared with Figure 86 h), however, most of the pixels are having $R^2 > 0.8$. The degree of phase separation maps can be then obtained from the GaN and InN weight maps, the result being shown in Figure 90.

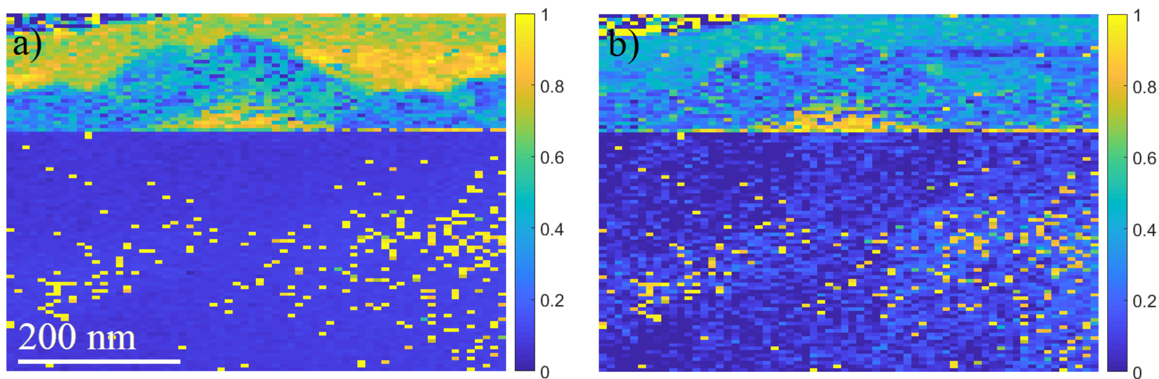

Figure 90 phase separation maps for the region shown in Figure 89 a) calculated from plasmon loss, b) calculated from core loss.

From Figure 90, the mean difference in phase separation calculated from plasmon loss and low core losses is ΔW=0.03, which indicates a consistent. Therefore, from EELS, the strong phase separation near the bottom of the large island with x>0.8 can be explained by a large fraction of InN rather than high In content InGaN ternary alloy or even metallic In in case of beam

damage; whereas close to the top of the island, the region is mainly formed by a perfect InGaN ternary alloy with x~0.5. This is somewhat unexpected because phase diagrams would predict the strongest driving force for phase separation to occur near x=0.5, where we observed a random alloy.

5.3 bandgap determination from STEM mode

Bandgap is an important parameter in semiconductor science it is usually determined by Tauc plots from optical absorption spectroscopy [30, 31, 32], the Tauc plot is known as $(\alpha hv)^{1/n}$ plot as a function of $\beta(hv-E_g)$ [33], where the α is the absorption coefficient, hv is the incident photon energy, and E_g is the bandgap, n=2 can be selected For most direct bandgap semiconductors, β can be obtained by linear fitting the experimental curve. The bandgap can be then determination by extracting the E_g at $(\alpha hv)^{1/2}=0$ [33]. However, the absolute value of E_g is strongly depending on the fitting range of the spectrum. Previously, a lot of studies indicated the bandgap could be measured by high quality valence EELS data. In this chapter, we try to extract the bandgap value from high quality EELS spectrum images.

The InGaN bandgap varies from 0.7eV (InN) to 3.4eV (GaN) [34]. In conventional TEM, the EELS energy resolution of 0.8~ 0.9eV is no longer sufficient to measure the bandgap of high In content InGaN. Therefore, an aberration corrected (S)TEM with a monochromator is needed.

The valence EELS spectrum image was recorded under the same conditions as in chapter 5.2. The recorded valence EELS spectra image is depicted in Figure 91

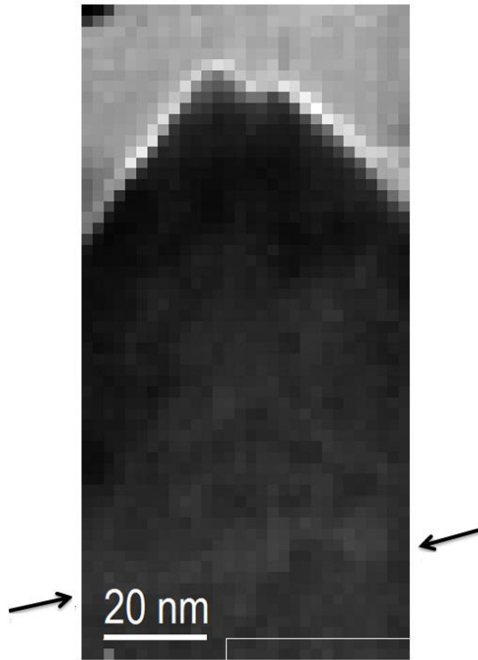

Figure 91 spectrum image and integral region for GaN spectrum research (white square near bottom corner), the arrows indicate the InGaN/GaN interface.

Before applying the bandgap fit to the spectrum image, several spectra in GaN are integrated to decrease the signal-noise ratio and the determination of the known GaN bandgap can serve as a calibration point for InGaN bandgap extraction. To avoid any contribution from InGaN influencing the GaN bandgap determination, the EELS region for extraction of the spectrum should be several 10 nm away from the interface (Figure 91 white square).

The reference GaN spectrum can be constructed by simply integrating all extracted EELS spectra from each pixel within the white rectangle in Figure 91. The GaN reference spectrum is shown in Figure 92.

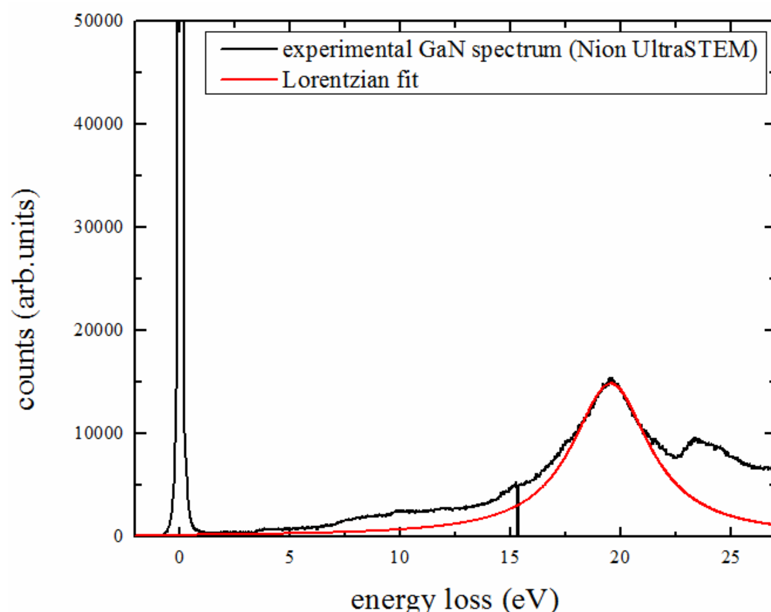

Figure 92 GaN reference spectrum (black) and plasmon loss fit (red).

As illustrated in chapter 2.3.4. The zero-loss peak tail of a field emission TEM can be modelled by the Fowler-Nordheim distribution, where the intensity decreases exponentially as the energy loss increases. Here we applied an exponential decay function to simulate the tail of the zero loss. The fitting window for the zero-loss model is operated from 0.2eV to 0.6eV to make sure the fitted zero loss tail is not interfering with possible InN band edge onset [34]. The R^2 parameter (R^2=0.994) demonstrates a reasonable model for zero-loss tail.

As illustrated in chapter 4.1, the plasmon loss energy can be fitted with a Lorentz function, the tail of which will approximate but never reach 0 level if the energy axis is >0. Therefore, the plasmon loss tail will also contribute to intensity at the band edge onset. By subtracting the plasmon loss fit, the plasmon and its subsequently core-loss edge can be modelled, which will be explained in detail in chapter 4. The modelled zero-loss tail and plasmon energy loss tail in the energy range of 0eV to 10eV of the raw spectrum are plotted in Figure 93.

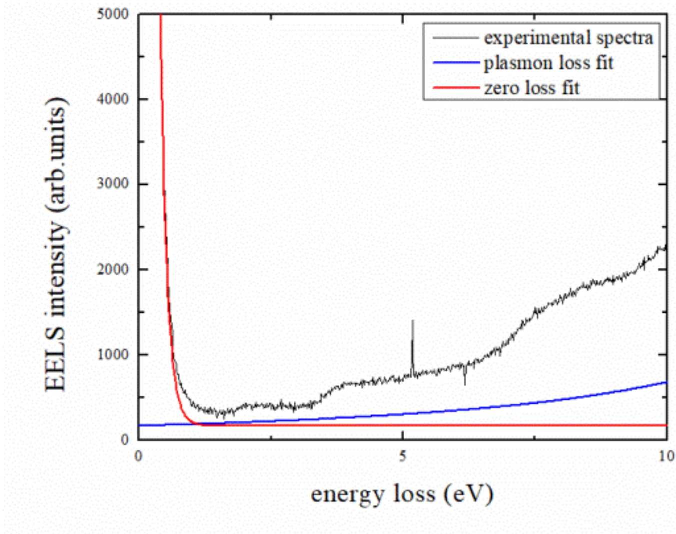

Figure 93 Valence EELS of GaN with extrapolations of zero loss and plasmon loss tails

The zero-loss tail and plasmon loss tail should be subtracted from the raw spectrum to get the bandgap onset. After the background subtraction, the intensity in the energy range from before the band edge onset is shown in Figure 94.

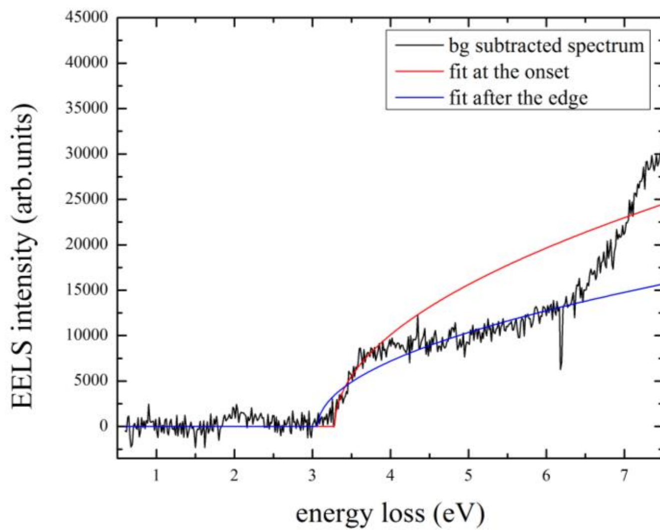

Figure 94 square-root fits to onset of spectrum intensity after zero loss and plasmon loss subtraction (red line for fitting interval 2.85-3.98eV, blue line for fitting interval 2.85-6.41eV).

The fitting of VEELS after elimination of zlp and plasmon peak, ignoring intraband scattering; Cerenkov effects and surface plasmons, can be assumed to follow the density of state (DOS) [35, 36]. As demonstrated in Figure 94, the intensity before the bandgap edge onset is close 0, which indicates a satisfactory background subtraction of zlp and plasmon loss tail, no further off-set intensity needs to be corrected before fitted the bandgap edge with square-root function. However, the spectrum after background subtraction in Figure 94 does not follow an ideal behaviour expected for the DOS of a bulk semiconductor ($\propto\sqrt{(E-E_g)}$). As shown in Figure 94, the intensity increases drastically at the onset, then the intensity flattens before a second rise at much higher energy. To precisely determine the band onset, two fitting windows has been applied to fit a square root function to the processed spectrum. The first window was set at the energy interval 2.85~3.98eV which covers the initial region of intensity increase. The second window covers the energy range from 2.85-6.41 eV, which covers the whole flatten intensity area. The fitted curves are also shown in Figure 94.

The fitting quality is illustrated by R^2, for the first fit window, R^2= 0.8933, and the apparent onset of the band edge is at E_g=3.38 eV, which is a reasonable result for GaN bandgap (3.4~3.5 eV) [34, 37, 38]. For the second fit window, the R^2 decrease to 0.786 and gives a band edge onset of 3.26eV, which is a slightly lower value. The result indicates the extracted bandgap value is strongly depending on the fit window selection, the realistic bandgap value remains question if different bandgap value obtained from different fitting interval. Therefore, the band edge onset is hard to determine even for a high quality VEELS spectrum.

As Erni [39] showed, Cerenkov radiation can be limited by an accelerating voltage below 40 kV. In addition, M Stoger-Pollach [40] showed the Cerenkov losses joint with surface plasmon effects can limited the bandgap measurement accuracy. Therefore, our bandgap measurement at 60 kV accelerating voltage is perhaps not sufficient to accurately measure the absolute

bandgaps. From relativistic factor formula [41], the electron velocity is calculated as 1.29×10^8 m/s for 60 kV. The light speed in GaN can be estimated as 1.25×10^8 m/s from equation (27) in chapter 2.3.6. As the electron speed is faster than light, Cerenkov radiation cannot be neglected for 60 kV acceleration voltage. Therefore, to eliminate the Cerenkov effect in VEELS, the ideal (S)TEM operation voltage should less than 56 kV.

Due to the more realistic bandgap value from smaller fit window, the first window fit seems a reasonable method to determine the band edge onset in GaN a

nd should also work for InGaN with reduced bandgap. As the R^2 will decrease for an increasing fitting window interval, for an unknown band edge onset, I decided the fit energy window range will remain at 0.5eV and its possible be swept in energy range from 0.7eV to 3.5eV with 0.15eV per step size to find the best R^2 value and the corresponding band edge onset. The result of bandgap and corresponding R^2 maps are shown in Figure 95.

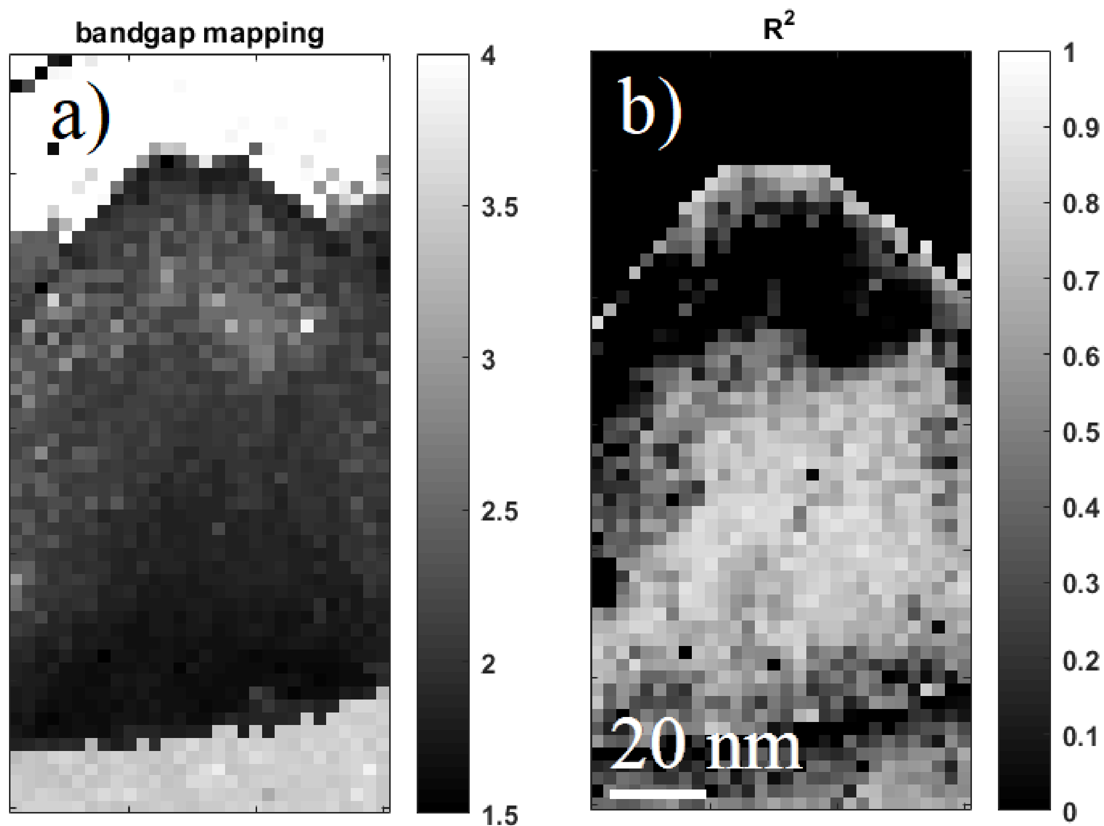

Figure 95 a) extracted direct E_g (in eV) bandgap map, b) R^2 map

As shown in Figure 95 b), the R^2 map demonstrates a reasonable fitting result for most of the region, however, the GaN near the InGaN/GaN interface and the InGaN on the top of the island are showing a somewhat poor fit. The reliability of the bandgap measured in those areas will be questionable and probably depend on the delocalization of the VEELS spectrum.

Following the delocalization calculation approach in chapter 5.2, here, we have used the spectra extracted from Figure 88 to calculate the delocalization, and the spectra for pixel numbers from 50~58 are shown in Figure 96.

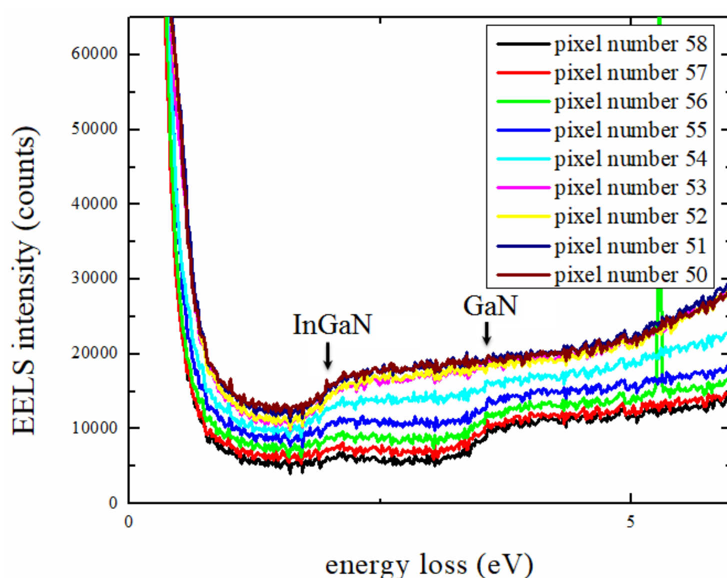

Figure 96 evolutions of VEELS spectra from GaN buffer region to InGaN thin film shown line in Figure 88.

As demonstrated in Figure 96, the band edge onset evolves from GaN to InGaN, where at the InGaN/GaN interface, a clear superposition of two band edges is observed. The GaN and InGaN bandgap are fitted with two square root functions superimposed. The weight parameter for GaN is presented in Figure 97. The transition width is estimated as 20%-80%, and the theoretical d_{50} curve is also simulated and presented in Figure 97.

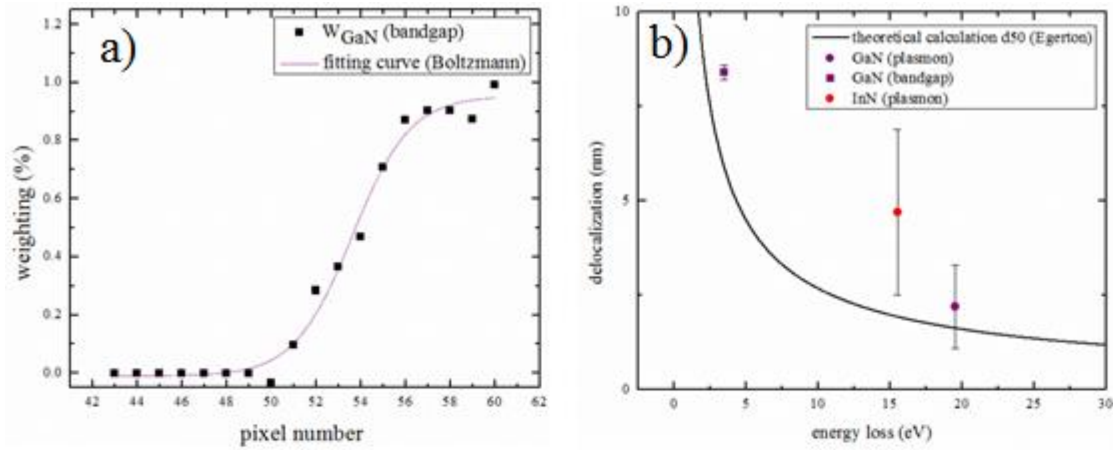

Figure 97 a) the weight of GaN band edge across the GaN/InGaN interface, as function of the pixel number in the growth direction. b) compares the estimated 20% → 80% transition widths of the three signals with a simple model calculation for the delocalization of the inelastic scattering event due to finite momentum transfer [41].

As observed in Figure 97, at each probed position, in principle, for the measured GaN band edge at 3.38eV, the bandgap information at this energy will leak about 8.4 nm. While for InGaN ternary alloy with a bandgap of ~1.7eV, the bandgap information will leak around 15 nm in EELS, which will contribute to the GaN spectra taken 15 nm away from the InGaN/GaN interface. The measured delocalization width is following the trend of theoretical delocalization simulation. If phase separation was observed near the InGaN/GaN interface, the bandgap of 0.7eV for pure InN will make delocalization even worse extending to over 20 nm. At the high In content region underneath the island we expected an E_g of the order of 1eV, where our measurement indicates 1.2eV, This may be tentatively explained by an apparent superposition of bandgaps from GaN and $In_{0.8}Ga_{0.2}N$ in EELS from the vicinity of the InGaN/GaN interface if the bandgaps of both materials (and in particular the lower bandgap) are noticeably delocalized. Take a close look at the Figure 96, a small kink located around 1.5eV can be

observed and indicating that the InGaN bandgap information leaks into the GaN region even several nm away.

The bandgap determination from VEELS remains difficult even with monochromated high quality VEELS. Due to the problem of fit window selection, a small fit interval can obtain a bandgap value similar to what would be expected from others measurement, however, a high fitting quality will be only obtained for small energy range. If a large fit interval is selected, the extracted bandgap suggests a slightly lower value for GaN. Therefore, it is not possible to point out which value extracted from two different fitting windows will be more reliable.

Chapter conclusion

In this chapter, I have applied our phase separation analysis approach to EELS spectrum images collected from a conventional TEM and an aberration corrected monochromated (S)TEM system. Poor energy resolution in conventional TEM causes a problem in MLLS fitting. Therefore, to accurate quantify phase separation, the operating microscope should be equipped with an aberration corrector and monochromator, also low accelerating voltage is necessary to obtain high quality spectrum images without any electron beam damage. It is notable that at the high dispersion conditions, the detector size limits the recorded energy interval, and if the spectrum energy range is less than 30eV, a problem occurs since the GaN M_4 edge intensity is not fully included in the weight calculation, which leads to a systematically lower GaN fraction in the quantification. Decreasing the dispersion or increasing the size of detector are two possible solutions to deal with underestimating the GaN fraction. By decreasing the energy dispersion from 0.015eV to 0.05eV, the x value and degree of phase separation in each pixel can be evaluated consistently from both plasmon and core losses. The experimental indicates the formation of big island structures in our $In_{0.68}Ga_{0.32}N$ sample is mainly due to phase separation, which correlates well with STEM EDXS result. The high In content region (x~0.8)

underneath the island consists of InN and GaN binary alloys instead of high In content InGaN ternary alloy. Bandgap determination is also illustrated in this chapter, due to the large EELS delocalization, possible Cerenkov radiation and problems associate with the selection of fit window, the absolute band gap mapping with 2 nm resolution is currently not possible by using high quality valence EELS.

References

[1] D Holec, P M F J Costa, M J Kappers and C J Humphreys (2007), Critical thickness calculation for InGaN/GaN. *J. Cryst. Growth* **303** (1)**,** 314-317.

[2] C Tessarek, S Figge, T Aschenbrenner, S Bley, A Rosenauer, M Seyfried, J Kalden, K Sebald, J Gutowski and D Hommel (2011), Strong phase separation of strained InGaN layers due to spinodal and bimodal decomposition: formation of stable quantum dots. *Phys. Rev.* ***B*** **83,** 115316.

[3] M Leyer, J Stellmach, Ch Meissner, M Pristovsek and M Kneissl (2008), The critical thickness of InGaN on (0001) GaN. *J. Cryst. Growth* **310,** 4913-4915.

[4] H Ye, P F Lu, Z Y Yu, Z H Chen, B Y Jia, H Feng and Y M Liu (2010), Equilibrium critical thickness for a wurtzite InGaN/GaN heterostructure. *Superlattices & Microstructure* **48**, 58-64.

[5] M J Reed, N A EI-Masry, C A Parker, J C Roberts and S M Bedair (2000), Critical layer thickness determination of GaN/InGaN/GaN double heterostructures. *Appl. Phys. Lett* **77**, 4121.

[6] P M Coulon, S H Vajargah, A Bao, P R Edwards, E D L Boulbar, I Girgel, R W Martin, C J Humphreys, R A Oliver, D W E Allsopp and P A Shields (2017), Evolution of the m-plane quantum well morphology and composition within a GaN/InGaN core-shell structure. *Cryst. Growth& Des* **17**, 474-482.

[7] A Yamamoto, T Md Hasan, K Kodama, N Shigekawa and M Kuzuhara (2015), Growth temperature dependent critical thickness for phase separation in thick (~1□m) InGaN (x=0.24-0.4). *J. Cryst. Growth* **419,** 64-68.

[8] J Yang, D G Zhao, D S Jaing, P Chen, J J Zhu, Z S Liu, W Liu, F Liang, X Li, S T Liu, L Q Zhang and H Yang (2017), Increasing the indium incorporation efficiency during InGaN layer growth by suppressing the dissociation of NH_3. *Superlattices & Microstructure* **102**, 35-39.

[9] R Czernecki, S Kret, P Kempisty, E Grzanka, J Plesiewicz, G Targowski, S Grzanka, M Bilska, J Smalckoziorowska, S Krukowski, T Suski, P Perlin and M Leszczynski (2014), Influence of hydrogen and TMIn on indium incorporation in MOVPE growth of InGaN layers. *J. Cryst. Growth* **402,** 330-336.

[10] R Singh, D Doppalapudi, T D Moustakas and L T Romano (1997), phase separation in InGaN thick films and formation of InGaN/GaN double heterostructures in the entire alloy composition. Appl. Phys. Lett **70**, 1089.

[11] E Alves, S Pereira, M R Correia, E Pereira, A D Sequeira and N Fracnco (2002), Strain relaxation and compositional analysis of InGaN/GaN layers by Rutherford backscattering. Nuclear Instruments & Methods in Physics Research Section B: Interactions with Material and Atoms **190**, 560-564.

[12] S Pereira, M R Correia, E Pereira, K P O'Donnell, C Trager-Cowan, F Sweeney, E Alves, A D Sequeira, N Franco and I M Watson (2001), Depth resolved studies of Indium content and strain in InGaN layers. *Phys. Stat. Sol* ***B*** **228**, 59-64.

[13] M D McCluskey, L T Romano, B S Krusor, D P Bour, S Brennan and N M Johnson (1998), phase separation in InGaN/GaN multiple quantum wells. *Appl. Phys. Lett* **72**, 14.

[14] Y T Moon, D J Kim, K M Song, I H Lee, M S Yi, D Y Noh, C J Choi, T Y Seong and S J Park (1999), Optical and structural studies of phase separation in InGaN film grown by MOCVD. *Phys. Stat. Sol* ***B*** **216**, 167.

[15] A Eljarrat, L Lopez-Conesa, C Magen, N Garcia-Lepetit, Z Gacevic, E Calleja, F Peiro and S Estrade (2016), Quantitative parameters for the examination of InGaN QW nultilayers by low-loss EELS. *Phys. Chem. Chem. Phys* **18**, 23264-23276.

[16] M W Moseley, B Gunning, J Greenlee, J Lowder, G Namkoong and W A Doolittle (2012), Observation and control of the surface kinetics of InGaN for the elimination of phase separation. *J. Appl. Phys* **112**, 014909.

[17] H Woo, H Jo, J Kim, S Cho, Y Jo, C H Roh, J H Lee, Y Seo, J Park, H Kim, C K Hahn and H Im (2017), Phase separation suppression in InGaN on a Si substrate using an indium modulation technique. *Current. Appl. Phys* **17** (8), 1142-1147.

[18] D Doppalapudi, S N Basu, K F Ludwig Jr and T D Moustakas (1998), phase separation and ordering in InGaN alloys grown by molecular beam epitaxy. *J. Appl. Phys* **84** (3), 1389.

[19] M Krysko and M Leszczynski (2007), quantification of In clustering in InGaN/GaN multi-quantum-wells by analysis of X-ray diffraction data. *Appl. Phys. Lett* **91**, 061915.

[20] M Muller, G D W smith, B Gault, C R M Grovenor (2012), Phase separation in thick InGaN layers-A quantitative nanoscale study by pulsed laser atom probe tomography. *Acta. Materialia* **60** (10), 4277-4285.

[21] Y Kanitani, S Tanaka, S Tomiya, T Ohkubo and K Hono (2016), Atom probe tomography of compositional fluctuation in GaInN layers. *Jpn. J. Appl. Phys* **55**, 05FM04.

[22] J R Riley, S Padalkar, Q M Li, P Lu, D D Koleske, J J Wierer, G T Wang and L J Lauhon (2013) Three-dimensional mapping of quantum wells in a GaN/InGaN core-shell nanowire light-emitting diode array. *Nano. Lett* **13** (9), 4317-4325.

[23] O L Krivanek, J P Ursin, N J Bacon, G J Corbin, N Dellby, P Hrncirik, M F Murfitt, C S Own and Z S Szylagyi (2009), High-energy-resolution monochromator for aberration-corrected scanning transmission electron microscope / electron energy-loss spectroscopy. *Phil. Trans. Roy. Soc. Lond. A* 367 (1903) 3683.

[24] T Walther, F Wolf, A Recnik and W Mader (2006), Quantitative microstructural and spectroscopic investigation of inversion domain boundaries in zinc oxide ceramics sintered with iron oxide. *Int. J. Mater. Res* **97**, 934.

[25] D Vlachos, M Kamaratos, S D Foulias, F Bondino, E Magnano and M Malvestuto (2010), Indium growth on reconstructed Si (111) $\sqrt{3}\times\sqrt{3}$ and 4×1 In surface. *J. Phys. Chem. C* **114**, 17693-17702.

[26] J Olivier (1980), low-energy electron losses by plasmon excitation as control means of the growth of epitaxial layers. *J. Appl. Phys* **51**(10), 5406.

[27] T M Smeeton, M J Kappers, J S Barnard, M E Vickers and C J Humphreys (2003), Electron-beam-induced strain within InGaN quantum wells: false indium 'cluster' detection in the transmission electron microscope. *Appl. Phys. Lett* **83** (26), 5419.

[28] J P O'Neill, I M Ross, A G Cullis, T Wang and P J Parbrook (2003), Electron-beam-induced segregation in InGaN/GaN multiple-quantum wells. *Appl. Phys. Lett* **83** (10), 1965.

[29] S J Pearton (2000), GaN and related materials II, Gordon & Breach science Publisher, Australia, 2nd ed.

[30] Y Feng, S Lin, S Huang, S Shrestha and G Conibeer (2015), Can Tauc plot extrapolation be used for direct-band-gap semiconductor nanocrystal?, *J. Appl. Phys* **117**, 125701.

[31] D Jain, O Mangla and S Roy (2016), Wide band gap gallium arsenide nanoparticle fabricated using plasma method. *AIP conference Proceeding* **1731**, 050143.

[32] A S Hassanien and A A Akl (2015), Influence of somposition on optical and dispersion parameters of thermally evaporated non-crystalline $Cd_{50}S_{50-x}Se_x$ thin films. *Journal of Alloy and compounds* **648**, 280-290.

[33] J Tauc (1974), Amorphous and liquid semiconductors, Plenum press, New York.

[34] G Orsal, Y El Gmili, N Fressengeas, J Streque, R Djerboub, T Moudakir, D Sundaram, A Ougazzaden and J P Salvestrini (2014), Bandgap energy bowing parameter of strained and relaxed InGaN layers. *Opt. Mater. Express* **4**(5), 1030.

[35] D Keller, S Buecheler, P Reinhard, F Pianezzi, D Pohl, A Surrey, B Rellinghaus, R Erni and A N Tiwari (2014), Local band gap measurement by VEELS of thin film solar cells. *Microsc & Microanal* **20**, 1246-1253.

[36] S Schamm and G Zanchi (2003), Study of the dielectric properties near the band gap by VEELS: gap measurement in bulk materials. *Ultramicrosc* **96**, 559-564.

[37] J F Muth, J H Lee, I K Shmagin, R M Kolbas, H C Casey, B P Keller, U K Mishra and S P Denbaars (1997), Absorption coefficient energy gap, exciton binding energy, and recombination lifetime of GaN obtained from transmission measurements. Appl. Phys. Lett 71(18), 2572.

[38] M D McCluskey, C G Van de Walle, C P Master, L T Romano and N M Johnson (1998), Large band gap bowing of InGaN alloys. *Appl. Phys. Lett* **72**(21), 2725.

[39] R Erni (2016), On the validity of the Cerenkov limit as a criterion for precise band gap measurement by VEELS. *Ultramicros* **160**, 80-83.

[40] M Stoger-Pollach, H Franco, P Schattschneider, S Lazar, B Schaffer, W Grogger and H W Zandbergen (2006), Cerenkov losses: A limit for bandgap determination and Kramers-Kronig analysis. *Micron* **37**, 396-402.

[41] R F Egerton (2nd ed 1996), Electron Energy-loss Spectroscopy in the Electron Microscope. Plenum Press, New York.

Chapter 6

6. Quantification of In and Al concentration in InGaN/ AlGaN quantum wells in GaN nanowires

For the established methods of X-ray absorption correction in analytical transmission electron microscopy (TEM) estimates of specimen thickness and density (Cliff & Lorimer 1975 [1]), mass-thickness (August & Wernisch 1987 [2]) or probe current (Watanabe et al. 1996 [3]) are needed. We recently developed a self-consistent absorption correction method based on effective sensitivity factors (denoted as *k**-factors) based on Monte Carlo simulations and K/L intensity ratios of at least one heavier element directly measured from the spectrum to be quantified [4]. If maps have very low counts they are susceptible to shot noise and the background cannot be estimated from an integer valued map because it will be below a single count on average. In our case of InGaN and AlGaN layers in GaN nanowires forming radial quantum discs, the Ga L, Al K and In L X-ray lines will be strongly absorbed before they reach the detector, resulting in elemental maps with typically fewer than ten counts per pixel and hence subject to heavy shot noise. For our absorption correction we need the Ga K/L ratio at each pixel in the map, which will itself be not only even noisier but also suffer from quantisation effects as X-rays are detected as individual X-rays hitting the detector, so all elemental maps will have lots of zero, single and double counts. In our case these low counts are due to the low detector efficiency (with a collection solid angle of only 0.12srad, which can be increased to 1-2srad in more modern set-ups with optimised silicon drift detectors [5]), however, it will remain principal issue in any experiments conducted with low beam current or short exposure times as needed for beam sensitive materials or for capturing nanoparticles moving on surfaces refer to Au/TiO_2 work so we thought it worth reporting our work-around to the problem in this case.

i) We have acquired maps from X-ray lines by integrating the intensities over certain energy windows both, centred on the actual X-ray lines of interest as well as centred around the (hypothetical) lines of elements not actually present in the specimen, such as S K-line and Ti L-line for InGaN, from the local averaging of which we can estimate the background for the lines of interest by linear interpolation. (In L) or extrapolation (Al K below S K, Ga K above)

ii) Outside the (Al, Ga, In)N nanowires all relevant line intensities in a map of characteristic X-ray lines should vanish: outside the InGaN quantum well the In signal and outside the AlGaN layer the Al signal should vanish, i.e. yield an average of zero. If this is not the case outside a few nanometres of the nanowire where electron beam broadening may occur, fluorescence from stray X-rays due to the supporting carbon film and/or copper grid will be responsible for this, and this background is to be evaluated and subtracted.

Several groups used quantification of the In concentration of InGaN quantum wells in GaN nanowire by using the Cliff-Lorimer method [6, 7]. Tan et al. [8] demonstrated that the apparent elemental distribution in InGaAs nanowires using EDXS elemental mapping is strongly dependent on sample geometry so they could not quantify the In distribution fully. Johannes et al evaluated the composition of GaAs embedded in a silicon nanowire by using energy dispersive X-ray fluorescence (XRF) [9], neglecting X-ray absorption effect in a ~190 nm thick nanowire where the absorption effect for soft X-ray lines (Ga L or As L) should not be neglected. Bender et al [10] investigated X-ray absorption for quantifying the Ge distribution in a $Si_{0.75}Ge_{0.25}$ nanorod using 4 silicon drift detectors that different in orientation with the nanowire axis, however, the results from the quantification of Ge K and Ge L lines were not consistent, which indicated the absorption correction applied to the various detectors did not match their model. Lari et al. [11] showed a quantification of the aluminium content of AlGaN

nanowires by using k-factors calculated from EDAX software, however, they have used the thin film approximation. As the nanowires in our case have hexagonal structure, a thin film model is not applicable, and absolute measurement of X-ray absorption lengths are difficult. This clearly demonstrates that reliable absorption correction method is needed to obtain quantitative chemical information from nanowires.

6.1 Monte Carlo simulation of AlGaN k* factor as function of Ga K/L ratio

In order to apply our absorption correction method to quantify the Al concentration in AlGaN ternary alloy, the absorption corrected k* factor for Al K line have been simulated by Monte Carlo simulation.

The CASINO software is used to simulate the AlGaN k* factor as a function of thickness, and is then plotted versus Ga K/L ratio as illustrated in chapter 3.1. The x_{Al} for AlGaN ternary alloy ranges from 0 to 0.9, the simulation thickness ranges from 10-2000 nm. The accelerating voltage is 200 kV with a 25° nominal take-off angle of the X-ray detector. The $Al_xGa_{1-x}N$ density for simulation is estimated by $\rho_{Al_xGa_{1-x}N}=x*\rho_{AlN}+(1-x)*\rho_{GaN}$, where wurtzite AlN and GaN density can be obtained as 3.28g/cm^3 [12] and 6.15g/cm^3 [12], respectively.

To calculate the k* factor for Al, equation (37) in chapter 3.1 needs to be rewritten as

$$\begin{cases} k^*_{\text{AlK, GaL}} = x_{Al}\, I_{\text{GaL}} A_{\text{Al}}/[(1-x_{Al})\, I_{\text{AlK}} A_{\text{Ga}} \\ k^*_{\text{AlK, GaK}} = x_{Al}\, I_{\text{GaK}} A_{\text{Al}}/[(1-x_{Al})\, I_{\text{AlK}} A_{\text{Ga}} \end{cases} \quad (45)$$

By extrapolating the simulated X-ray intensity for Al K, Ga K and Ga L, the $k^*_{\text{Al K, Ga K}}$ and $k^*_{\text{Al K, Ga L}}$ dependence on Ga K/L ratio is shown in Figure 98.

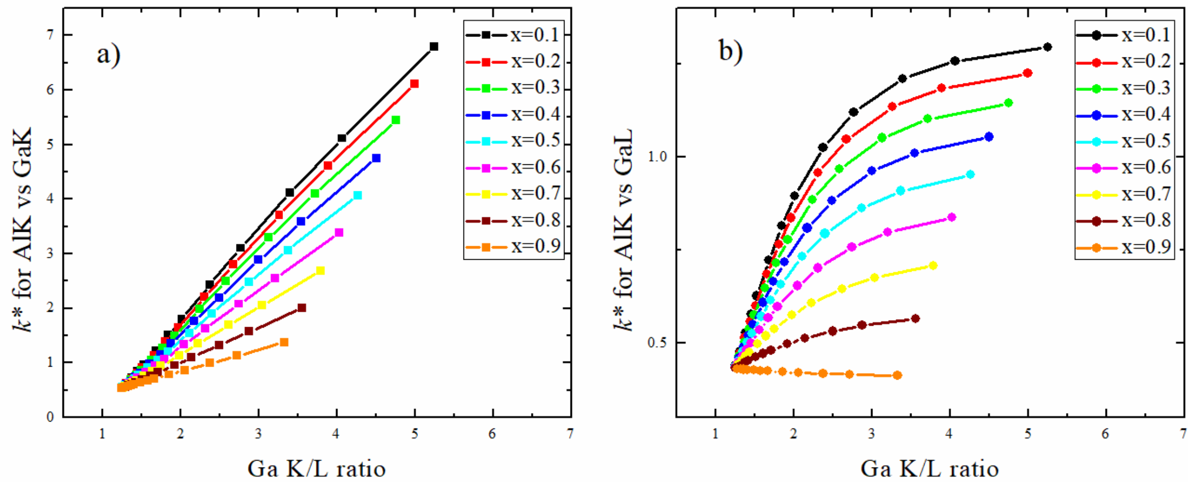

Figure 98 CASINO simulations of a) $k^*_{AlK,GaK}$ and b) $k^*_{AlK,GaL}$ with different x value of $Al_xGa_{1-x}N$

Unlike the k^* factors calculated for InGaN ternary alloys, both k^* factors for AlGaN tend to grow with increasing the thickness, except the $k^*_{AlK,GaL}$ for $Al_{0.9}Ga_{0.1}N$, $k^*_{AlK,GaK}$ shows an approximately linear relation with Ga K/L ratio similar to $k^*_{InL,GaK}$ for $In_xGa_{1-x}N$. Since the X-ray energy for Al K and Ga L lines are located at 1.48keV and 1.09 keV respectively, a similar absorption coefficient is expected for both Ga L and Al K lines, but the fluorescence from Al K onto Ga L is strong, resulting in a stronger Ga L X-ray intensity compared to Al K X-ray, which is responsible for the exponential growth of $k^*_{AlK,GaL}$.

The k^* factor algorithm for AlGaN can be then applied to AlGaN layers embedded in GaN nanowires to determine their Al concentration.

6.2 Comparison of nanowire and thin film absorption geometry

Before applying the k^* factor calculated from InGaN and AlGaN to quantify the In and Al content in $Al_yIn_xGa_{1-x-y}N$ nanowires, the absorption geometry of a nanowire compared with a thin film of same projected thickness should be studied. The X-ray paths in a thin film and a nanowire are sketched in Figure 99.

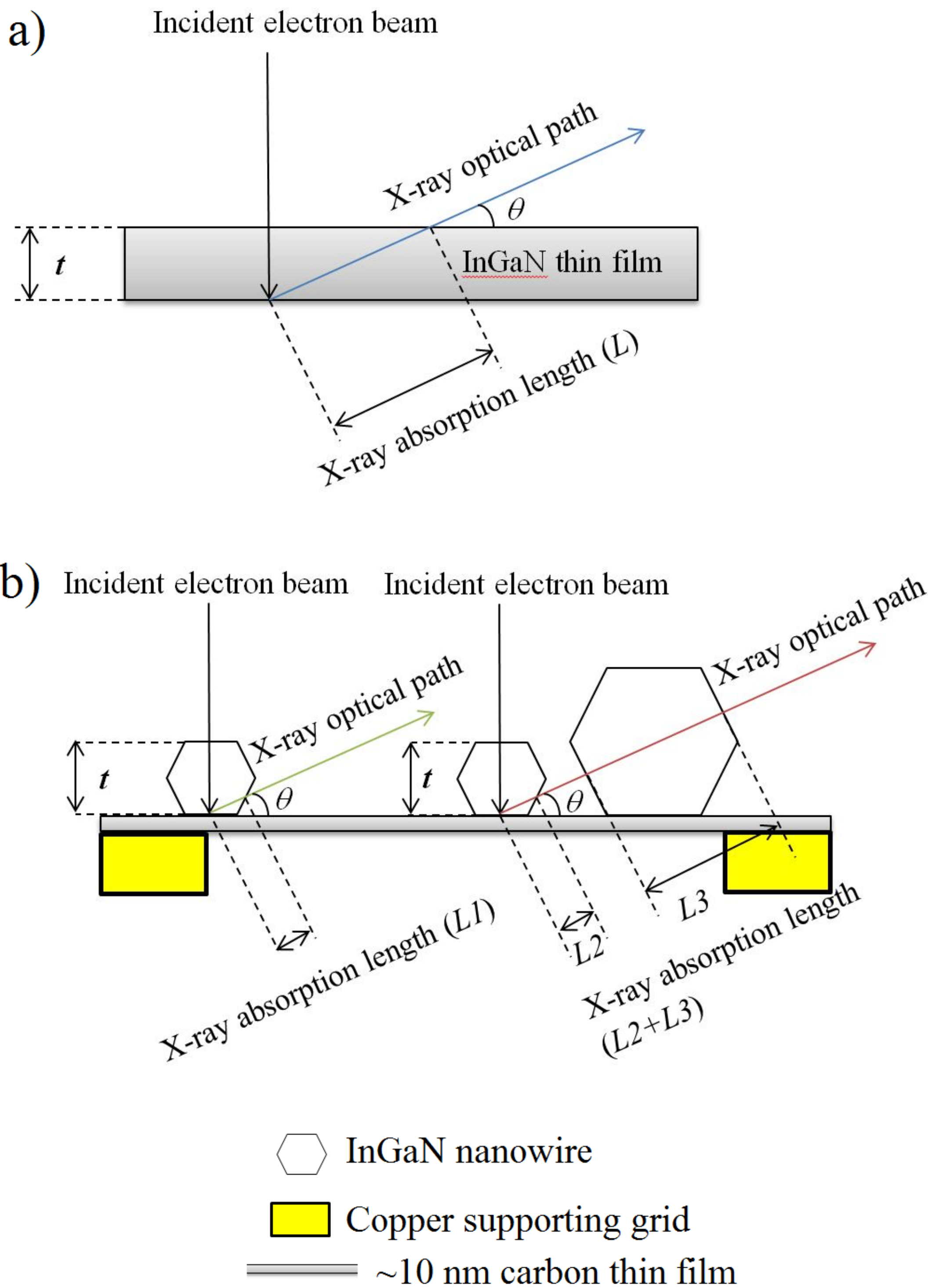

Figure 99 schematic of X-ray absorption lengths in a) thin film, b) single nanowire (left side) and thin nanowire shielded by thick nanowire (right side).

As observed in Figure 99, the X-ray absorption length L in a thin film (blue line) is obviously longer than the absorption length in a single nanowire (green line), therefore, the thin film

absorption correction estimated from sample thickness would be too strong for a nanowire. As our nanowire samples are cleaved and randomly distributed on a thin carbon film, if a bigger nanowire sits between the investigated nanowire and the X-ray detector, the X-ray will pass through the big nanowire which increases the X-ray absorption length. Overall, it is difficult to precisely quantify the In(Al) concentration from a nanowire with mass thickness correction.

To overcome the issues listed above, we have used the STEM EDXS mapping approach with small electron beam diameter, instead of using mass thickness correction method, we have applied our k^* factor absorption correction method from chapter 3.1, where the Ga K/L ratio depends only on the X-ray path length and X-ray take-off angle [13]. Therefore, our absorption correction method will also work for quantifying the In (Al) concentration in an $Al_yIn_xGa_{1-x-y}N$ nanowire.

6.3 quantification of In/Al concentration from low counts element maps in an $Al_yIn_xGa_{1-x-y}N$ nanowire

The studied nanowires were fabricated from a commercial sapphire wafer with GaN-based thin films employ blue light emitting diodes (LEDs) that nominally consist of the following layers, on a corundum (0001) substrate (from bottom to top): n-GaN buffer, InGaN/GaN superlattice, InGaN multiple quantum wells (MQWs), and p-GaN top contact. A 200 nm SiO_2 thin film was then deposited by plasma enhanced chemical vapour deposition (PECVD), followed by thermal evaporation of 10 nm nickel (Ni). The sample was then annealed at 820 ˚C in N_2 ambient for one minute, allowing the Ni thin film to transform into Ni islands. Then reactive ion etching was used to remove the free-standing SiO_2. The remaining SiO_2 nanorods with Ni on top were finally employed as a mask to etch down to the top of the n-GaN epilayer to fabricate the GaN-based nanowires using inductively coupled plasma etching.

The nanowires were harvested for transmission electron microscopy (TEM) by breaking and scraping them off the substrate using a scalpel and dispersing them onto a holey carbon foil supported by a 200 mesh copper grid.

EDXS elemental maps were recorded in a Schottky field-emission JEOL 2010F transmission electron microscope equipped with an Oxford Instruments Si:Li detector with ultrathin polymer window. A slightly increased emission gun current of 162 µA, a large spot size and a 40 µm condenser aperture were used in STEM, yielding ~ 9.5mrad semi-angle of convergence and an electron probe just under 1nm diameter with ~1nA beam current sufficient to excite X-rays. Three coarsely scanned elemental maps were recorded at nominal magnifications of 500kX with 128×100 pixels in size, yielding a real space sampling of 1.9nm/pixel.

X-ray mapping was undertaken for three GaN based nanowires of different thicknesses. Figure 100 shows overviews of the three nanowires acquired by tilting the specimen holder so the contrast of the InGaN layers and GaN region in the ADF image was maximal, which means the quantum wells appeared almost edge-on. The white rectangles in Figure 100 demonstrate the used regions for X-ray mapping.

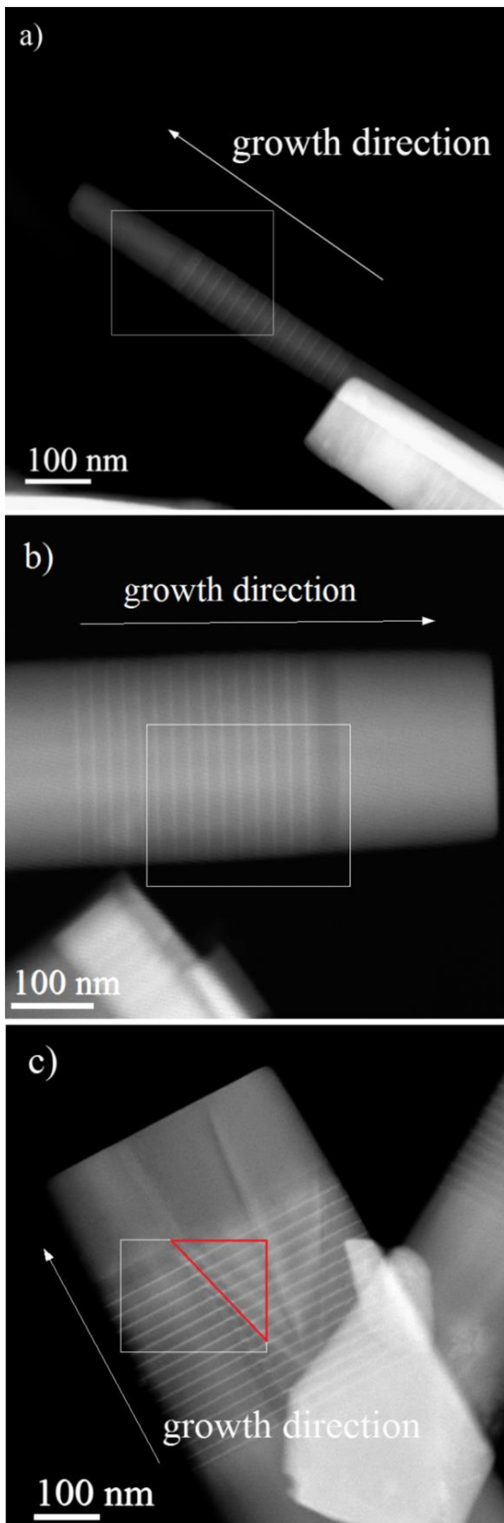

Figure 100: Annular dark-field (ADF) images (35-170mrad collection angle, 0.7 nm/pixel sampling) of three GaN nanowires with 15 embedded InGaN quantum wells and single AlGaN layers. Their projected widths are: a) 78 nm, b) 265 nm and c) 433 nm.

In each of the ADF images of Figure 100 we can clearly see a multiple quantum well (MWQ) structure of 15 bright layers (InGaN) and an additional ~30nm wide dark layer of unknown origin on top. No traces of any alleged superlattices could be found.

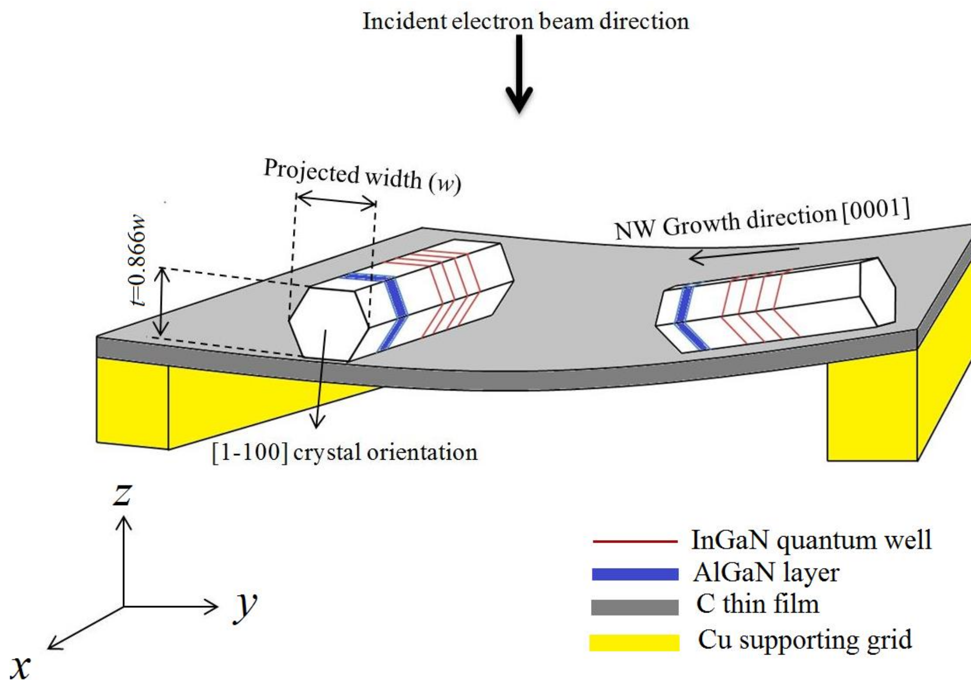

Figure 101 sketch of hexagonal nanowires resting on the support film.

From the nanowires resting inclined on the carbon support film as shown in Figure 101, a hexagonal cross-section can be inferred; and all nanowires imaged above lie on one their {1-100} side facets, the short top facets being ±{0001}hexagons. If the thin carbon support is not perfectly flat but sagging between the stronger and more rigid copper grid bars, then there are two distinct possibilities of arrangement for nanowires lying flat on the carbon film, as sketched in Figure 101. For a nanowire oriented so that [0001] remains in the (x, y) plane perpendicular to the electron beam direction (left side), the interface will remain edge-on; For a nanowire oriented so that [0001] is tilted out of the (x, y) plane (right side) the interfaces will no longer be edge-on and appear blurred in projection along the e-beam direction.

For both cases, the projected thickness t in the centre of the nanowire is directly given geometrically by $\frac{1}{2}\sqrt{3} \approx 0.866$ times their projected widths w. This yields the centred thicknesses of the three nanowires in Figure 100 and 3 of 66nm (a), 217nm (b), and 375nm (c). Weak thickness/strain contours running in the axial directions indicate the tops of the nanowires have remained intact during harvesting, without chipping off parts.

In annular dark field imaging regions thicker or richer in heavy elements such as indium appear brighter [13], while regions thinner or where lighter elements like aluminium are enriched appear darker. Hence, in Fig. 1 the multiple thin bright layers can tentatively be identified as InGaN, the thick darker layers as AlGaN. Between InGaN and AlGaN there is a region of presumably pure GaN. The sampling in the mapped regions is just sufficient to resolve the thin quantum wells, their thicknesses corresponding to 2-3 pixels only. .

Elemental maps of the X-ray signals including background for In_L, Al_K, Ga_K, Ga_L are shown in Figure 102. Also shown are maps of Cu_L and Ti_K as examples of elements not actually present in the sample but the lines of which can be used for background estimation.

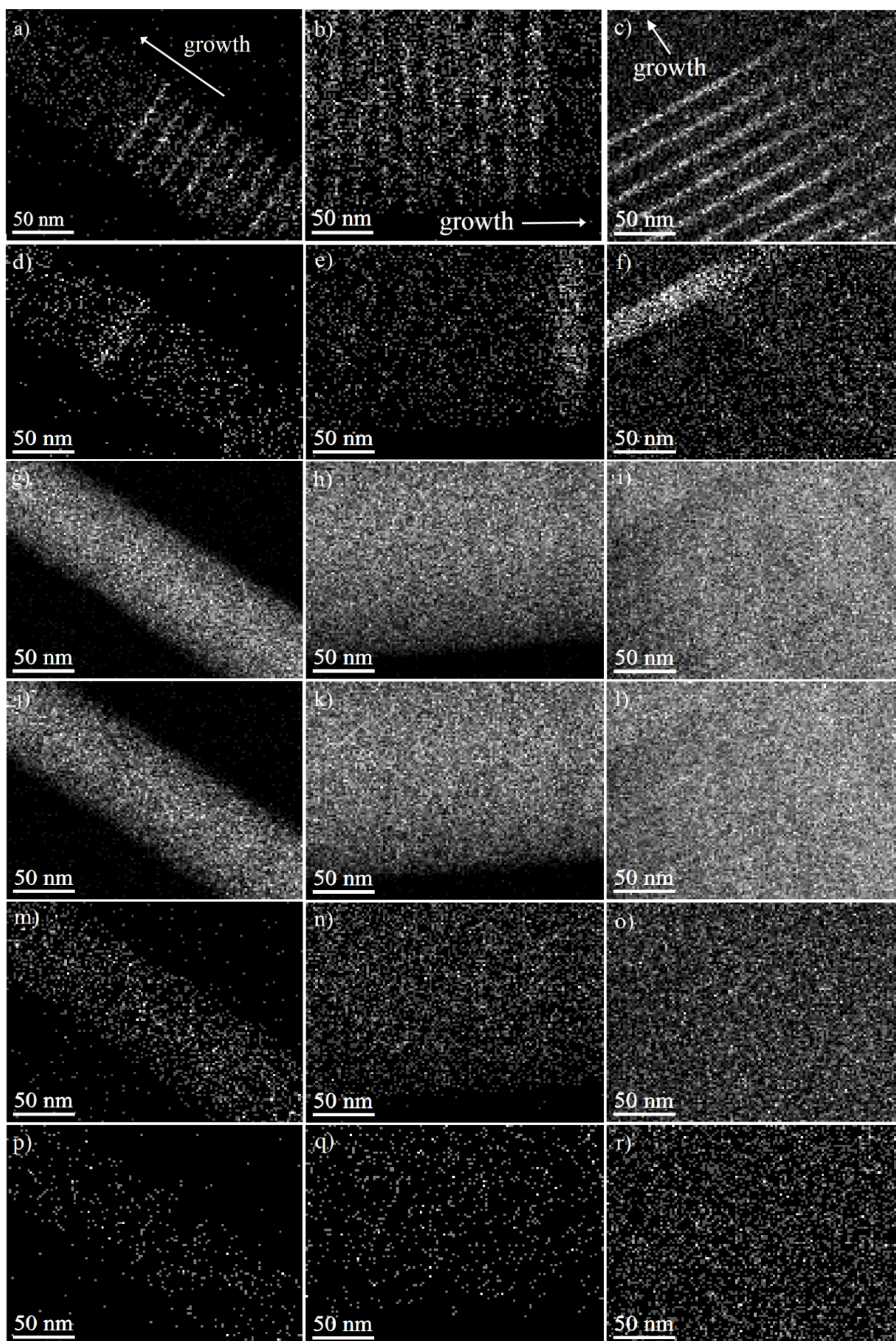

Figure 102: Groups of X-ray maps from nanowires: 66 nm thin (left column), 217 nm thick (middle column) and 375 nm thick nanowire (right column), top row: In_L (max_{66nm}=4 a), max_{217nm}=6 b), max_{375nm}=13 c)), second row: Al_K (max_{66nm}=2 d), max_{217nm}=5 e), max_{375nm}=7

f)), third row: Ga_K (max_{66nm}=17 g), max_{217nm}=18 h), max_{375nm}=42 i)), fourth row: Ga_L (max_{66nm}=14 j), max_{217nm}=16 k), max_{375nm}=35 l)), fifth row: Cu_L (max_{66nm}=3 m), max_{217nm}=5 n), max_{375nm}=9 o)), sixth row: Ti_K (max_{66nm}=2 p), max_{217nm}=3 q), max_{375nm}=5 r)). Min=0 for all maps.

For quantification, we first calculate the Ga K/L ratio for each nanowire and compare it to simulation for thin films [4]. The Ga K/L ratio from the raw maps for the 217 nm thin nanowire is only 1.125 which is smaller than the minimum of 1.24 predicted for only a few nanometres thin GaN specimen from Monte Carlo simulations [4,10]. This indicates the background to the Ga L line needs to be corrected as its subtraction would increase the measured Ga K/L ratio. For the Ga K-line background correction is far less relevant, as this line is more intense and has a much lower background. Four EDXS spectra were recorded from various locations of nanowire of different thicknesses for estimating the background contribution to the Ga L line, and are shown on a logarithmic scale in Figure 103a). The background can be fitted by a superposition of two exponential functions which model bremsstrahlung background and detector window efficiency, cf. Figure 103 b). The ISIS 300 software quantifies the line intensity by simply integrating the peak intensity over an energy interval a few channels wide (0.8275-1.0275 keV for CuL and 0.9875-1.2075 keV for Ga L). It is clear the Cu L and Ga L peaks overlap and part of the Cu L line contributes to the Ga L background. To evaluate the Cu L tail contribution to the Ga L intensity, the background is subtracted from the spectrum, and each characteristic line is fitted by a Gaussian function. In the four spectra shown in Figure 103a), each spectrum has a different Cu intensity, depending on the proximity to the copper support grid and the amount of stray X-rays generated. The ratio of fitted Ga L background to gross integrated Ga L intensity from ISIS turns out to be a linear function of the gross Cu L/Ga L ratio measured by ISIS by window summations, as shown in Figure 103 c).

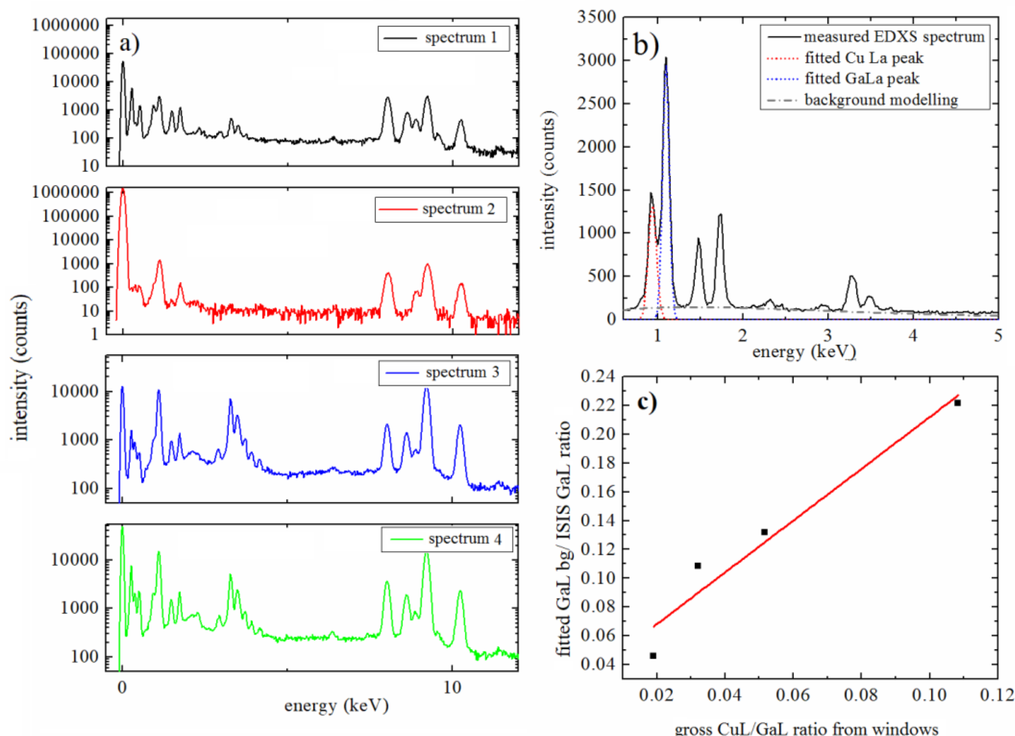

Figure 103 a) four spectra from (In) GaN nanowires of different thicknesses and locations on Cu support grid, displayed on log scale, b) modelled background intensity and fit of Cu_L and Ga_L lines by Gaussian functions, c) linear relationship between relative Ga_L background under Ga_L line and ISIS Cu_L/Ga_L ratio (window integrals).

The total intensity in maps can be calculated by adding the intensities at each pixel. Then the proportion of the Ga_L background intensity to be subtracted from the gross peak measurement can be obtained from Figure 103 c). The results for the three nanowires are listed in Table 9.

nanowire thickness (nm)	Cu_L intensity	Ga_L intensity	Ga_L background of windowing gross Ga_L intensity from ISIS
66	1858	21886	0.18481
217	5132	59937	0.18612
375	18463	232040	0.17523

Table 9 evaluated CuL, GaL intensities and relative GaL background for the three nanowires

Thus, reliable background values can be subtracted from the Ga_L maps. The In_L and Al_K maps are very noisy and also need to be background corrected. Here, we evaluated elemental maps of Cu_L, Si_K, S_K and Ti_K, calculated their averages and then subtracted correspondingly interpolated constants from the above maps to avoid a further increase of the noise. Then, background corrected Ga K/L ratio maps were used to derive maps for the k^* factors as shown in Figure 104 for the 66 nm thin nanowire as an example. The evaluated In_L and Al_K background of the maps amounted to only 0.2 and 0.1 counts, respectively, showing the sensitivity of the technique and that simple integer maps from multi-channel analyser outputs are not sufficient accurate if the absolute counts rates are low.

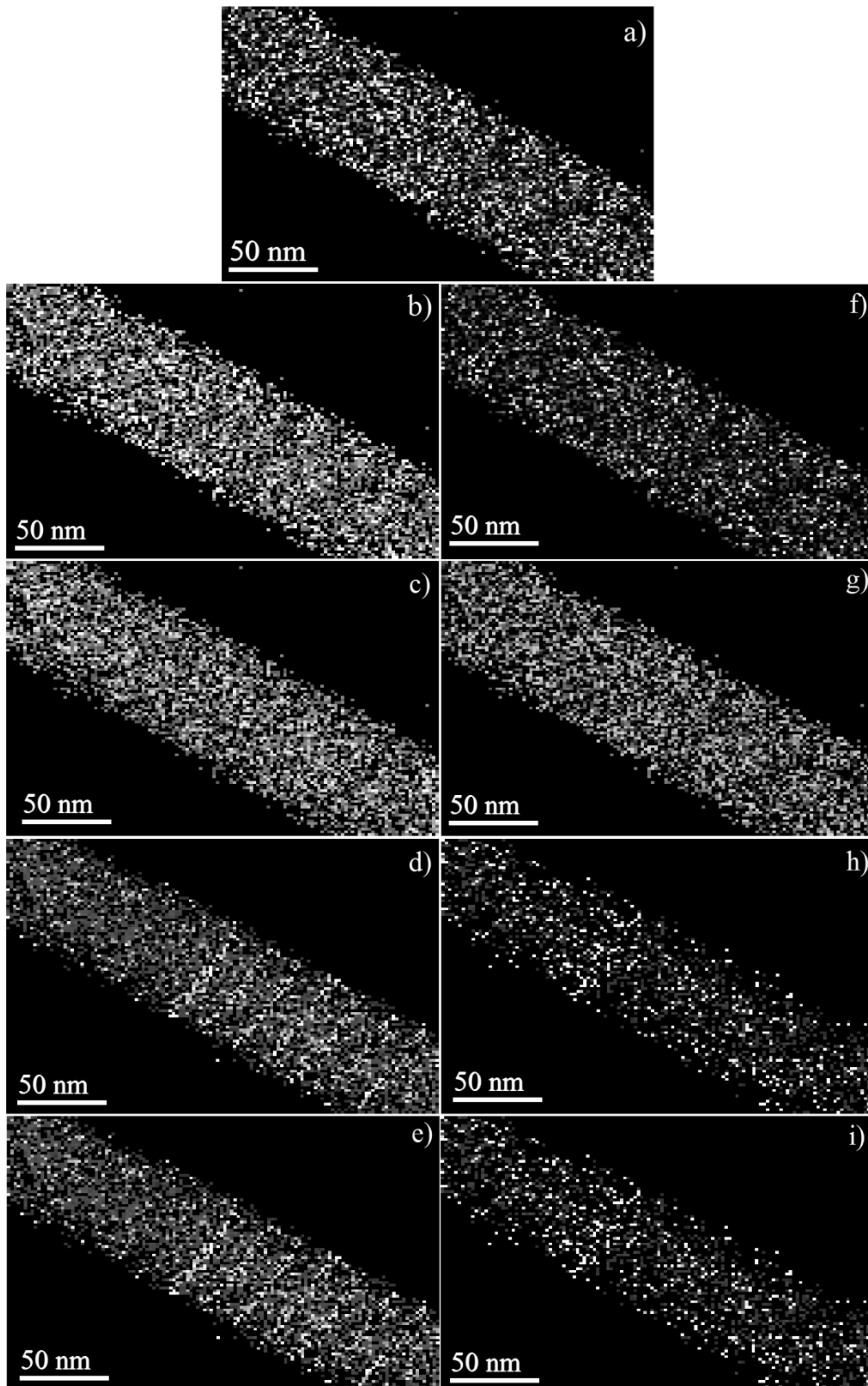

Figure 104: maps for the 66 nm thin nanowire of a) Ga K/L ratio after optimal background correction (min=0, max=3.36), b) $k^*_{InL, GaK}$, c) $k^*_{InL, GaL}$ d) x_{In} calculated from Ga_K, e) x_{In}

calculated from Ga_L, f) $k^*_{AlK,GaK}$, g) $k^*_{AlK, GaL}$, h) y_{Al} calculated from Ga_K, i) y_{Al} calculated from Ga_L.

Figure 104 show that the maps of indium content, $x_{In.}$ and the aluminium content, $y_{Al,}$ calculated from the corresponding k^*-factors for Ga L- and Ga K-lines are qualitatively similar. The InGaN quantum wells are well visible in Figure 104 d) and e), while the AlGaN layer on top is only faintly visible in Figure 104 h) and i).

To check quantitative consistency of results from K- and L-lines, line profiles have been integrated perpendicular to the layers over the whole maps for 66 nm and 217 nm nanowires. While the 375 nm thick nanowire line profile has been integrated excluded the red triangle region in Figure 100 c), where the In_L and Al_K signal are almost vanished in Figure 102 c) and f). The results are plotted in Figure 105.

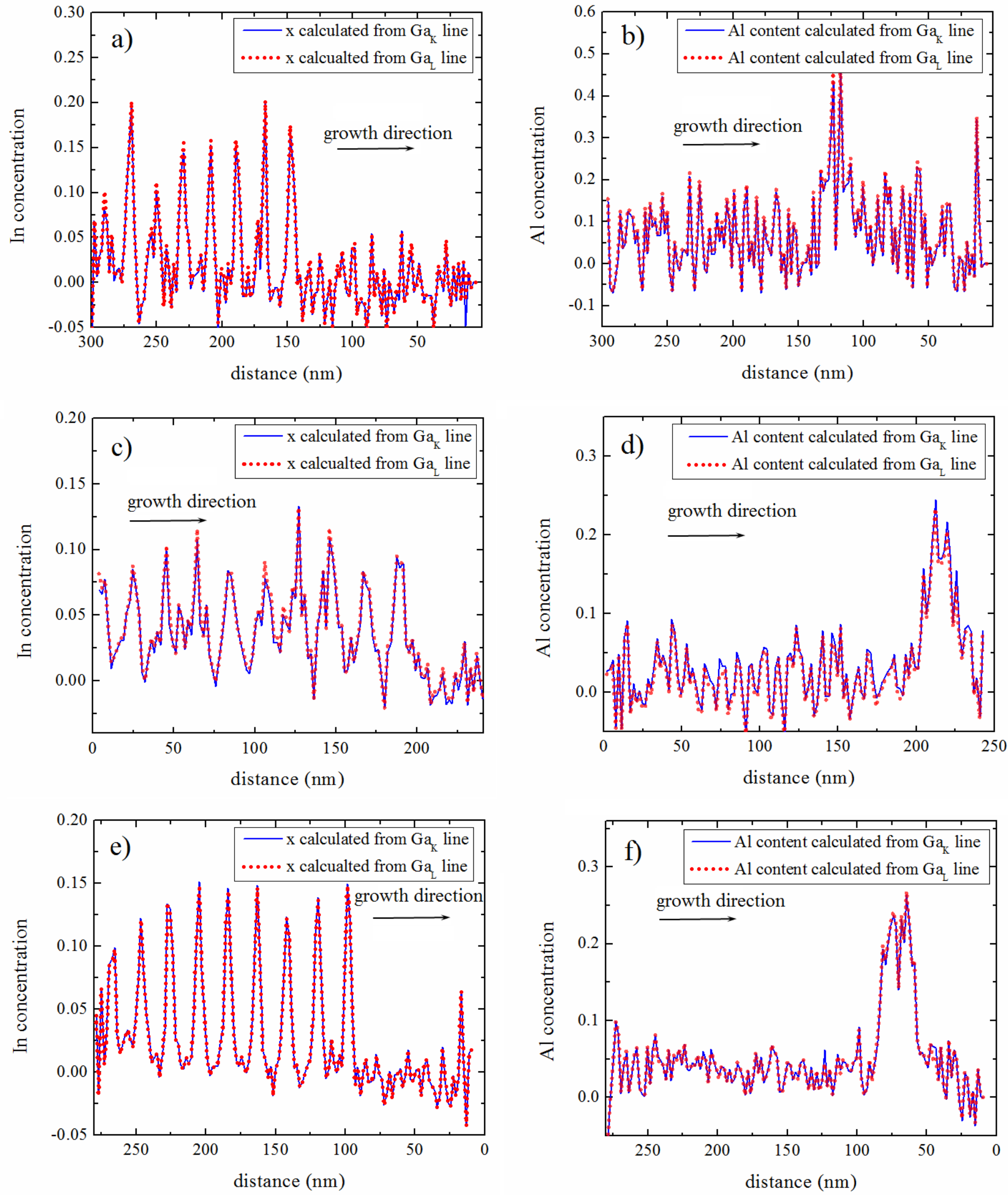

Figure 105: profile of x_{In} (left column) and y_{Al} (right column) calculated from Ga_K and Ga_L for (a, b) 66 nm thin nanowire, (c, d) 217 nm thick nanowire, (e, f) 375 nm thick nanowire.

As shown in Figure 105, the values of x_{In} and y_{Al} profiles in the GaN region to the right are close to zero, which indicates a satisfactory background subtraction for both In_L and Al_K. The In and Al content calculated from Ga_K and Ga_L lines give consistent results. The x_{In} profiles are sharp and clear within the noise level. As observed in Figure 105 b), the y_{Al} profile for the 66 nm thin nanowire is very noisy. The mean Ga K/L ratio of the 66 nm thin nanowire is ~2.5,

which is higher than for the 217 nm thick nanowire for which it is only ~1.4. As observed in Figure 100 a), the investigated thin nanowire is surrounded by two much thicker nanowires that may absorb some of the low energetic Ga_L X-rays, which leads to the sample appearing thicker in X-ray absorption correction than it actually is [2]. Similarly, the Al_K X-ray will be strongly absorbed, thereby reducing the Al peak in the concentration profile, although this is difficult to judge in view of the poor signal to noise ratio.

Applying the same approach to the thicker GaN nanowires in Figure 101 b) and c), the estimated average background of In_L and Al_K for 375 nm thickness were found to be 0.72 and 0.40 counts, while for the 217 nm thick nanowire the In_L background was 0.14 counts and the Al_K background 0.15 counts. The integral x_{In} and y_{Al} profiles for both nanowires x are also shown in Figure 105. The Al concentration within the AlGaN layer for the 375 nm thick nanowire is measured as y_{Al}=0.23±0.04.

As shown in Figure 105, the x_{In} and y_{Al} profiles calculated from Ga_K, Ga_L and Al_K for both thin and thickest nanowire are consistent: the x_{In} profile for the 375 nm thick nanowire is similar to that of the 66 nm nanowire, with peak values in the range x_{In}=0.17±0.02 whereas the x_{In} profile calculated for the 217 nm thick nanowire appears broader and lower in average In concentration, which may be explained by some residual tilt of this nanowire around of short axis, the Al concentration within the AlGaN layer for the 375 nm thick nanowire is measured as y_{Al}=0.23±0.04. The y_{Al} profile for the 217 nm thick nanowire is similar to that of the 375 nm thick nanowire, however, yielding y_{Al}=0.26±0.04, as for this much thicker layer a blur of the concentration profile due to crystal tilt is less relevant than for the thinner quantum wells.

To accurately determine the In concentration the x_{In} profile has been fitted with a Gaussian function for the 375 nm thick nanowire (Figure 106 a)). For each individual InGaN quantum well; the average In distribution profile can then be constructed by using the mean value of FWHM and integral area from each Gaussian peak. Since the nanowire FWHM from ADF

imaging was measured as 4.5-5 nm in Figure 100, the scattering of the electron beam into the GaN region will lead to a decrease in the apparent In peak concentration. Therefore, the measured In concentration profiles need to be deconvolved with the correspondence beam broadening function to get a reliable measurement of the absolute In concentration profile. As the In profile is integrated perpendicular to the growth direction, only beam broadening along the growth direction needs to be considered. Also the beam broadening effect is stronger in the centre of nanowire than in its side facets, therefore the In profile is mainly determined by the beam broadening function in the centre region of the nanowire. Here the beam broadening function correlated with nanowire projection thickness in a thin foil can be used for deconvolving the In profile as an approximation. The beam broadening function (BBF) for a 66 nm, 217 nm and 375 nm thick foil has been simulated and is shown in Figure 106 b) [14].

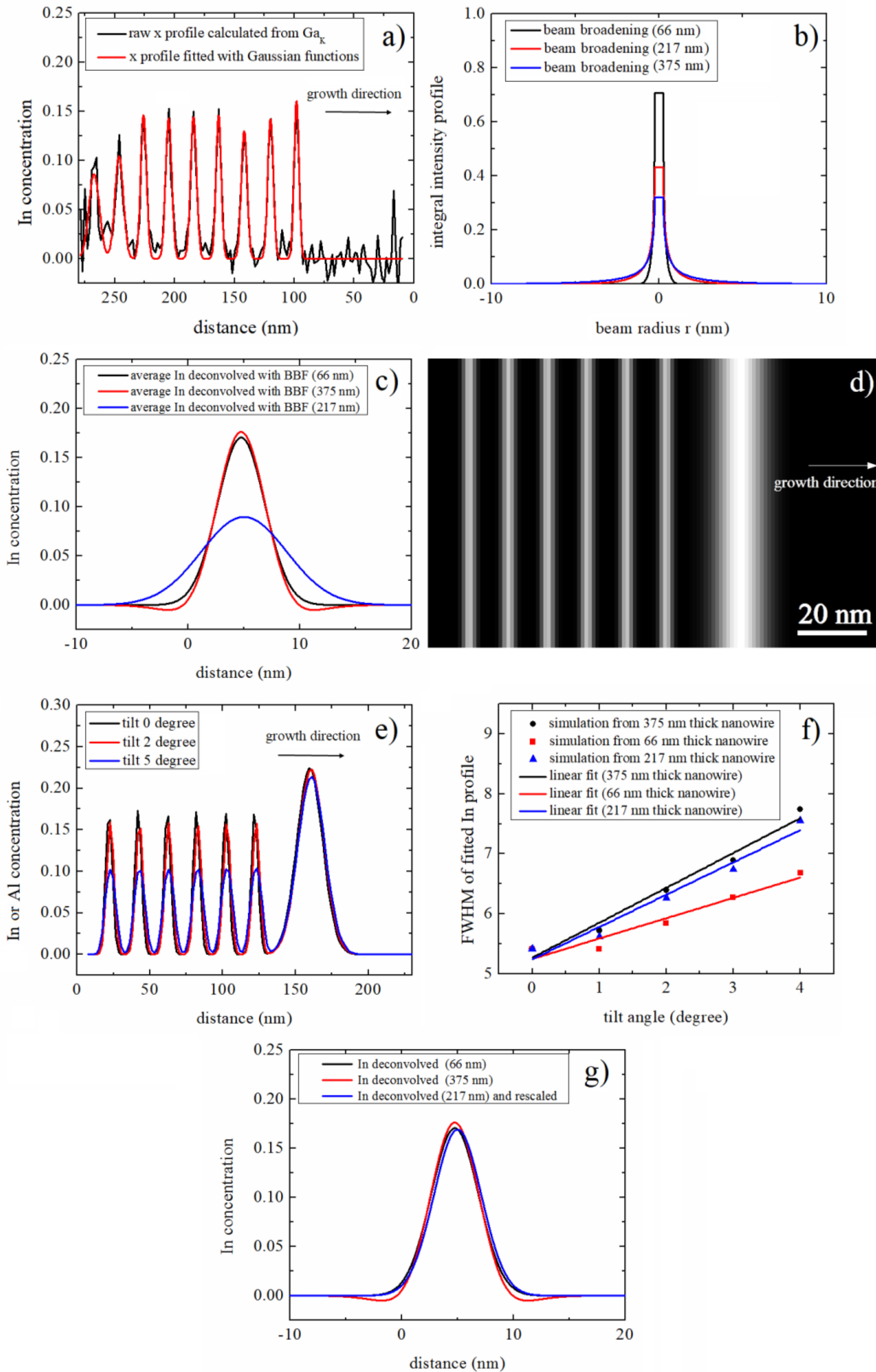

Figure 106: a) In profile from 375 nm thick nanowire with Gaussian fits, b) normalized beam profile with beam broadening due to multiple electron scattering in 66 nm, 217 nm and 375 nm thick $In_{0.2}Ga_{0.8}N$, c) deconvolved average In profiles, d) simulation of In/Al concentration profile of InGaN quantum well and AlGaN layer, e) effect of tilt over an axis perpendicular to

the growth direction on the In/Al concentration profile, f) tilt angle versus FWHM of the averaged In profile, g) comparison of averaged In profiles after deconvolution for all three nanowires and rescaling of the profile for the 217 nm fitted nanowire to same FWHM, retaining the integral.

The absolute In distribution can be obtained by deconvolution of the averaged In profile with its corresponding beam broadening function. Such deconvolved x_{In} profiles are plotted in Figure 106 c), and the absolute In distribution profile for the 66 nm thin nanowire (maximum of $\hat{x}_{In}$=0.171) is in good agreement with the In profile evaluated from the 375 nm thick nanowire (maximum $\hat{x}_{In}$=0.177), while the In profile for the 217 nm nanowire is much broader and underestimates the peak In concentration. If this nanowire lies inclined on the carbon thin film, the electron beam direction may no longer be perfectly perpendicular to the InGaN/AlGaN interfaces, resulting in an apparently broader In profile with decreased maximum In concentration. This hypothesis has been tested by simulation of the tilt influence on In and Al distributions as demonstrated in Figures 7 d) and e).
Figure 106 e) shows that the FWHM and maximum peak concentrations of the In profiles are strongly influenced by tilting the sample over an aixs with a component perpendicular to the growth direction, and the tilt angle follows a linear relationship with the FWHM of the fitted In distribution, shown in Figure 106 f). Tilting a 217 nm thick nanowire by 5° perpendicular to its long axis, the apparent FWHM of the InGaN layers increases from 5 nm to 8nm, which correlates well with the experimental observation. Compressing the FWHM of In profile from 8nm to 5nm while retaining the integral of the total amount of indium measured, the resulting rescaled profile would be in good agreement with the In concentration quantified from the 66 nm thin and the 375 nm thick nanowire (Figure 106 g)). Therefore, the peak In concentration in the InGaN quantum wells is believed to be $\hat{x}$=0.174±0.014.

From Figure 106 c), a sample tilt of ~5° would have negligible ($\Delta x \leq 0.01$) effect on the apparent maximum concentration of the Al profile since the AlGaN layer is much thicker than the InGaN quantum wells. This explains the consistency of the Al quantification result obtained from the 217 nm and the 375 nm thick nanowire, while the Al K signal of the thinnest nanowire is too noisy to be to be interpreted quantitatively.

Photoluminescence spectra were recorded from a wider region of the as-grown sample and from the fabricated nanowire array, and are compared in Figure 107. Both samples were illuminated with a 325 nm wavelength He-Cd laser, the emission was monochromated by a 0.5 m monochromator and recorded by a cooled silicon charge-coupled device (CCD) camera.

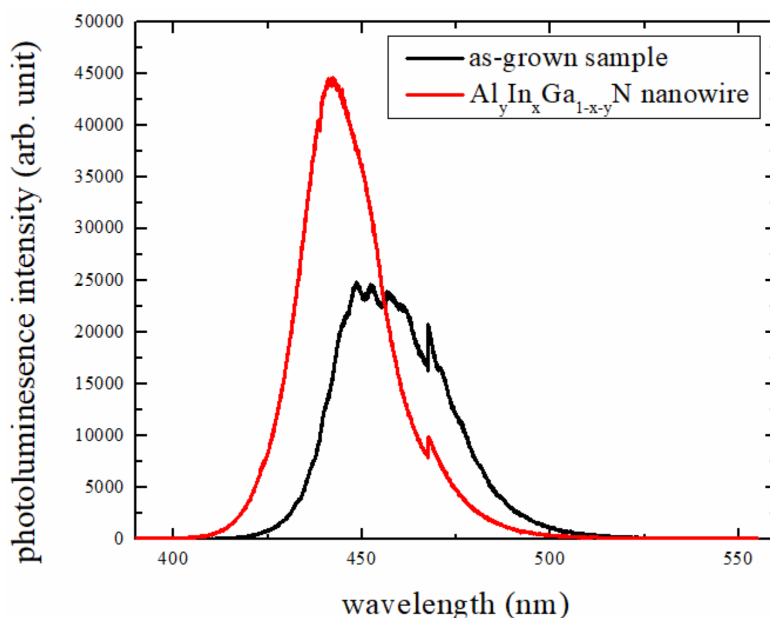

Figure 107: PL spectrum from the as-grown GaN/InGaN multiple quantum wells (black line) and of processed nanowire array with embedded InGaN and AlGaN layers (red line).

The as-grown sample shows several characteristic peaks at energies of 2.73±0.03 eV that are presumably due to the thin film interference, and a spike at 2.64eV, which is a detection artefact. The as-grown quantum wells can be assumed to be completely strained, so their In

concentration can be obtained from Vegard's law for the bandgap of an InGaN bulk alloy as reproduced in equation (46)

$$E_g(In_xGa_{1-x}N) = x \times E_g(InN) + (1-x) \times E_g(GaN) - bx\,(1-x) \qquad (46)$$

where E_g(GaN)=3.39eV and E_g(InN)=0.77eV are the bandgaps of GaN and InN [15, 16] and b is a bowing factor which is believed to be b=1.32eV for a fully strained and b= 2.87eV for a relaxed InGaN layer [17]. The In concentration correlated with the broad PL peak in the as-grown sample would then indicate values of x= 0.175±0.06, respectively, which correlates well with our above quantification from EDXS, the blue shift of the nanowire PL spectrum cannot be explained by strain relaxation alone [14] but probably result from a reduction of the piezoelectric effect after strain relaxation [18, 19].

6.4 Chapter conclusion

We have successfully evaluated the background effect on quantification of the In and Al content of very noisy maps of thin GaN/InGaN quantum wells. Accurate background subtraction will lead to consistent results of the In and Al concentration calculated from Ga_K and Ga_L lines. However, for thin InGaN quantum wells, the beam broadening effect and small residual tilts of the sample will lead to a broadening of the apparent In distribution profile which can result in underestimating their maximum In concentration. To determine the correct In profile, the measured In distribution profile needs to be deconvoluted by this broadening. The result obtained after deconvolution correlated well with the In concentration measurement near the zone axis. From the PL measurement, the In concentration extracted from the optical emission spectrum agrees extremely well with the In concentration determined from EDXS.

References

[1] G Cliff and G W Lorimer (1975), The quantitative analysis of thin specimens. *J. Microsc.* **103**, 203-207.

[2] H J August and J Wernisch (1987), A method for determining the mass thickness of thin films using electron probe microanalysis. *Scanning*. **9**, 145-155.

[3] M Watanabe, Z Horita, and M Nemoto (1996), Absorption correction and thickness determination using ζ-factor in quantitative X-ray microanalysis. *Ultramicrosc*. **65**, 187–198.

[4] T Walther and X Wang (2016), Self-consistent method for quantifying indium content from X-ray spectra of thick compound semiconductor specimens in a transmission electron microscope. *J. Microsc.***262**(2),151-156.

[5] H Harrach, P Dona, B Freitag, H Soltau, A Niculae and M Rohde (2009), An integrated silicon drift detector system for FEI schottky field emission transmission electron microscopes. *Microsc & Microanal*. **15**, 208-209.

[6] B Bonef, M Catalano, C Lund, S P Denbaars, S Nakamura, U K Mishra, M J Kim and S Keller (2017), Indium segregation in N-polar InGaN quantum wells evidenced by energy dispersive X-ray spectroscopy and atom probe tomography. *Appl. Phys. Lett*. **110**,143101.

[7] X Zhang, M Belloeil, P H Jouneau, C Bougerol, B Gayral and B Daudin (2016), Chemical composition fluctuations and strain relaxation in InGaN nanowires: the role of the metal/nitrogen flux ratio. *Material Science in Semiconductor Processing*. **55**, 79-84

[8] H Tan, C Fan, L Ma, X Zhang, P Fan, Y Yang, W Hu, H Zhou, X Zhuang, X Zhu and A Pan (2016), Single-crystal InGaAs nanowire for room-temperture high-performance near-infrared photodetectors. *Nano-Micro. Lett*. **8** (1), 29-35.

[9] A Johannes, D Salomon, G Martinez-Criado, M Glaser, A Lugstein and C Ronning (2017), In operando x-ray imaging of nanoscale devices: Composition, valence and internal electrical fields. *Sci. Adv*. **3**, eaao4044.

[10] H Bender, F Seidel, P Favia, O Richard and W Vandervorst (2017), X-ray absorption in pillar shaped transmission electron microscopy specimens. *Ultramicrosc*. **177**, 58-68.

[11] L Lari, T Walther, K Black, R T Murray, T J Bullough, P R Chalker, C Cheze, L Geelhaar and H Riechert (2010), GaN, AlGaN, HfO_2 based radial heterostructure nanowire. Journal of Physics: Conference Series. **209**, 012011.

[12] H Morkoc (2008) Handbook of Nitride semiconductor and devices. Wiley, Weinheim. **Vol 1**, ISBN:978-3-527-40837-5.

[13] X Wang, M P Chauvat, P Ruterana and T Walther (2017), Effective absorption correction for energy dispersive X-ray spectroscopy in a scanning transmission electron microscope: analyzing the indium distribution in rough samples of InGaN alloy layers. *J. Microsc*. **268**, 248-253.

[14] T Walther (2004) Development of a new analytical electron microscopy technique to quantify the chemistry of planar defects and to measure accurately solute segregation to grain boundaries. *J. Microsc*. **215**, 191-202.

[15] M R Islam, M R Kaysir, M J Islam, A Hashimoto, and A Yamamoto (2013), MOVPE growth of $In_xGa_{1-x}N$ ($x \approx 0.4$) and fabrication of homo-junction solar cells. *J. Mater. Sci. Technol*. **29**(2), 128-136.

[16] T Matsuoka, H Okamoto, M Nakao, H Harima and E Kurimoto (2002), Optical bandgap energy of wurtzite InN. *Appl. Phys. Lett.* **81**, 1246-1248.

[17] G Orsal, Y El Gmili, N Fressengeas, J Streque, R Djerboub, T Moudakir, S Sundaram, A Ougazzaden and J P Salvestrini (2014), Bandgap energy bowing parameter of strained and relaxed InGaN layers. *Opt. Mat. Exp.* **4**(5), 1030-104.

[18] L H Peng, C W Chuang and L H Lou (1999), Piezoelectric effects in the optical properties of strained InGaN quantum wells. *Appl. Phys. Lett.* **74**(6), 795-797.

[19] N I Bochkateva, A L Bogatov, R I Gorbunov, F E Latyshev, A S Zubrilov, A I Tsyuk, A V Klochkov, Y S Lelikov, Y T Rebane and Y G Shreter (2009), Effect of the electric field on the intensity and spectrum of emission from InGaN/GaN quantum wells. *Semiconductors*. **43** (11), 1499-1505.

Chapter 7

7. Conclusion

In this thesis, the microstructure, thickness, element distribution, phase separation and bandgap of $In_xGa_{1-x}N$ thin films and $Al_yIn_xGa_{1-x-y}N$ nanowires have been investigated. The analyses have been performed by EDXS and EELS in analytical transmission electron microscopy.

In chapter 3, the k^* factor in the self-consistent absorption correction method is simulated by Monte Carlo simulation (CASINO), an iterative process is then introduced to obtain convergence of the x value, calculated from Ga K and Ga L X-ray lines. Comparing with normal ZAF correction and the Zeta-factor correction method, the absolute sample thickness, material density or incident beam current no longer needs to be known in order to obtain a reliable In concentration. A series of $In_xGa_{1-x}N$ with nominal In concentration ranges from 0 to 1 are investigated. The In concentration obtained from the absorption correction method can serve as a calibration point for the corresponding bulk plasmon energy research in chapter 4. The approach is then applied to research the $In_{0.68}Ga_{0.32}N$ thin films grown on sapphire substrates where a pronounced In-rich area is observed underneath the big island. The volume ratio of the In-rich region seems to increase exponentially as the island height grows, the high In content area produced by In segregation is probably responsible for the formation of the big island. However, whether the areas of high In content are pure $In_xGa_{1-x}N$ with $x>0.8$, InN or even contain metallic In cannot be answered from the X-ray maps.

In chapter 4, the bulk plasmon energy associated with its corresponding In concentration is investigated. The plasmon energy position can be determined by fitting the experimental plasmon peak in low-loss EEL spectra with the Lorentz function. By using the calibrated In concentration, which was found from the absorption correction method in chapter 3, the results show the plasmon energy decays linearly as a function of In concentration. The analysis of phase separation in InGaN is based on the constructed reference plasmon and core loss spectra

for each $In_xGa_{1-x}N$ ternary, with different x value. The MLLS fitting is then introduced to fit experimental spectrum, with GaN, InN and InGaN reference spectra. The degree of phase separation and average In concentration can be determined by the fitting weights of GaN, InN and InGaN. The analysed results from $In_{0.59}Ga_{0.41}N$ and $In_{0.68}Ga_{0.32}N$ experimental spectra demonstrate a consistent degree of phase separation, quantified from plasmon and core loss. Also, the average In concentration determined from EEL spectra seems to correlate well with the corresponding EDXS measurements in chapter 3.

The InGaN phase separation analysis method is then applied in the STEM EELS, where the phase separation in the nanoscale can be directly observed. In chapter 5, the approach is first introduced to process the spectrum image of a big island structure in $In_{0.68}Ga_{0.32}N$. The spectrum image is recorded by conventional STEM which was operated at 200kV (JEOL JEM 2010F), the degradation of energy resolution caused by aberration decreases the spectra quality in the spectrum image, indicating that accurate quantification is difficult for conventional STEM. A similar island structure is then investigated by using advanced aberration corrected low voltage TEM equipped with a monochromator (NION Ultra STEM 100). High quality spectrum images lead to consistent phase separation analysis results, from plasmon and core loss. The average In concentration maps, calculated from spectrum images, are in a good agreement with the In concentration maps determined from EDXS.

In chapter 6, the absorption correction method is applied to evaluate the In distribution in a $Al_yIn_xGa_{1-x-y}N$ nanowire system, the quantified result is verified by PL spectra. A satisfactorily quantified result can be obtained if proper EDXS spectrum background modelling and sample geometry simulation is introduced. The analysis approach in this chapter is mainly focused on the accurate quantification from noisy and low X-ray count element maps, which will benefit chemistry research in InGaN based nanostructures.

7.1 Suggestion for future work

My future work will be based on the preliminary EELS and EDXS results obtained from this project. From the problem stated in the chapter 5, the bandgap determination from valence EELS is currently insufficient to provide an accurate result. In future work, cathodoluminescence seems to be an alternative way to evaluate the bandgap of semiconductors. Most commercial CL state energy resolution better than 1meV depending on signal wavelength, while high quality EELS recorded from the most advanced aberration corrected and monochramated TEM can only achieve 0.15eV at present. Therefore, CL seems to be more reliable than low loss EELS in bandgap measurements. However, as CL suffers from the electron beam broadening effect and photon absorption, in a similar fashion to EDXS, the accurate measurement for CL is strongly dependent on the sample thickness, sample surface geometry, and detector take-off angle. The situation deteriorated for a phase separated InGaN sample, as the InN is surrounded by InGaN. The infrared emission from InN allows proper absorption to take place in InGaN, resulting in a weak or absent InN emission signal in CL spectrum, therefore it is worth developing a duel EELS and CL measurement approach to explore how the material chemistry is related to its emission mechanism.

As observed in chapter 3 and 5, the In-rich region constitutes of a large fraction of InN. It would be interesting to apply our low-loss EELS analysis method to in-situ TEM, with a proper growth kit the formation process can be explored. As InGaN is an electron beam sensitive material, basic research should be conducted prior to applying our method in-situ. For example, incident electron dose rate influence on InGaN atomic structure, strain, and chemical properties; InGaN growth precursor EELS research; EELS measurements for InGaN specimens at

different temperatures, and EELS recorded from an environmental TEM, to observe different gas flow influences on EELS spectrum quality.

Recently, most of the advanced TEMs are equipped with four EDXS detectors (X detector) to enhance the recorded X-ray intensity, it would therefore be interesting to apply our absorption correction method to that system. It will benefit the quantification of materials chemistry under low electron beam current conditions, which can serve as a supplementary tool to support the in-situ EELS analysis of the mechanism of high In content InGaN growth.